# INVESTIGATION OF A JET PUMP SYSTEM PERFORMANCE FOR CLEANING OF PHOTOVOLTAICS PANELS

SAMI ALSALEH

**Thesis submitted to the University of Nottingham for the degree of Doctor of Philosophy**

**March 2017**

# Abstract

This study is to investigation and development of the PV self –cleaning impacted of dust that would enable a wider deployment of solar photovoltaic systems in the Middle East and Gulf region which enjoys abundant solar radiation throughout the year, and where sandstorm dust and elevated ambient temperature persist. The dust reduces the power generated by the solar devices or hinders the visibility through windshields. The research intends to combine a number of technologies to assist and improve the operational performance of photovoltaic (PV) systems. This investigation covered some of systems which employed PV self-cleaning techniques to remove the particles of dust from the PV panel surface.

Regular cleaning of the panels is often necessary to prevent serious degradation of their performance, especially in regions with dusty climates. However, manual cleaning of solar panels, especially in the context of large installation, can be a labour-intensive process and thus often prohibitively costly. Even in small buildings, cleaning a PV system can involve complicated issues of access that might require the intervention of specialist staff. Some of the technologies involve the use of electrodynamic screens for electrostatic dust removal, robotic cleaning tools, vibrating mechanisms featuring piezo-ceramic actuations, as well as $TiO_2$-treated chemical or nano-films. Nevertheless, none of these technologies has to date been able to establish itself as an industry standard and achieve the necessary commercial breakthrough.

The numerical and experimental results demonstrate that the diameter of the nozzle throat has a significant impact on the mass flow rate of the water vapour; some results in a high mass flow rate whereas a larger diameter leads to a lower rate. The nozzle diameter also affects the magnitude of the velocity and the mass fraction of the water

.

vapour. It was found that a nozzle throat of a 5 mm diameter above the PV surface by 50 mm with 222m/s is optimum for the jet pump design for water vapour production and dust removal covering sufficient PV surface area. Moreover, variations in the length of the mixing chamber have a significant effect on the mass flow rate of the water vapour. It was found that the mass flow rate of the water vapour is higher in a shorter mixing chamber than it is in a longer mixing chamber. Therefore, to be more effective, a jet pump should have a smaller nozzle diameter, a shorter mixing chamber and a smaller jet pump throat.

In light of the above, self-cleaning technologies could present the perfect solution to these issues and help address many of the obstacles preventing solar panel technology from becoming more widely adopted. This would help reduce dependence on the fossil-fuel based energy resources which can be devoted to the generation of national revenues and also leads to a reduction of CO2 emissions to the environment.

# Acknowledgments

الحَمْدُ لله

The first and the last to thank is Allah, for his blessings and mercy without which I wouldn't have existed and consequently, this work wouldn't have existed either.

I would like to express my sincere thanks and gratitude to my supervisors Dr Siddig A Omer and Dr Boukhanouf Rabah for patiently guiding me to conduct the whole research project.

Thanks and praise to Allah, who blessed me with the most beautiful parents and family who were there for me; with their love, support and the many prayers they said for me.

I would like to thank my colleagues and friends at the Department of Architecture and Built Environment for the beautiful days and memories.

# Nomenclature

NOMENCLATURE
A = Area $m^2$
$C_p$ = specific heat at constant pressure kJ/kg-K
$C_v$ = specific heat at constant volume kJ/kg-K
d = Diameter m
$h_g$ = enthalpy, saturated vapour kJ/kg
$h_g$ = enthalpy, saturated liquid kJ/kg
k = index of expansion
M = Mach number
$\dot{m}$ = mass flow rate kg/s
$N_n$ = Nozzle pressure ratio
$N_s$ = critical pressure ratio
P = Pressure Pa
R = gas constant kJ/kg-K
T = temperature K
U = velocity m/s
ω = entrainment ratio
ŋ = isentropic efficiency
ρ = density $kg/m^3$
$\tau$ = stagnation temperatures ratio

Subscripts
d = diffuser
e = evaporator
i = initial stagnation state of primary stream
n = nozzle
o = initial stagnation state of secondary stream
p = primary stream
s = secondary stream
su = sound
t = nozzle throat
$T_c$ = enthalpy in a condenser
$T_e$ = enthalpy in an evaporator
$T_g$ = enthalpy in generator
x = condition at primary nozzle exit
1 = condition of mixed stream before normal shock
2 = condition of mixed stream after normal shock
3= condition of mixed stream at diffuser exit

Superscripts
* = critical

# Contents

.

.

# List of Figures

.

.

.

.

.

# List of Table

# Chapter 1: Introduction

## 1.1 Background

This research aims to investigate and develop a PV self –cleaning system using air and water-mist jet nozzle that would enable a wider deployment of solar photovoltaic systems in the Middle East and Gulf region which enjoys abundant solar radiation throughout the year, and where sandstorm dust and elevated ambient temperature persist. The research intends to combine several technologies to assist and improve the operational performance of photovoltaic (PV) systems. These include cleaning of PV panels by use of a combined innovative preparation that utilises high-pressure air and water vapour mix for PV panels cleaning and cooling. The system will employ PV self-cleaning techniques including application of compressed air, carried along water-mist jets using the special design of jet pump to remove the particles of dust from the PV panel surface.

## 1.2 Aim and objectives

The core aim is to use an air jet combined with water vapour to enhance the PV surface cleaning in the dusty area as Gulf region.

The research objectives have been summarised as follows;

1- Review for Photovoltaic (PV) energy system, the effect of heat and dust on PV, self-cleaning techniques system.
2- Investigation a PV self-cleaning system and jet pump device using an air compressor and water vapour as a secondary flow.
3- Designed air and water vapour jet pump capable of producing an appropriate mixture jet for PV cleaning to reducing the use of the water.

4- The air and water vapour jet pump nozzle will be confirmed following computational fluid dynamic analysis (CFD), which should help to optimise the jet pump nozzle and diffuser geometry (primary nozzle and diffuser dimensions), size and distribution of the nozzles to fulfil the purpose.

5- Laboratory tests will be performed for the optimised nozzle to ensure proper nozzles design and determine the air compressor and water supply rates for a range of PV panel sizes and tilt angles suitable for Gulf climate conditions.

## 1.3 Problem statement

This research proposes the use of a special design of jet pump able to use a high-pressure air to entrain water vapour as a secondary fluid, producing an air jet containing sufficient water mist for cleaning of the PV panels. The jet pump nozzles will be arranged along the upper frame edge of the PV panels, in a way to provide a well distributed high-speed mixture jets able to clean off the dust in an automated way.

The amount of air flow rate and the corresponding water consumption rate and hence the power requirement to operate the air compressor are functions of the jet pump design specifications, the type and amount of the dust and surface tilt of the PV panels, and can be estimated only after a thorough CFD modelling for the varying conditions .

The laboratory tests and the computer modelling will provide information on the fundamental design parameters of the PV cleaning devices and will provide dynamic information and assess the performance of the system under real conditions difficult to simulate in the laboratory environment.

Computer modelling and laboratory testing will assist design optimisation of the field demonstration units.

However, the air combined water vapour jet pump design will be the subject of this research investigation to establish a correlation between the air and water vapour entrainment ratio, dust particles size and dust density, with minimum water consumption. It is worth highlighting that in addition to the PV cleaning process, the jet pump will also contribute in rejecting the heat energy extracted from the PVs during the PV cooling process, through water evaporation, as well as through air-water mist blowing and therefore the operation of the proposed technologies complements each other to improve the operational performance of the PV panels.

## 1.4 Research design

The main aim of this research project is to develop a device that is able to remove dust particles from PV panels, through a self-cleaning mechanism, through the use of the jet pump system. Design and development of high-pressure air and water vapour jet pump nozzle that utilises the heat extracted from PV panels, and capable of dust particles removed from the PV panel surface.

This would help reduce dependence on the fossil-fuel based energy resources which can be devoted to the generation of national revenues and also leads to a reduction of CO2 emissions to the environment.

An appropriate jet pump will be designed and fabricated to enhance and perform the cleaning process of the PV panels under Gulf climate conditions. The design parameters are determined by the ability of the produced mixture jet to thoroughly clean the PV panel surface at speed sufficient to flush off the dust particles broken down by the photocatalyst. The jet pump will first be designed and evaluated using computational fluid dynamic (CFD) analysis and optimised for a range of PV surface sizes and compressed air and water consumption rates. The optimum designs will be fabricated and tested in the laboratory.

Measurements will be made of the primary air flow rate, water consumption rate, jet speed at the exit of the diffuser and the corresponding temperatures and pressures. A high-resolution camera will be used to visualise the surface quality of the PV glass under different air/water-mist mixture jet form and speed. The test will be repeated with different air flow rate and water temperature to simulate the real conditions under Gulf climate. PV panels of different glass type and texture will be assessed.

During the tests, the air compressors power requirement will be evaluated. This will lead to specifications of the jet pumping capacity for varying PV panel sizes. The assessment will also involve the distribution of the jet pump nozzles along the PV panel upper frame for effective cleaning of the panel with minimum use of water and energy.

Manual valves will be used for the suction line of the jet pump, to ensure the release of water vapour in stages. First, the jet pump will use air jet alone to blow off the dust, and when the primary air flow is stabilised, the suction valves will be opened to allow water into the suction chamber for mist production.

Following the cleaning process, the water valve will be closed and allow drying of the PV panels using air jet alone to avoid the formation of dust cementation on the wet surface. The cleaning process could also be initiated by the temperature of the cooling water, to ensure that the extracted heat is dissipated immediately, through the jet pump to enable effective PV cooling as well as PV cleaning.

Data from the laboratory tests will be used to verify results of the CFD model and these will be used to conclude and design of the prototype jet pump nozzle for the field prototype.

The study will be conducted in the following stages to achieve the predefined research objectives. The steps followed in this project approach:

1- Literature review on Photovoltaic (PV) energy system, the effect of dust on PV, self-cleaning Techniques system. This review contains some data from previous studies concerned with identifying the concept of Photovoltaic (PV) energy system, the effect of dust on PV, Self-cleaning Techniques system and types of these systems. Also literature review on for jet pump system. The data were collected by reviewing the literature concerning it; including books, journals and website. Google Scholar and Web of Science ® provide enormous data that have many kinds of articles and books as Business Premier Source, and Emerald Group Publishing Limited which finding the background and to learn about for Photovoltaic (PV) energy system and jet pump system, the effect of dust on PV, Self-cleaning Techniques system.

2- Creating the data collected from the literature to plan and develop an overall modelling and experimental analysis to include the necessary data to be examined as the mathematical equations for the jet pump system. Also, investigate the data via the modelling analysis through using the simulation software techniques to assess the system performance.

Develop the design and construct rig for the system via lab testing (experimental) to integrate jet pump with the PV system under several conditions for removing the dust. Also, this data will be gathered through observation and monitor and from reviewing the literature concerning it for evaluating and analysing the final data and to write some recommendations and conclusion after discussing all the results.

## 1.5 Structure of the thesis

The thesis is divided into eight Chapters, following this introductory Chapter, the work is presented in the following Sections:

**Chapter 1**- Background sets the stage for the thesis by introducing the concept of the PV self–cleaning impact of dust by using the air and water-mist jet pump nozzle, and the research objectives have been summarised with research design

**Chapter 2**- Literature review on for Photovoltaic (PV) energy system, the effect of dust on PV, self-cleaning Techniques system. This review contains some data from previous studies concerned with identifying the concept of Photovoltaic (PV) energy system, the effect of dust on PV, Self-Cleaning Techniques system and types of these systems.

**Chapter 3-** The concept of a jet pump and theoretical equations for a high pressure jet pump system, and modelling.

**Chapter 4**- Development of CFD simulation for a jet pump system, and set up the Fluent® program to use turbulence model.

**Chapter 5**- Results of CFD study of the jet pumps system and discuss visualise flow behaviour and explain the flows in a jet pump system.

**Chapter 6**- Simplified jet pump cleaning arrangement using the PV panel system and use the CFD to design and analysis the flow behaviour on PV surface.

**Chapter 7**- Laboratory rig set up and testing procedure, and design and assembly for the jet pump and PV panel, with validation of result with CFD result.

**Chapter 8**- Conclusions and future work with a review of the thesis-hypothesis and how the study contributes knowledge, and provides a summary of the thesis and indicate for further research.

# Chapter 2: Literature Review

## 2.1 Introduction

Over the past decades, the explosion in global population combined with the advent of modernisation to wider parts of the globe has meant that the demand for energy has continued to grow, most of which continues to be based on fossil fuel sources. However, in the context of the high pollution levels caused by fossil fuel extraction, and an increasing awareness and alarm over the dangers of climate change, the search for alternative renewable energy sources that are lasting, reliable and cost-effective has become more urgent and critical than ever. Over recent years, four main forms of such alternative energy sources have emerged: wind, solar, hydroelectric and geothermal energy, the adoption of which has varied greatly across the globe due to geographical, topological and other factors. For instance, hydroelectric dams are harder to build in non-mountainous regions and solar panels are not suited to the cloudy weather. While some regions, such as Japan, Australia and many African countries have naturally given prominence to solar energy, the US, Denmark or Germany have seen the emergence of wind turbines (Ishengoma and Norum, 2002). Meanwhile, several European nations have been increasingly integrating photovoltaic and wind energy into their future infrastructure plans (Blanco, 2009). In this context, one factor that has proven problematic for the use and implementation of solar panels has been the sedimentation of dirt and/or dust deposits on their surfaces, which can significantly hamper the performance and longevity of the panels, even leading to their failure (Sarver et al., 2013). In terms of solar Photovoltaic (PV) energy, while wind and water-based energy sources have been exploited for centuries, photovoltaic power has been a relatively modern development which has been gathering momentum steadily over the past few decades. At the basic level, solar panel technology involves electricity production by panels of serially-connected photovoltaic cells. The cells use captured photons to create a stable current by freeing electrons (Penick and Louk, 1998). As such, a panel's performance depends both on the materials and the process adopted in its construction, with more efficient materials being costlier. There are three main categories of solar panels: amorphous, monocrystalline, and polycrystalline (Messenger and Ventre, 2002). A panel's design, notably its size and the choice of components used (such as converters and solar trackers), depends principally on the power needs it is expected to address. Panels produce fluctuating and irregular levels of outputs (e.g. affected by changes in the sun's position, the panel's composition and environmental conditions). As such, converters help maximise the panel's performance by converting its variable output into constant voltages (Penick and Louk, 1998). Moreover, since panels can only accumulate power during sunlight hours, using their output at night requires the use of a storage solution, whether by transferring the output to the power grid or using a battery. However, the performance of PV solar collectors might be reduced by the rise of the cells temperature and the accumulation of the dust on the tops of PV panels. Hence, cooling and cleaning methods should be applied in PV system to improve the efficiency of PV cells. In this report, several approaches applied to do the self-cooling and self-cleaning on PV panels are introduced.

## 2.2 Factors Affecting PV System Performance

In terms of PV performance, solar panels performance is clearly affected by environmental factors, especially those relating to weather conditions, such as cloud presence and movements, temperatures and the sun’s position, many of which change on a seasonal basis. For instance, the light intensity is greater during the summer than in the winter due to changes in the sun's position (Intusoft, 2005; Bollinger, 2007; Sarver et al., 2013). A solar panel's positioning and angles are hugely consequential for its performance, though most panels use fixed-angle mounts positioned for a specific season or at an average angle based on summer and winter outputs. As such, in order to increase the number of hours a panel can generate power at peak efficiency levels, a power tracker is needed to adjust the panel's angle in accordance with the sun's changing movements. Moreover, changes in the temperature have a significant impact on photovoltaic cells, with increases in temperature leading to decreases in panel efficiency (although higher temperatures coincide with higher illumination levels) (Intusoft, 2005). Moreover, a system's design should clearly take into account key parameters such as the size of the panel, the type of converters, as well as the different storage options under various seasonal weather patterns (Ishengoma and Norum, 2002).

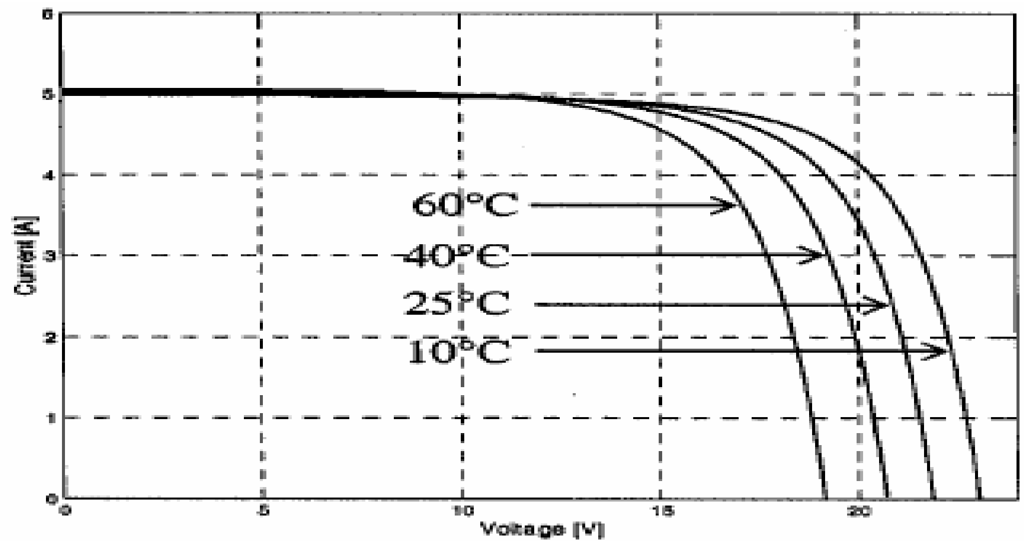


Figure 2-1: Voltage and Temperature Variations of a Photovoltaic Cell (Ishengoma and Norum, 2002).

Meanwhile, Figure 2-1 above shows the relationship between voltage and temperature, with a reduction in voltage as temperatures rise. The figure also shows that the generated power is proportional to the temperature. As such, when establishing the maximum energy for a specific time of year, the effect of temperature must be considered. Figure 2-2 shows the points where maximal power and voltage are achieved, which correspond to maximal cell outputs (Messenger and Ventre, 2002).

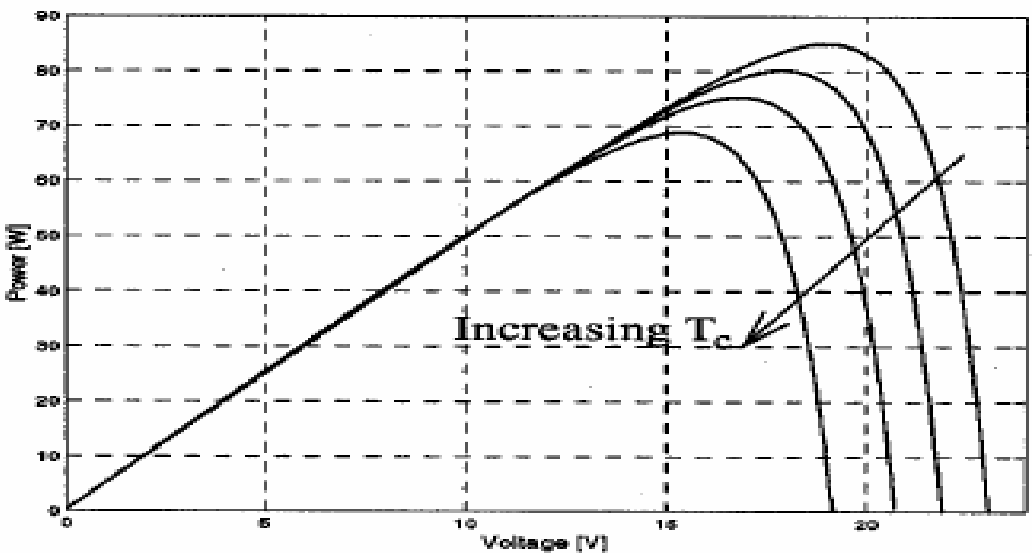


Figure 2-2: Output Power and the Effects of Temperature (Messenger and Ventre, 2002).

## 2.3 Dust effect

Although numerous factors are usually considered when examining PV system performance, one of the most significant factors is one that is often ignored, namely the presence of dust and dirt. As is to be expected, several studies confirm that the impact of dust is greater in some regions of the globe than others. Areas of greater impact include the Middle East, North Africa and Asia, where arid winds can accentuate the impact of the problem. Indeed, hours of exposure to dust in these areas produce the same level of damage to PV performance than usually occurs over months in other regions with milder climates. This is highlighted in Figure 2-3 which illustrates panel performance levels over time in the United States, Oman and Egypt as an example (Sarver et al., 2013).

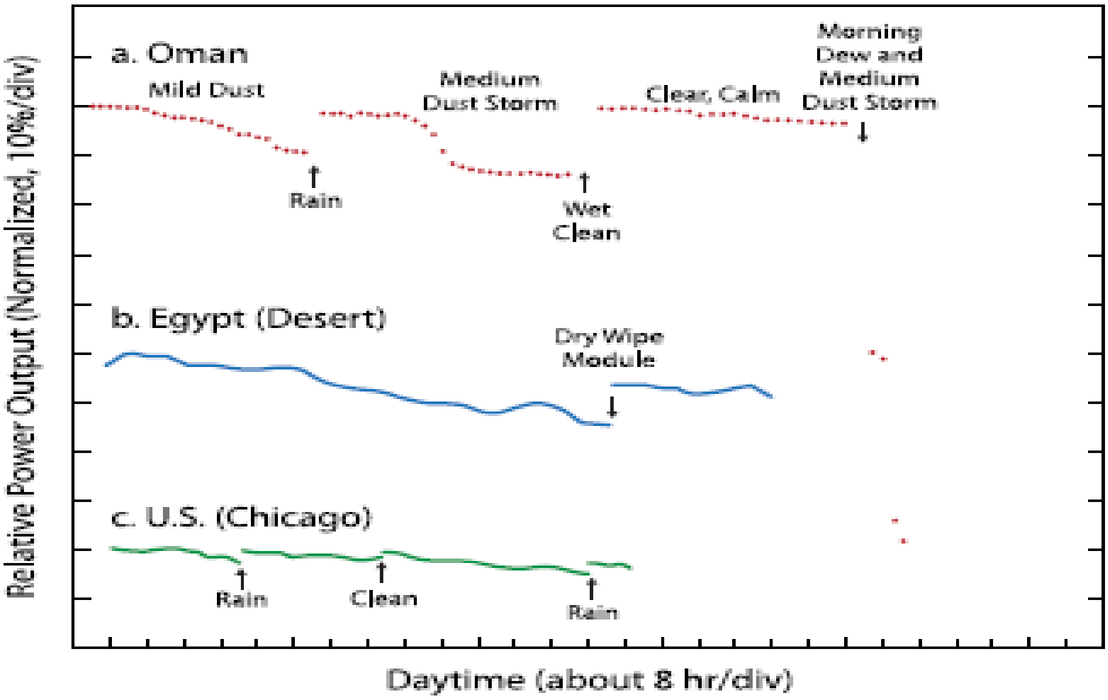


Figure 2-3: Comparison of PV module performances under various dust (Sarver et al., 2013).

Manifestations of hazards to PV panels are numerous and include bird droppings, dust deposits and water stains, all of which can degrade significantly the PV panel's performance. Indeed, PV module efficiency is estimated to be reduced by 10–25% as a result of losses related to damage to the inverter, the wiring, or the soiling of the module with dust and debris (Mani and Pillai, 2010). Of course, the susceptibility of PV panels to the damaging impact of dust reduces their appeal as an alternative energy source. As such, a thorough understanding of this phenomenon is essential in helping enhance PV technology's robustness in resisting the effects of dust. However, research on the topic remains limited, partly due to the complexities of the phenomena involved.

Broadly defined, the term ‘dust’ refers to solid particles that can be found in the atmosphere and are less than 500 µm in diameter (Mani and Pillai, 2010). Examples include dust lifted into the air by urban traffic, airborne particles caused by pollution, and particles emitted by volcanic eruptions. In the context of this study, dust can also refer to pollens (such as bacteria) and microfibers (from fabrics, carpets etc.) that are ubiquitous in the atmosphere. The two key factors that determine the characteristics of dust settlement on PV systems are the local environment and dust particle properties. Aspects of the local environment include weather conditions, environmental features (e.g. vegetation), and built environment characteristics (height, orientation and surface finish). Dust properties include chemical, biological and electrostatic properties; particle size, shape and weight; as well as dust aggregation or accumulation characteristics. Moreover, the surface finish of the PV panel surface is of great impact, since a sticky surface (i.e. one that is rough, furry, has electrostatic build-up or contains adhesives residues) presents a greater likelihood of dust accumulation than other factors. In terms of the effect of gravity, horizontal surfaces are more liable to collecting dust than vertical or inclined ones, although this depends greatly on wind conditions. Moreover, dust settlement tends to be hampered by high-speed wind and aggravated by the low-speed wind. However, the distribution of dust settlement at specific locations of the PV panel can be influenced by the PV system’s orientation relative to the wind movement, with dust likelier to settle in low-pressure areas of the panel (brought about by high-speed wind movements impacting on inclined or vertical surfaces). Meanwhile, dust dispersal is determined by the properties of the dust particles (notably weight, size, type) (Mani and Pillai, 2010). In light of the above, Figure 2-4 below illustrates the various factors influencing dust settlement (Mani and Pillai, 2010).

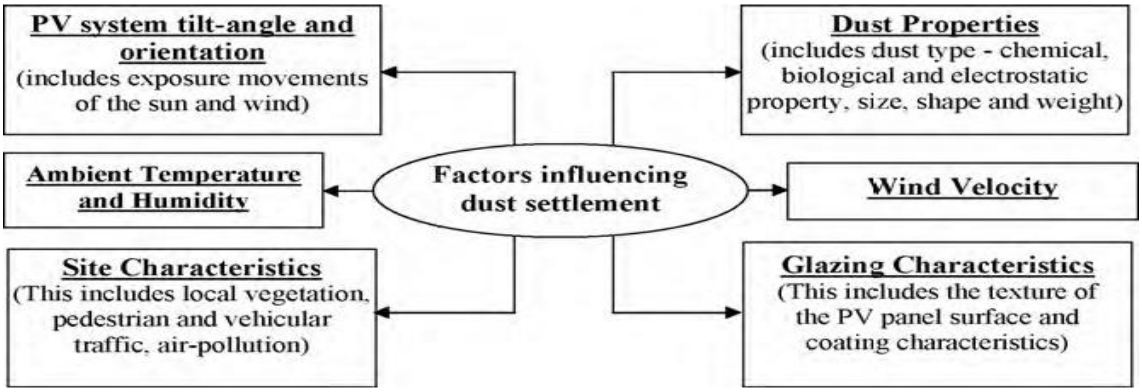


Figure 2-4: Factors influencing dust settlement (Mani and Pillai, 2010).

In terms of dust, the mechanisms through which mud gets deposited were studied by Cuddihy and Willis (1984), Cuddihy (1980 and 1983), who divided them into four primary mechanisms, as shown in Figure 2-5. These are cementation by water or soluble salts, organic material deposition, surface tension, and particle energetics. Inorganic and organic particulates, often containing water soluble and insoluble salts, can often be found in atmospheric dust. As such, in high humidity conditions, microscopic droplets of salt containing insoluble particles are formed on surfaces. As a result, when these dry the precipitated salts cement the insoluble particles onto the surface of the panel. Moreover, the fact that the surface tends to be first coated with an ultrathin layer of deposited organic material renders removing the salt deposits especially challenging, necessitating complex cleaning processes.

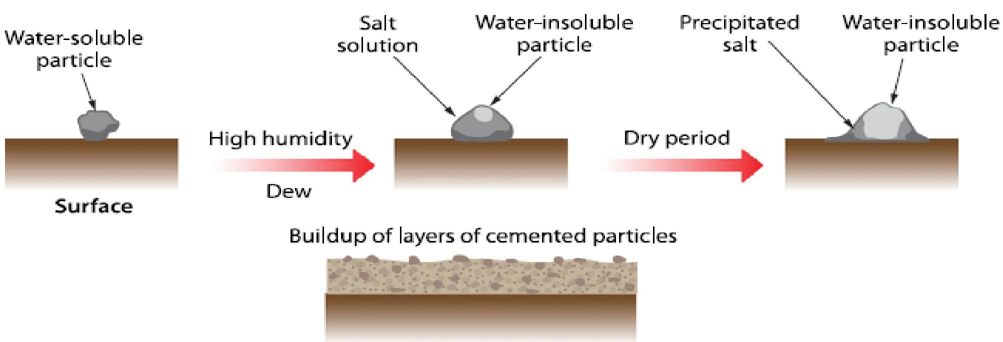


Figure 2-5: Dust–Moisture Cementation Process (Sarver et al., 2013).

Several research studies have been undertaken on dust settlement and its impact in a solar PV systems context. For instance, at a solar village near Riyadh, in Saudi Arabia, Salim et al. (1988), devised a PV test system to investigate the impact on PV energy output of long-term dust accumulation. Using an array tilted at a fixed angle of $24.6^0$, the team compared the difference in monthly energy outputs between an array that was cleaned daily and one that was left to gather dust, finding a drop of 32% between the two after eight months. However, not only were the test site's dust levels and dust particle properties not investigated in the study, the results were arguably misleading since energy reductions usually would occur within weeks in such highly polluted sites, rather than 8 months. Indeed, Hassan et al. (2005), found that PV panel degradation takes place quickly, usually within the initial 30 days of exposure. Moreover, the results obtained by Salim et al. seem to suggest that while the panel's efficiency decreases by 33.5% after 30 days, it actually subsequently rises to 65.8% after a six months period despite no cleaning taking place. Garg (1974) established a similar examination over a 30-day period, the normal transmittance (of direct radiation through glass) for a horizontally-mounted system had fallen from 90% to 30%. Meanwhile, in Kuwait, Sayigh et al. (1985) investigated reductions in transmittance at tilt angles of $0^0$, $15^0$, $30^0$, $45^0$ , and 60%, obtaining reduction rates of 64%, 48%, 38%, 30% and 17% respectively after a 38-day-long exposure period to the environment. However, an accurate and useful interpretation of Sayigh's results presents several issues. The tests on clean and dirty panels were conducted on different days, and therefore under different insolation conditions. In this context, the study undertaken by El-Shobokshy and Hussein (1993) seems to be the most complete to date. El-Shobokshy and Hussein (1993) conducted a laboratory investigation into the impact of different physical properties of five dust varieties on PV cell performance and used three types of dirt: limestone (commonly found as dust in the atmosphere), cement (key construction material) and coal (present in industrial environments). Three different sizes of limestone were used, bringing the total number of dirt varieties tested to five. Figure 2-6 have shown the variation in short circuit intensity according to that in the amount of deposited dust was measured for the five varieties of dirt. The dirt particles were characterised based on their diameter and density (El-Shobokshy and Hussein, 1993).The authors established that the reduction in PV performance chiefly depends on the accumulated dust's density as well as on the type of powder involved and its size distribution. They also concluded that the greater effect was produced by the finest particles of dust rather than the thick ones. This was explained as the result of the evener distribution of finer particles, which leaves little spaces between them for the light to pass through. Figure 2-6 shows the relationship between the density of dust deposited and the power produced.

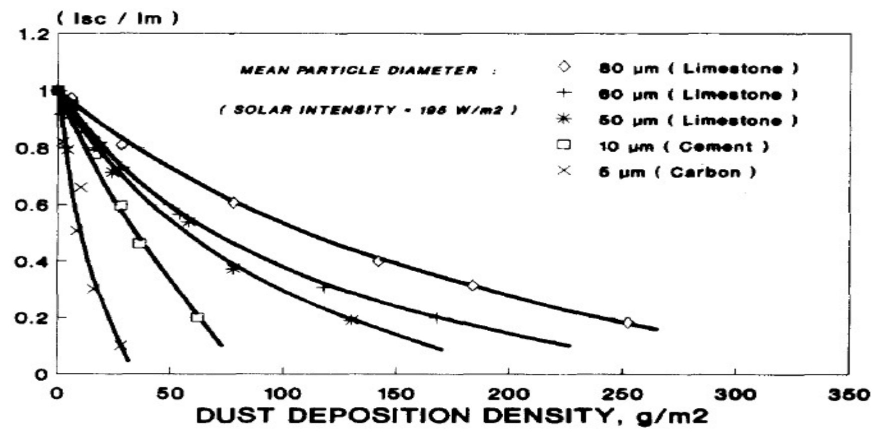


Figure 2-6: Variation circuit current with dust for the five types of dirt used (El-Shobokshy and Hussein, 1993).

As such, the study offers a number of key conclusions. Not only does dust accumulation affect PV cell performance, it is important to establish accurate information about the dust variety, particularly the type of material involved, its density and size distribution, to assess its effect on power output. Furthermore, a study by Elminir et al. (2006) conducted in Cairo, Egypt, examined the influence of natural soil dust on the transmittance of glass covers of 3-mm thickness, commonly used in solar collectors and at seven tilt angles ($0^0$, $15^0$, $30^0$, $45^0$, $60^0$, $75^0$ and $90^0$). The monthly averages of suspended particles obtained in the study are shown in Figure 2-7, which seems to confirm that the acuter the tilting angle, the likelier it is that dust particles would roll off the surface. Moreover, increases in accumulated dust levels reduce the transmittance of the transparent cover, thus affecting the panel's energy yield amount. Figure 2-8 shows average decreases in transmittance caused by various levels of dust deposition densities

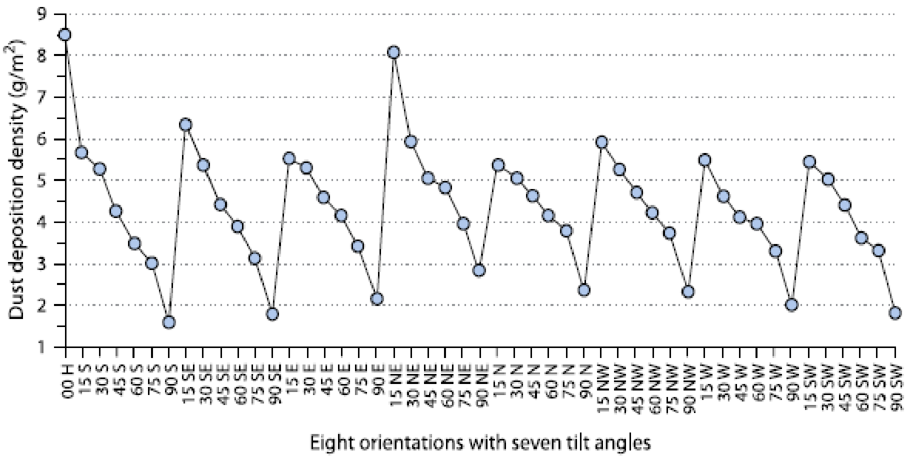


Figure 2-7: Quantity of dust accumulate on glass samples installed in eight different orientations with seven tilted angles in an arid location (Elminir et al., 2006).

In this context, the decrease in transmittance is calculated as the difference between that of a clean sample and a dust-covered one, and Figure 2-8 seems to confirm that this reduction is caused by dust accumulation on the surface of the sample. However, a law of diminishing returns seems to be in operation in that the reduction in transmittance increases at a progressively smaller rate until the reduction reaches an upper plateau beyond which additional dust levels no longer result in further reductions in transmittance.

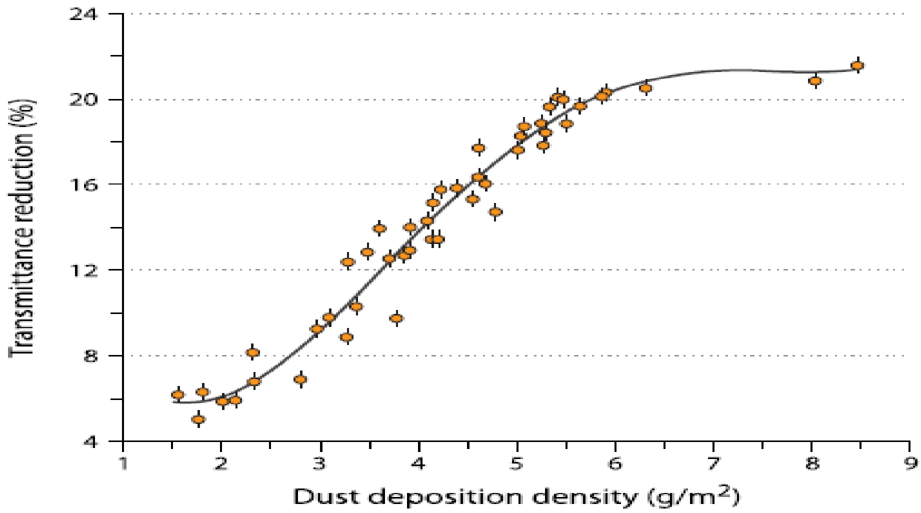


Figure 2-8: Reduction in transmittance as a function of dust deposition density (Elminir et al., 2006).

## 2.4 Self-cleaning techniques

As has been mentioned in the previous Section, the effect of dust accumulation on PV panels can be quite damaging. As such, regular cleaning of the panels is often necessary to prevent serious degradation of their performance, especially in regions with dusty climates. However, manual cleaning of solar panels, especially in the context of large installation, can be a labour-intensive process and thus often prohibitively costly. Even in small buildings, cleaning a PV system can involve complicated issues of access that might require the intervention of specialist staff. Self-cleaning technologies could present the perfect solution to these issues and help address many of the obstacles preventing solar panel technology from becoming more widely adopted.

A number of solar panels self-cleaning technologies have been explored by He et al., (2011) and Sarver et al. (2013). Some of the technologies involve the use of electrodynamic screens for electrostatic dust removal, robotic cleaning tools, vibrating mechanisms featuring piezo-ceramic actuators, as well as $TiO_2$ treated chemical or nano-films.

### 2.4.1 Self-Cleaning Nano-Film

Covering the surface of solar panels with a pellucid self-cleaning nano-film made of a super-hydrophilicity material or super-hydrophobic material would have been shown to be quite effective in keeping the surface clean of dust. Nano-film technology involves the following two strategies:

**Super-hydrophilicity film***:* Following a photocatalytic process, the $TiO_2$ film reacts to UV light by breaking up accumulated organic dirt. The film's hydrophilicity then induces rainwater to diffuse across the entire panel surface, rinsing the dust away. However, because of its reliance on rainfall, this method is unsuitable for desert regions, (He et al., 2011) and research has been focused on how best to prepare, dope and modify the material. Using $TiO_2$-based nano-films has generated a significant level of interest after proving quite successful both in terms of research and in terms of practical implementation (Pilkington, 2014, Wheal, 2005). The technology combines two processes. First, a photocatalyst process uses ultraviolet light and water molecules to disintegrate organic dirt by converting it into a gaseous carbon dioxide. A second process than deploys a hydrophilic effect to wash out the dust and dirt particles by inducing rainwater to propagate across the PV system glass. This technology, by its very nature, is ideal for use in regions with regular and sufficient rainfall levels. By contrast, use in regions with dry climate or insufficient levels of precipitation would render these processes quite ineffective.

**Super-hydrophobic film** - Studies have been conducted on the development of superhydrophobic surfaces using special microstructures or nanostructures that can enhance the contact angle (CA) to higher than $150^0$, in order to ensure falling Water droplets quickly roll off the surface, carrying dust away in the process. While research on superhydrophobic films has mostly focused on improving their non-wettability, doubts remain over the technique's applicability in desert circumstances. Further research is clearly needed to truly investigate such real-world applications (Park et al., 2011; Zhu et al., 2009a; Niu et al., 2009).

### 2.4.2 Electrostatic Dust Removal

In this regard, a technology that has been of particular interest to researchers is electrostatic dust removal which involves using electrostatic and dielectric forces to displace charged and uncharged dust and dirt particles (Atten et al., 2009). However, although this process can remove dirt and dust deposits quite effectively, a significantly high-voltage is required by the electric curtain (film). This can significantly affect solar transmission and reduce the output of the solar panel by up to 15% (Sharma et al., 2009). The notion of 'electric curtain', put forth by Tatom and collaborators (1967) and later further developed by Aoyoma and Masuda (1971) is the most popular of electro dust removal methods, and has been shown to be effective in using electrostatic and dielectrophoretic forces to displace charged and uncharged particles (Calle et al., 2008).Electric curtains are constituted of parallel electrodes embedded in a dielectric surface, across which oscillations in the electrode potentials are transmitted, Figure 2-9 shown electric curtain basic structure.

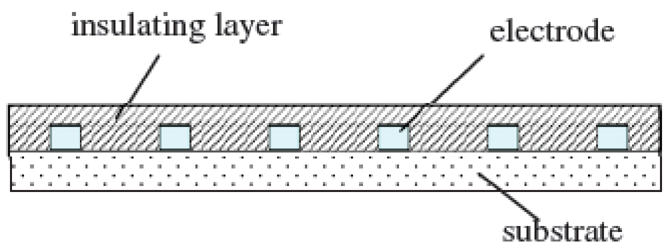


Figure 2-9: Electric curtain basic structure (Matsunaga et al., 1985).

When connected to a single-phase AC voltage, the electrodes cause a travelling-wave electric curtain to be excited, Figure 2-10 illustrates. The charged particles, under the right frequency and amplitude conditions, are prevented from settling but are instead dragged across the surface following the electric field, keeping the surface clean (Liu and Marshall, 2010).

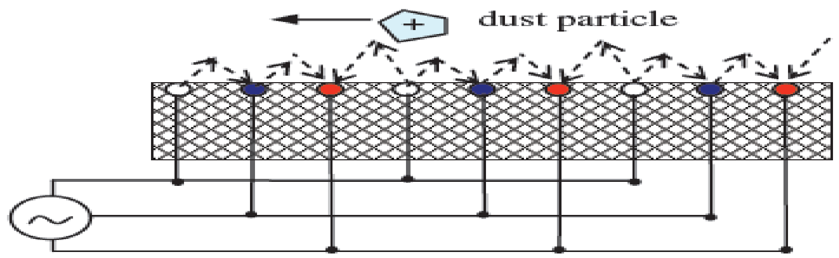


Figure 2-10: Three-phase electric curtain (Liu and Marshall, 2010).

### 2.4.3 Mechanical PV Panel Vibration

Another technology that has been the subject of recent examination is PV panel vibration techniques, which usually deploy piezo-ceramic actuators. The technology remains at an early stage of development and has been mostly considered in the context of space technology missions, such as probes to Mars, where the impact of dust on solar panel performance is both significant and of critical consequences. Nevertheless, this technology has been investigated in a number of studies, notably by

Williams et al. (2007) who established the effectiveness of higher vibration resonances, which can restore up to 95% of the generating capacity of the panel's output power. However, it must be noted that the study does not specify the power consumption requirements involved in operating the actuators (Williams et al., 2007).

### 2.4.4 Electrodynamic Screens

A number of studies have examined the effectiveness of cleaning methods in improving the performance of PV panels. For instance, Biris et al. (2004) investigated the use of electrodynamic screens to remove contaminant particles and found that higher voltages correspond to a better dust removal rate. Biris et al. (2004) examined the role of surface mass density on electrodynamics dust removal, found that phased voltage renders the surface dust particles electro-statically charged, allowing for them to be removed using an alternating electric field. Using this method resulted in 90% of deposited dust being removed within 2 minutes. For their part, Bock et al. (2008) and Sims et al. (2003) investigated an efficient power management approach for self-cleaning PV panels featuring integrated electro-dynamic screens, confirmed that voltage was the decisive parameter, with higher voltages producing better dust removal performance. In this light, electro-dynamic screen-based cleaning, in addition to the high initial and operating costs it involves, can only be deployed in a limited range of applications due to the fact it unused any liquid, and cannot be used for the removal of muddy or the sticky particles.

### 2.4.5 Mechanical Removal of Dust

***Robotic cleaning****:* A robotic device was developed by Anderson et al. (2010) for the purpose of cleaning PV panel arrays using water spray. The robot-sprayed water was found to cool the panels during the cleaning, increasing the array's performance by

15% in the process. Fernández et al. (2007) in their examination of the effects of low-mass robotic dust wiper technology on the MSL rover, found that the robotic dust wiper can enhance the PV panel's efficiency by 7%. However, the robotic-based technology involves significant initial and operating costs; as well as complex mechanical and control design requirements.

***Washing Surfaces*** : Moharram et al. (2013) describe the adoption by a PV power plant in Cairo, Egypt, of a combination of non-pressurised water and the surfactant developed by Abd-Elhady et al. (2011) for its PV cleaning so as to examine the efficacy of this technology. Three experiments, illustrated in Figure 2-11, were conducted, subjecting each of the panels to 45 days under one of the following cleaning regimes: no cleaning, cleaning using non-pressurised water and cleaning using pressurised water and surfactant. At the end of the experiment, as Figure 2-11a shows, panels in the first regime had accumulated a thick dust layer, panels under the second regime (water) had significantly lesser dust accumulation, while the dust on the panels in the third experiment (surfactants) was practically negligible. Figure 2-11b highlights that while regular cleaning is mandatory in dusty areas, using non-pressurized water is not enough and a mix of cationic and anionic surfactants should be used as an effective cleaning solution (Moharram et al., 2013).

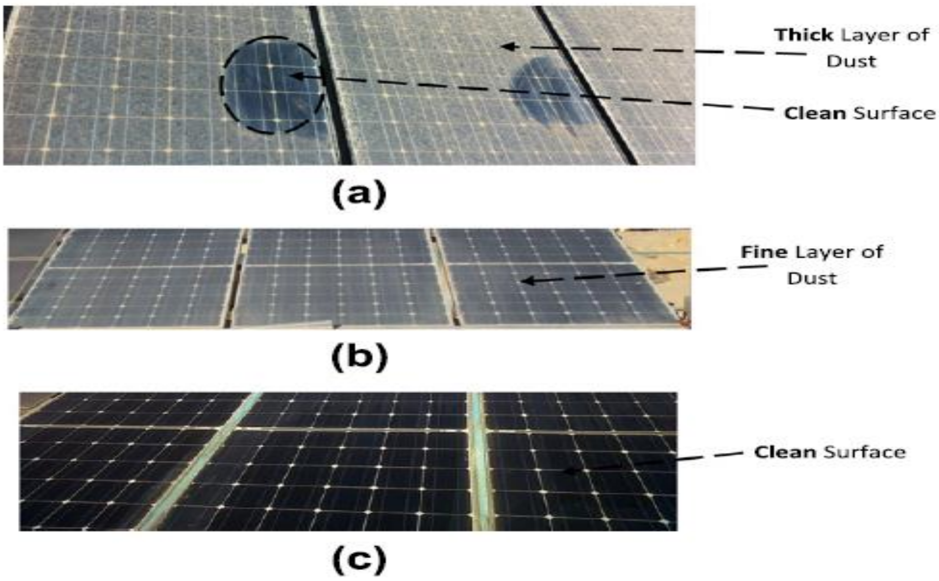


Figure 2-11: The solar modules under different cleaning mechanisms, (a) no cleaning, (b) cleaning by water, and (c) cleaning by surfactants after 45 days of operation (Moharram et al., 2013).

Moreover, as Figure 2-12 highlights, the performance of PV panels that undergo non-pressurised water cleaning is reduced by an average of 0.14%/day and thus by 50% after 45 days, which confirms that this cleaning option is not sufficiently effective.

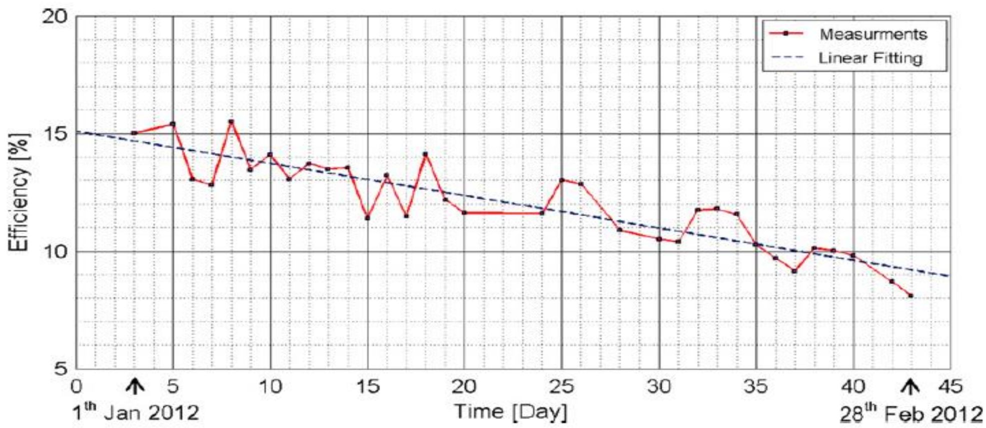


Figure 2-12: The efficiency of the PV panels versus time due to cleaning using water (Moharram et al., 2013).

### 2.4.6 Forced Air

Schumacher et al. (1979) designed several devices using airflow and air vibrations to clean solar collectors and tested their abilities for removing dust from mirror surfaces. To identify a suitable cleaning method, two approaches were investigated in the experiment. The first approach tested several nozzles, including vortex-generating nozzles which imparted the rotational and translational motion to air and converging nozzles which allowed the air directly flow to the surface.

The second approach applied a mechanical transducer to provide ultrasonic energy through the air to the surface. Results indicated that vortex nozzle and converging could present a good performance for the cleaning of the mirror, while providing ultrasonic energy to the airflow could give a better performance for the surface cleaning. Meanwhile, a number of water-based PV cleaning systems were presented by Elsherif and Kandil (2011) featuring a range of devices such as a sliding brush, sliding nozzles, rotating brushes and fixed nozzles. Programmable logic controllers (PLCs) and sensors were used on all systems to control and monitor their operations. In the fixed nozzles version, the surface is cleaned by high-speed water jets released through a set of nozzles (fixed onto a manifold mounted atop the PV panel). In the sliding nozzles version, the manifold was adapted so that it could move across the surface of the panel to ensure a uniform cleaning process. In the moving brush version, the fixed-nozzles system was supplemented with a moving brush, one variant of this system used a moving brush while another had a sliding brush. The system's ability to clean all varieties of dirt ensured its performance was superior. This confirms that water-based cleaning improves the performance of PV panels but that it requires pressurised water or the use of a brush to deal especially persistent dirt such as mud.

Moreover, jet pumps are found extensive use in energy plant, aerospace, propulsion, electronics and PV cleaning and cooling assistant because of the above features. It has also found that 99% of the panel's surface reflectance of heliostat reflectors can be recovered using a hybrid technique involving a combination of air-blowing and water mist. Also has found that 99% of the panel's surface reflectance of heliostat reflectors can be recovered using a hybrid technique involving a combination of air-blowing and water mist (Schumacher et al., 1979). According to the study, such a recovery rate requires the injection of water supply at 2.14ml/min, pumped at a minimum pressure of 690 mbar (10 psi) air from a nozzle placed at a distance of 10 cm from the PV panel's surface.

Also, there are many studies focus on droplet dynamics and size characterization of high-velocity air blast atomization presented by Urbán et al. (2017) and, the droplet size and velocity characteristics of water-air impinging jet atomizer presented by Xia et al. (2017). Consequently, this thesis has placed emphasis on a jet pump, which can be used in creating a combination of a high-velocity air flow and water vapour. Trials pertaining to this research have been conducted on a PV and also on a rig of a jet pump. All these experiments have been conducted in a controlled environment.

## 2.5 Description of the Photovoltaic Cleaning Using the Jet Pump System

As it is known, photovoltaic maintenance (such as cleaning) and issues related to the cooling of PV panels are complex and require essential information regarding the working mechanisms of the systems. Following the scrutiny of various methods, which were stated in Section 2.4 of this thesis, it has been recognised that strong channelized air can be used for cleaning purposes with a minimal use of water. Another understanding developed from the scrutiny of evidence is that the use of channelized air can also enhance the mechanism of ventilation, which is on the exterior of the photovoltaic panels. They also aid the process of self-cooling the photovoltaic cells. As per Schumacher et al. (1979), the combination of strong channelized and water vapour can enhance the process of self-cleaning in solar panels

### 2.5.1 Description of the cleaning process.

This technology is proposed to remove sandstorm dust, which currently hinders the large-scale deployment of photovoltaic systems in the region. The project aims to use an automated mix of a high-pressure air and water vapour inside the jet pump to clean the photovoltaic panels. The hot water, which results from the photovoltaic cooling process, will be used as a secondary fluid in the jet system. Due to the relatively high temperature of the secondary fluid, this would enhance the evaporation rates of the water under entrainment of an air-driven jet, and it would enrich air-water vapour quality for dust removal from the surfaces of photovoltaic panels. The entrainment process will also produce a direct cooling effect, which will be used to cool the water used for photovoltaic module cooling.

Generally, photovoltaic panels are installed with a certain tilt angle to maximise the sunlight on the panels. In a large solar power generation plant, photovoltaic panels are placed in several linear rows for the maximum utilisation of ground area and solar energy. Hence, it is possible to install a number of jet pumps at the top of each array of the photovoltaic installation. Figure 2-13 shows the concept of the air-water jet pump nozzles system for a row of PV panels.

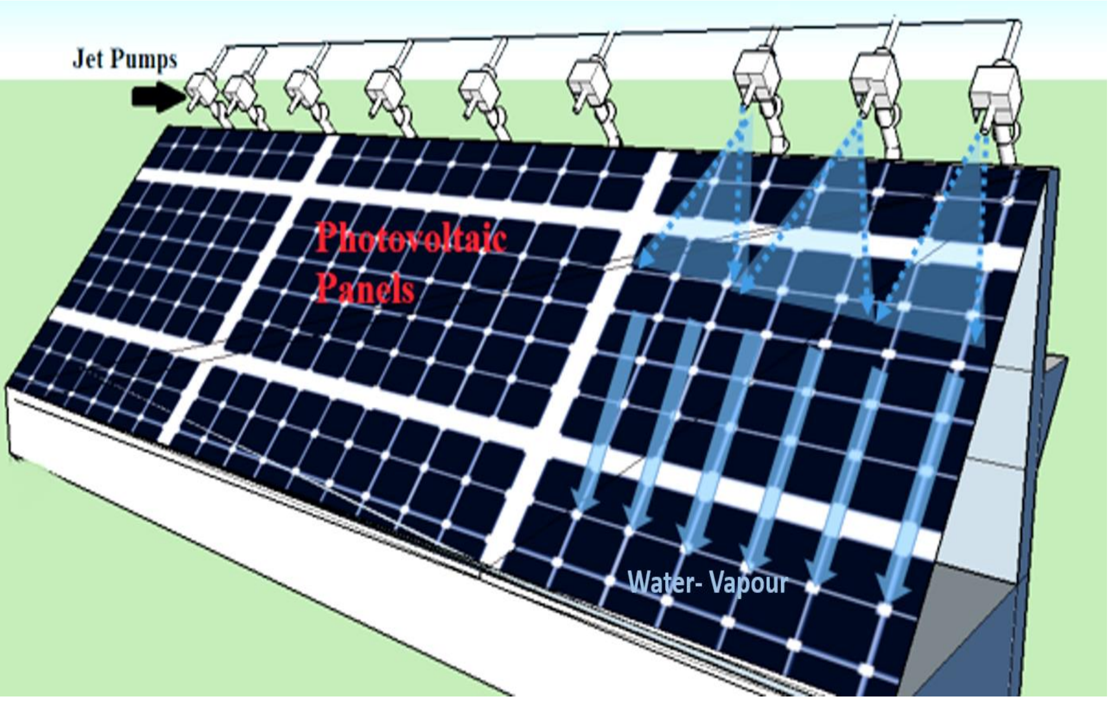


Figure 2-13: The concept design of the air-water jet pump system for a row of PV panels.

There are two fluids. The first fluid through the primary nozzle is high-pressure air using a compressed air feed, and water vapour is the secondary flow, coming from a water vessel. The direction of the nozzles is along the PV’s surface. The distance between the panel and the moving velocity of the jet pump examined in Chapter 7. The air is supplied from a central air compressor or individual air compressors. Figure 2-14 shows a jet pump as well as the air flow and water vapour flow.

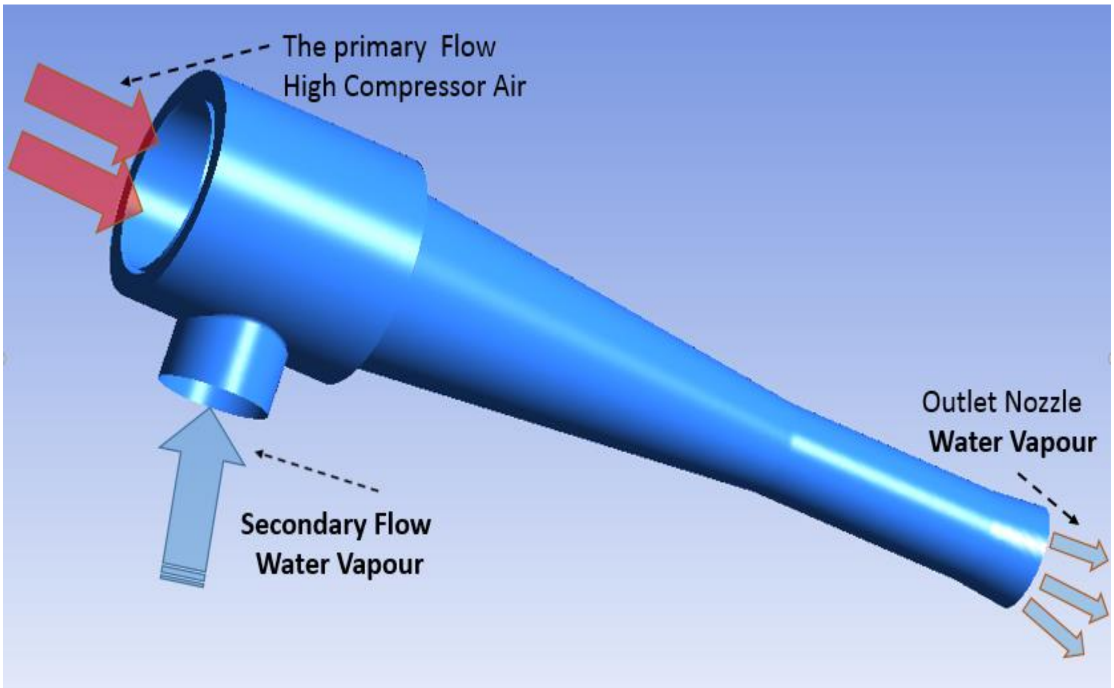


Figure 2-14: A jet pump and the air flow and water vapour flow.

According to Mani and Pillai (2010), most of the studies that have been conducted recommend a minimum of weekly panel cleaning for most of the dry, tropical climates within a 15$^o$ to 25$^o$ latitude zone and with an annual precipitation less than 15 cm. In areas with high sand storms, daily cleaning may be required. For higher latitudes where larger tilt angles are desirable, weekly cleaning would be adequate to minimize the effect of dust accumulation on solar panels.

The system is operated for several minutes at a certain time in the day. The time of operation is dependent on the conditions of the climate and atmosphere. It should be done at the peak solar radiation time when the peak PV panel power output occurs. The system can be manually operated or automatically operated if there is a sensor installed on the panel to measure the dust deposition and light transmission situation.

The electricity required to drive the air pump could be supplied by PV panels. It has been shown in the literature review in Chapter 2 that almost one-third of original PV output is reduced by the shading of dust accumulation in a climate. Thus, using a small part of the PV power to operate the air compressor to generate one third more energy is a desirable strategy. A simple evaluation of the required air compressor power for air nozzles of a single panel will be conducted at the end of the thesis.

### 2.5.2 Concept of cleaning process of jet impingement

To determine an appropriate position for the jet pump nozzle and for the regulation of jet pump nozzles, a methodical study and the comprehensive process of removal of particles has been performed. The nozzles on the surface of the photovoltaic cell are the primary focus of the study. Each particle is held by its own adhesive energy and by other external forces. To move a particle, the following three initial motions are necessary. These three basic, or essential, initial motions are: (1) the rotating motion, (2) sliding motion and (3) lifting motion. All these motions are acknowledged as primary or basic initial motions. As per the research of Wang (Wang, 1990), the most effective and efficient manner to separate a sphere from a surface is through a rotation motion. As per the same research, lifting motion is a combination of external and adhesive forces that give motion and momentum to the particle. To make the particle move, the force used must be equal to the adhesive force. When the rotation motion is contrasted with the sliding motion, results suggest that sliding motion requires less energy. Figure 2-15 depicts a balance related to the force of an object of a special shape on a hard and unbending exterior. It can be deduced that there are three points of references in this figure, namely A, B and C, which are situated on a sphere for assisting the rotation. The rotation of the spherical body through the force exerted relies on the angle of projection of force or the angle through which the force has been channelized. This force is called $F_{cr}$, and it can be recognized as a jet impingement angle, which is located on the surface. Consequently, the angle between the vapour nozzle and the photovoltaic exterior can be ascertained. Figure 2-15 shows the rotation force F changing with force angle θ.

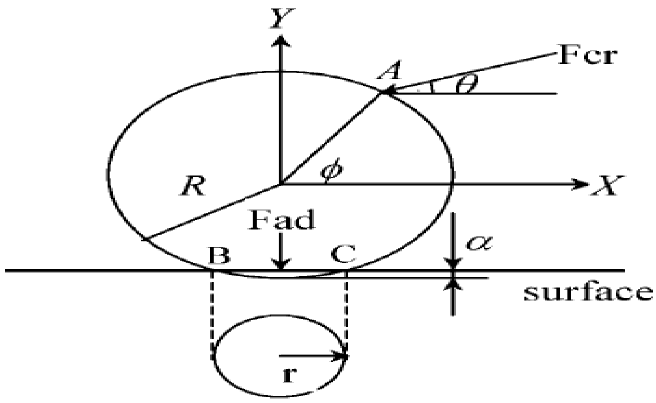


Figure 2-15: The forces required for the movement of a particle from a surface (Wang, 1990).

It has been suggested by Wang (1990) that rotating with the focus of force on B is a highly efficient way to make particles move. As per Figure 2-16, we can deduce that the angle of force θ is not in a position to get in a 45$^o$ position to push forward the spherical object depicted in the Figure 2-16. From this analysis, it has been deduced that the angle must be between 0$^o$ and 45$^o$ for the forward thrust.

A similar study, which was conducted by Zhang et al. (2002), and actually followed up the theory proposed by Wang (1990) asserted that there are different standards and parameters, such as theory, that influence removal efficiency. These three parameters are (1) impingement of jet pressure P, (2) impingement distance and (3) the angle of the jet to the surface.

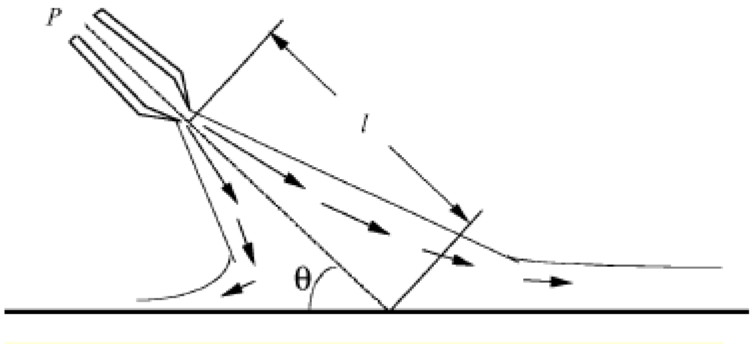


Figure 2-16: A schematic showing nozzle impingement on a surface (Zhang et al., 2002).

In their research, has a system of processing an image, which aids in observing the spread of glass particles in a spherical object, and estimates the detachment or dissociation space when the jet cleaned. The research provided information in the form of statistics regarding surface and its characteristics; it also provided information regarding the adhesive force of the particle. It has been suggested that a strong vapour force, in the form of pressure, must be employed when the adhesive force is great. However, there is still a threshold number, which must be considered. When this threshold is penetrated, the cleaning mechanism becomes less effective and efficient. Other than jet force authority, it is also imperative to adjust and regulate the angle of the nozzle and the displacement of the outlet of the nozzle, as directly impacts the efficiency of cleaning. From the study, they have deduced that, for an efficient cleaning and for the particle removal, the optimal distance is around 13 to 20 times when contrasted with the outlet of a nozzle with the diameter *d*. In addition, for this objective, the surface tilt θ must be around 30$^{o}$. This is the optimal angle for this particular objective. Other than that, the trials, which were carried out in a controlled environment, an indeed, called an efficiency index, which has also been employed in other similar studies and experiments.

$$\text{Removal Efficiency} = \frac{N_{before} - N_{after}}{N_{before}} \tag{2-1}$$

In addition, the study by Young et al. (2013) conducted a trial, which was based on the removal of particles by use of the forced air channel, which was aimed directly at the particles. The study assesses the efficiency of maintenance, such as cleaning, by only employing strength/force (τ) of the device used (Jet Impinge) on the particular body. This can be estimated by using a particular formula by Tanner and Blows (1976). The formula is as follows:

$$\tau = \frac{2\mu_0}{th^2 r}\int_{r0}^{r} hrdr \tag{2-2}$$

In this equation, *fluid viscosity* $\mu_0$ is represented by mathematical symbols. (t) Denotes the time that is needed by the fluid to travel from a point (Jet) to a point that has been estimated. In this mathematical equation, h denotes *standoff* displacement and distance; r denotes what we describe as the radical distance from the centre of a jet to a point that has been estimated.

Therefore, shear strength can be estimated when we have the values pertaining to speed, viscosity and the standoff displacement or distance. From this given information, we can estimate or discover the most apposite jet for the entire operation, for maintenance of photovoltaic panel (cleaning). Figure 2-18 provides a graphical depiction of various speeds of different jets. The jets used are sonic, sub-sonic and supersonic with a particular relation with r/h.

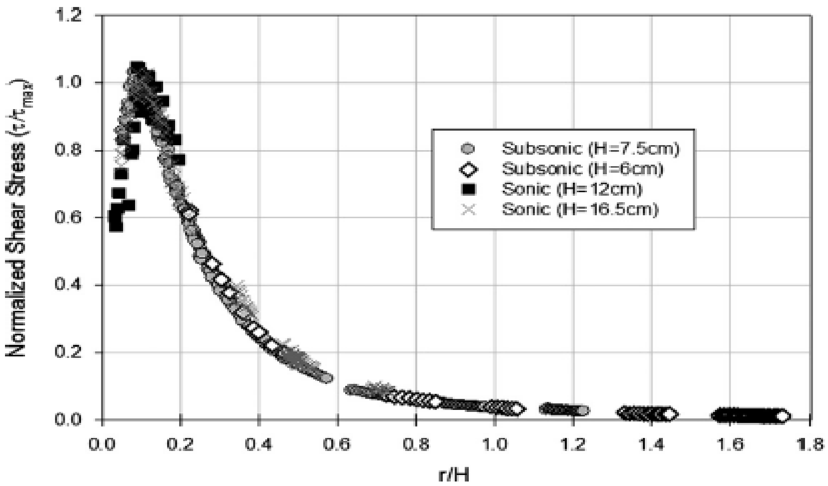


Figure 2-17: Normalized Shear Stress profile by (r/h) (Young et al., 2013).

However, as stated in the summary of this thesis, the system is operated for several minutes at a certain point in the day. The time of operation is dependent on the conditions of climate and atmosphere. It should be the peak solar radiation time when the peak PV panel power output occurs. The system can be manually operated or automatically operated using some sensors installed on the panel to measure the dust deposition and light transmission condition on PV efficiency.

The electricity consumed by the air pump is supplied by PV panels. It has been shown in the previous Section that almost one-third of the original PV output is reduced by the shading of dust accumulation in an arid climate. Thus, using a small part of the PV power to operate the air pump to generate one third more energy is a desirable strategy. A simple evaluation of the required air pump power for water vapour nozzles of a single panel will be conducted at the end of this thesis. In addition, the vital part of the design of this system is creating an appropriate water vapour distribution on the PV surface. It determines whether the whole PV surface will be cleaned effectively. A suitable selection of the air input velocity may also influence the energy consumption of the air pump.

To obtain a desired steam distribution on the PV surface, the Computational Fluid Dynamic (CFD) techniques will be used to test and design suitable nozzle conditions for the water vapour blowing system. In this case, the software package ANSYS Workbench 16.1 is applied for the CFD simulation task.

## 2.6 Summary

This paper has discussed factors affecting PV system performance including environmental factors, especially those relating to weather conditions, such as dust, temperatures and the sun's position. The effect of dust accumulation on PV panels can be quite damaging. Hence, regular cleaning of the panels is often necessary to prevent serious degradation of their performance, especially in dusty climates. Self-cleaning technologies could present the perfect solution to these issues and help address many of the obstacles preventing solar panel technology from becoming more widely adopted. Nevertheless, none of these technologies has to date been able to establish itself as an industry standard and achieve the necessary commercial breakthrough.

# Chapter 3: Review the Jet Pump System and Theoretical Equations

## 3.1 Introduction

The concept of a jet pump is not new. The device uses the converging-diverging nozzle to create a Venturi effect and converts the pressure energy of a primary fluid to velocity energy which creates a low-pressure area that draws in and entrains a secondary fluid. Steam driven jet pumps have been used extensively in power generation, chemical processing and the nuclear industry for many years. The most notable use has been to produce or maintain a practical vacuum in gas-filled vessels. The main advantage of jet pumps over conventional compressors or pumps is that they have no moving parts and thus require little maintenance, which made it a very attractive device to many researchers in different fields such as refrigeration, power generation and medical applications. Reviews on the jet pump development can be found in many publications (Chunnanond and Aphornratana, 2004; Riffat et al., 2005 and Abdulateef et al., 2009).This Chapter highlights the latest developments on jet pump technology.

## 3.2 The jet pump theory and design

A jet pump is a kind of fluid machinery and mixing equipment that transfers momentum from a high velocity primary jet flow to a secondary flow. Jet pumps and educators are the mechanical devices which used to operate the jet pumps by the compressed fluid.

The major distinction between the two, in addition, the functioning liquid states, choked flow plunger of the gas jet pump system, is supersonic. This approach allows the exchange of primary fluid energy to the secondary fluid. However, this may occur with the penalty of substantial thermodynamic complication in the mixing and dispersion sections. Figure 3.1 is the archetypal cross componential view of air jet pumps. The process of working in the air jet pump is the same. A high pressure fluid with very low speed at the prime inlet is expedited to high velocity jet through the focalized nozzle for the converging-diverging supersonic nozzle fluid jet pump or for the air jet pump (Liao, 2008). The supply force at the inlet is to a certain extent converted to be the jet impetus at the nozzle exit according to the Bernoulli equation. Fixed low force primary jet induces a secondary flow from the suction port and high velocity too and accelerates it in the course of the driving jet. The two tributary then coalesce in the mixing section, and by computation of the material such process will be completed by the ending of this segment. A diffuser is typically inducted at mixing chamber exit to elevate the inert pressure of diverse flow (Liao, 2008).

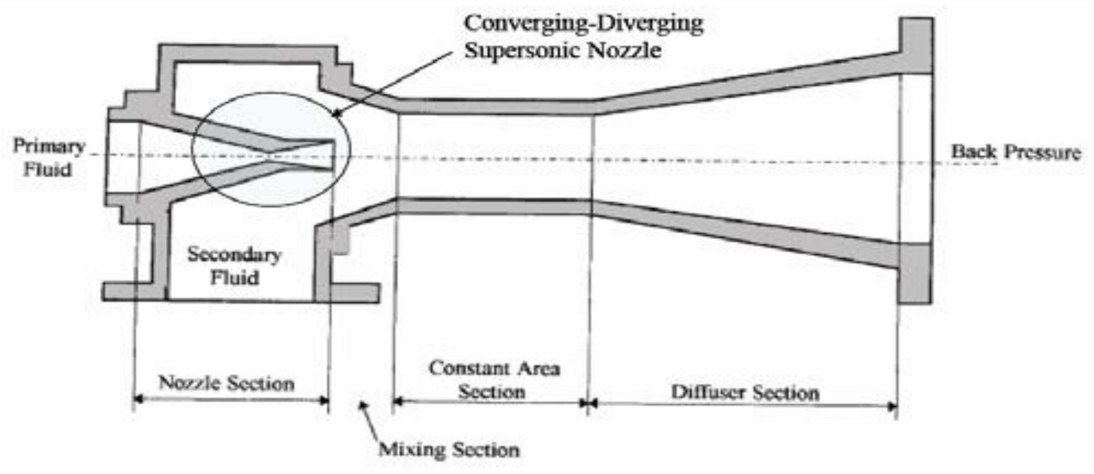


Figure 3-1: Typical Air jet pump (Liao, 2008).

Moreover, jet pumps, also known as ejector pumps, jet pump is a type of pump that uses the Venturi effect of a converging-diverging nozzle to convert the pressure energy of a motive fluid to velocity energy which creates a low pressure zone that draws in and entrains a suction fluid, are devices accomplished of control and transporting all forms of motive fluid including gas, steam, or liquid. They can be considered mixers or circulators since the intake combines multiple fluid sources. Multiple inlets are used to draw in a constant stream of fluid, using pressure to create lift through suction. The combination of intake pressure and velocity of the liquid or air jets the media up from a well, tank, or pit through the pump to the discharge point. Jet pumps are less efficient than typical centrifugal pumps due to such factors as friction loss but may be more efficient when working with combined media that includes gases, and invariably good conditions where the surface characteristics involve turbulence.

Jet pumps are employed in the industry in numerous, unique and even sometimes bizarre ways. They can be used singly or in stages to create a wide range of vacuum conditions, or they can be operated as transfer and mixing pumps. The jet pumps have the following advantages over other kinds of pumps:

• Rugged and simple construction

• Capability of handling enormous volumes of gases in relatively small sizes of equipment

• Fewer maintenance requirements

• Simple operation

All jet pumps operate on a common principle. The single stage jet pump in its simplest form consists of an actuating nozzle, suction chamber and a diffuser. The actuating fluid, which may be a gas, vapour or liquid, is expanded from its initial pressure to a pressure equal to that of the secondary fluid. In the process of being expanded, the actuating fluid is accelerated from its initial entrance velocity, which is negligibly small, to a high velocity. In the suction chamber, the actuating fluid induces a region of low pressure-high velocity flow which causes the secondary fluid to become entrained and mixed with the actuating fluid. During the mixing process, the actuating fluid is retarded and the secondary fluid is accelerated. As the mixture enters the diffuser, it is compressed to the exit pressure by rapid deceleration. The purpose of the jet pump is to transport and compress a weight of induced fluid from the suction pressure to the exit pressure. By staging jet pump, it is possible to obtain a very large range of suction pressures from atmospheric down to as low as one micron of mercury absolute.

In multistage jet pumps, it is generally beneficial to condense the steam from each stage in a water-cooled inter condenser so as to reduce the load to the succeeding stage. This reduces the mass and steam consumption of the following stages and results in a much more efficient jet pump system. Of course, the steam condensing must take place at a pressure above that corresponding to the saturation pressure of the cooling water.

Liquid Jet pumps: In a liquid Jet pump, the motive fluid is a non-compressible liquid (generally water) with no heat energy hence with a single stage centrifugal pump we cannot increase its pressure much. As a result, motive fluid velocity at the nozzle tip is very less and it affects its non-condensable load handling capacity radically.

Steam Jet pumps: In a steam jet pump, the motive fluid is a jet of high pressure and low-speed compressible steam which exists from the nozzle at the designed suction pressure and supersonic speed hence entraining the vapour into the suction chamber.

Due to the supersonic speed of the steam at the tip of the nozzle, its non-condensable load control capacity is much higher than liquid jet pumps.

Combination of both: In this type of jet pump system, both liquid jet and steam jet pumps are working simultaneously to produce low absolute pressure. The suction of liquid Jet pump is linked to the discharge of the last step of the steam jet pump.

Jet pumps have uncomplicated geometry and no stirring components. Their process does not demand electrical or mechanical power effort. This heavily reduces equipment mass and increases consistency.

However, the basic goal of this theory is to utilize the innovative techniques for removing the dust with the help of the self-cleaning technology by utilizing the water mist and high pressured air because they have the capacity to remove the duct and to investigate the feasibility and the disadvantage of using air jet pump to decrease the quantity of water that requires for clean the panels. The aim of this project is to explore and observe the usage of $TiO_2$-based nano-films with the combination of water or air mist ejects techniques that arrange according to the demand of every customer in the scenario of a PV-panel that is one of the self- cleaning applications. The main focus of this project on the climate of the Gulf region that distinctive due to a feature of insufficient rainfall level. The working mechanism of the jet pump and its hypothetical conditions, the basic concepts and operated equations of aerodynamics are acquainted as the first step. Equations of the continual-pressure jet pump replica and continual-area jet pump replica are then consequential in great details. 1-D analytical models for air jet pump have been performed through the parametric analysis with single-phase flow. The 1-D analytical models are used to design the general air jet pump procedures and rules which are discussed. In order to make the gain of better sympathetic of the mixing process in the jet pump, to model the air jet pump the commercial Computational Fluid Dynamics (CFD) software FLUENT is used. In the near future, it will be shown that The CFD simulation results and experimental data are under the great agreement. According to this benchmark, FLUENT is engaged to optimize the jet pump geometric arrangement. Confidence in the jet pump working mechanism is gained from Riffat et al. (1996).This model will study and cover the possibilities and disadvantages of using air eject to decrease the consumption of the water utilization to clean the panels. Another purpose to keep the focus on this research is to design such types of working jet pump for making the PV cleaning system better.

In summary, this Section describes the recent development of jet pumps and their applications. One may conclude that jet pumps could be used over a wide range of applications. They are increasingly attracting research from many disciplines in view of the fact that jet pumps not only can serve the need for air-conditioning and refrigeration but can also meet the demand for environmental protection and energy conservation. The advancements in CFD analysis are evident as it has become widely accepted as a reliable simulation tool. Additionally, CFD analysis has led to advancements in the jet pump design and to a better understanding of the behaviour of the fluid in different types and configurations of jet pumps. Nevertheless, jet pumps systems such as jet pump system for cleaning PV panels still immature compared to other technologies despite the noticeable improvement in all design and manufacturing aspects of jet pumps.

## 3.3 Air jet pumps theory and design

The jet pump was familiarizing as a mechanical engineering device. At the same time, researchers are in the progress to examine its working mechanism. In 1950 a paper published the first comprehensive theoretical and experimental analysis of the jet pump problem was presented by Keenan (1950), Keenan and Neumann (1942) were developed the constant-pressure mixing model and the constant-area mixing model and became the fundamental of jet pump design and performance analysis since then. According to the 1-D analytical approaches, a lot of research attempts has been dedicated to the enhancement of jet pump design methods and thousands of papers regarding the supersonic jet pump has been published. In the review of Bonnington and King Bonnington et al. (1976), 413 jet pumps reverence about jet pump dating prior to 1976 were cited; 33.33% of them are about air jet pump. Most recently, a research published widespread review related to the design and implications of the supersonic jet pump are given by D.W. Sun and I.W. Eames (1995), Sun and Eames (1995). Munday and Bagster (1977) adopted the constant pressure mixing module, their theory depends on the assumption that the motive and secondary stream remain two discrete streams down the converging duct of the diffuser and when the secondary vapour reaches sonic velocity the phenomenal of shocking occurs at some cross-section of the jet pump.

In the application of constant-pressure mixing model, Keenan and Neumann (1942) assumed that the fluids of the primary flow and secondary flow were the same gas. Nozzle and diffuser efficiencies and frictional effects were also neglected by Keenan and Neumann (1942). This method is not very precise, but it avoids the intricate terminology of thermodynamic characteristics for mixed flow as well as the use of experimentally gritty constants. In general, investigational values of pressure-rise are found to be approximately 85% of the estimated values.

The derivation of DeFrate and Hoerl (1959) involves the modified constant-pressure mixing model by taking the ideal gas law with molecular weight since gas constant is determined by the molecular weight and universal gas constant by the relationship of

$R = \check{R} / W$.

Different heat ratios of the primary and secondary liquefied were also integrated into their method. According to the constant-pressure mixing, Emanuel (1976) developed a simple analytical model for optimizing the steady-state performance of a jet pump. Rice and Dandachi (1991) derived equations for the steam jet pump to predict the primary flow rate by including the friction and mixing losses which have usually been neglected. Huang et al. (1999) assumed constant-pressure mixing to occur inside the constant-area section of the jet pump with the entrained flow in a choking condition.

Huang et al. (1999) strong-minded, a variety of loss factor coefficients in their developments by matching the sample test data with the analytical results.

One other 1-D analytical model, which is the constant-area mixing jet pump was considered too, by Keenan (1950), Keenan and Neumann, (1942). The assimilation in a constant-area jet pump functions in two different regimes and it depends on whether the flow characteristics of this jet pump are independent or dependent of the back pressure $P_b$. Fabri and Siestrunck (1958) introduced the idea of “aerodynamic throat” and they included the primary nozzle wall thickness in constant-area mixing model. In that concept, they referred to $P_b$-dependent regime as “mixed” regime (MR) and they referred to $P_b$-independent regime as “supersonic” regime (SR) and sometimes the "saturated-supersonic" regime (SSR). To understand the mixing mechanism in a better way Dutton and Carroll (1986), Addy and Chow (1964b), Addy and Chow, (1964a) showed these two different regimes on a three-dimensional operating surface which is shown in Figure 3.2. Three-dimensional jet pump operating surface depicting the different flow regimes is based on the following three variables (Dutton and Carroll, 1986; Addy and Chow, 1964a; Addy and Chow, 1964b) $Pp_0/Ps_0$ is the primary-to-secondary stagnation pressure ratio, $P_b/Ps_0$ is the static-to-secondary stagnation pressure ratio and ω is the entrainment ratio. A constant-area jet pump is constrained to operate at some point on t the surface. Entrainment ratio ω is predicted by other two ratios.

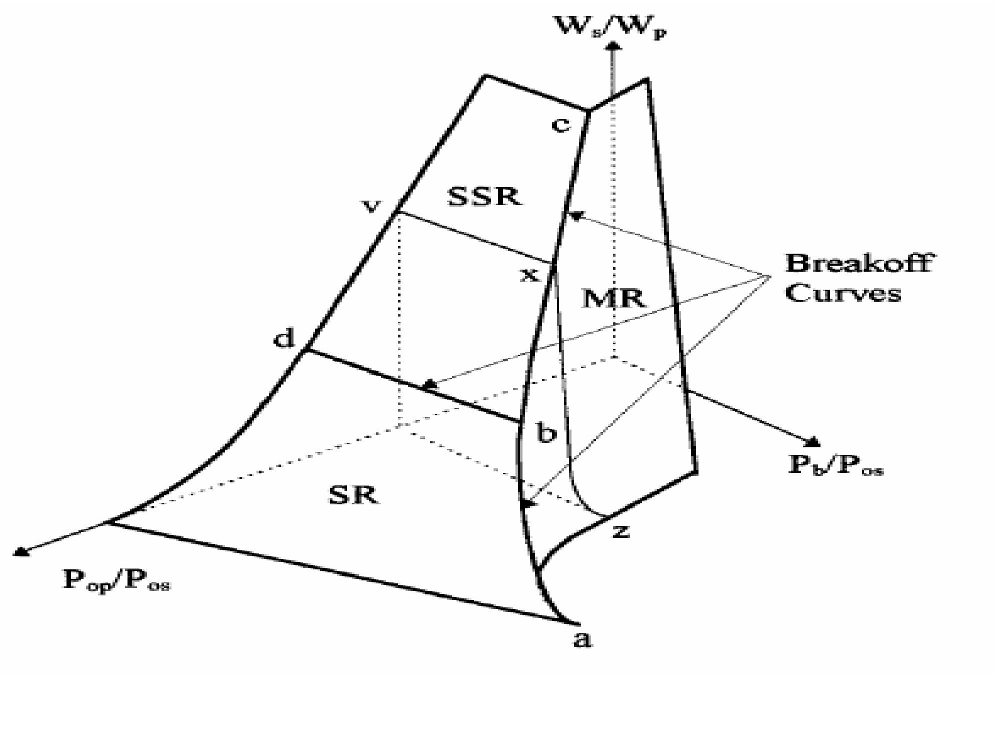


Figure 3-2: Three-dimensional jet pump operating surface depicting the different flow regimes (Addy and Chow, 1964b).

The conditions that 1-D models require are not as restrictive as they appear. If the flow can be simplified to 1-D and mean values which are suitable can be used then these models are applied for non-uniform flow conditions. But, this is not the case when turbulent flow is required through very short sections. A 1-D analysis can be used for engineering design purposes because, even though it is relatively simple, it has been shown to provide reasonably accurate and consistent results within its limitations. Since 1950, considerable progress has been made in these models but there are still some problems which are unsolved. There is no technique that can determine, for the constant-pressure jet pump, optimum shape of the mixing section. Besides this, no one has been able to establish the exact link between the constant-pressure jet pump and performance of constant-area. It is greatly required to develop a new jet pump model that will be able to unify all jet pump models and also provide solutions for the problems in existing models.

A lot of researchers have used different 2-D models to better understand the flow process in the jet pump, especially within the mixing section. The first ones who considered two-dimensional characteristics of jet pump performance were Goff and Coogan (1942). Mikhail (1960) supposed different velocity profiles at every stage of the mixing process that was carried out in a constant-area tube. There is a possibility that predictions of 2-D models are more accurate than 1-D models, a lot of disadvantages are connected with them. The 2-D models are more complicated and involve more specialized knowledge for implementation. Moreover, there are generally empirical coefficients and constants that have to be determined from experiment, and sometimes they are applicable only in case of the certain jet pump.

Hedges and Hill (1974) were the first to step into Computational Fluid Dynamics (CFD) and they developed a finite-difference scheme in order to model the flow process that takes place within an air jet pump. Gilbert and Hill (1975) refined this method and the theoretical results they got were in agreement with the experimental results. Due to the availability of complicated supersonic flow and mixing problems exist in the gas period, now the researchers use the commercial CFD software programs because of the easiest availability of it in the software market. It should try to avoid the study inflow in a jet pump, especially in the diffusion section. Neve (1993) and Riffat et al. (1996) uses commercial codes and FLUENT to study the impacts of the primary nozzle in it. Especially, Riffat et al. (1996) have adopted the standard $k - \varepsilon$ model in the CFD modelling. Bartosiewicz et al. (2006) is one of the researchers that also use FLUENT to pretend jet pump. But the conclusion of all discussion shows that the shear stress transport version of the $k-\omega$ turbulence model agrees with this kind of data that exist in the best form CFD is one of the alone jet pump design, and there is no existed any other study about the jet pumps flow. The major reason behind these facts is that there are only a few similarities between data and CFD predictions. In order for obtaining benefits from it, need to identify the similarities between data and CFD prophecies.

## 3.4 Geometric parameters of jet pump

A number of factors influence the performance of a jet pump. In this Section, three geometrical factors the primary nozzle geometry and position, the diffuser and the constant area section were considered. The geometric parameters of jet pump design are shown in Figure.3-3 along with their respective notations.

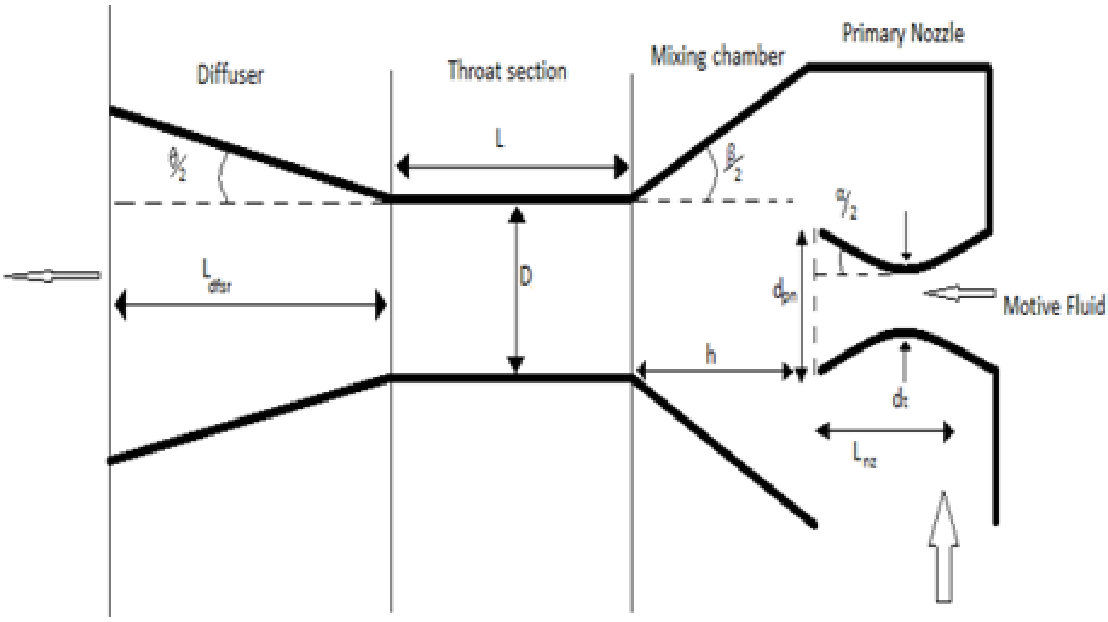


Figure 3-3: Notations of jet pump geometric parameters (Eames et al., 1995).

### 3.4.1 Primary Nozzle

Nozzle position should be aligned with the flow in the middle axis of the jet pump to work properly. Moreover, proper attention is required in the material selection and manufacturing of the nozzle as it should be as plain as possible. There are several reasons for its internal surface roughness because the increase in roughness the friction also increases (Chen et al., 2013).

In the mixing chamber, when prime flow passes through the nozzle, there is an increase in velocity and pressure reduces which causes the secondary flow comes tangentially to mix with primary flow throughout the length of the chamber. However, geometrical position of the nozzle along with area ratio mixing chamber flow and pressure at the end of the nozzle where fluids meet. Maximum area ratio not only helps to attain the highest entrainment but also depends on the geometric parameters of another jet pump. Many studies showed that nozzle flow behaviour strongly changes the performance of the jet pumps. That is why researchers paid much attention to nozzle geometry while designing the jet pump.

According to Researchers Chaiwongsa and Wongwises (2008), primary nozzle angle θ must be designed as so that it reduces the turbulence. This turbulence is caused by the separation of the boundary layer. Divergent / convergent primary nozzle with different divergent angles was experimentally tested by Nakagawa et al. (2011), who found that there are many variations has been shown in decompression throat profiles. It has been found that with the increase in divergence angle, there has been a faster trend in the decompression after the nozzle throat and decreasing trend is found in the nozzle outlet pressure which ultimately increasing the divergence angle thus causing a rapid decrease in the pressure.

But the additional increase in this angle would not attain further decompression. It is because that the pressures already become constant and no effect has been found on decompression. Eames et al. (1995) conducted the experiment on the steam jet pump and tested the nozzle's divergent sections with varying angles by increasing in $A_{pn}$, the result was found that the entrainment ratio was reduced for the large-sized nozzle.

### 3.4.2 Nozzle exit position.

There are many experimental research studies which found the nozzle exit geometrical position NXP a very important variable which largely affects the jet pump functioning (Chen et al., 2013). Zhang and Shen (2006) made experiments on the subsonic jet pump. He connected the jet flow boundary's extension with the alignment at a point in the convergent section of the nozzle and this point is known as jet stagnation point. When the jet blow-out the nozzle exit space, which is the jet mixing region in between the jet flow boundary and jet core region where the mixing of secondary flow arises. To determine the effect of nozzle exit position, the nozzle is adjusted for primary flow to nozzle exit geometrical positions of 0, 20, 40, 60 and 80 mm. Different results were found at these different NXP points. At 60mm, the mixing flow was very trivial to be measured. However, at 80mm, entrainment flow reversed the primary flow can be found at specific NXP. According to the findings of Pianthong et al. (2007), he suggested that if the nozzle moves further in the jet pump inlet then the jet pump throat area will become bigger, in this way we can get higher entrainment ratio or mixing ratio. Though, by moving too far the NXP in the jet pump, the primary stream thrust lowers which reduces the entrainment ratio. For the purpose to determine the maximum NXP, a total of 24 jet pumps with 96 cases were tested by Zhu et al. (2009b). Previous suggestions relating to determining optimum NXP in literature are given by researchers who suggested that NXP must be placed at 0.5-1.0 length of entrainment mixing section.

But a recent study found that maximum NXP lies in between the 1.7-3.3 length of the diameter of mixing section but it mainly depends on geometric parameters. However, it looks that by moving away from the primary nozzle from mixing chamber reducing the NXP, so the secondary flow takes more time to be started in the mixing chamber with the primary flow. For the purpose to accelerate the secondary flow adequately in the mixing chamber and to reduces the friction, nozzle exit position should be accurately selected so that kinetic energy losses decrease as much as possible. Many researchers found that when the nozzle of jet pump moves into the entrainment section, there is an increase in back pressure ($P_b$) and COP reduces significantly. Others researchers found that when NXP moves far away from the entrainment area, COP again drops. It is hard to predict the exact optimal NXP under given parameters. So, the researchers always experimentally determine the optimal nozzle position if the design of jet pump permits the axial adjustment with nozzle position.

In next Section will prove in details by mathematical equations the primary nozzle, conservation, choking phenomena constant- area mixing model and constant- pressure mixing model.

### 3.4.3 Convergent Mixing inlet

Mixing starts in this section for the constant pressure mixing jet pump and the secondary choking duct is normally located here. Flow choking sets the upper-performance limit of jet pump thus a good understanding of the choked flow condition existing in the jet pump is critical to the design process. The secondary flow may become chocked prior to contact with the primary flow (shoke I) or may occur before the secondary and primary flow steam are fully mixed (shoke II). There is a third possible occurrence that may take place in the mixed flow upstream of the diffuser (shoke III) (Chou et al., 2001). The flow structure of the converging duct mixing (constant pressure) apparently differs from that of the constant-area mixing. Ji et al. (2010) conducted a CFD investigation on the flow structure inside the jet pump and found that in a given operating parameters the entrainment ratio increased sharply in a constant pressure mixing at $\beta=0.5^{o}$ Less shear mixing in the converging duct results in an expanded wave with large expansion angle leaving the nozzle. Consequently, the primary jet core is larger and the converging duct is smaller. Increasing the converging duct above the optimum angle results in energy and entrainment ratio losses. The increase of converging duct angle is restricted by the increase in the nozzle exit pressure but that will result in a decrease the entrainment ratio. Figure 3-4 has shown CFD analysis on the effect of converging duct angle.

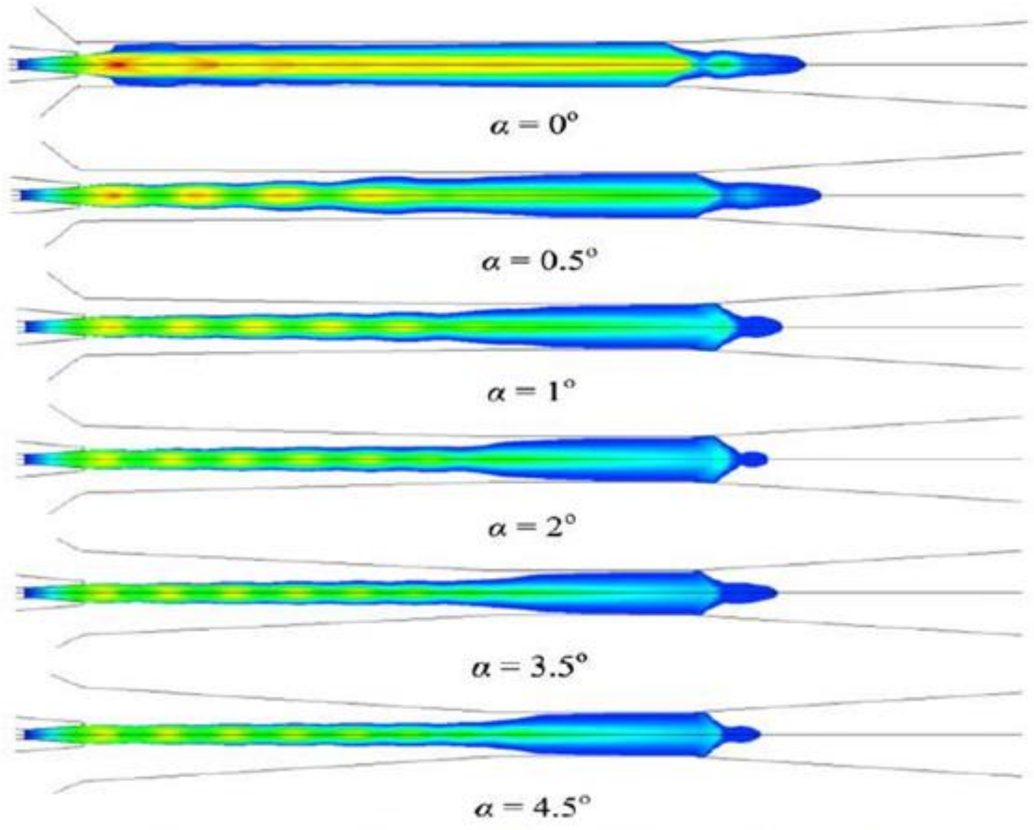


Figure 3-4: CFD analysis on the effect of converging duct angle (Zhang and Shen, 2006).

Guo and Shen (2009) found that the optimum converging angle with the maximum entrainment ratio is about 2.07$^o$ but when by varying NXP the results were different and that varying the convergent angle in large range does not affect the entrainment ratio. They concluded that less primary nozzle exit position NXP requires smaller converging angles to obtain better entrainment performance. Yadav and Patwardhan (2008) suggested that for maximum entrainment the converging section angle should be between 5$^o$-15$^o$ depending on the converging section diameter, further increase in the converging angle result in a drop in the rate of entrainment. Zheng and Weng (2010) found that an increase of the expansion ratio results in a drop in the primary fluid inlet pressure and entrainment ratio accordingly. However, the secondary fluid inlet pressure and the pressure at the outlet of the jet pump do not change.

## 3.5 Theoretical background

In the derivation of 1-D analytical models the theoretical model normally used for introducing the air jet pump. All 1-D analytical model of compressible gas streams in the jet pump that made with the help of many applications in which include continuity equation of conversation, energy, momentum and also includes ideal-gas law. For continuing the flow, the users use important parameters. For representing the frictions and others loss, normally researchers use loss factor coefficient that obtained during experimental analyses of data. The isentropic expansion is one of the important assumptions during the derivations and some researchers prefer to use this for represented the loss factor during experimental analyses of data. Supersonic condition use at the exit of the primary nozzle for achieving better performance level. That is one of the reason due to which it is necessary to introduce the phenomena of an aerodynamic choke that occurs at the throat of the primary nozzle.

The basic purpose of an air jet pump is to collect the flow of motive to converge the diverging nozzle supersonically. Where the primary flow exists then the secondary flow induces in a high velocity form at the suction chamber. To induce the pressure recovery, in the most of the cases at existing of the mixing section, normally any kind of diffusion system installed in it. For accelerating, decelerating and depressurizing the compressible flow, nozzle normally uses.

### 3.5.1 Conservation and Ideal Gas Law

According to Figure 3-5, describing the conservation equations and ideal gas law in a detail and efficient form and explains the steady 1-D compressible flow in a random area that show control volume (Liao, 2008). For obtaining detail information about the terminologies, may help from the nomenclature section. The jet pump geometries were designed by adopting the one-dimensional analysis described by Keenan et al (1950) and later modified by Eames et al (1995). Energy, momentum, and continuity equations are applied to predict the flow conditions through the jet pump.

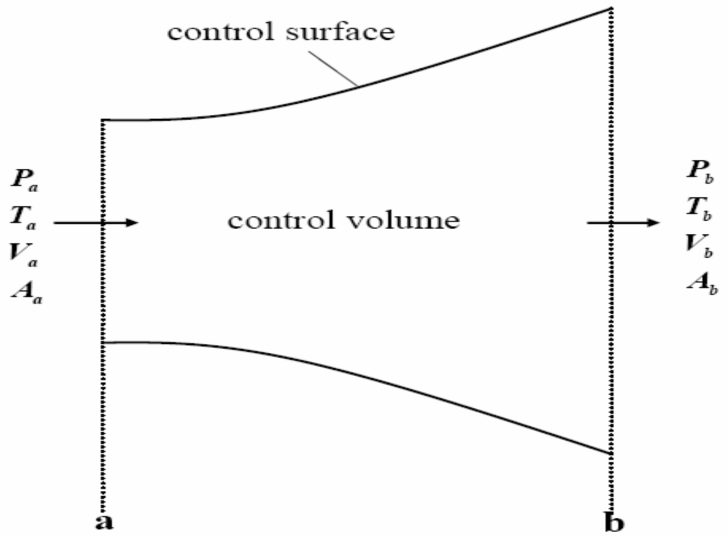


Figure 3-5: Control volume for 1-D flow. (Eames et al., 1995).

Continuity Equation

$$m = \rho_a V_a A_a = \rho_b V_b A_b \tag{3.1}$$

Momentum Equation

$$P_a A_a + m_a V_a + \int_{A_a}^{A_b} P dA = P_b A_b + m_b V_b \tag{3.2}$$

Energy Equation

$$\boldsymbol{h_a} + \frac{\boldsymbol{V_a^2}}{\boldsymbol{2}} = \boldsymbol{h_b} + \frac{\boldsymbol{V_b^2}}{\boldsymbol{2}} \tag{3.3}$$

Ideal gas law

$$\frac{P}{\rho} = RT \tag{3.4}$$

Where the P is the pressure of the gas, one of another P shows the momentum and R is the gas constant and T show the absolute temperature of the gas. In the ideal gas law, we divide momentum from the pressure of the gas that is equivalent to the gas constant and temperature

$$R = \frac{\overline{R}}{W} \tag{3.5}$$

In the above Equation, $\overline{R}$ shows the universal gas with unit of $J\,/\,(kmol.K)$ and $W$ is the molecular weight with unit of *kg/* (*kmol*).

*Mach number*

Mach number, M shows the Mach number that is a very important parameter for the compressible flow and especially for the supersonic flow. For calculating the Mach number, you need to obtain the ratio by dividing the local fluid velocity from the local sonic speed

$$M = \frac{local\ fluid\ velocity}{local\ sonic\ speed} = \frac{V}{C} \tag{3.6}$$

The local sound speed c in a medium with temperature T is given by:

$$C = \sqrt{\gamma RT} \tag{3.7}$$

Isentropic expansion of ideal gas

Equation (3.8) is the process Equation for the isentropic flow of an ideal gas:

$$\frac{p}{\rho^{\gamma}} = \text{constant} \tag{3.8}$$

The basic equations: momentum, second law, continuity, the equation of state, and also the above mentioned process equation, temperature, density, and the local pressure can be related with their matching values at stagnation condition by means of isentropic flow functions which are expressed in Equations (3.9) through (3.11). Those parameters that are with subscript 0 deal with the stagnation properties. These stagnation properties are steady throughout a stable, isentropic flow field.

Pressure:

$$\frac{P_0}{P} = \left(1 + \frac{\gamma-1}{2} M^2\right)^{\gamma/\gamma-I} \tag{3.9}$$

Temperature:

$$\frac{T_o}{T} = 1 + \frac{\gamma-1}{2} M^2 \tag{3.10}$$

Density:

$$\frac{\rho_0}{\rho} = \left(1 + \frac{\gamma-1}{2} M^2\right)^{1/\gamma-1} \tag{3.11}$$

### 3.5.2 Choking Phenomena

Choking phenomena can be explained by a convergent-divergent nozzle with the distribution of its static pressure along the flow direction as shown in Figure 3.6. In Figure 3.6 the flow through this converging-diverging nozzle is induced by adjustable lower downstream pressure while upstream supply is steady and stagnation conditions with $V_0 \cong 0$. The back pressure and the static pressure at nozzle exit plane are represented by $P_b$ and $P_e$. The effect of the difference in back pressure which is represented by $P_b$ on the pressure distribution in the nozzle is graphically illustrated in Figure 3.6. When the back pressure $P_b$ is less than the static pressure at the nozzle exit plane which is $P_e$, the flow rate is low. In this case, the pressure distribution in the nozzle is shown by curve *i.* The flow is essentially incompressible (if local Mach number M < 0.3) and subsonic at every point on the curve, if the flow rate is too low (Fox et al., 2011).

In this condition, the nozzle behaves as a Venturi, when the flow is accelerating in the converging portion until, at the throat, a point of minimum pressure and maximum velocity is reached, then the flow in the diverging portion decelerates to the nozzle exit. The more reduction in the back pressure increases the flow rate but it is still subsonic at all points and the distribution of pressure is shown as curve *ii* which is similar to curve *i*, even if the compressibility effects become significant. The flow rate continues to increase the back pressure $P_b$ continues to be reduced.

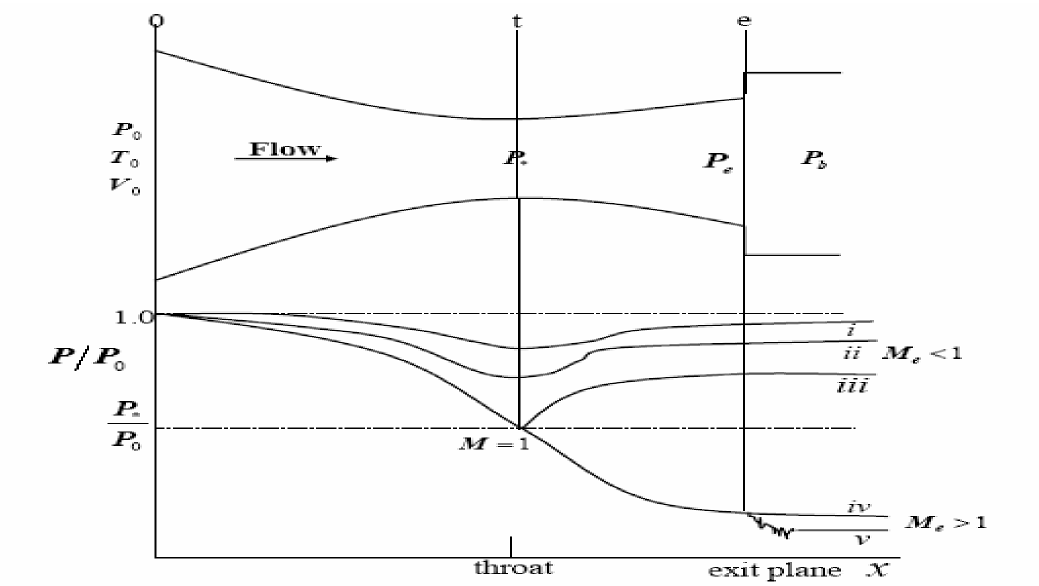


Figure 3-6: Pressure profile for isentropic flow in a converging-diverging nozzle (Fox et al. 2011).

If the back pressure $P_b$ is lowered too much, the flow at the nozzle throat ultimately reaches M = 1. The nozzle throat is the portion of minimum flow area, as illustrated on curve iii and at that point, the nozzle is choked. When the point of curve iii is reached, the throat is in a critical condition and for the given nozzle; the mass flow rate achieves the maximum possible and stagnation conditions. The corresponding pressure is, $P^*$, the critical back pressure.

## 3.6 Jet pump modelling governing equations

Figure 3-7 shows a schematic diagram of a jet pump with the symbols referred to in the analysis below. There are three dimensionless parameters that can define the performance of an air jet pump: entrainment ratio, pressure lift ratio, and nozzle pressure ratio. The entrainment ratio can be defined as the ratio of the secondary mass flow to the primary mass flow.

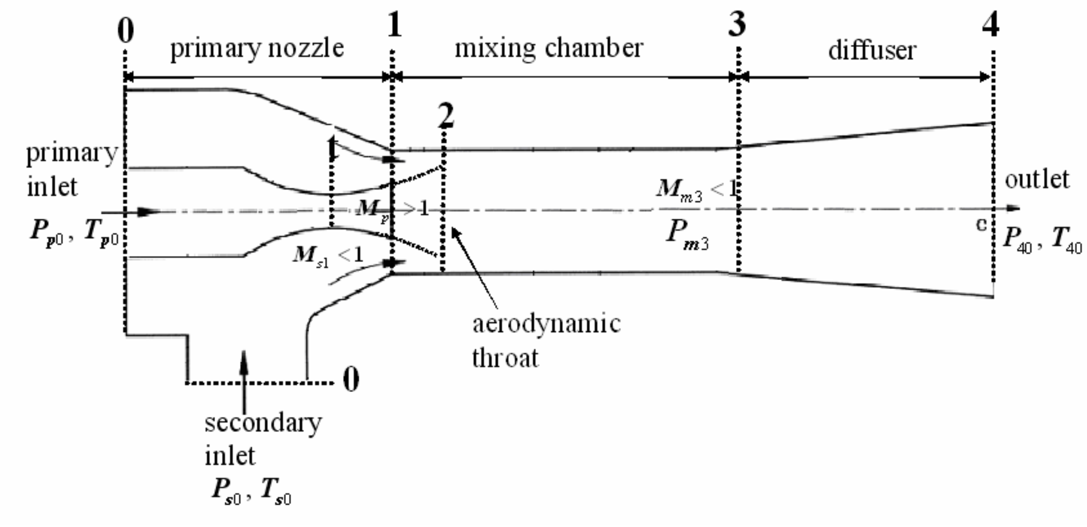


Figure 3-7: A schematic diagram of the jet pump (Liao, 2008).

$$\omega = \frac{m_{s1}}{m_{p1}} \tag{3.12}$$

Nozzle pressure ratio is the ratio of primary stagnation pressure to secondary stagnation pressure.

$$N_n = \frac{P_{p0}}{P_{s0}} \tag{3.13}$$

The critical pressure ratio is the ratio of the critical condenser pressure to the secondary stagnation pressure. Note that this ratio will vary with condenser operating conditions, the one-dimensional analysis will only provide us with diffuser outlet pressure which can be considered as the condenser critical pressure.

$$N_s = \frac{P_{p4}}{P_{s0}} \tag{3.14}$$

In the present hypothetical case, assumptions are made to establish the jet pump design and analysis. The design method for determining the geometries of the jet pump is described next.

### 3.6.1 Jets pump Design analysis.

The jet pump geometries were designed by adopting the one-dimensional analysis described by Keenan (1950) and later modified by Eames et al. (1995). Energy, momentum, and continuity equations are applied to predict the flow conditions through the jet pump.

For a one-dimensional adiabatic process between states 2 and 3, the conservation of energy can be described by:

$$\sum m_2 \left(h_2 + \frac{U_2^2}{2}\right) = \sum m_3 \left(h_3 + \frac{U_3^2}{2}\right) \tag{3.15}$$

The momentum Equation is:

$$P_2A_2 + \sum m_2\, U_2 = P_2A_2 + \sum m_3\, U_3 \tag{3.16}$$

The continuity Equation is:

$$\sum \rho_2 A_2\, U_2 = \sum \rho_3 A_3\, U_3 \tag{3.17}$$

### 3.6.2 Assumptions made in the one-dimensional analysis

The jet pump is operating with a single fluid thus the primary and secondary fluid are assumed to have the same molecular weight and ratio of specific heats. Additionally, the vapour is assumed to behave as a perfect gas. The primary and secondary fluids are supplied at zero velocity at points $P_0$ and $S_0$. The static pressure at 1 where the two streams mix is assumed to be uniform and the two streams mix at a constant pressure between 1 and 2. It is also assumed that the two streams are fully mixed before the normal shock that occurs somewhere in the constant area section and transverse shocks may occur between 2 and 3. Finally, the efficiencies of primary nozzle $\eta_n$, diffuser $\eta_d$, and mixing chamber $\eta_m$ were assumed 0.90, 0.85, and 0.95 respectively.

#### 3.6.2.1 State of primary and secondary streams at 1-1

According to Eames et al. (1995) the velocity of the primary and secondary streams at the primary nozzle exit plane 1-1 can be determined by the following energy conservation Equation:

$$U_{p1} = \sqrt{2\eta_p\left(h_{p0} - h_{p1}\right)} \tag{3.18}$$

Where $\eta_p$it the primary nozzle isentropic efficiency. Secondary flow velocity at 1-1 is:

$$U_{s1} = \sqrt{2(h_{s0} - h_{s1})} \tag{3.19}$$

The isentropic index of compression/expansion $\gamma$ is defined as

$$\gamma = \frac{c_p}{c_v} \tag{3.20}$$

Where $c_p$ the specific heat at constant is pressure and $c_v$ is the specific heat at constant volume. The isentropic index $\gamma$ is assumed to be constant at 1.4 for gas through the jet pump.

The change in pressure and temperature between states 2 and 3 is described by the isentropic relationship,

$$\frac{T_2}{T_3} = \left(\frac{P_2}{P_3}\right)^{\frac{\gamma-1}{\gamma}} \tag{3.21}$$

As shown by Eames et al. (1995) , the local Mach numbers and pressure ratios can be expressed by applying Equations 3.18,3.19 and 3.21 to Equation 3.6. The local Mach number of the primary stream at nozzle exit is found from Equation 3.24

$$M_{p1} = \sqrt{\frac{2\eta_p}{\gamma_s-1}\left[\left(\frac{P_{p0}}{P_1}\right)^{\frac{\gamma_p-1}{\gamma_p}} - 1\right]} \tag{3.22}$$

Where $P_1$ is the static pressure at the nozzle exit plane. The local Mach number for the secondary fluid at the exit plane 1-1 is found from

$$M_{s1} = \sqrt{\frac{2}{\gamma_s-1}\left[\left(\frac{P_{s0}}{P_1}\right)^{\frac{\gamma_s-1}{\gamma_s}} - 1\right]} \tag{3.23}$$

Eames et al. (1995)showed that primary and secondary streams can be expressed by one variable called the critical Mach number by using the Equation 3.24

$$M^* = \frac{\sqrt{(\gamma+1)\frac{M^2}{2}}}{\sqrt{1+(\gamma-1)\frac{M^2}{2}}} \tag{3.24}$$

Where $M^*$ is the critical Mach number.

#### 3.6.2.2 State of mixed stream at section 2

Applying the conservation of momentum between 1and 2,

$$\eta_m\left(m_p U_p + m_s U_s\right) = m_2 U_2 \tag{3.25}$$

$$U_1 = \left(\frac{\eta_m(U_p+\omega U_s)}{1+\omega}\right) \tag{3.26}$$

The critical Mach numbers obtained from Equation 3.24 can now describe the state of the combined stream at 2 in terms of critical Mach number,

$$M^*{}_2 = \frac{\eta_m\left(M^*{}_{p1} + \omega M^*{}_{s1}\sqrt{\tau}\right)}{\sqrt{(1+\omega\tau)(1+\omega)}} \tag{3.27}$$

Where τ is defined as the ratio of inlet stagnation temperatures,

$$\tau = \frac{T_{s0}}{T_{p0}} \tag{3.28}$$

The critical Mach number found from Equation 3.27 can be converted back into local Mach number upstream of the shock wave by using Equation 3.29

$$M = \frac{\sqrt{2M^{*2}}}{\sqrt{(1+\gamma)-M^{*2}(\gamma-1)}} \tag{3.29}$$

#### 3.6.2.3 State of mixed stream after shock process

A normal shock wave occurs between Section 2 and 3 resulting in decelerating the mixed stream to subsonic velocity the Mach number at this point is given by,

$$M_2 = \frac{\sqrt{2+(\gamma-1)M_2^2}}{\sqrt{(\gamma-1)+2\gamma M_2^2}} \tag{3.30}$$

The pressure rise across the normal shock wave is given by,

$$\frac{P_{m3}}{P_{m2}} = \frac{1+\gamma M_2^2}{1+\gamma M_3^2} \tag{3.31}$$

#### 3.6.2.4 State of Mixed stream at diffuser outlet

The mixed recovers pressure in the diffuser and the pressure increase is given by Equation 3.32.

$$\frac{P_{40}}{P_{m3}} = \left(\frac{(\gamma-1)\,\eta_d M_3^2}{2} + 1\right)^{\frac{\gamma}{\gamma-1}} \tag{3.32}$$

The critical pressure lift ratio described in 3.14 can also be found from Equation 3.33 Since a constant pressure mixing is assumed between 1 and 2, then $\boldsymbol{P_1 = P_{m2}}$, ($P_{p1} = P_{s1} = P_{m2} = P_1$) therefore the critical pressure lift ratio is given by

$$\frac{P_{40}}{P_{s0}} = \frac{P_{40}}{P_{m3}}\frac{P_{m3}}{P_1}\frac{P_1}{P_{s0}} = N_S^* \tag{3.33}$$

Since the static pressure $\boldsymbol{P_1}$ at the nozzle exit is not known, an iterative scheme can be used to find the optimum value. In this case, a ratio between $\boldsymbol{P_1}$ and $\boldsymbol{P_{s0}}$ and was assumed to determine $\boldsymbol{P_1}$.

#### 3.6.2.5 Outlet stagnation state

The stagnation temperature of the diffuser outlet is the temperature of the flow when it decelerated to rest adiabatically. By applying the conservation of energy between primary and secondary,

$$m_p h_{p0} + m_s h_{s0} = (m_p + m_s) h_4 \tag{3.34}$$

Where the specific enthalpy is defined as,

$$h = c_p T \tag{3.35}$$

Rearranging Equation 3.34 gives,

$$T_{p0} + \omega T_{s0} = (1 + \omega) T_3 \tag{3.36}$$

### 3.6.3 Jet pump geometry

By applying the continuity equation, the conservation of energy and momentum between stagnation and local states, the nozzle throat area, primary nozzle exit area, and diffuser throat can be determined. The secondary flow entrainment area can be found by the relationship between the stagnation state $P_{so}, T_{s0}$ and local Mach number at that point.

$$A = \frac{1}{M} \frac{m}{P_{s0}} \left( \frac{RT_{so}}{\gamma} \left( 1 + \frac{\gamma - 1}{2} M^2 \right)^{\frac{\gamma+1}{\gamma-1}} \right)^{\frac{1}{2}} \tag{3.37}$$

The primary nozzle throat area can be found by Equation 3.38.

$$A_t = \frac{m}{P_{p0}} \left( \frac{RT_{p0}}{\gamma} \left( 1 + \frac{\gamma - 1}{2} \right)^{\frac{\gamma+1}{\gamma-1}} \right)^{\frac{1}{2}} \tag{3.38}$$

The primary nozzle is assumed to be circular thus the primary nozzle diameter is,

$$d_t = \sqrt{\frac{4A_t}{\pi}} \tag{3.39}$$

The ratio between the primary nozzle exit and throat areas can be found from,

$$\frac{A_{p1}}{A_t} = \frac{1}{M_{p1}}\left(\frac{2}{(\gamma+1)}\left(1+\frac{\gamma-1}{2}M_{p1}^2\right)^{\frac{\gamma+1}{2(\gamma-1)}}\right) \tag{3.40}$$

The primary nozzle exit area is found, then the diameter of nozzle exit is,

$$d_{p1} = \sqrt{d_t^2\,\frac{A_{p1}}{A_t}} \tag{3.41}$$

The ratio between the primary nozzle to diffuser throat area can be found from Equation 3.40.

$$\frac{A_t}{A_{m3}} = \left(\frac{N_S^*}{N_p}\sqrt{\frac{1}{(1+\omega)(1+\omega\tau)}}\right)\left(\frac{\left(\frac{P_{m3}}{P_{40}}\right)^{\frac{1}{\gamma}}\sqrt{1-\left(\frac{P_{m3}}{P_{40}}\right)^{\frac{\gamma-1}{\gamma}}}}{\left(\frac{2}{\gamma+1}\right)^{\frac{1}{\gamma-1}}\sqrt{1-\frac{2}{(\gamma+1)}}}\right) \tag{3.42}$$

# Chapter 4: Development of CFD Simulation for a Jet Pump System

## 4.1 Introduction

Many factors affect the mechanisms of a jet pump that pertain to self-cooling and PV cleaning, especially the environment and geometry. However, inclusive research on this subject is not readily available, a few studies have been conducted on this subject and more evidence is required. Still, it is apparent that the entire system and its mechanisms are simple, although they operate in different manners.

In this research, various tests and procedures were performed to produce and optimise the design. ANSYS Fluent 16.1 was used to perform the numerical simulations required to conduct the necessary experiments. It was used to validate the experimental data required for different steps, including the measurements of heat, moisture and air velocity collected using various devices and gauges. These measurements were crucial to obtaining in order to conduct this research. Next, simulations were conducted using computational fluid dynamics (CFD).

It is important to note that the modelling of CFD cannot substitute real experiments carried out in controlled environments; however, CFD modelling provides accurate figures in a short amount of time and at a low cost. Therefore, CFD models should not be discarded as irrelevant or insignificant

## 4.2 Overview of Computational Fluid Dynamics

Real experiments provide better insight and understanding than simulations. However, some studies conducted on the patterns to verify the significance of simulated systems have revealed that the difference between actual and simulated systems is marginal (Riffat and Omer, 2001). It must be recognised that, over time, computer hardware and software have evolved dramatically and are being used more and more frequently, as they are able to produce valid and credible results. In engineering fields, simulated experiments are often conducted, and various studies have validated the use of CFD modelling.

CFD is a statistical method employed to generate results quickly and efficiently. Since the 1990s, researchers have increasingly employed this technique (Wang, 1990). In addition, special equations, such as Navier–Stokes equations, are used, which are very complex in structure; however, they are useful for analyses.

The basic doctrine of the method is quite mature and is in the realm of fluid dynamics investigation and statistical scrutiny. The method itself is employed for an extended period. The system has the capacity to provide accurate results regarding fluid momentum and other parameters (Fletcher, 2012). In addition, CFD has many benefits. It is time, energy and cost efficient, and it can be used to reproduce results by revising certain mechanisms. Further, CFD is able to provide a holistic picture and a good amount of information to help researchers identify the behaviour of the fluid. Finally, few resources are required to perform CFD analysis.

To perform a satisfactory CDF analysis for system descriptions and working principles, the following steps must be followed:

1. Carefully define the shape and geometry of the model.
2. Study the issues related to the meshing of the domain.
3. Clearly, specify the conditions of the boundaries.
4. Exploit the model to ensure that the right model has been adopted

## 4.3 Computational Fluid Dynamics Simulation Process

CFD and the process of configuring are multistage processes. In the current study, ANSYS was used, which is more accurate and more effective according to the research. It must be acknowledged that, in real experiments, many complexities are involved; thus, technology was used for this evaluation, as it has been determined to be precise in previous studies.

In CFD simulation, the area of interest in terms of the geometry is known as the flow domain, and this was first defined in a three-dimensional design. The flow domain was divided into discrete control volumes as cells after creating the geometry in a process known as grid generation or meshing. For this purpose, Design Modeler, which is a part of the ANSYS Workbench (i.e., Fluent's geometry-creation programming) was used. Two- and three-dimensional geometry models integrating the ANSYS Workbench meshing model were generated by a computer-aided design interface to characterise their boundary conditions and to produce an estimation. This computational mesh was sent to Fluent, which was used to calculate the fluid properties as energy and momentum of jet pump

## 4.4 Description of the Geometry and Grid

Before introducing and discussing the applicable simulation results in Section 5.5, some essential elements of the CFD simulations are provided in this Section. The specific components for every case are given as inlet stream conditions in the following Sections. Commercial CFD code Fluent 16.1 was used to simulate the jet pump model under various conditions to visualise flow.

The properties of the fluid in a jet pump can be studied by determining their requirements through a simulation. In general, it is vital to run calculations twice to obtain accurate results; the simulation is reset or the model is redesigned if the second calculation shows any errors. In the event that the outcome indicates that a model can give the appropriate amount of fluid required for PV cleaning, the simulation and model conditions are used as the elementary conditions, and the model is used as the elementary model.

It was assumed that the mixing chamber length and all other conditions were the same to obtain the data and the results of the simulations. However, after finding contrasting outcomes in the simulations, certain conditions were altered. To enhance the precision and dependability without affecting the conditions, 14 models were developed and analysed.

### 4.4.1 Geometry Creation

Generating flow domain geometry is a complicated and interesting process. It is important to ensure that the maximum possibility of each CFD geometry model was represented throughout. Each model is composed of two-dimensional illustrations with any two of the following inlets: $D_1$, $D_2$, $D_3$ and $D_4$, where $D_1$ represents the diameters of the primary inlet jet pump and $d_1$ the nozzle throat, $D_2$ represents the diameters of the secondary inlet jet pump and $d_2$ the nozzle outlet, $D_3$ is the diameter of the inlet of the mixing chamber and $D_4$ is the constant area section inlet diameter. The lengths of the nozzle diffuser, mixing chamber and pump diffuser are denoted as $L_1$,$L_2$ , $L_{throat}$ and $L_3$, respectively.

Primary and secondary fluids flow through these pipes, and their rate of flow is different at each point. Their velocities are denoted by $v_1$ for primary fluids, $v_2$ for secondary fluids and $v_{out}$ for mixing fluids in the jet pump outlet. The mass flow rates of the primary fluid and secondary fluid are also different in the inlet and outlet pipes; they are expressed as $m_1$ for the primary inlet and $m_2$ for the secondary inlet, while the outlet jet pump's mass flow rate is denoted by $m_{out}$. Figure 4-1 shows the elementary model of the jet pump.

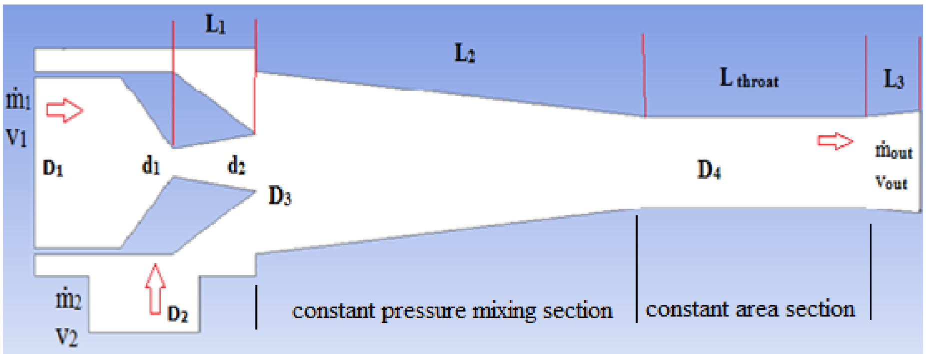


Figure 4-1:Two-dimensional view of the elementary jet pump model.

The dimension was assumed according to the studies on jet pump principles presented in Chapter 3. In the first model, it was assumed that $D_1$ = 30 mm, $D_2$ = 20 mm, $D_3$ = 32 mm, $D_4$ = 16 mm, $d_1$ = 5 mm, $d_2$ = 10 mm, $L_1$ = 15 mm, $L_2$ = 80 mm, $L_{throat}$ = 40 mm and $L_3$ = 10 mm. Table 4-1 shows the basic model of the jet pump.

The dimensions of the other models were the same as those of the first model; however, the diameter of the nozzle throat and the lengths of the mixing chamber and jet pump throat varied.

Table 4-1: Basic case model of the jet pump

| Case | $D_1$ | $D_2$ | $D_3$ | $D_4$ | $d_1$ | $d_2$ | $L_1$ | $L_2$ | $L_{throat}$ | $L_3$ |
|---|---|---|---|---|---|---|---|---|---|---|
| **Basic Case** | **30** | **20** | **32** | **16** | **5** | **10** | **15** | **80** | **40** | **10** |

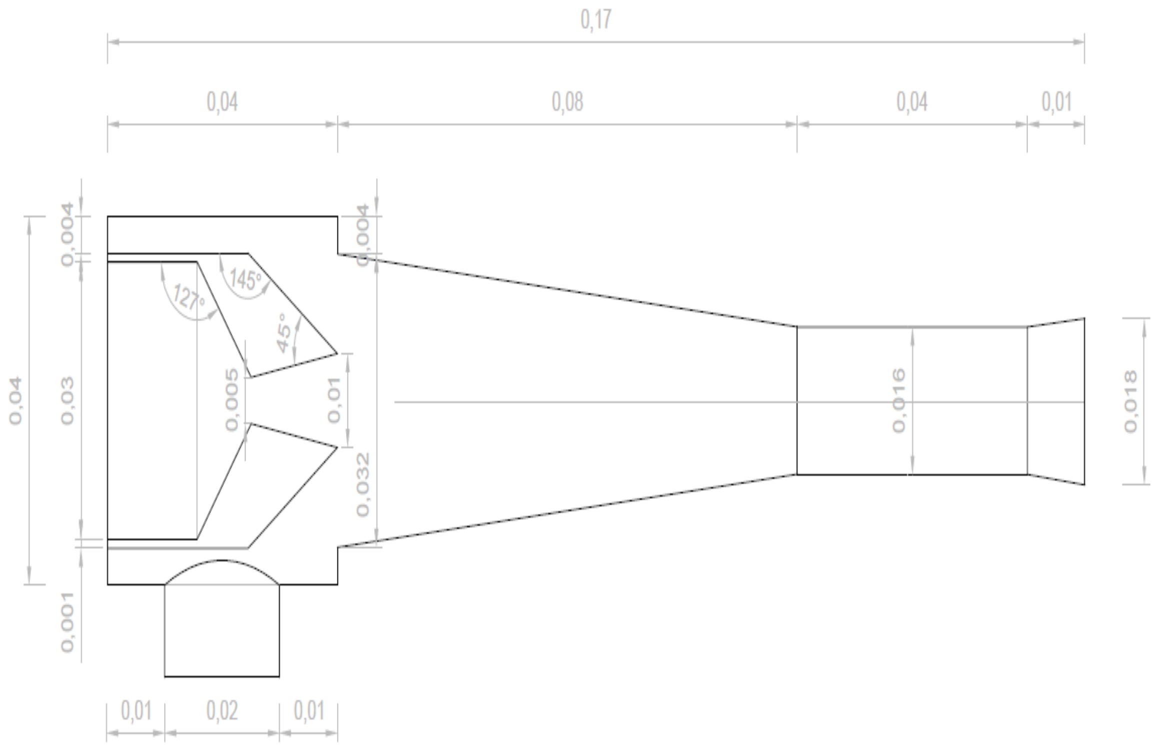


Figure 4-2: Jet pump two-dimensional model

## 4.4.2 Variation values of the 14 models

The variation values studied were small to ensure that the verification was reasonable and acceptable. The diameter of the nozzle throat ($d_1$) was 2, 3, 4, 6 and 7 mm in different models. The length of the mixing chamber, constant pressure-mixing section

($L_2$) was 60, 70, 90 and 100 mm in different models. Finally, the length of the jet pump throat or constant area section ($L_{throat}$) was 20, 30, 50 and 60 mm in different models. A three-dimensional jet pump model (Figure 4-3) was built using DesignModeler.

Table 4-2: Diameters of the nozzle throat ($d_1$).

| Case A | $D_1$ | $D_2$ | $D_3$ | $D_4$ | d1 | d2 | $L_1$ | $L_2$ | $L_{throat}$ | $L_3$ |
|---|---|---|---|---|---|---|---|---|---|---|
| A-1 | 30 | 20 | 32 | 16 | 2 | 10 | 15 | 80 | 40 | 10 |
| A-2 | 30 | 20 | 32 | 16 | 3 | 10 | 15 | 80 | 40 | 10 |
| A-3 | 30 | 20 | 32 | 16 | 4 | 10 | 15 | 80 | 40 | 10 |
| A-4 | 30 | 20 | 32 | 16 | 6 | 10 | 15 | 80 | 40 | 10 |
| A-5 | 30 | 20 | 32 | 16 | 7 | 10 | 15 | 80 | 40 | 10 |

Table 4-3: Lengths of the mixing chamber, constant pressure-mixing section ($L_2$).

| Case B | $D_1$ | $D_2$ | $D_3$ | $D_4$ | d1 | d2 | $L_1$ | $L_2$ | $L_{throat}$ | $L_3$ |
|---|---|---|---|---|---|---|---|---|---|---|
| B-1 | 30 | 20 | 32 | 16 | 5 | 10 | 15 | 60 | 40 | 10 |
| B-2 | 30 | 20 | 32 | 16 | 5 | 10 | 15 | 70 | 40 | 10 |
| B-3 | 30 | 20 | 32 | 16 | 5 | 10 | 15 | 90 | 40 | 10 |
| B-4 | 30 | 20 | 32 | 16 | 5 | 10 | 15 | 100 | 40 | 10 |

Table 4-4: Lengths of the mixing chamber ($L_{throat}$).

| Case C | $D_1$ | $D_2$ | $D_3$ | $D_4$ | d1 | d2 | $L_1$ | $L_2$ | $L_{throat}$ | $L_3$ |
|---|---|---|---|---|---|---|---|---|---|---|
| C-1 | 30 | 20 | 32 | 16 | 5 | 10 | 15 | 80 | 20 | 10 |
| C-2 | 30 | 20 | 32 | 16 | 5 | 10 | 15 | 80 | 30 | 10 |
| C-3 | 30 | 20 | 32 | 16 | 5 | 10 | 15 | 80 | 50 | 10 |
| C-4 | 30 | 20 | 32 | 16 | 5 | 10 | 15 | 80 | 60 | 10 |

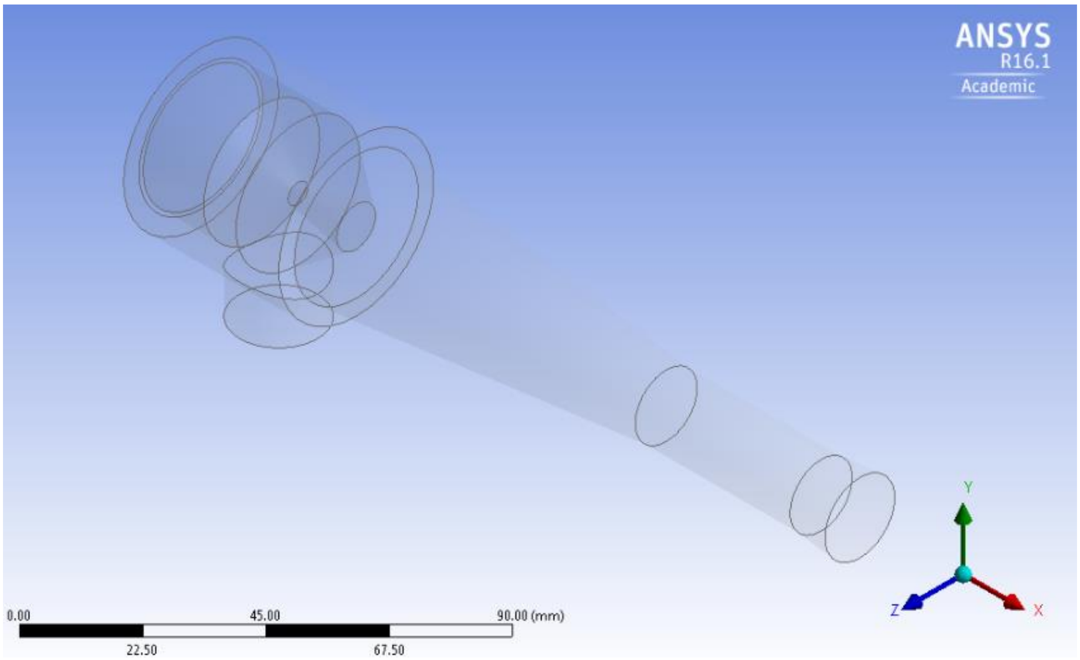


Figure 4-3: Three-dimensional model built using DesignModeler.

### 4.4.3 Grid Generation

Grid generation comprised of different subdomains and small control volumes and was solved using various equations. This process of solving individual parts is known as meshing. In this process, each unit of the mesh is solved individually to satisfy the whole system.

ANSYS is a highly efficient automated process that generates an exact solution for each mesh condition; these solutions are applied to different areas. This parallel processing is automatic; thus, it is time efficient. Its lattice apparatuses have the capacity to parametrically build hexahedral, tetrahedral, kaleidoscopic and pyramidal cells. In this work, the geometry was produced using ANSYS Meshing and imported into Fluent 16.1, where the calculations and post-processing of the outcomes were conducted.

During mesh processing, the flow characteristics of fluids are set to achieve the grid density required for each flow domain, which is done using a specific grid density for different parts in order to accommodate movement in different domains.

In addition, tetrahedral mesh cells were used in the robust combination and automated surface meshing conducted in this study. Scientists use tetrahedral mesh cells to control quality in order to achieve perfect simulations and push-button meshing. Local control is used to determine dimensions, topology, matching and other controls that are applied only when necessary.

Patch conforming generates surface mesh over volume mesh to allow for fluid flow analysis. To enhance the quality of surface mesh, multiple triangular surface meshing processes are used to generate layers on the surface of the mesh, which consists of pipes that contain fluids with different flow rates.

An example of patch conforming in CFD jet pump models is shown in Figure 4-4. Both the quality and size of the function can be measured using mesh control methods in the system. In this study, the mesh model is 0.06 mm as cell size and includes fast transitions. For triangular surface mesh, the most frequently adopted method is a controlled program consisting of 547,997 nodes and 322,060 elements, and it gives reasonable simulations to allow for precise calculations.

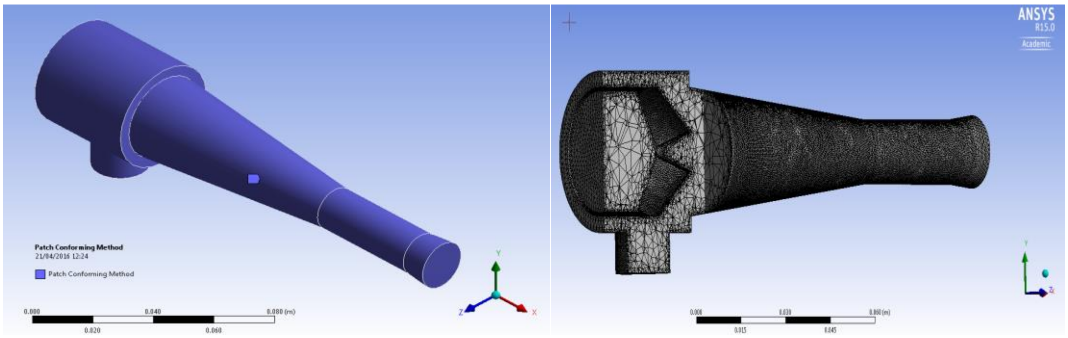


Figure 4-4: Patch conforming in a CFD jet pump model in (left) and the generated grids for the CFD jet pump model (right).

Regarding setting the mesh of the jet pump, it is essential to generate names for the faces of the primary inlet, the secondary inlet and the jet pump outlet. As displayed in Figure 4-5, the primary inlet, secondary inlet and jet pump outlet were named *inlet*$_1$, *inlet*$_2$ and *outlet* in the grid programme.

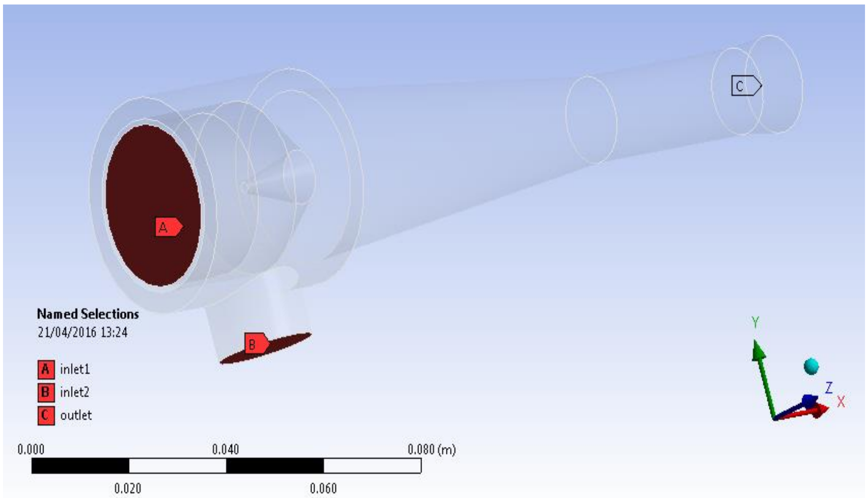


Figure 4-5: Inlet and outlet of the CFD model.

## 4.5 General Solution format settings

ANSYS Fluent gives finished work adaptability, including the capacity to handle fluid issues utilising different unstructured cross sections, which can be created for complex geometries without difficulty. The upheld work sorts two-dimensional triangular networks and three-dimensional tetrahedral networks. ANSYS Fluent allows the user to refine or coarsen work considering the stream's arrangement and to set different non-relaxation factors identified in the work or the Solver.

In this case, Pressure-Based was set as the Solver, using absolute as the velocity formulation and steady as the time. In this study, the species model was chosen to be Species Transport in the simulation, as it is able to compute the fluid properties of several materials in one species individually.

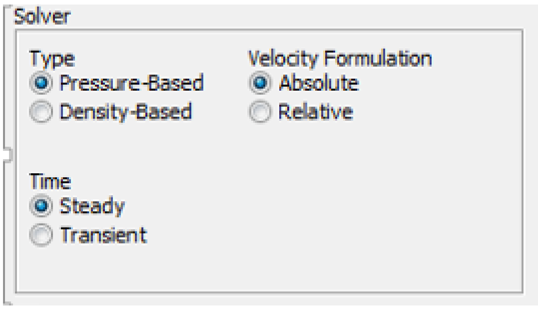


Figure 4-6: Solver setting of the jet pump using Fluent.

## 4.6 Governing equations

Governing equations allow for the definition of a flow field using non-linear partial differential equations to determine conserved mass, momentum and energy. Three main governing equations are discussed in this section.

### 4.6.1 Mass conservation

The most common terms to describe the conservation of mass in fluids are Eulerian terms, which can be written as follows:

$$\frac{\partial \rho}{\partial t} + div\rho\, V = S_m, \tag{4-1}$$

Where $\rho$ is the density, t is the time, V is the velocity vector for flowing fluids and $S_m$

is the mass of the source. The above Equation can be reduced to be applied to constant density conditions in ventilation systems where the temperature differences are not too large; the reduced Equation can be expressed as follows:

$$div\, V = 0. \tag{4-2}$$

### 4.6.2 Transport of momentum

The most familiar equations in fluid dynamics are derived from Newton's second law of the conservation of momentum. These are the set of equations that can be written as Eulerian terms as a single vector form with identical notations. These equations are known as Navier–Stokes Equations, one of which is illustrated below:

$$\frac{\rho dv}{dt} = \rho g - \nabla p + \frac{\partial}{\partial x_j}\left[\mu\left(\frac{\partial v_i}{\partial x_j} + \frac{\partial v_j}{\partial s_i}\right) + \delta_u \lambda div\, V\right]. \tag{4-3}$$

This equation includes different constants and variables and gives a complete explanation for fluid flow in a certain area. It is defined using spatial coordinates $x_i$ and $x_j$i. The gravitational vector is defined by g. The coefficient of viscosity is represented by$\mu$, the coefficient of bulk viscosity is represented by $\lambda$ and the Kronecker delta function is defined by δij. Navier–Stokes equations allow researchers to hypothesise the ordinary viscosity and the bulk viscosity.

## 4.7 Turbulence Model selection

Turbulence takes place in different parts of a jet pump, including the nozzle throat, which has a high velocity in operation and contributes to high turbulence and turbulent flow, as high-pressure air enters the mixing chamber and is mixed with water vapour. By recognising the framework of turbulence, the correct model can be selected; thus, complex air conditions were tested. According to Malakas and Versteeg

(2007), turbulence can be specified by checking the CFD field; therefore, the correct turbulent model can be chosen. Different turbulent models have been developed, including the K-ε, K-w and Spalart–Allmaras models (Easom, 2000). The turbulence intensity can be estimated with the following Equation:

$$\mu_t = \rho C_\mu \frac{k^2}{\varepsilon} \qquad (4\text{-}4)$$

,

Where ε is the turbulence kinetic energy and μ represents the viscosity of the turbulent form.

## 4.8 Boundary conditions

Different boundary conditions are specified according to operational and physical characteristics and represent the characteristics of a model's topology. The boundary conditions of the CDF model used in this study are summarised in Table 4-5.

Table 4-5: Summary of boundary conditions.

| Zone Name | Boundary Type |
|---|---|
| Process dry air inlet | Mass flow inlet |
| Process water vapour inlet | Pressure inlet |
| Process wet air outlet | Pressure outlet |
| Wall | Wall |

The working environment of the jet pump is assumed to have a pressure of 101.325 KPa and a temperature of nearly 300 K. The primary fluid in the inlet was set with different air pressures but equal molecular weights, and the mass flow of the inlet in the first simulation was used. The boundary conditions of inlet1, inlet2 and the outlet are shown in Figures 4-7, 4-8 and 4-9.

Mass flow inlet was selected for inlet1. In the model, the rate of mass flow in inlet1 was set to be 0.01, 0.02, 0.03, 0.04, 0.05 and 0.06 kg/s. Pressure inlet was selected for both inlet2 and the outlet. Table 4-5 shows a summary of inlet1, inlet2 and the outlet. The itemised settings for inlet1, inlet2 and the outlet are represented in Figures 4-7, 4-8 and 4-9, respectively.

The type of inlet1 is chosen to be "mass-flow-inlet" and in the first simulation, the inlet2 and the outlet are set as "pressure-inlet" and “pressure-outlet” respectively. However, because the inlet flow is not supersonic, the Supersonic/Initial Gauge Pressure is not set, as the ANSYS Fluent will calculate this from the specified stagnation quantities. In this case, the flow is subsonic in inlet2, therefore not set as shown in Figure 4-8.

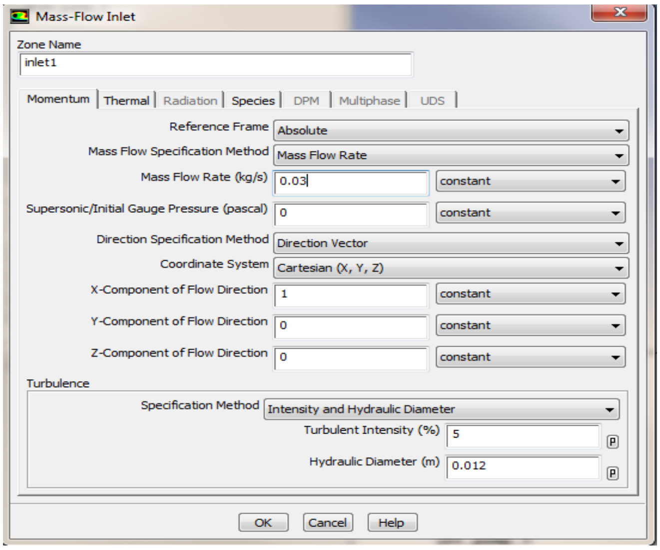


Figure 4-7: Boundary condition settings for inlet 1.

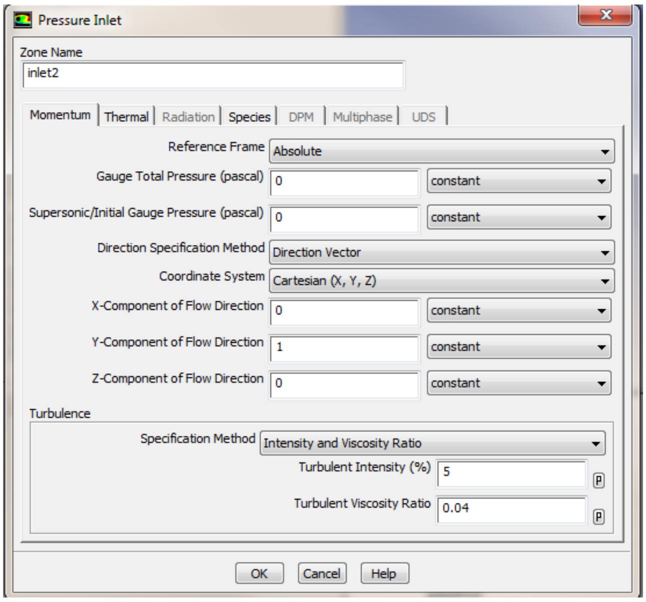


Figure 4-8: Boundary condition settings for inlet 2.

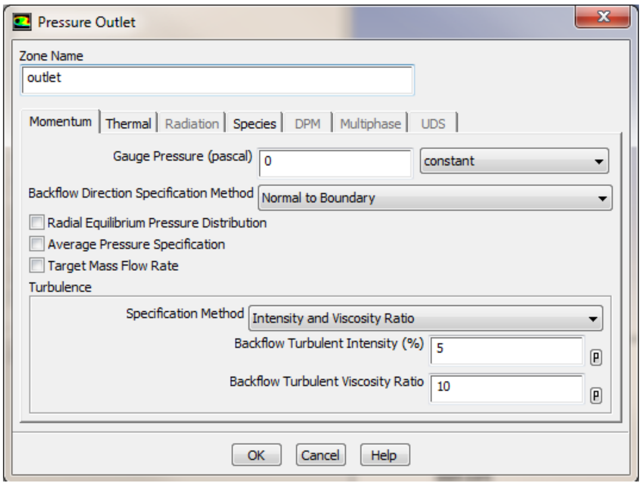


Figure 4-9: Boundary condition settings for the outlet.

Before running Fluent, it was important to define the surface and the centre of the model. Analysing the surface using a two-dimensional picture allowed for the determination of the fluid properties of the jet pump, including the pressure and velocity vectors and counters. The surfaces were generated by cutting through the solution domain over arbitrary planes in the three-dimensional model. The values of the fluid properties along the centre were plotted in diagrams, as shown in Figures 4-

11 and 4-12, including the surface (Figure 4-10, top) and the centre (Figure 4-11, black line) in the basic model. The circle in Figure 4-11 indicates the centre of the nozzle throat in the model.

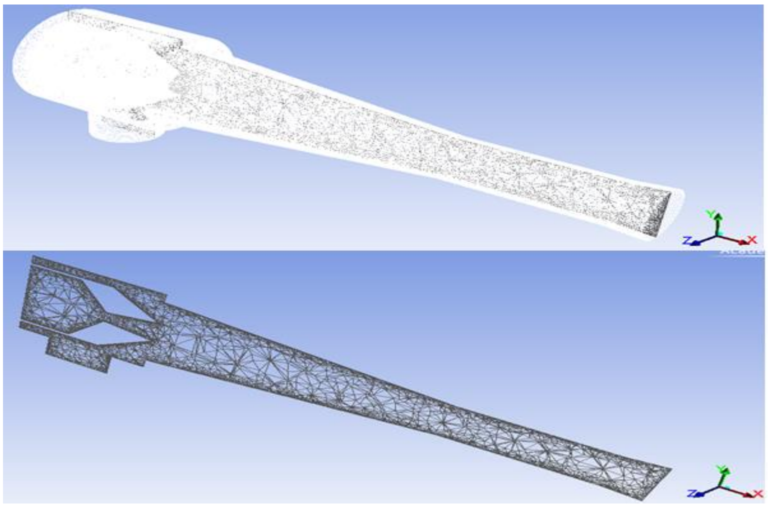

Figure 4-10: Mesh surface of the jet pump model.

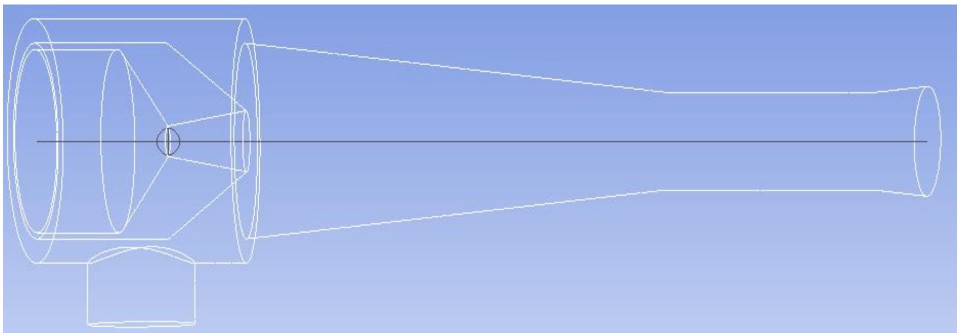

Figure 4-11: Centre line and the centre point of the nozzle throat in the jet mode.

## 4.9 Discretization and method of solution

Discretisation methods are well known; in CFD, the finite-difference method is popular. Other methods in Fluent include the boundary element method and the finite volume method. To analyse and numerically solve these, partial differential equations are used. In this study, discretisation was carried out using different partial equations of the finite volume method. The Semi-Implicit Method for Pressure-Linked

Equations was used by Patankar and Spalding (1972) because of its strong ability to find solutions rapidly.

## 4.10: Solver controls

The simulations in this work were performed using a pressure-based solver. Pressure-based solvers utilise under-unwinding equations to control the design of calculated factors at every iteration. The default under-unwinding parameters for all the factors were set to close-to-ideal values for the largest conceivable number of cases.

At every interval time, iterations were run to determine the transport equations for each time. To ensure that the procedures of each iteration would converge, variation in the factors was controlled from one iteration to the next using under-relaxation factors of 0.3, 0.7 and 0.8 connected to the pressure, force and turbulence kinetic power, as prescribed by Fluent. Figure 4-12 illustrates the solution method and control settings of the jet pump.

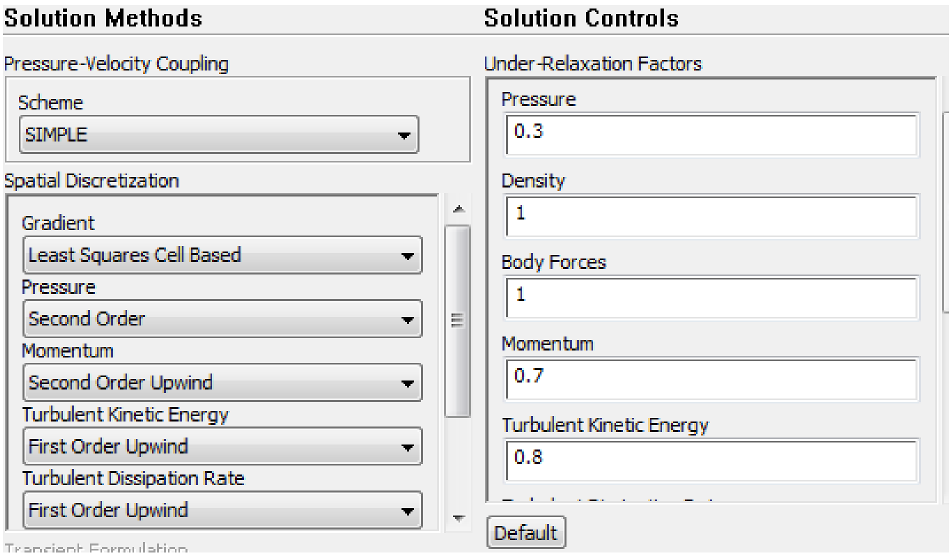


Figure 4-12: Solution method and control settings of the jet pump.

# Chapter 5: Results and Discussion of CFD Study of the Jet Pump System

## 5.1 Introduction

The development of computer hardware and numerical analysis has resulted in the use of CFD tools to better understand the process of mixing the design of systems and evaluating their hydrodynamic performance. Simulations have been found to be the most efficient method for determining the effect that CFD has on jet pump systems. The main advantage of CFD simulations is the opportunity to visualise flow behaviour and explain the flows in a jet pump system. Thus, a simulation has many advantages over experimental work. An additional advantage is that simulation takes less time and is more cost-efficient than the experimentation method. In this study, CFD simulations of the flow in a jet pump model were used to analyse the fluid flow in the jet and establish the directions of the fluid flow in various areas in the system. In this study, the simulations were employed to establish the effect of varying the inlet air mass flow rate and water vapour mass rate of the fluid flow throughout the jet pump system the jet pump. The results are shown in subsequent Sections, and these are discussed in reasonable detail in following Sections.

The purpose of the CFD simulations is to give an insight into the fluid behaviour inside the jet pump, under a different condition in order to optimise the jet pump design.

A post-processing tool has been used to show the various contours and vectors in the CFD models to study the behaviour of fluid through the jet pump and relate this for flow verification exercise. The contours for several flow settings are displayed in images at the end of this Chapter.

After the calculation in CFD, the values of a secondary mass flow rate, total outlet mass flow rate, a secondary velocity inlet ($v_2$) and the velocity outlet from the jet pump $v_{out}$ are assessed. The rest of the simulations, like the outlet for water vapour of the mass flow rate ($\dot{m}_w$), the total outlet of water mass fraction for the jet pump ($w_{out}$) and the entrainment ratio (ER) could also be assessed from the results of simulation of Fluent: $\dot{m}_{water} = \dot{m}_2 \times$ water mass fraction, $W_{out} = \dot{m}_{water} / \dot{m}_{out}$ and $ER = \dot{m}_2 / \dot{m}_1$. The secondary fluid in $inlet_2$ is set as the mixture of dry air and water vapour and the molecular weight of the water vapour is 18.01534 kg/kgmol. The species mass fraction of the water vapour in the secondary fluid is set as 0.0222, which is just equal to the water mass fraction when the air is humidity saturated at 101.325 kPa, 300 K

In addition, regarding of variation of a condition, once the simulation results of the elementary case were found to be positive in Fluent, $d_1$, $L_2$ and $L_{throat}$ were differentiated to determine whether certain differences could increase the efficacy of the jet pump. A difference in one term might affect an entire group of simulations. There are three groups and one individual case; each group has numerous cases under different boundaries.

The terms of the elementary model were varied to ensure confident results. The mass flow rates of inlet1 $\dot{m}_1$ were specified at 0.02, 0.03, 0.04, 0.05 and 0.06 kg/s for all cases. The diameters of the nozzle throat (Group A) were designated to be 2, 3, 4, 5, 6, 7 and 8 mm. The lengths of the mixing chamber (Group B) were designated to be 60, 70, 90 and 100 mm. Finally, the lengths of the jet pump throat (Group C) were designated to be 20, 30, 50 and 60 mm.

Regarding to the calculation, the velocity magnitude contours displayed in 2D part of a jet pump model, the diagrams around a velocity magnitude values over the centre line and the statistical values about the values of a secondary mass flow rate, total outlet mass flow rate, the primary velocity inlet ($v_1$), a secondary velocity inlet ($v_2$) and the velocity outlet from the jet pump $v_{out}$ will be noted as the results of simulation that able to use for discussion. Figure 5-1 shows two dimensional view of the basic case model.

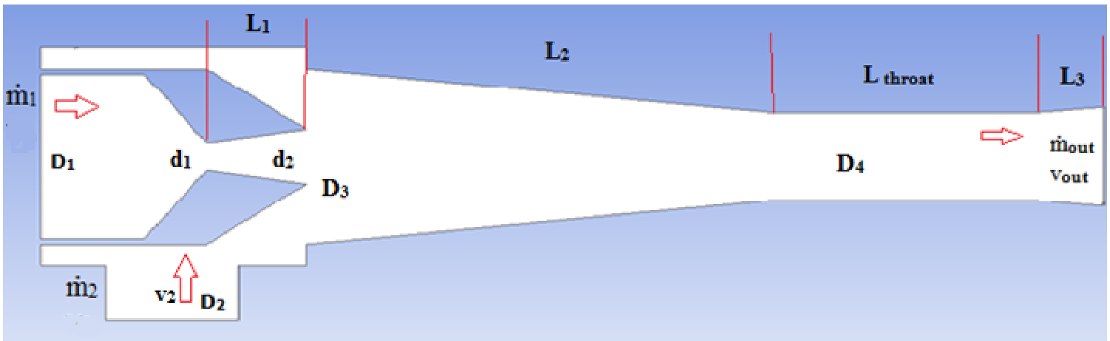


Figure 5-1: Two dimension view of the basic case model.

## 5.2 The position along the centre line on all the geometry.

The flow is assessed along the centre line of the jet pump, by plots in the X-Y plane at the different parameters .These graphs are present the velocity magnitude (m/s) of the fluid along the centre of the line of jet pump and which is in the jet pump of the models. In the graph, the red colour or line of red indicate the fluid velocity which is in the nozzle centre in the throat.

The yellow colour presents the position along the centre line which can draw from the 0.00m to 0.17 m. The value of the position increase and which depends on the length of $L_1$ and $L_2$, the throat can be shown in Figure 5-2, as we said that the line of red colour shown the centre of the nozzle.

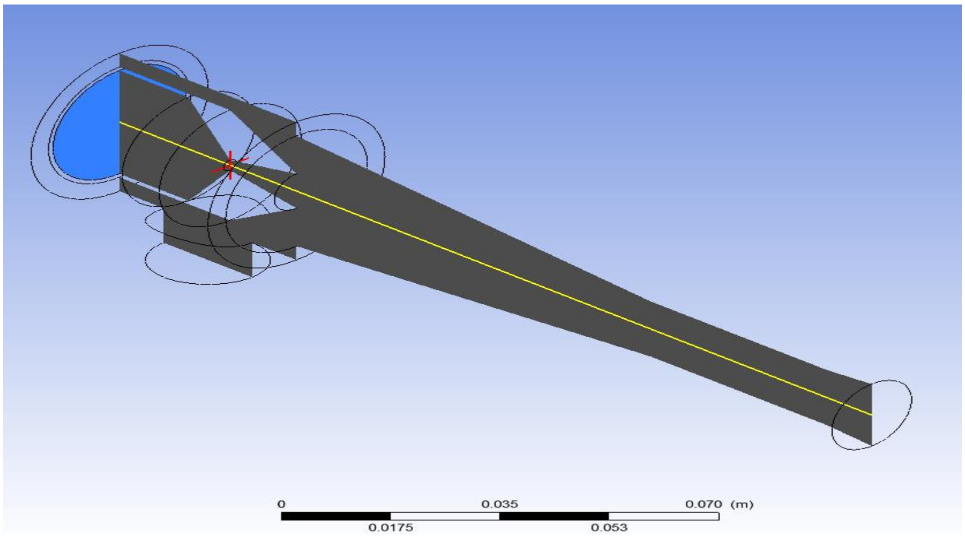


Figure 5-2: The position along the centre line (in yellow colour) and the nozzle throat (in red).

## 5.3 The Nozzle throat diameter (Group A) variation of $d_1$

In this Section, the numerical results of the simulation for different diameters nozzle throat are presented in Group A models are shown in Table 5-2 to Table 5-7, the basic values are shown in Table 5-1.

Table 5-1: Basic case model of Group A

| $D_1$ (mm) | $D_2$ (mm) | $D_3$(mm) | $D_4$ (mm) | d1 (mm) | d2 (mm) | $L_1$ (mm) | $L_2$ (mm) | $L_{throat}$ (mm) | $L_3$ (mm) |
|---|---|---|---|---|---|---|---|---|---|
| 30 | 20 | 32 | 16 | variable | 10 | 15 | 80 | 40 | 10 |

Table 5-2: Simulation results of the varied nozzle throat diameter models in Group A (variation of $\dot{m}_1$, $d_1$=2mm)

| $\dot{m}_1$ (kg/s) | $\dot{m}_2$ (kg/s) | $\dot{m}_{out}$ (kg/s) | $\dot{m}_w$ (kg/s) | $v_1$ (m/s) | $v_2$ (m/s) | $v_{out}$ (m/s) | $w_{out}$ | ER |
|---|---|---|---|---|---|---|---|---|
| 0.01 | 0.0314 | 0.0414 | 0.000697 | 12.02 | 86.34 | 140.97 | 0.016838 | 3.14 |
| 0.02 | 0.0638 | 0.0838 | 0.001416 | 24.05 | 175.03 | 284.86 | 0.016902 | 3.19 |
| 0.03 | 0.096 | 0.126 | 0.002131 | 36.07 | 263.56 | 428.88 | 0.016914 | 3.205 |
| 0.04 | 0.128 | 0.168 | 0.002842 | 48.1 | 391.59 | 624.68 | 0.016914 | 3.21 |
| 0.05 | 0.16 | 0.21 | 0.003552 | 60.12 | 441.05 | 716.75 | 0.016914 | 3.216 |
| 0.06 | 0.193 | 0.253 | 0.004285 | 72.156 | 530.65 | 862.1 | 0.016935 | 3.22 |

Table 5-3: Simulation results of the varied nozzle throat diameter models in Group A (variation of $\dot{m}_1$, $d_1$=3mm)

| $\dot{m}_1$ (kg/s) | $\dot{m}_2$ (kg/s) | $\dot{m}_{out}$ (kg/s) | $\dot{m}_w$ (kg/s) | $v_1$ (m/s) | $v_2$ (m/s) | $v_{out}$ (m/s) | $w_{out}$ | ER |
|---|---|---|---|---|---|---|---|---|
| 0.01 | 0.0222 | 0.0322 | 0.000493 | 12.02 | 61.1 | 109 | 0.015306 | 2.22 |
| 0.02 | 0.047 | 0.067 | 0.001043 | 24.05 | 137.9 | 238.3 | 0.015573 | 2.35 |
| 0.03 | 0.073 | 0.103 | 0.001621 | 36.07 | 202 | 244 | 0.015734 | 2.43 |
| 0.04 | 0.098 | 0.138 | 0.002176 | 48.1 | 270 | 470 | 0.015765 | 2.45 |
| 0.05 | 0.125 | 0.175 | 0.002775 | 60.12 | 339 | 588 | 0.015857 | 2.50 |
| 0.06 | 0.149 | 0.209 | 0.003308 | 72.156 | 530.61 | 862.16 | 0.015827 | 2.48 |

Table 5-4: Simulation results of the varied nozzle throat diameter models in Group A (variation of $\dot{m}_1$, $d_1$=4mm)

| $\dot{m}_1$ (kg/s) | $\dot{m}_2$ (kg/s) | $\dot{m}_{out}$ (kg/s) | $\dot{m}_w$ (kg/s) | $v_1$ (m/s) | $v_2$ (m/s) | $v_{out}$ (m/s) | $w_{out}$ | ER |
|---|---|---|---|---|---|---|---|---|
| 0.01 | 0.0153 | 0.0253 | 0.00034 | 12.02 | 42.03 | 85.63 | 0.013425 | 1.53 |
| 0.02 | 0.03185 | 0.05185 | 0.000707 | 24.05 | 87.37 | 175.4 | 0.013637 | 1.59 |
| 0.03 | 0.0483 | 0.0783 | 0.001072 | 36.07 | 132.56 | 265 | 0.013694 | 1.61 |
| 0.04 | 0.0647 | 0.1047 | 0.001436 | 48.1 | 177.7 | 354.67 | 0.013719 | 1.62 |
| 0.05 | 0.08137 | 0.13137 | 0.001806 | 60.12 | 223.2 | 444.75 | 0.013751 | 1.63 |
| 0.06 | 0.09697 | 0.15697 | 0.002153 | 72.156 | 266 | 530.8 | 0.013714 | 1.62 |

Table 5-5: Simulation results of the varied nozzle throat diameter models in Group A (variation of $\dot{m}_1$, $d_1$=5mm)

| $\dot{m}_1$ (kg/s) | $\dot{m}_2$ (kg/s) | $\dot{m}_{out}$ (kg/s) | $\dot{m}_w$ (kg/s) | $v_1$ (m/s) | $v_2$ (m/s) | $v_{out}$ (m/s) | $w_{out}$ | ER |
|---|---|---|---|---|---|---|---|---|
| 0.01 | 0.0114 | 0.0214 | 0.000253 | 12.02 | 31.32 | 72.42 | 0.011826 | 1.14 |
| 0.02 | 0.0236 | 0.0436 | 0.000524 | 24.05 | 64.82 | 147.65 | 0.012017 | 1.18 |
| 0.03 | 0.0358 | 0.0658 | 0.000795 | 36.07 | 98.28 | 222.7 | 0.012078 | 1.19 |
| 0.04 | 0.0479 | 0.0879 | 0.001063 | 48.1 | 131.4 | 297.5 | 0.012098 | 1.20 |
| 0.05 | 0.06 | 0.11 | 0.001332 | 60.12 | 165 | 372 | 0.012109 | 1.20 |
| 0.06 | 0.0721 | 0.1321 | 0.001601 | 72.156 | 197.9 | 447.2 | 0.012117 | 1.20 |

Table 5-6: Simulation results of the varied nozzle throat diameter models in Group A (variation of $\dot{m}_1$, $d_1$=6mm)

| $\dot{m}_1$ (kg/s) | $\dot{m}_2$ (kg/s) | $\dot{m}_{out}$ (kg/s) | $\dot{m}_w$ (kg/s) | $v_1$ (m/s) | $v_2$ (m/s) | $v_{out}$ (m/s) | $w_{out}$ | ER |
|---|---|---|---|---|---|---|---|---|
| 0.01 | 0.0075 | 0.0175 | 0.000167 | 12.02 | 20.8 | 59.25 | 0.009514 | 0.75 |
| 0.02 | 0.016 | 0.036 | 0.000355 | 24.05 | 44.45 | 122 | 0.009867 | 0.80 |
| 0.03 | 0.0247 | 0.0547 | 0.000548 | 36.07 | 68 | 185 | 0.010024 | 0.82 |
| 0.04 | 0.033 | 0.073 | 0.000733 | 48.1 | 92 | 248 | 0.010036 | 0.83 |
| 0.05 | 0.0429 | 0.0929 | 0.000952 | 60.12 | 117 | 312.5 | 0.010252 | 0.86 |
| 0.06 | 0.05065 | 0.11065 | 0.001124 | 72.156 | 139 | 373.35 | 0.010162 | 0.84 |

Table 5-7: Simulation results of the varied nozzle throat diameter models in Group A (variation of $\dot{m}_1$, $d_1$=7mm)

| $\dot{m}_1$ (kg/s) | $\dot{m}_2$ (kg/s) | $\dot{m}_{out}$ (kg/s) | $\dot{m}_w$ (kg/s) | $v_1$ (m/s) | $v_2$ (m/s) | $v_{out}$ (m/s) | $w_{out}$ | ER |
|---|---|---|---|---|---|---|---|---|
| 0.01 | 0.0058 | 0.0158 | 0.000129 | 12.02 | 16 | 53.28 | 0.008149 | 0.58 |
| 0.02 | 0.01223 | 0.03223 | 0.000272 | 24.05 | 33.57 | 108.5 | 0.008424 | 0.61 |
| 0.03 | 0.0186 | 0.0486 | 0.000413 | 36.07 | 51 | 163.7 | 0.008496 | 0.62 |
| 0.04 | 0.0249 | 0.0649 | 0.000553 | 48.1 | 68.47 | 218.8 | 0.008517 | 0.62 |
| 0.05 | 0.03121 | 0.08121 | 0.000693 | 60.12 | 85.6 | 273.5 | 0.008532 | 0.62 |
| 0.06 | 0.0376 | 0.0976 | 0.000835 | 72.156 | 103.14 | 328.8 | 0.008552 | 0.63 |

Table 5-8 Simulation results of stagnation pressure of secondary flow rare for the nozzle throat diameter models in Group A (variation of $\dot{m}_1$, $d_1$=5mm)

| $d_1$=5 | $P_1$ | $P_2$ |
|---|---|---|
| 0.1 | 95742.742 | -570.27399 |
| 0.2 | 387767.06 | -2442.9692 |
| 0.3 | 861138.75 | -5618.8164 |
| 0.4 | 1540803.6 | -10044.814 |
| 0.5 | 2370461.7 | -15773.638 |
| 0.6 | 3452532.6 | -22775.241 |

Apart from the simulation result, the Fluent able to present plot diagrams and graphs to characterize the numerical values for Group A and all Figures have been shown in Appendix A.

The plot diagrams that show a velocity magnitude (m/s) of the fluid over the line of the centre for the jet pump (m) in all cases, where the red sign illustrates the fluid velocity in the centre throat of the nozzle. For instance, Figure 5-3 to 5-8 are the plot results of Group A simulations that show the variation of $d_1$ when $\dot{m}_1$ is 0.04 kg/s.

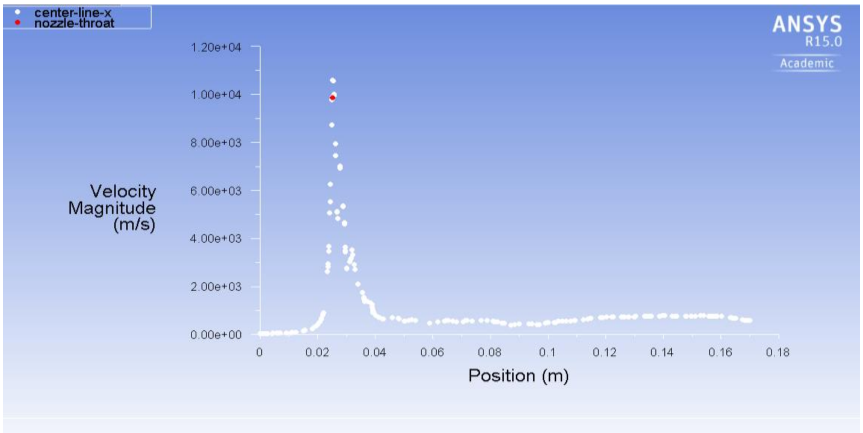


Figure 5-3: Diagram of a velocity magnitude along the line of the centre in the Group A case model $d_1$= 2 mm ($\dot{m}_1$ = 0.04 kg/s)

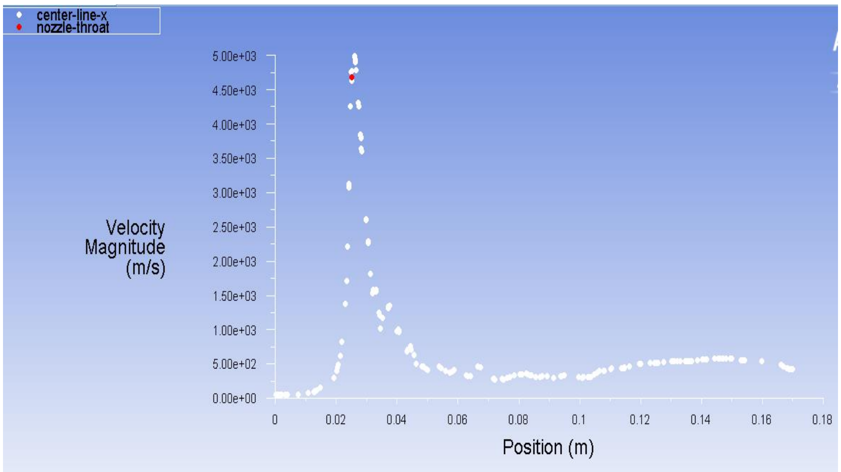


Figure 5-4: Diagram of a velocity magnitude along the line of the centre in the Group A case $d_1$=3 mm ($\dot{m}_1$= 0.04 kg/s)

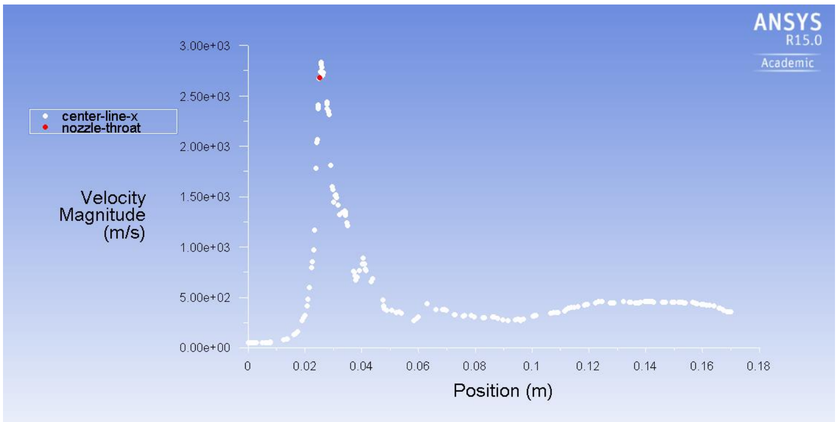


Figure 5-5: Diagram of a velocity magnitude along the line of the centre in the Group A case $d_1$= 4 mm ($\dot{m}_1$ = 0.04 kg/s)

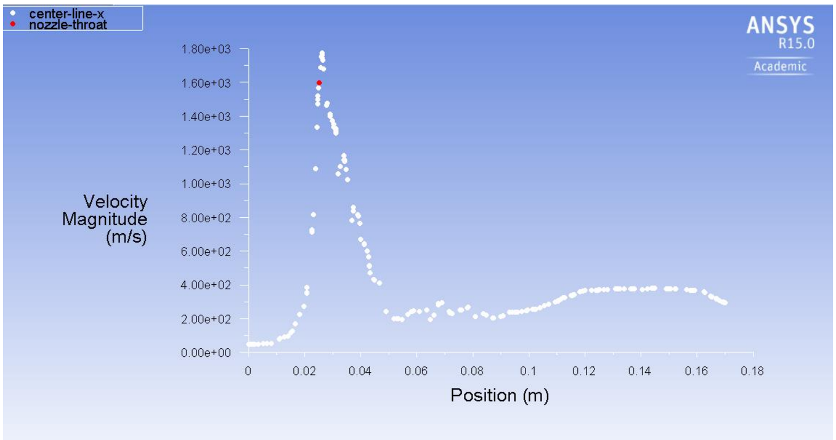


Figure 5-6: Diagram of a velocity magnitude along the line of the centre in the Group A case $d_1$= 5 mm ($\dot{m}_1$ = 0.04 kg/s)

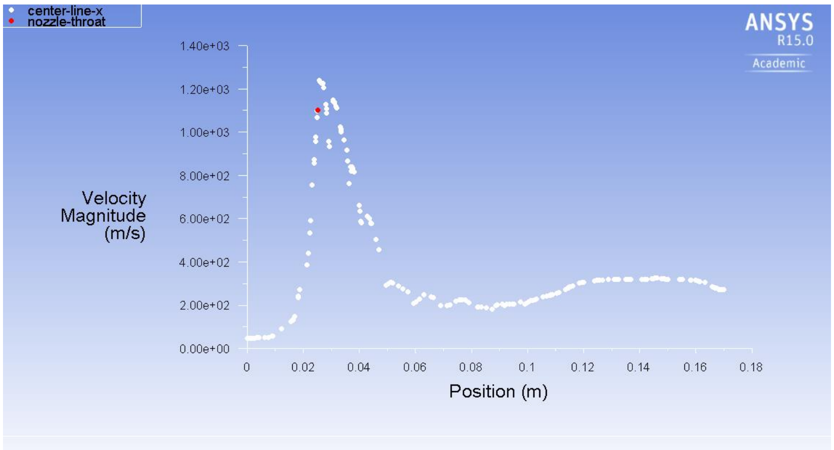


Figure 5-7: Diagram of a velocity magnitude along the line of the centre in the Group A case $d_1$= 6 mm ($\dot{m}_1$ = 0.04 kg/s)

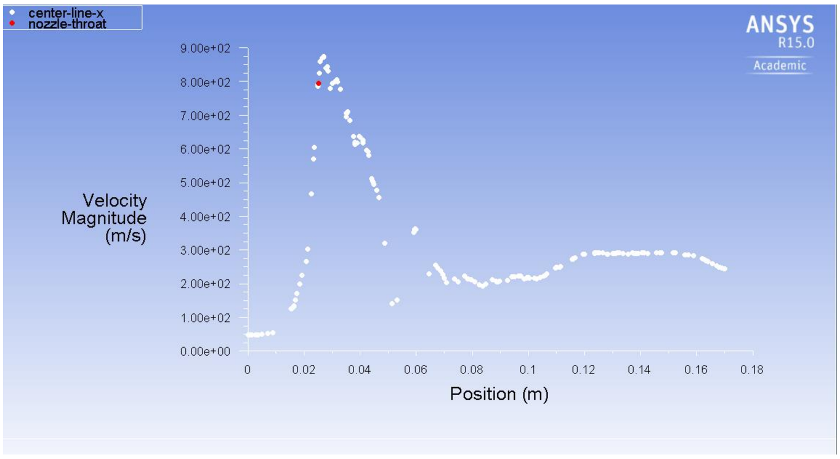


Figure 5-8: Diagram of a velocity magnitude along the line of the centre in the Group A case $d_1$= 7 mm ($\dot{m}_1$ = 0.04 kg/s)

Regards to the difference of the velocity magnitude contour and vector show accessible in the Fluent software have been used as a post-processing tool to analyse the fluid pattern inside a jet pump and then relate this to flow confirmation exercise in nozzle throat diameter models in Group A have been shown in Appendix A.

## 5.4 The lengths of the mixing chamber $L_2$ (Group B)

In this Section, similar the numerical results of the simulation for the lengths of the mixing chamber $L_2$ (Group B) models are shown in Table 5-10 to Table 5-13, the original values shown in Table 5-9

Table 5-9: Basic case model of Group B

| $D_1$ (mm) | $D_2$ (mm) | $D_3$(mm) | $D_4$ (mm) | d1 (mm) | d2 (mm) | $L_1$ (mm) | $L_2$ (mm) | $L_{throat}$ (mm) | $L_3$ (mm) |
|---|---|---|---|---|---|---|---|---|---|
| 30 | 20 | 32 | 16 | 5 | 10 | 15 | variable | 40 | 10 |

Table 5-10: Simulation results of the varied the lengths of the mixing chamber models in Group B (variation of $\dot{m}_1$, $L_2$= 60mm)

| $\dot{m}_1$ (kg/s) | $\dot{m}_2$ (kg/s) | $\dot{m}_{out}$ (kg/s) | $\dot{m}_w$ (kg/s) | $v_1$ (m/s) | $v_2$ (m/s) | $v_{out}$ (m/s) | $w_{out}$ | ER |
|---|---|---|---|---|---|---|---|---|
| 0.01 | 0.01 | 0.02 | 0.000222 | 12.02 | 27.5 | 67.6 | 0.0111 | 1.00 |
| 0.02 | 0.0206 | 0.0406 | 0.000457 | 24.05 | 56.7 | 137.46 | 0.011264 | 1.03 |
| 0.03 | 0.0327 | 0.0627 | 0.000726 | 36.07 | 89.72 | 212.11 | 0.011578 | 1.09 |
| 0.04 | 0.0446 | 0.0846 | 0.00099 | 48.1 | 122.48 | 286 | 0.011704 | 1.12 |
| 0.05 | 0.0558 | 0.1058 | 0.001239 | 60.12 | 153.17 | 357.5 | 0.011709 | 1.12 |
| 0.06 | 0.0668 | 0.1268 | 0.001483 | 72.15 | 183.27 | 428.6 | 0.011695 | 1.11 |

Table 5-11: Simulation results of the varied the lengths of the mixing chamber models in Group B (variation of $m_1$, $L_2$= 70mm)

| $\dot{m}_1$ (kg/s) | $\dot{m}_2$ (kg/s) | $\dot{m}_{out}$ (kg/s) | $\dot{m}_w$ (kg/s) | $v_1$ (m/s) | $v_2$ (m/s) | $v_{out}$ (m/s) | $w_{out}$ | ER |
|---|---|---|---|---|---|---|---|---|
| 0.01 | 0.012 | 0.022 | 0.000266 | 12.02 | 33.1 | 72.618 | 0.012109 | 1.20 |
| 0.02 | 0.0238 | 0.0438 | 0.000528 | 24.05 | 65.26 | 148.359 | 0.012063 | 1.19 |
| 0.03 | 0.0364 | 0.0664 | 0.000808 | 36.07 | 99.87 | 224.934 | 0.01217 | 1.21 |
| 0.04 | 0.05255 | 0.09255 | 0.001167 | 48.1 | 144.172 | 313.216 | 0.012605 | 1.31 |
| 0.05 | 0.0668 | 0.1168 | 0.001483 | 60.12 | 183.3 | 395.9 | 0.012697 | 1.34 |
| 0.06 | 0.0793 | 0.1393 | 0.00176 | 72.15 | 217.775 | 472 | 0.012638 | 1.32 |

Table 5-12: Simulation results of the varied the lengths of the mixing chamber models in Group B (variation of $\dot{m}_1$, $L_2$= 90mm)

| $\dot{m}_1$ (kg/s) | $\dot{m}_2$ (kg/s) | $\dot{m}_{out}$ (kg/s) | $\dot{m}_w$ (kg/s) | $v_1$ (m/s) | $v_2$ (m/s) | $v_{out}$ (m/s) | $w_{out}$ | ER |
|---|---|---|---|---|---|---|---|---|
| 0.01 | 0.0105 | 0.0205 | 0.000233 | 12.02 | 29.038 | 57.162 | 0.011371 | 1.05 |
| 0.02 | 0.0223 | 0.0423 | 0.000495 | 24.05 | 61.399 | 119.72 | 0.011704 | 1.12 |
| 0.03 | 0.0339 | 0.0639 | 0.000753 | 36.07 | 93.054 | 181.67 | 0.011777 | 1.13 |
| 0.04 | 0.0464 | 0.0864 | 0.00103 | 48.1 | 127.48 | 241.73 | 0.011922 | 1.16 |
| 0.05 | 0.0588 | 0.1088 | 0.001305 | 60.12 | 161.4 | 304.311 | 0.011998 | 1.18 |
| 0.06 | 0.0719 | 0.1319 | 0.001596 | 72.15 | 197.3 | 372.005 | 0.012101 | 1.20 |

Table 5-13: Simulation results of the varied the lengths of the mixing chamber models in Group B (variation of $\dot{m}_1$, $L_2$= 100mm)

| $\dot{m}_1$ (kg/s) | $\dot{m}_2$ (kg/s) | $\dot{m}_{out}$ (kg/s) | $\dot{m}_w$ (kg/s) | $v_1$ (m/s) | $v_2$ (m/s) | $v_{out}$ (m/s) | $w_{out}$ | ER |
|---|---|---|---|---|---|---|---|---|
| 0.01 | 0.0112 | 0.0212 | 0.000249 | 12.02 | 30.965 | 59.229 | 0.011728 | 1.12 |
| 0.02 | 0.0233 | 0.0433 | 0.000517 | 24.05 | 63.907 | 122.188 | 0.011946 | 1.17 |
| 0.03 | 0.0356 | 0.0656 | 0.00079 | 36.07 | 97.689 | 185.69 | 0.012048 | 1.19 |
| 0.04 | 0.048 | 0.088 | 0.001066 | 48.1 | 131.717 | 248.75 | 0.012109 | 1.20 |
| 0.05 | 0.0605 | 0.1105 | 0.001343 | 60.125 | 166.192 | 312.663 | 0.012155 | 1.21 |
| 0.06 | 0.0731 | 0.1331 | 0.001623 | 72.15 | 200.51 | 377.537 | 0.012192 | 1.22 |

The plot diagrams that show a velocity magnitude (m/s) of the fluid over the line of the centre for the jet pump (m) in all cases, where the red sign illustrates the fluid velocity in the centre throat of the nozzle. For instance, Figure 5-9 to 5-12 are the plot results of Group B simulations that show the variation of $d_1$ when $\dot{m}_1$ is 0.04 kg/s.

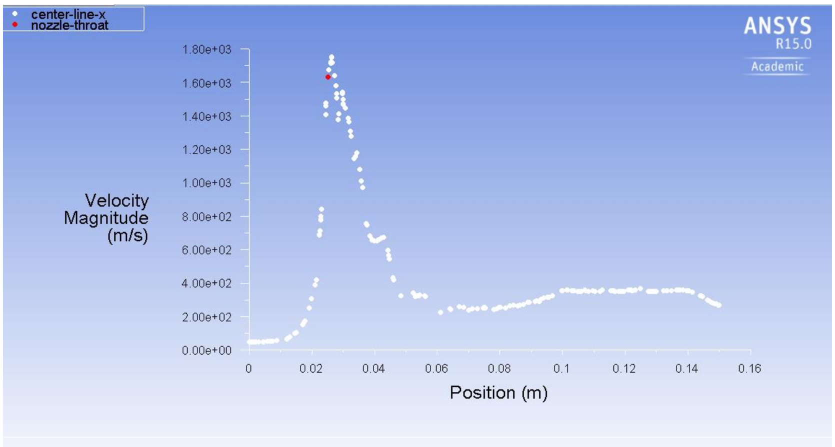


Figure 5-9: Diagram of a velocity magnitude along the line of the centre in the Group B case $L_2$= 60 mm ($\dot{m}_1$ = 0.04 kg/s)

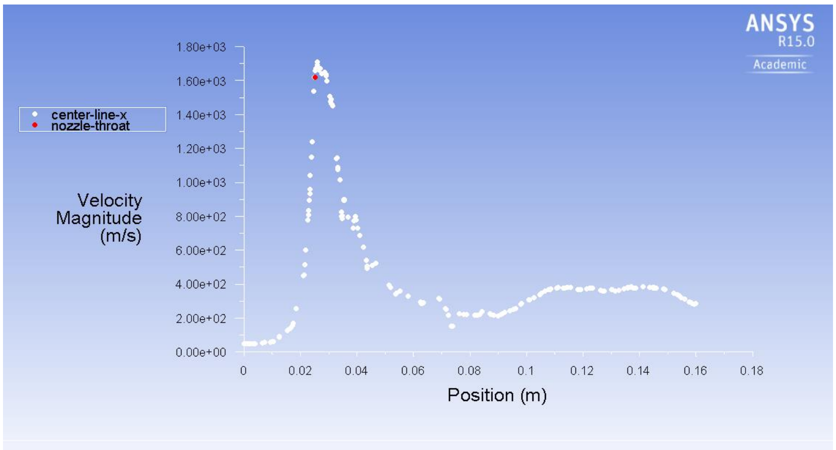


Figure 5-10: Diagram of a velocity magnitude along the line of the centre in the Group B case $L_2$= 70 mm ($\dot{m}_1$ = 0.04 kg/s)

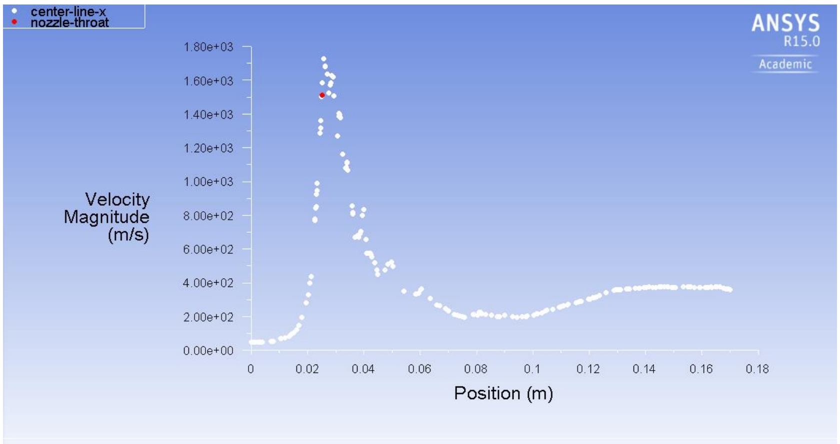


Figure 5-11: Diagram of a velocity magnitude along the line of the centre in the Group B case $L_2$= 90 mm ($\dot{m}_1$ = 0.04 kg/s)

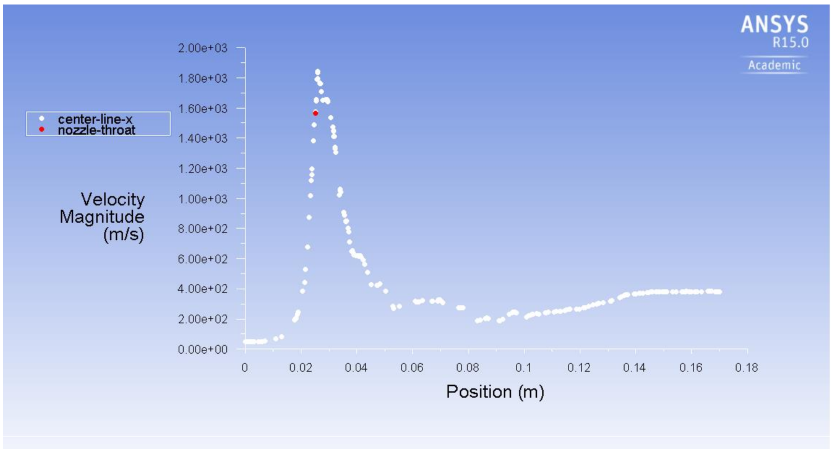


Figure 5-12: Diagram of a velocity magnitude along the line of the centre in the Group B case $L_2$= 100 mm ($\dot{m}_1$ = 0.04 kg/s)

The fluent software it can use to analysis about the post-processing tool for the behaviour of the fluid and which analyses the fluid inside the jet. Hence the flow verification can be moving from the length of the chamber $L_2$ where all the mixture of the fluid and this has been shown in Appendix A.

## 5.5 The lengths of the Jet pump throat $L_{throat}$ (Group C)

In this Section, similar the numerical results of the simulation for the lengths of the Jet pump throat $L_{throat}$ (Group C) models are shown in Table 5-15 to Table 5-18, the original values shown in Table 5-14.

Table 5-14: Basic case model of Group C

| $D_1$ (mm) | $D_2$ (mm) | $D_3$(mm) | $D_4$ (mm) | d1 (mm) | d2 (mm) | $L_1$ (mm) | $L_2$ (mm) | $L_{throat}$ (mm) | $L_3$ (mm) |
|---|---|---|---|---|---|---|---|---|---|
| 30 | 20 | 32 | 16 | 5 | 10 | 15 | 80 | variable | 10 |

Table 5-15: Simulation results of the varied the lengths of the Jet pump throat models in Group C (variation of $\dot{m}_1$, $L_{throat}$= 20mm)

| $\dot{m}_1$ (kg/s) | $\dot{m}_2$ (kg/s) | $\dot{m}_{out}$ (kg/s) | $\dot{m}_w$ (kg/s) | $v_1$ (m/s) | $v_2$ (m/s) | $v_{out}$ (m/s) | $w_{out}$ | ER |
|---|---|---|---|---|---|---|---|---|
| 0.01 | 0.0123 | 0.0223 | 0.000273 | 12.02 | 33.867 | 63.673 | 0.012245 | 1.23 |
| 0.02 | 0.0252 | 0.0452 | 0.000559 | 24.05 | 69.347 | 128.744 | 0.012377 | 1.26 |
| 0.03 | 0.03937 | 0.06937 | 0.000874 | 36.07 | 107.919 | 196.5 | 0.012599 | 1.31 |
| 0.04 | 0.05002 | 0.09002 | 0.00111 | 48.1 | 137.228 | 255.81 | 0.012336 | 1.25 |
| 0.05 | 0.0664 | 0.1164 | 0.001474 | 60.12 | 182.32 | 330.114 | 0.012664 | 1.33 |
| 0.06 | 0.079 | 0.139 | 0.001754 | 72.15 | 216.724 | 393.909 | 0.012617 | 1.32 |

Table 5-16: Simulation results of the varied the lengths of the Jet pump throat models in Group C (variation of $\dot{m}_1$, $L_{throat}$= 30mm).

| $\dot{m}_1$ (kg/s) | $\dot{m}_2$ (kg/s) | $\dot{m}_{out}$ (kg/s) | $\dot{m}_w$ (kg/s) | $v_1$ (m/s) | $v_2$ (m/s) | $v_{out}$ (m/s) | $w_{out}$ | ER |
|---|---|---|---|---|---|---|---|---|
| 0.01 | 0.0115 | 0.0215 | 0.000255 | 12.02 | 31.716 | 60.892 | 0.011874 | 1.15 |
| 0.02 | 0.02447 | 0.04447 | 0.000543 | 24.05 | 67.123 | 124.807 | 0.012216 | 1.22 |
| 0.03 | 0.03771 | 0.06771 | 0.000837 | 36.07 | 103.44 | 189 | 0.012364 | 1.26 |
| 0.04 | 0.0504 | 0.0904 | 0.001119 | 48.1 | 138.453 | 254.41 | 0.012377 | 1.26 |
| 0.05 | 0.0641 | 0.1141 | 0.001423 | 60.12 | 175.995 | 317.567 | 0.012472 | 1.28 |
| 0.06 | 0.07725 | 0.13725 | 0.001715 | 72.15 | 211.75 | 375.148 | 0.012495 | 1.29 |

Table 5-17: Simulation results of the varied the lengths of the Jet pump throat models in Group C (variation of $\dot{m}_1$, $L_{throat}$= 50mm).

| $\dot{m}_1$ (kg/s) | $\dot{m}_2$ (kg/s) | $\dot{m}_{out}$ (kg/s) | $\dot{m}_w$ (kg/s) | $v_1$ (m/s) | $v_2$ (m/s) | $v_{out}$ (m/s) | $w_{out}$ | ER |
|---|---|---|---|---|---|---|---|---|
| 0.01 | 0.0109 | 0.0209 | 0.000242 | 12.02 | 28.895 | 59.216 | 0.011578 | 1.09 |
| 0.02 | 0.02372 | 0.04372 | 0.000527 | 24.05 | 65.069 | 124.611 | 0.012044 | 1.19 |
| 0.03 | 0.0355 | 0.0655 | 0.000788 | 36.07 | 97.395 | 186.463 | 0.012032 | 1.18 |
| 0.04 | 0.05086 | 0.09086 | 0.001129 | 48.1 | 139.512 | 258.63 | 0.012427 | 1.27 |
| 0.05 | 0.06405 | 0.11405 | 0.001422 | 60.12 | 175.667 | 325.71 | 0.012467 | 1.28 |
| 0.06 | 0.0777 | 0.1377 | 0.001725 | 72.15 | 213.334 | 389.451 | 0.012527 | 1.30 |

Table 5-18: Simulation results of the varied the lengths of the Jet pump throat models in Group C (variation of $\dot{m}_1$, $L_{throat}$= 60mm).

| $\dot{m}_1$ (kg/s) | $\dot{m}_2$ (kg/s) | $\dot{m}_{out}$ (kg/s) | $\dot{m}_w$ (kg/s) | $v_1$ (m/s) | $v_2$ (m/s) | $v_{out}$ (m/s) | $w_{out}$ | ER |
|---|---|---|---|---|---|---|---|---|
| 0.01 | 0.0098 | 0.0198 | 0.000218 | 12.02 | 26.879 | 54.38 | 0.010988 | 0.98 |
| 0.02 | 0.021768 | 0.041768 | 0.000483 | 24.05 | 59.698 | 115.421 | 0.01157 | 1.09 |
| 0.03 | 0.03308 | 0.06308 | 0.000734 | 36.07 | 90.737 | 175.128 | 0.011642 | 1.10 |
| 0.04 | 0.0456 | 0.0856 | 0.001012 | 48.1 | 125.128 | 239.29 | 0.011826 | 1.14 |
| 0.05 | 0.0566 | 0.1066 | 0.001257 | 60.12 | 155.332 | 298.313 | 0.011787 | 1.13 |
| 0.06 | 0.0649 | 0.1249 | 0.001441 | 72.15 | 178.273 | 343.965 | 0.011535 | 1.08 |

The plot diagrams that show a velocity magnitude (m/s) of the fluid over the line of the centre for the jet pump (m) in all cases, where the red sign illustrates the fluid velocity in the centre throat of the nozzle. For instance, Figure 5-13 to 5-16 are the plot results of Group C simulations that show the variation of $d_1$ when $\dot{m}_1$ is 0.04 kg/s.

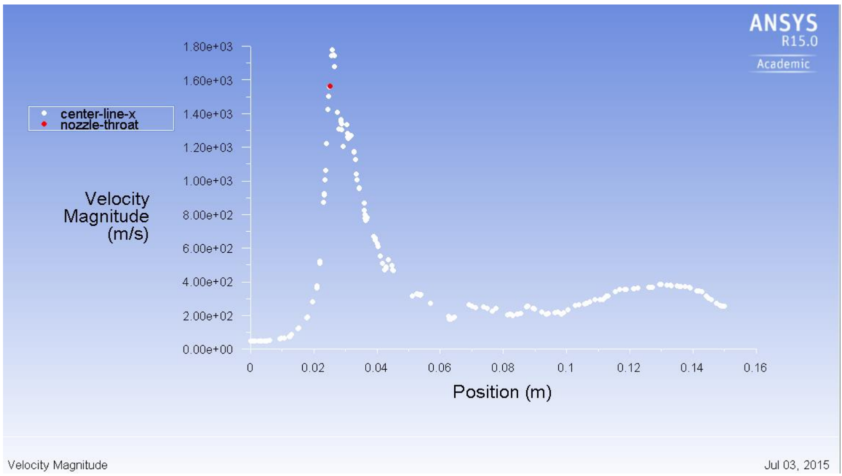


Figure 5-13: Diagram of a velocity magnitude along the line of the centre in the Group C case L $_{throat}$ = 20 mm ($\dot{m}_1$ = 0.04 kg/s)

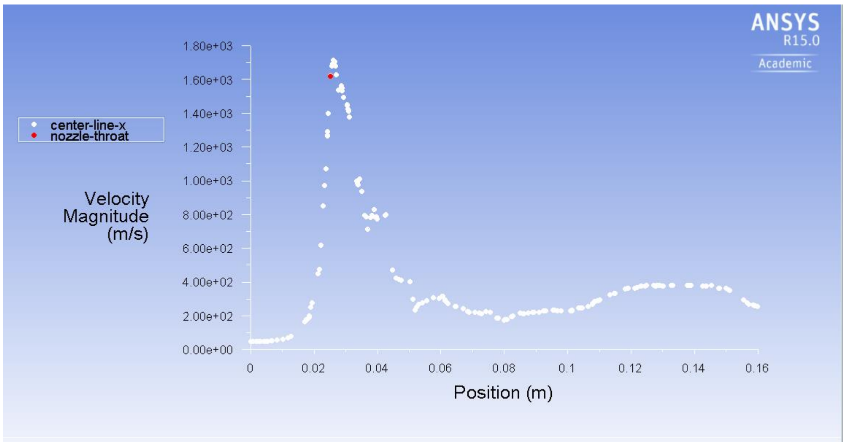


Figure 5-14: Diagram of a velocity magnitude along the line of the centre in the Group C case L $_{throat}$ = 20 mm ($\dot{m}_1$ = 0.04 kg/s)

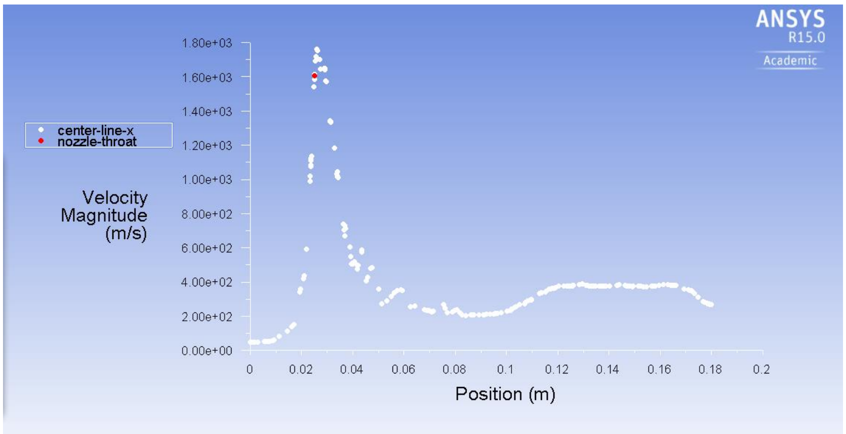


Figure 5-15: Diagram of a velocity magnitude along the line of the centre in the Group C case L $_{throat}$ = 50 mm ($\dot{m}_1$ = 0.04 kg/s)

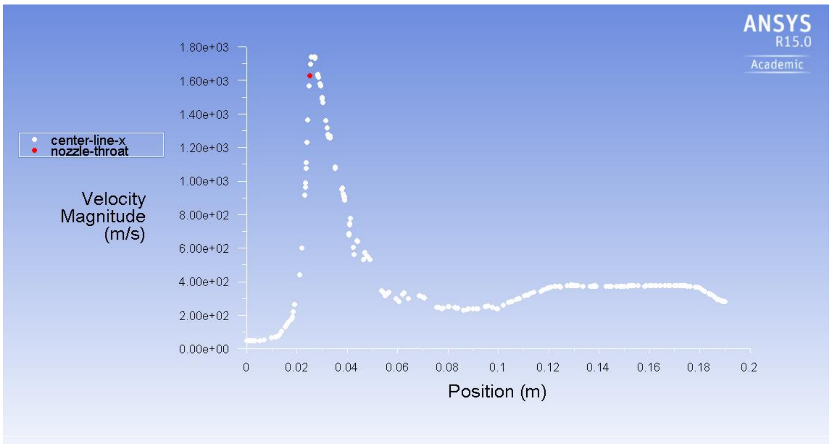


Figure 5-16: Diagram of a velocity magnitude along the line of the centre in the Group C case $L_{throat}$ = 60 mm ($\dot{m}_1$ = 0.04 kg/s)

The fluent software it can use to analysis about the post-processing tool for the behaviour of the fluid and which is analysing the fluid inside the jet. Hence the flow verification can be moving from the jet pump throat $L_{throat}$ and which is showing in Appendix B.

## 5.6 Discussion of General Jet Pump fluid Behaviour

From the simulation results reported in Section 5.3, Section 5.4 and Section 5.5, the proposed method predicted an increase in the velocity magnitude that steadily increases when the convergence of the primary fluid occurs in the nozzle; this then decreases as a result of the diffusion of the same fluid. Consequently, acceleration increases in the mixing chamber when the two fluids are mixed, thereby improving the flow towards the nozzle of the jet pump.

Based on the diagrams plotted for velocity and presented in Chapter 5, and Appendix A and considering the plots of the velocity magnitude along the centre line in the Group A model with $d_l$= 2 mm ($m_1$ = 0.01kg/s), the velocity magnitude rapidly increased when the primary fluid converged in the nozzle. Subsequently, the velocity magnitude was observed to increase in a short jet, after which it decreased due to the diffusion of the fluid. The primary fluid later flowed into the mixing chamber after it left the nozzle. A decrease in the velocity occurs in the first part of the chamber even though the mixing chamber has a converged shape where the fluid pressure concurrently would have increased. This is because when the velocity of the primary fluid is high, it provides a shear force to the secondary fluid, which tends to speed up the secondary fluid; thus, a loss in the velocity of the primary fluid occurs simultaneously. Acceleration of the primary and secondary fluid tends to take place when the two fluids are mixed. Thus, the fluids flow swiftly into the mixing chamber due to convergence. When these fluids flow, the velocity tends to be constant in the throat of the jet pump, and then it decreases in the diffuser.

A contours graph can be used to depict the fluid velocity properties. For example, Figure 5-17 shows the velocity contours for the Group A model where $d_2$ = 6 mm for the condition of $\dot{m}_1$ = 0.04 kg/s.

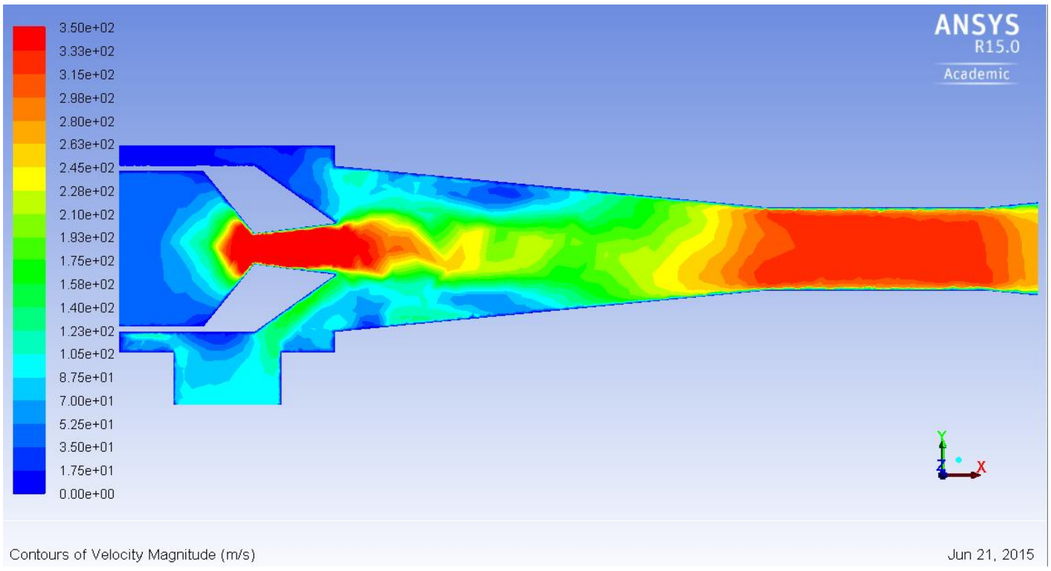


Figure 5-17: The velocity contour in the Group A model; $d_1$ = 6 mm at $\dot{m}_1$ = 0.04 kg/s, $L_{throat}$ = 40 mm.

A contours graph can also demonstrate the dispersion of the water vapour mass fraction of the jet pump. Figure 5-18 shows the prototypical water mass curves in Group A at the circumstance where $\dot{m}_1$ = 0.06 kg/s and $L_2$ = 60 mm.

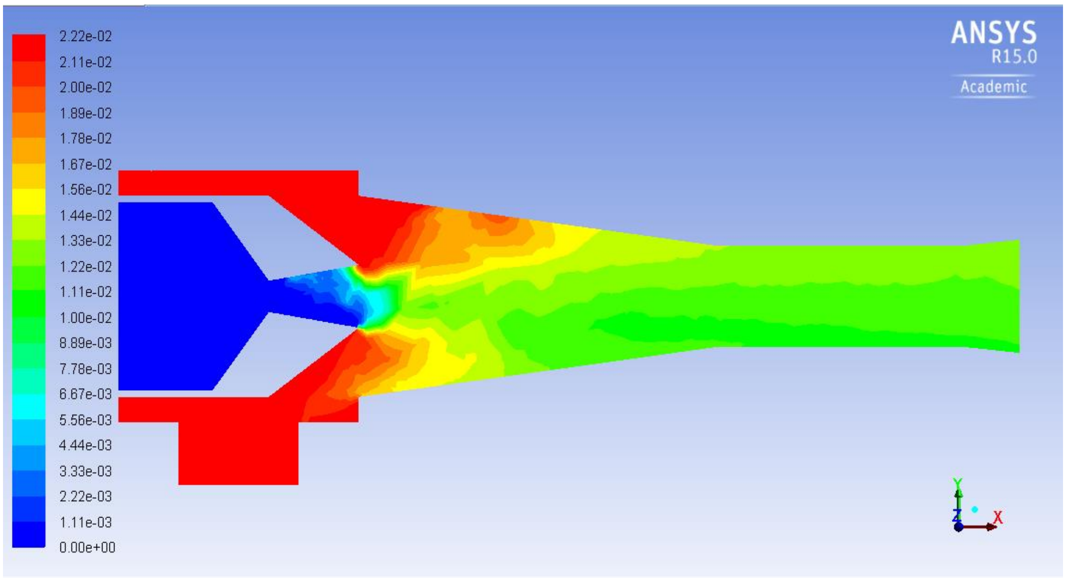


Figure 5-18: Distribution contours of the water vapour mass fraction in the Group A model; $\dot{m}_1$ = 0.06 kg/s, $L_2$ = 60 mm and $L_{throat}$ = 40 mm.

From the information presented in Figure 5-18, it can be reasoned that, for the most part, the blend of both the primary and secondary fluid occurs in the mixing chamber of the jet pump. When the primary inlet leaves the nozzle, it starts to combine with the secondary water vapour. Nevertheless, the mixing procedure is not abruptly completed in the chamber because the steam is contained in the focal point of the mixing chamber, whereas, in most cases, it is contained around the side of the pump. At that point, the water mass fraction in the middle of the mixing chamber develops, whereas the steam tumbles, bit by bit, along with the mixing chamber in the jet pump.

Lastly, the water mass fraction tends to remain consistent in the direction of the jet throat. This implies that the mixing of the primary fluid and the secondary fluid is complete. In any case, the mixing chamber length ($L_2$) presented in Figure 5-18 is 60 mm. This is considered to be the shortest brief estimation of $L_2$ in all of the models.

Consequently, the mixing occurred in the mixing chamber and was completed before the fluid entered the jet throat.

## 5.7 Effect of the Nozzle Throat

The calculations for Group A are based on different settings using an elementary design in which the diameter in the nozzle throat $d_1$ was modified at a different inlet primary mass flow rate $\dot{m}_1$. In general, Figure 5-19 and Figure 5-20, respectively, show the relationship between the primary mass flow rate $m_1$ and the mass flow rate of the water vapour outlet ($\dot{m}_w$), $m_1$, the velocity outlet from the jet pump $v_{out}$, $m_1$ and the entrainment ratio, $m_1$ and the mass fraction of water in the jet pump outlet $w_{out}$ inline charts with variations of $d_1$.

Furthermore, $\dot{m}_2$ can be calculated as ($\dot{m}_{water}$ /water mass fraction) and $\dot{m}_{out}$ can be calculated as ($\dot{m}_2 + \dot{m}_1$). Hence, the line diagram of $\dot{m}_2$ and $\dot{m}_{out}$ will be similar to the line diagram of $\dot{m}_w$; however, this calculation it is not important in this study. In Appendix A, Figure 5-25 and Figure 5-31 show plots of the velocity magnitude along the middle line in the Group A model, where $d_1$ = 6 mm ($\dot{m}_1$ = 0.01 kg/s) and $d_1$ = 7 mm ($\dot{m}_1$ = 0.01 kg/s); thus, the focal point of nozzle throat has a speed value less than 340 m/s, which is low and which does not achieve supersonic speed like the rest of the values in the plot charts. However, in the other plot graphs for the simulations of Group A, the focal point speed of the nozzle throat is supersonic.

A comparison of the information in the plotted graphs shows that the magnitude of the velocity magnitude has a tendency to decrease more when the ultimate value is extended. As shown in (Appendix A) Figure A.1, when $d_1$ = 2 mm, the velocity magnitude decreases sharply. As seen in Figure A.36 in the plots of the velocity magnitude along the middle line in the Group A model, when $d_1$ = 7 mm ($\dot{m}$ = 0.06 kg/s), the velocity magnitude gradually decreases. Furthermore, the valley value of the velocity magnitude in Figure A.1 only appears after the highest value is attained, as shown in Figure A.2 to Figure A.35.

Likewise, the tendency of the plots does not indicate a statistically significant distinction between every chart at various inlet mass flow rates. The most evident contrast is the general estimations of the velocity magnitude (m/s). It was demonstrated that simply differing the mass flow rate of the primary fluid without altering the jet pump does not change the inclination of the vapour speed through the jet. In any case, increasing the mass stream rate of the primary fluid can increase the general estimations of the velocity magnitude, which are directly connected to each other.

Therefore, it can be deduced that a restricted nozzle throat in the jet pump tends to allow the kinetic energy that results in the exchange of the primary and the secondary fluid. After the indispensable fluid flows through a restricted throat, its active vitality is quickly transformed into the secondary stream, which results in a rapid velocity loss of the indispensable fluid and a rapid increase in the velocity of the secondary fluid.

Regarding the velocity magnitude contours, in the case where $d_1$ is fixed to a small value, for example, 2 mm, the fluid velocity at the centre tends to drastically decrease to the value corresponding to the fluid at the side, as depicted in Figure 5-19. At the point when $d_1$ is set at a high value, for example, 7 mm, the velocity of the centre fluid tends to decrease the value corresponding to the velocity in the area adjacent to the end of the mixing chamber in Figure 5-20.

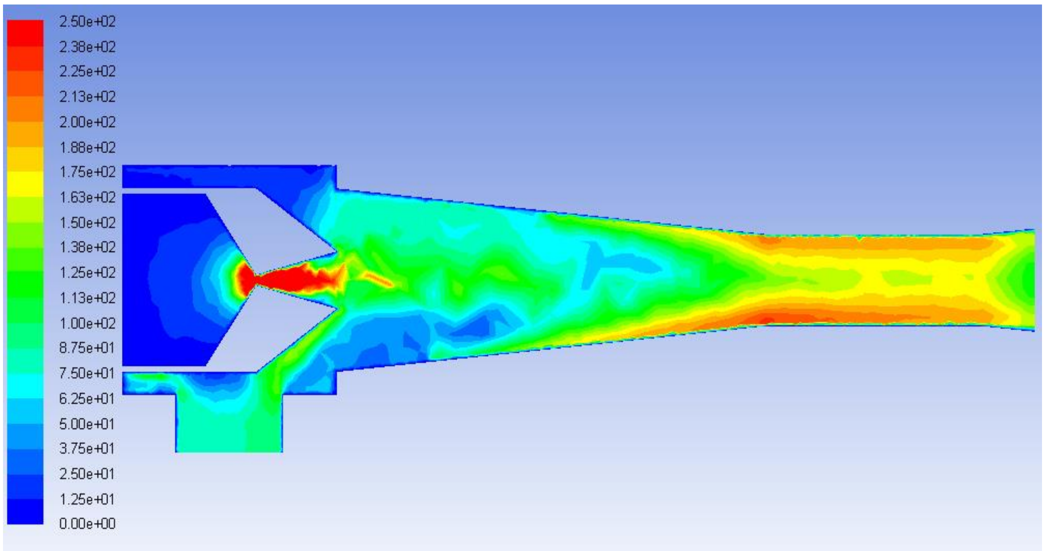


Figure 5-19: Velocity magnitude contours for $d_1$ = 2 mm ($\dot{m}_1$=0.01 kg/s) and $L_{throat}$ = 40 mm.

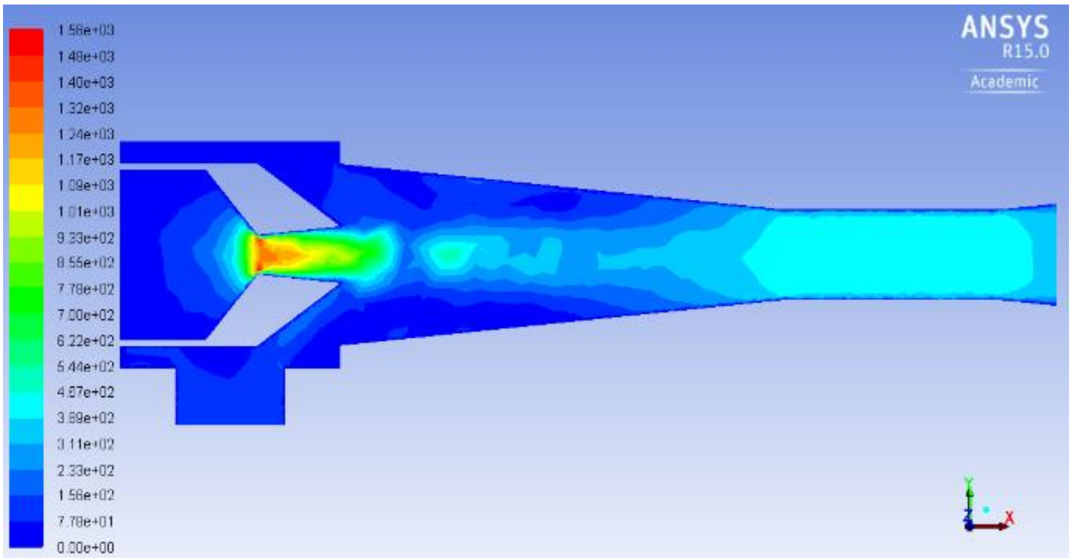


Figure 5-20: Velocity magnitude contours for $d_1$ = 7 mm ($\dot{m}_1$=0.06 kg/s) and $L_{throat}$ = 40 mm.

### 5.7.1 Effect of nozzle throat diameter ($d_1$) variations on the water vapour mass flow rate

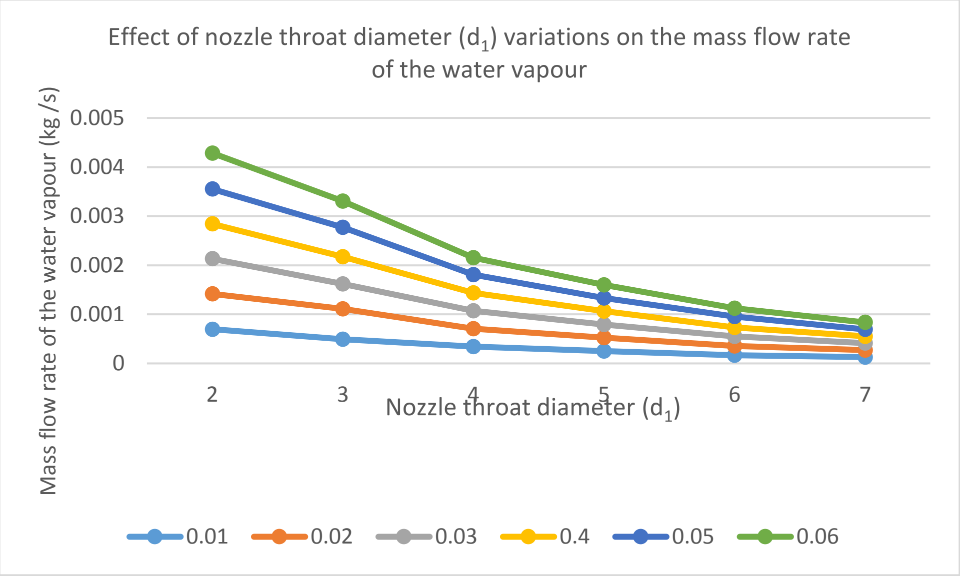


Figure 5.21: Effect of nozzle throat diameter ($d_1$) variations on the mass flow rate of the water vapour at different inlet mass flow rates.

The mass flow rate of the water vapour differs depending on the diameter of the nozzle. As seen in Figure 5-21, the mass flow rate of the water vapour at different inlets decreases as the diameter of the nozzle throat increases. For example, at a diameter of 2 mm, the mass flow rate is 0.0007 kg/s. The mass flow rate of the water vapour decreases to 0.0005 kg/s when the diameter of the nozzle increases to 3 mm. This trend continues; when the nozzle diameter increases to 5 mm, 6 mm and 7 mm, the mass flow rate of the water vapour decreases to 0.0004 kg/s, 0.0003 kg/s, 0.0002 kg/s and 0.0001kg/s, respectively. For $\dot{m}_1$ = 0.02 kg/s, the mass flow rate of the water vapour is 0.0014 kg/s when the diameter is 2 mm and it decreases to 0.0011 kg/s, 0.0007 kg/s, 0.0005 kg/s, 0.0004 kg/s and 0.0003 kg/s as the nozzle diameter increases to 3 mm, 4 mm, 5 mm, 6 mm and 7 mm, respectively. For $\dot{m}_1$= 0.03 kg/s, the mass flow rate of the water vapour is 0.0021 kg/s when the nozzle diameter is 2 mm. As the nozzle diameter is increased by 1 mm reaching a diameter of 7 mm, the flow rate changes to 0.0016 kg/s, 0.001 kg/s, 0.0008 kg/s, 0.0005 kg/s and 0.0004 kg/s, respectively. With the nozzle diameter is 2 mm, the water vapour flows at a rate of 0.0028 kg/s; when the nozzle diameters are 3 mm, 4 mm, 5 mm, 6 mm and 7 mm, the flow rate is 0.0021 kg/s, 0.0014 kg/s, 0.001 kg/s, 0.0007 kg/s and 0.0005 kg/s, respectively. When $\dot{m}_1$ = 0.05 kg/s., a nozzle with a 2 mm diameter has a mass flow rate of 0.0035 kg/s, a nozzle with a 3 mm diameter has a mass flow rate of 0.0075 kg/s, and nozzles with 4 mm, 5 mm, 6 mm and 7 mm diameters have mass flow rates of 0.0016 kg/s, 0.0014 kg/s, 0.0009 kg/s and 0.0006 kg/s, respectively. Lastly, $\dot{m}_1$= 0.06 kg/s has the highest flow rates for each nozzle diameter. When the nozzle diameter is 2 mm, 3 mm, 4 mm, 5 mm, 6 mm, and 7 mm, the mass flow rate of the water vapour is 0.0043 kg/s, 0.0033 kg/s, 0.0021 kg/s, 0.0016 kg/s and 0.0008 kg/s, respectively. Clearly, $\dot{m}_1$= 0.01 kg/s has the lowest mass flow rate, kg/s; additionally, the mass flow rate of the water vapour is higher when the nozzle diameter is smaller, and it decreases as the diameter increases. For instance, as the diameter of the nozzle increases from 2 mm to 3 mm, there is a negative shift in the flow rate and the trend continues. Therefore, the nozzle diameter and the mass flow rate of the water vapour are inversely related; one increases as the other decreases. Thus, the higher pressure gradient and the mass flow rate of water vapour are uniformly related.

### 5.7.2 Effect of nozzle throat diameter ($d_1$) variations on the jet pump outlet velocity

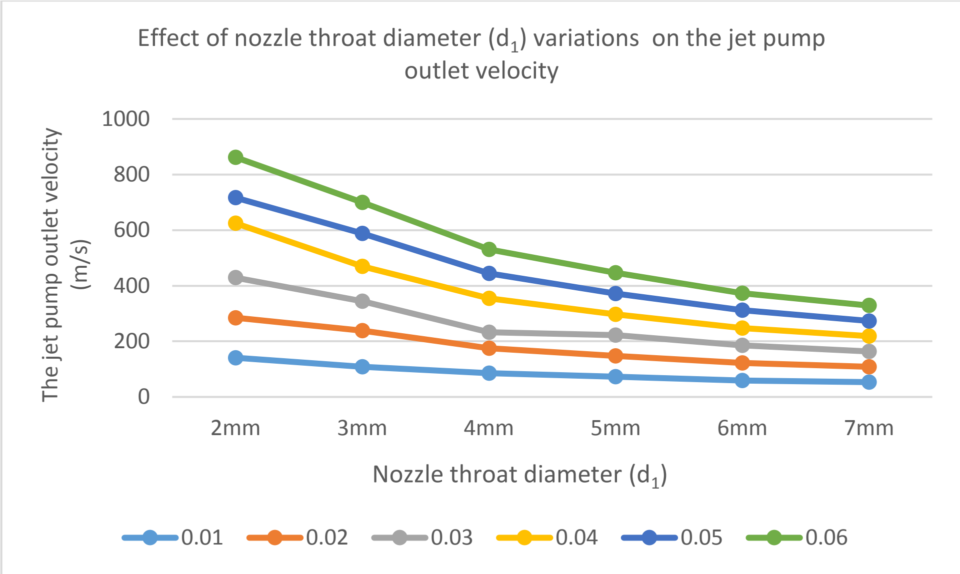


Figure 5.22: Effect of nozzle throat diameter ($d_1$) variations on the jet pump outlet velocity.

As seen in Figure 5-22, variations in the nozzle diameter significantly affect the outlet velocity in the jet pump. When $\dot{m}_1 = 0.01$ and when the nozzle diameter is 2 mm, the outlet velocity in the jet pump is higher and it decreases when the diameter of the nozzle is increased further. A 1 mm increase in the diameter of the nozzle results in a decrease in the outlet velocity in the jet pump outlet. For example, the mass fraction of water in the jet pump outlet is 100 m/s when the nozzle diameter is 3 mm whereas it is 40 m/s when the nozzle diameter is 7 mm. Similarly, when $\dot{m}_1 = 0.02$, the outlet velocity at the jet pump is higher when the nozzle diameter is 2 mm in comparison to when the diameter is 7 mm. This trend also applies when $\dot{m}_1 = 0.04$, 0.05 and 0.06. Thus, it is evident that the diameter of the nozzle determines the level of a mass fraction of water in the jet pump outlet. A smaller nozzle diameter allows for a higher level of mass friction in the outlet velocity in the jet pump, whereas a larger diameter allows for a lower level mass friction in the outlet velocity in the jet pump. Nozzles with smaller diameters are associated with a high pressure that accelerates the rate at which water flows through the jet pump; however, nozzles with larger diameters are associated with the minimal pressure that slows the rate at which water flows through the jet pump. The graph in Figure 5-22 shows that different categories have different mass friction levels for the outlet velocity in the jet pump; $\dot{m}_1$ = 0.05 has the highest outlet velocity all the nozzle diameters, followed by 0.04, 0.03, 0.02 and 0.01. Moreover, the differences between the outlet velocities at the jet pump in the categories are closer to a constant value at each nozzle diameter since the graph depicts some parallel lines at every point. Therefore, increasing the diameter of the nozzle reduces the outlet velocity of the jet pump.

### 5.7.3 Effect of nozzle throat diameter ($d_1$) variations on the entrainment ratio

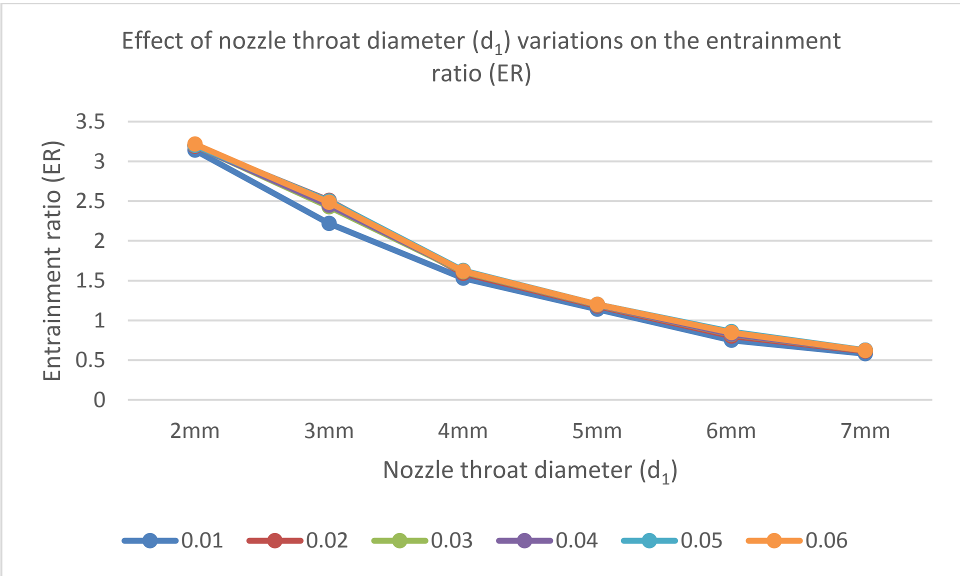


Figure 5.23: Effect of nozzle throat diameter ($d_1$) variations on the entrainment ratio.

Figure 5-23 shows the relationship between the entrainment ratio and the nozzle throat diameter. The line graph depicts a decreasing trend or a graph with a negative gradient. In addition, most of the categories have similar entrainment ratios at various nozzle throat diameters, except when $\dot{m}_1 = 0.01$ at 3 mm. At a nozzle throat diameter of 2 mm, the entrainment ratio is 3.1 for $\dot{m}_1 = 0.01$, 0.02, 0.03, 0.04, 0.05 and 0.06. At a diameter of 3 mm, the entrainment ratio for $\dot{m}_1 = 0.01$ is 2.2, whereas the other categories have an entrainment ratio of 2.5 at the same nozzle throat diameter. The entrainment ratio is 1.5, 1.1, 0.7 and 0.6 when the nozzle throat diameter is 4 mm, 5 mm, 6 mm and 7 mm, respectively. The ratio of the entrainment flow to the driving flow tends to decrease as the nozzle throat diameter increases. The pressure is higher when the nozzle diameter is smaller than when the nozzle diameter is larger. Thus, the entrainment ratio is likely to be higher when the diameter of the nozzle is smaller, and it decreases when the diameter increases.

### 5.7.4 Effect of nozzle throat diameter ($d_1$) variations on the mass fraction of water in the jet pump outlet

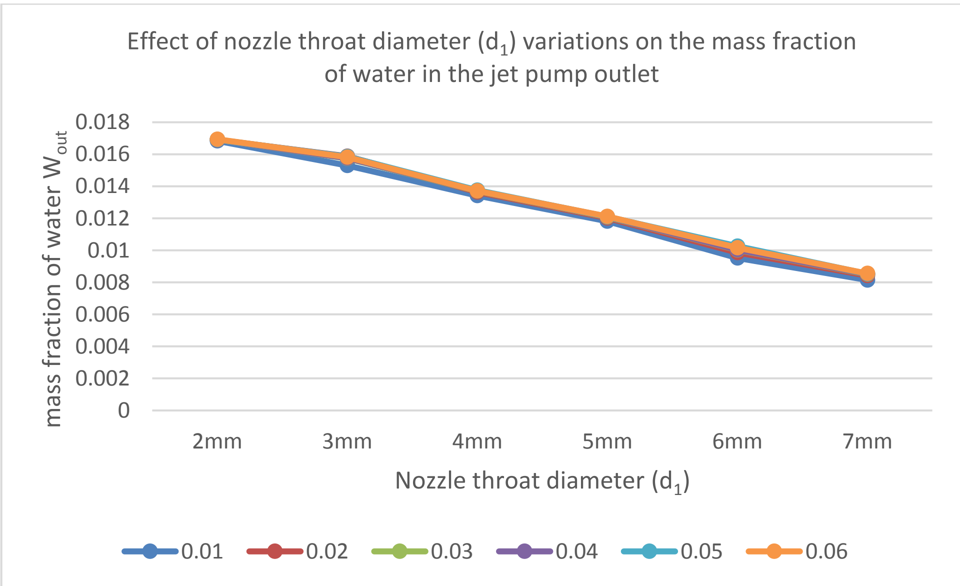


Figure 5.24: Effect of nozzle throat diameter ($d_1$) variations on the mass fraction of water in the jet pump outlet.

Similar to the nozzle diameter and the outlet velocity data presented in Figure 5-22, the nozzle throat diameter affects the mass fraction of water in the jet pump outlet. However, this aspect of the jet pump affects the mass fraction for every category equally, except for 0.01 at a nozzle throat diameter of 3 mm. As shown in Figure 5-24, the mass fraction of water in the jet pump outlet is 0.017 $w_{out}$ for all the categories, 0.01, 0.02, 0.03, 0.04, 0.05 and 0.06, when the nozzle throat diameter is 2 mm. At a nozzle throat diameter of 3 mm, the mass fraction of water is 0.016 for 0.01, 0.03, 0.04, 0.05 and 0.06; however, 0.02 has a mass fraction of 0.015 $w_{out}$ when the nozzle throat diameter of the jet pump is 3 mm. For nozzle throat diameters of 4 mm, 5 mm, 6 mm and 7 mm, the mass fractions of water in the jet pump outlet are 0.013, 0.012, 0.01 and 0.008, respectively. The level of a mass fraction of water in the jet pump outlet is higher when the size of the nozzle is smaller, and it decreases when the diameter increases. This relationship is associated with the pressure at the nozzle throat of the jet pump outlet; the higher the pressure, the higher the mass fraction of water in the jet pump outlet; the lower the pressure, the lower the level of a mass fraction of water in the jet pump outlet. The pressure is higher in a smaller nozzle throat than a larger nozzle throat. Therefore, for a jet pump outlet to have a higher level of a mass fraction of water, nozzles with smaller diameters should be used.

### 5.7.5 Recommendation

It is known that when the fluid velocity is high, the cleaning performance of the external mean photovoltaic (PV) panel improves; the cooling performance of the PV improves when a larger amount of water is delivered to the board. Schumacher et al. (1979) found that an increase in the amount of water in the given fluid tends to also improve the ability of the surface of the mirror to clean itself. Consequently, the highest of $\dot{m}_w$, $v_{out}$ and $w_{out}$ values might offer superior PV self-cleaning and cooling efficiency for a jet pump. Based on previous analyses conducted for this present study, an increase in the $\dot{m}_1$ values tends to increase the $v_{out}$, $\dot{m}_w$ and $w_{out}$ values; thus, it seems that higher $\dot{m}_1$ value results in better cleaning and cooling performance in a jet pump.

Nevertheless, when $\dot{m}_1$ is high, the energy consumption of the jet pump increases. Solar panels play an important role in cooling and cleaning a pump because they increase the effectiveness of the PV cells, and they escalate the production of energy. The cooling system in pumps that do not have solar panels is not qualified for use in cleaning and cooling in the solar panels in pumps where the energy that is provided greater than the energy being produced by the PV cells. Consequently, it is very important to establish equilibrium between the enhancement of the performance of the PV and the mass flow rate that is provided to the jet. In order to ensure that the proper $\dot{m}_1$ value is accessible to a jet, it is important to complete a number of tests by using an actual apparatus that includes PV cells and a jet pump.

Once the results of the simulations in Group A have been scrutinized, a reduction in the nozzle throat diameter might be found to increase all the $\dot{m}_w$, $v_{out}$ and $w_{out}$ values. This gives the impression that the smaller the nozzle throat, the greater the efficacy of the cleaning and cooling of the PV panels. Nonetheless, a nozzle throat that is too small might tend to reduce the durability of the jet. This is presented in the diagrams that were plotted and shown in Figure A.2 to Figure A.37; smaller $d_1$ results in higher velocities of magnitude once the velocity reaches the ultimate point. A very high velocity would result in increased pressure to the nozzle's wall, which may also decrease the operational period of the jet. Additionally, a smaller nozzle throat might produce some noise when the fluid flows through the nozzle. Therefore, a $d_1$ value that is too low might not be appropriate for a jet pump. In the jet model for Group A used in this project, a nozzle throat diameter of 5 mm was selected. When $d_1$ = 5 mm, $\dot{m}_w$, vout and $w_{out}$ might have comparatively higher values, whereas the fluid velocity might be maintained at a value that is safe for a jet pump.

## 5.8 Discussion of the mixing chamber length ($L_2$) simulation results (Group B)

The simulations in Group B are different from the simulations built for the original model; in Group B, the mixing chamber length ($L_2$) was modified. Figures 5-26, 5-27, 5-28 and 5-29 show the relationship between $L_2$ and $\dot{m}_w$, $L_2$ and $v_{out}$, $L_2$ and ER, $L_2$ and $w_{out}$ in line charts, respectively.

As seen in the velocity magnitude plot diagrams presented in Figure 5-9 to Figure 5-12, in addition, Figures in appendix A, after the peak value is reached, the fluid velocity continues to drop until it reaches a constant value. However, it is essential to note that the velocity magnitude diagram values shown in the other the Group B model plot diagrams could attain a valley value before attaining a constant value. A good percentage of the valley values of the velocity magnitude in the Group B models take place at about the 0.06 m position. It is also important to note that there is very little variation among the plots made before the valley value. However, this could demonstrate that, when the length of the mixing chamber varies, the fluid properties do not have a significant effect on the jet as long as the velocity magnitude valley values are attained in the mixing chamber.

The contours graph in Figure 5-25 also specifies the distribution of water vapour mass fraction in a jet pump. A jet pump with a 60 mm mixing chamber indicates that the water vapour is not evenly distributed and the mass flow rate at this point is very low. However, in a jet pump with a 100 mm mixing chamber the water vapour is evenly distributed and the mass flow rate is higher in comparison to when the mixing chamber is shorter.

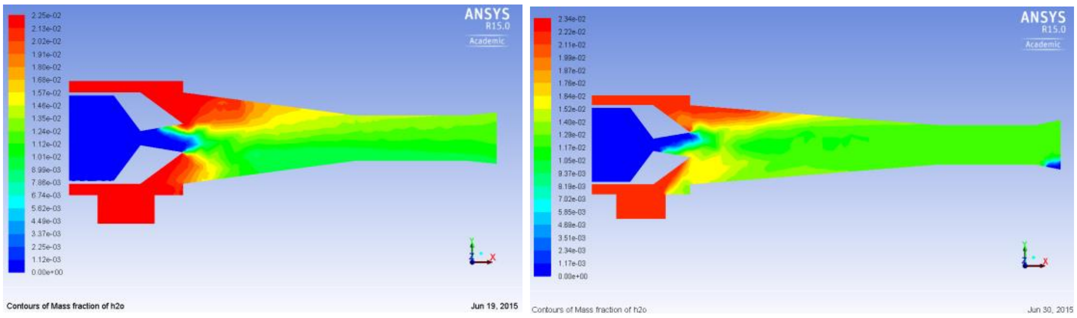


Figure 5.25: Distribution contours of the water vapour mass fraction when $L_2$ = 60 mm (left) and $L_2$ = 100 mm (right).

A conclusion that can be made from this is that synthesis of primary and secondary fluid principally takes place in the mixing chamber of the jet pump, and a jet pump with a longer mixing chamber has a higher water vapour mass flow rate.

### 5.8.1 Effect of varying the mixing chamber length ($L_2$) on the mass flow rate of the water vapour ($m_w$)

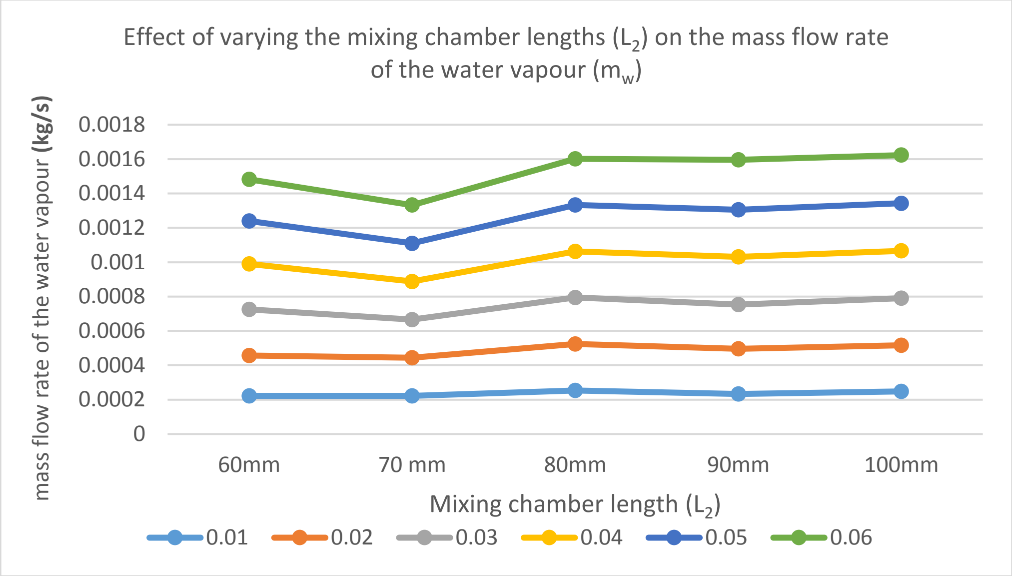


Figure 5.26: Effect of varying the mixing chamber lengths ($L_2$) on the mass flow rate of the water vapour ($m_w$).

As shown in Figure 5-26, the effect that changing the length of the mixing chamber has on the mass flow rate of the water vapour varies from category to category. For instance, $\dot{m}_1 = 0.01$ is the lowest mass flow rate when the length of the mixing chamber is 60 mm; however, the mass flow rate remains constant across all the other lengths. For $\dot{m}_1 = 0.02$, the mass flow rate of the water vapour is almost equal at 60 mm and 70 mm, but there is a shift when the length of the mixing chamber is increased to 90 mm. Thus, when the length of the mixing chamber varies between 60 mm and 70 mm, the mass flow rate decreases. However, when the length varies between 70 mm and 80 mm of the mass flow rate of the water vapour decreases.

### 5.8.2 Effect of variations in the mixing chamber length ($L_2$) on the jet pump outlet velocity ($v_{out}$)

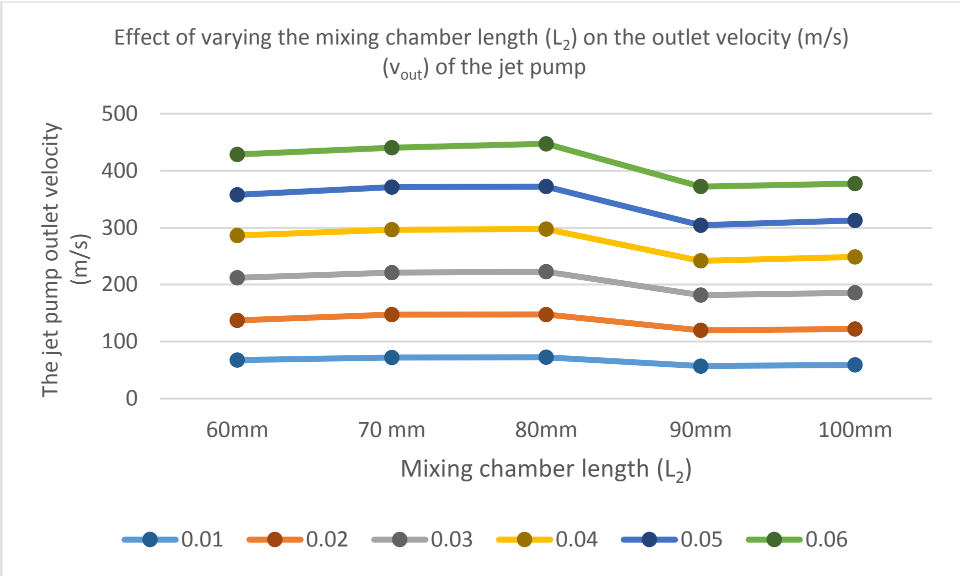


Figure 5.27: Effect of varying the lengths of the mixing chamber ($L_2$) on the jet pump outlet velocity ($v_{out}$).

As seen in Figure 5-27, the outlet velocity of the jet pump depends on variations in the length of the mixing chamber. For all six categories, the line graphs show that the outlet velocity from the jet pump increases when the length increases from 60 mm to 70 mm and from 70 mm to 80 mm. Therefore, varying the length of the mixing chamber between 60 mm and 80 mm increases the velocity output; and increasing the length of the mixing chamber between 80mm to 90mm decreases the velocity output. Finally, the velocity output from the jet pump is likely to remain constant in mixing chambers with a length ranging between 90 mm and 100 mm.

### 5.8.3 Effect of varying the mixing chamber length ($L_2$) on the entrainment ratio

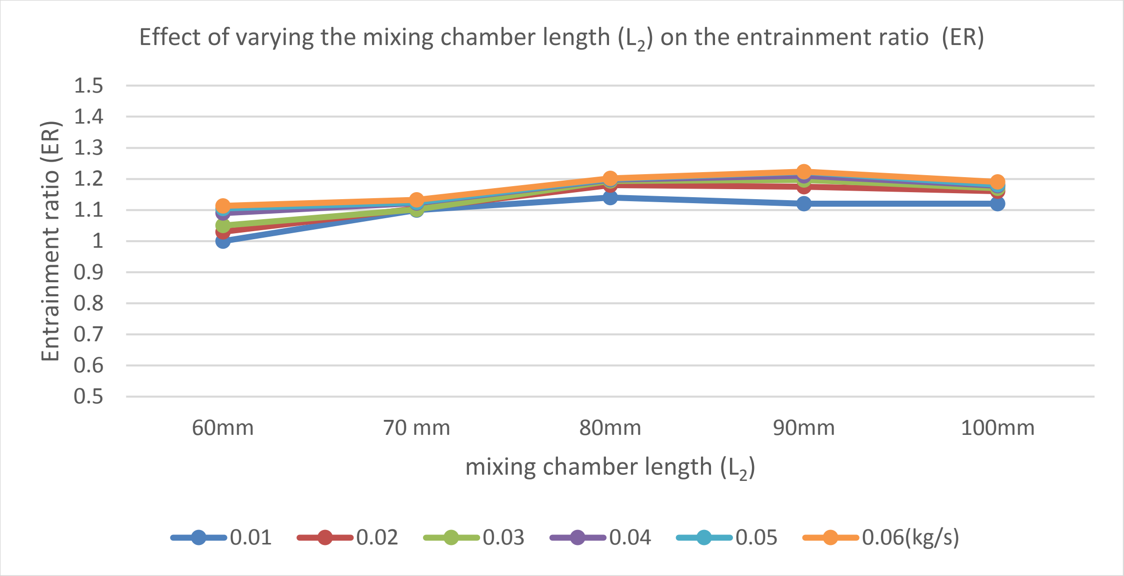


Figure 5.28: Effect of varying the mixing chamber length ($L_2$) on the entrainment ratio.

Varying the length of the mixing chamber has an effect on the entrainment ratio. As seen in Figure 5-28, increasing the mixing chamber length from 60 mm to 70 mm increased the entrainment ratio in all categories. Furthermore, the entrainment ratio also increases when the length of the mixing chamber is 80 mm. The entrainment ratio remains constant when the length is increased from 80 mm to 90 mm, but the entrainment ratio decreases when the length of the mixing chamber is increased from 90 mm to 100 mm. Thus, varying the length of the mixing chamber beyond 100 mm is likely to result in a further decrease in the entrainment ratio.

### 5.8.4 Effect of variations in the mixing chamber length ($L_2$) on the mass fraction of water ($w_{out}$) in the jet pump outlet

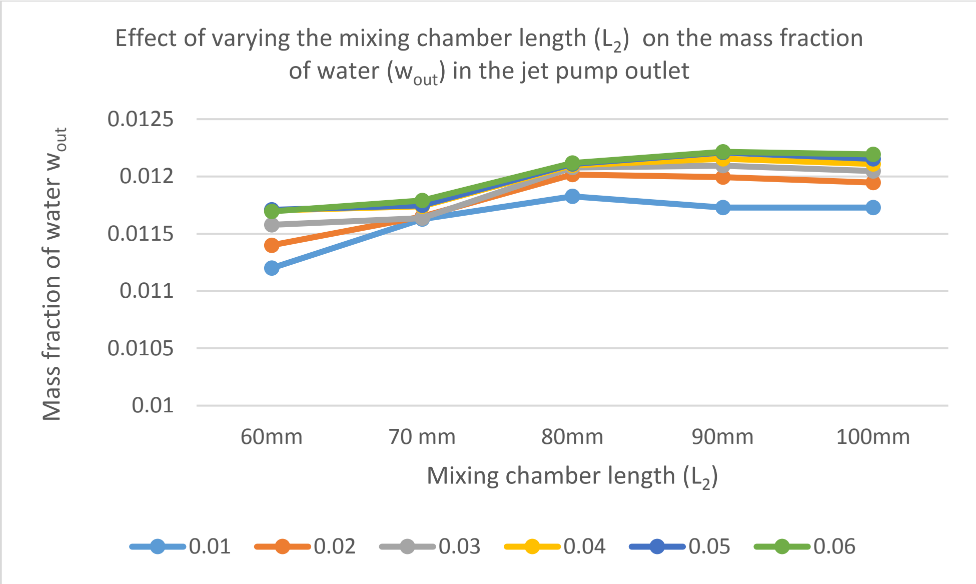


Figure 5.29: Effect of varying the mixing chamber length ($L_2$) on the mass fraction of water ($w_{out}$) in the jet pump outlet.

As seen in Figure 5-29 Variations in the mass fraction of water in the jet pump are significantly affected by varying the length of the mixing chamber. When the length of the mixing chamber is increased from 60 mm to 70 mm, the mass fraction level of water increases. Further increasing the length to 80 mm leads to an increase in the mass fraction level of water. However, when the length of the mixing chamber is increased beyond 80 mm, the mass fraction of water in the jet pump outlet decreases.

### 5.8.5 Recommendation

Based on the information presented in the diagrams, it might seem that the length of the mixing chamber does not have an effect on the cooling and cleaning performance of the models. However, this does not necessarily mean that the length of the mixing chamber should be established without making the necessary calculations in a jet pump. In the models used in this study, it was assumed that the friction coefficient of the internal wall in the jet could be ignored. This is not a realistic assumption because, in a real sense, some degree of friction exists between the fluid and the internal wall of the jet; therefore, a friction coefficient needs to be included in the calculations. When the mixing chamber is too long, the friction between the fluid and the internal wall could result in a decrease in the fluid velocity. Since decreasing the fluid velocity affects the cleaning performance of the jet, it can be concluded that internal wall friction causes a reduction in the self-cleaning performance of a jet pump. However, if the mixing chamber length is too short, a mixture made of the primary and secondary fluids could be insufficient. When $L_2$ = 60 mm, the primary and secondary fluids are mixed immediately before the throat of a jet pump. Thus, it can be assumed that when the $L_2$ value is lower than 60 mm, the resulting mixture of the primary and secondary fluids in the mixing chamber cannot be sufficient. In this thesis, the recommended length of the mixing chamber in the jet pump is set at 80 mm for the simulation models used in the project.

## 5.9 Discussion of the Jet Pump Throat Length ($L_{throat}$) Simulation Results (Group C)

The simulations in Group C are from a different simulation built on the original model with modification to $L_3$. Figures 5-31, 5-32, 5-33 and 5-34 display the relationship between $L_{\textbf{throat}}$ and $\dot{m}_w$, $L_{\textbf{throat}}$ and $v_{out}$, $L_{\textbf{throat}}$ and ER, $L_{\textbf{throat}}$ and $w_{out}$ in line charts, respectively.

As shown in the plot charts for the velocity magnitude diagrams presented in Figures 5-13 to 5-16,include Appendix A figures and the velocity magnitude values indicate that a higher mass flow rate of the water vapour occurs when the jet pump throat is 20 mm or when the size of the jet pump throat decreases. However, as the size of the jet pump throat increases, the mass flow velocity decreases significantly, as indicated by the downward sloping graph.

The contours of the velocity magnitude diagrams in Figure 5-30 verify this inference. However, when the $L_{throat}$ value is set at a low rate, such as 20 mm, the mass flow velocity is high, and when $d_1$ is set at a high value, such as 60 mm, the velocity is low. The mass flow rate is high when the jet pump throat is smaller since the pressure is high at that point. Thus, the fluid is forced out at a higher rate. However, when the $L_{throat}$ is larger, the pressure at that point is low and the mass flow rate is very low. Therefore, for the fluid to flow at a high velocity, the $L_{throat}$ should be small so as to allow for high pressure.

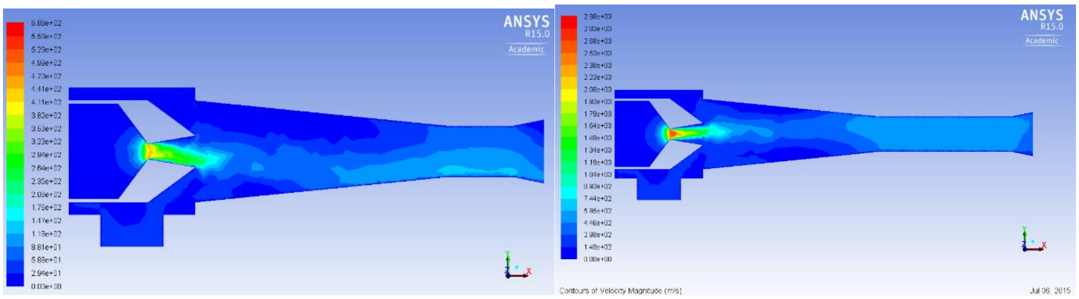


Figure 5-30: Velocity magnitude contours when the jet pump size is $L_{throat}$ = 20 mm (left) and $L_{throat}$ = 60 mm (right).

### 5.9.1 Effect of varying the jet pump throat length ($L_{throat}$) on the mass flow rate of the water vapour

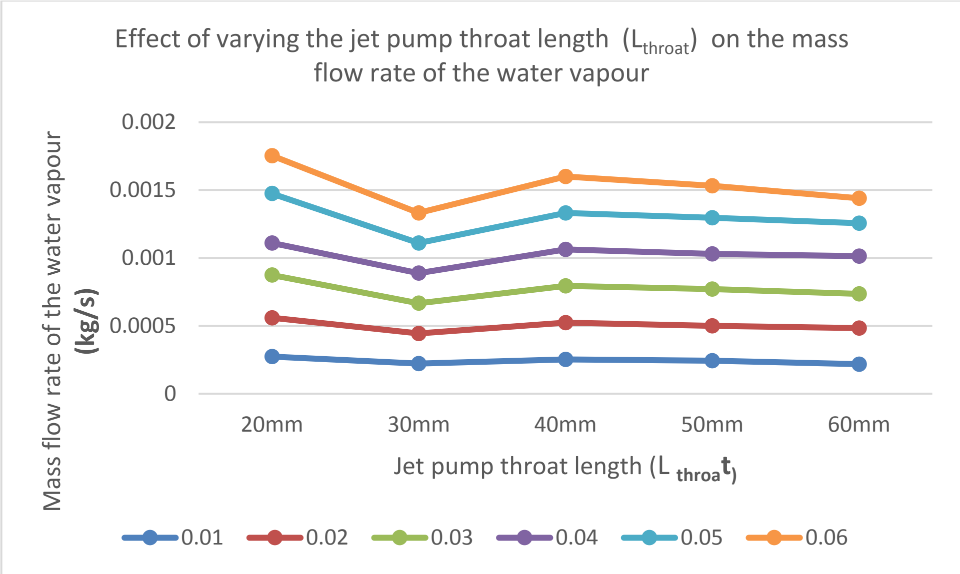


Figure 5-31: Effect of varying the jet pump throat length ($L_{throat}$) on the mass flow rate of the water vapour.

The mass flow rate of water vapour is influenced by variations in the length of the jet pump throat. As shown in Figure 5-31, an increase in the length of the jet pump throat from 20 mm to 30 mm results in a decrease in the mass flow rate of water vapour across all categories. An increase in the length of the jet pump throat from 30 mm to 40 mm results in an increase in the mass flow rate of water vapour; however, that rate decreases when the length increases from 40 mm to 50 mm and from 50 mm to 60 mm. Thus, 20 mm is the most appropriate length for the jet pump throat since it was found to have the highest mass flow rate for water vapour across the six categories.

### 5.9.2 Effect of varying the jet pump throat ($L_{throat}$) on the jet pump outlet velocity

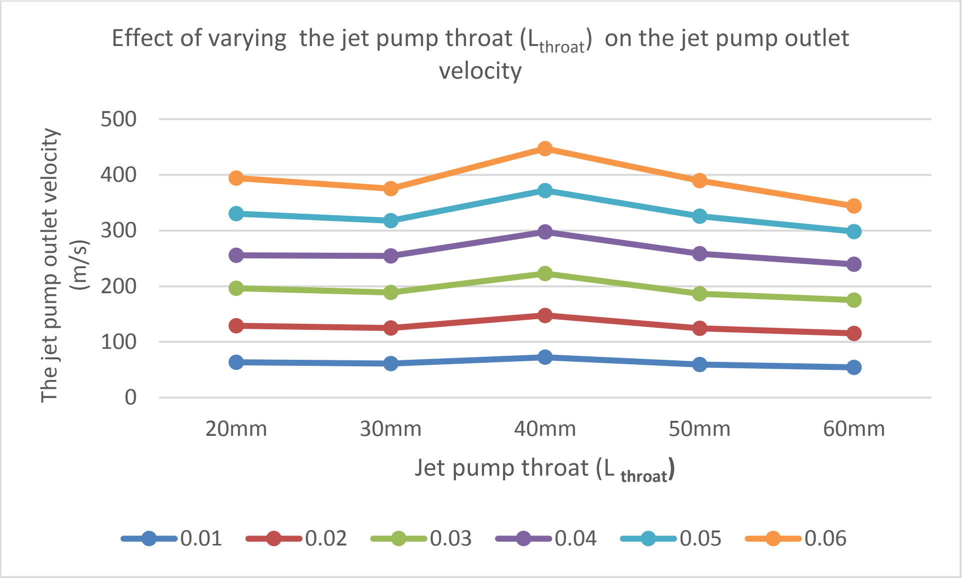


Figure 5-32: Effect varying the jet pump throat ($L_{throat}$) the jet pump outlet velocity

The length of the jet pump throat significantly affects the outlet velocity from the jet pump. An increase in the length of the jet pump from 20 mm to 30 mm results in a decrease in the velocity across all categories. When the length increases from 30 mm to 40 mm, the outlet velocity increases significantly, but it decreases when the length of the jet pump throat is increased from 40 mm to 50 mm. When the length of the jet pump throat increases to 60 mm, the outlet velocity is further decreased. As seen in Figure 5-32, 40 mm is the most appropriate length for the jet pump throat.

### 5.9.3 Effect of varying the jet pump throat length ($L_{throat}$) on the entrainment ratio

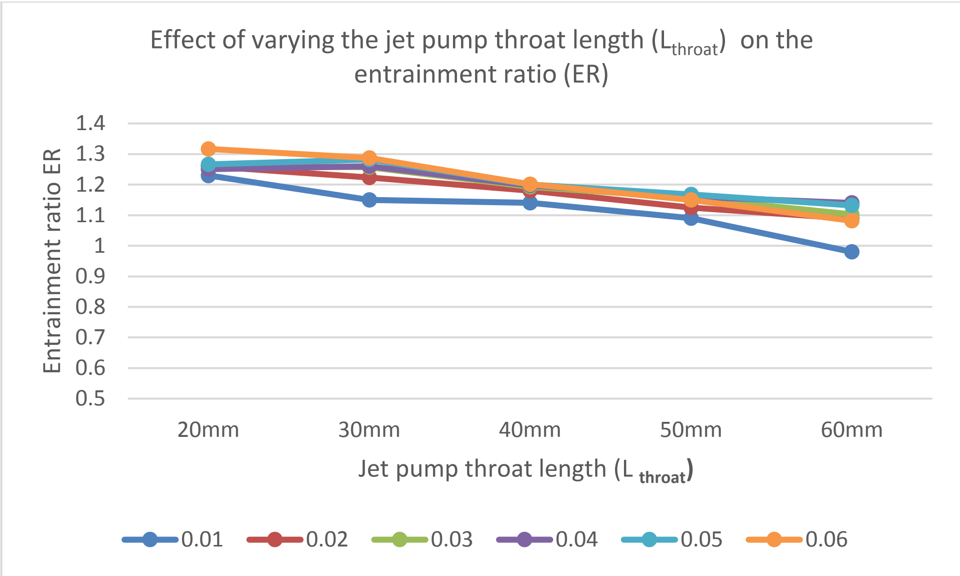


Figure 5-33: Effect of varying the jet pump throat length ($L_{throat}$) on the entrainment ratio.

As seen in Figure 5-33, the length of the jet pump throat affects the entrainment ratio. The line graphs for all the categories show that increasing the length of the jet pump throat reduces the entrainment ratio. Since the best jet pump throat length should be determined based on the highest entrainment ratio, 20 mm is the most appropriate jet pump throat length.

### 5.9.4 Effect of varying the jet pump throat length ($L_{throat}$) on the mass fraction of water in the jet pump outlet

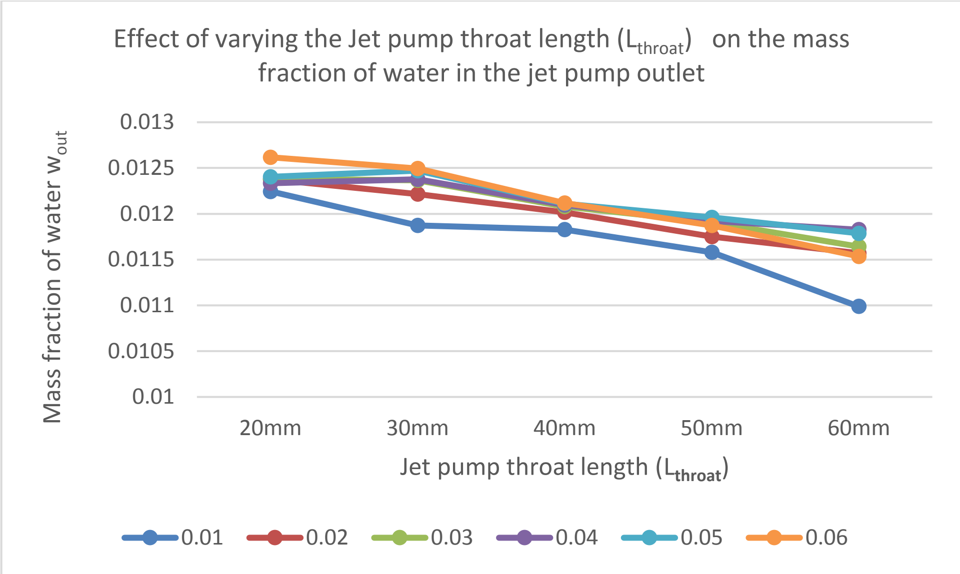


Figure 5-34: Effect of varying the jet pump throat length ($L_{throat}$) on the mass fraction of water in the jet pump outlet.

Varying the length of the jet pump throat also affects the mass fraction of water in the jet pump outlet. As seen in Figure 5-34, when the length of the jet pump throat increased from 20 mm to 30 mm the mass fraction of the water in the outlet decreased across all categories. Increasing in length from 30 mm to 40 mm, from 40 mm to 50 mm and from 50 mm to 60 mm also decreased the mass fraction of water in the outlet. Therefore, 20 mm is the most appropriate length for the jet pump throat.

### 5.9.5 Recommendation

The length of the jet pump throat plays a significant role in the system as it determines the mass flow rate, the velocity magnitude of the fluid, the entrainment ratio and the mass fraction of the water vapour. When the jet pump throat is small, the mass flow rate of the water vapour is high, the velocity magnitude is high, the entrainment ratio is high and the mass fraction of the water vapour is also high. However, when the jet pump throat is larger, the mass flow rate of the water vapour is low, the velocity magnitude is low, the entrainment ratio is low and the mass fraction of the water vapour is also low. Thus, setting the size of the jet pump throat to 20 mm exerts a significant amount of pressure on the fluid and facilitates a high mass flow rate for the water vapour, and the fluid moves at a higher velocity. Therefore, a smaller jet pump throat is the most appropriate size to use in a jet pump system as it facilitates fast operations.

## 5.10 Summary

The present dissertation uses a numerical simulation to determine the effects of a CFD on a jet pump system. The key aspects investigated in this study include the mass flow rate of the water vapour, the velocity magnitude of the fluid, the entrainment ratio and the mass fraction of the water vapour based on variations in the nozzle throat diameter, variations in the length of the mixing chamber and variations in the length of the jet pump throat. The study results demonstrate that the diameter of the nozzle throat has a significant impact on the mass flow rate of the water vapour; a smaller diameter results in a high mass flow rate whereas a larger diameter leads to a lower rate. As the diameter of the nozzle varied from 2 mm to 7 mm, the mass flow rate of the water vapour decreased. Moreover, the nozzle diameter affects the magnitude of the velocity and the mass fraction of the water vapour. Variations in the length of the mixing chamber have a significant effect on the mass flow rate of the water vapour. The study found that the mass flow rate of the water vapour is higher in a shorter mixing chamber than it is in a longer mixing chamber. Therefore, to be most effective, a jet pump should have a smaller nozzle diameter, a shorter mixing chamber and a smaller jet pump throat. In the jet model for Group A used in this project, a nozzle throat diameter of 5 mm was selected. The recommended length of the mixing chamber in the jet pump is set at 80 mm, and the length of the jet pump throat was selected 40 mm.

# Chapter 6: CFD Study of Jet Pump Integrated with the PV Panel System

## 6.1 Introduction

Computation fluid dynamics (CFD) is used to simulate water vapour jet pumps, recognise characteristics of impingement during assessments of PV surfaces and allow comparisons of velocity tests on panel surfaces that are based on the linear movement of jets covering the surface of a PV panel. In this Chapter, the recommended specifications obtained in Chapter 5 will be used.

## 6.2 Simplified Jet Pump Cleaning Arrangement Using the PV Panel System

To begin CFD simulations, the jet pump model must be simplified and concise. To do this, the PV panel and jet pump are analysed under certain conditions to reduce the meshing of the CFD grid to overcome the burden of calculation and to decrease running time. The simulation design should include the fundamentals of the CFD model, such as air velocity at the inlet of the PV system domain. The process of designing a CFD model should take into account simulations that are modified for different real-world conditions. The panel width of the PV determines the number of impingement of jet nozzles and the distance between nozzles, although the exact number of the nozzle is not necessary.

The testing and design of jet pumps have already been discussed in Section 5-6. High air pressure engages with the left supply pipe, and the divergent nozzle passes inside the pump and accelerates at supersonic speed, causing chamber suction that evacuates the contents and creates a vacuum. At the same time, water is heated above $45^{0}$C and stored in a water tank attached to the jet pump from a downward facing inlet. The vacuum creates low pressure inside the water tank, allowing the evaporation of water vapour to begin, which is sucked into the chamber and mixed with air before passing through a section of a divergent jet. The diameter of the outlet nozzle is 0.018 m. Table 6-1 shows the mass flow rate and velocity of the jet pump and provides information on air mass flow, $\dot{m}_{air}$, the mass of water vapour, $\dot{m}_{w}$, and the outlet flow of the mixture, $\dot{m}_{out}$, of air and water, accordingly, while $v_{out}$ is the velocity of the outlet, as recommended in Chapter 5.

Table 6-1: Mass flow rate and velocity of the jet pump, $d_1 = 5$ mm.

| $\dot{m}_1$ (kg/s) | $\dot{m}_2$ (kg/s) | $\dot{m}_{out}$ (kg/s) | $\dot{m}_w$ (kg/s) | $v_1$ (m/s) | $v_2$ (m/s) | $v_{out}$ (m/s) | $w_{out}$ | ER |
|---|---|---|---|---|---|---|---|---|
| 0.01 | 0.0114 | 0.0214 | 0.000253 | 12.02 | 31.32 | 72.42 | 0.011826 | 1.14 |
| 0.02 | 0.0236 | 0.0436 | 0.000524 | 24.05 | 64.82 | 147.65 | 0.012017 | 1.18 |
| 0.03 | 0.0358 | 0.0658 | 0.000795 | 36.07 | 98.28 | 222.7 | 0.012078 | 1.19 |
| 0.04 | 0.0479 | 0.0879 | 0.001063 | 48.1 | 131.4 | 297.5 | 0.012098 | 1.20 |
| 0.05 | 0.06 | 0.11 | 0.001332 | 60.12 | 165 | 372 | 0.012109 | 1.20 |
| 0.06 | 0.0721 | 0.1321 | 0.001601 | 72.156 | 197.9 | 447.2 | 0.012117 | 1.20 |

Six air flow rates, ranging from 0.01–0.06 m/s, were evaluated and based on $v_{out}$, outlet jets 1–4 were found to be at subsonic speed, while jets 5 and 6 were at supersonic speed as a better result of Chapter 5. The type of panel and sizing will be further discussed in this Chapter. The simplified model was used to distribute internal mixture in a will draw in CFD as a cube domain , with the bottom surface dimensions being the same as the surface of real-world PVs (1188*1060*44 mm) to create realistic simulations.

## 6.3 CFD Simulations of Impingement of jet on the PV Surface

The CFD simulations provided feasible design solutions for using jet pumps to clean PV panel surfaces. The velocity of impingement of jets and suitable distances between the surface and jets would be 2.8, 5-5 and 8.3 times greater than the outlet nozzle diameter of $d_1$. In addition, jets angled towards the surface were highly efficient for surface cleaning.

CFD was applied based on the internal flow of fluid and desired characteristics within the cube domain and on the PV surface. Impingement by jet can be simulated, analysed and visualised. CFD technique application was divided into four parts: modelling geometry, calculating the domain of the given model (mesh), creating a solution and calculating post processing. ANSYS Fluent 16.1, which includes specific attributes of the ICEM 16.1 CFD and software for analysis, was used for the simulations and three-dimensional (3D) models.

### 6.3.1 Geometry and mesh

An analysis of outlet jet distribution was conducted, and the bottom surface of the cube domain was assumed to be the same as the PV surface. The height of the cube domain was 500 mm, which was relative to the nozzle height; this provided a larger space on the surface for observations as well as for adjustments for different nozzle heights.

Table 6-2: Geometry datasheet.

| | |
|---|---|
| Cube domain Height | 500 mm |
| Bottom Surface Dimensions of the PV | 1188*1060*44 mm. |
| Positions of the Nozzles | The middle axis nozzle was located in the centre of the inlet wall.<br>1st t model: 150 mm.<br>2nd model: 100 mm<br>3rd model: 50 mm |

The first modelled jet hole was perforated under the well of the inlet of the cube domain at a height of 150 mm from the bottom surface of the PV, the second modelled jet hole was at 100 mm and the third modelled jet hole was at 50 mm. The bottom surface of the PV was under the front and back walls of the cube domain. Figure 6-1 shows the top, front, back and bottom surface of the cube domain when viewed as a geometric CFD design.

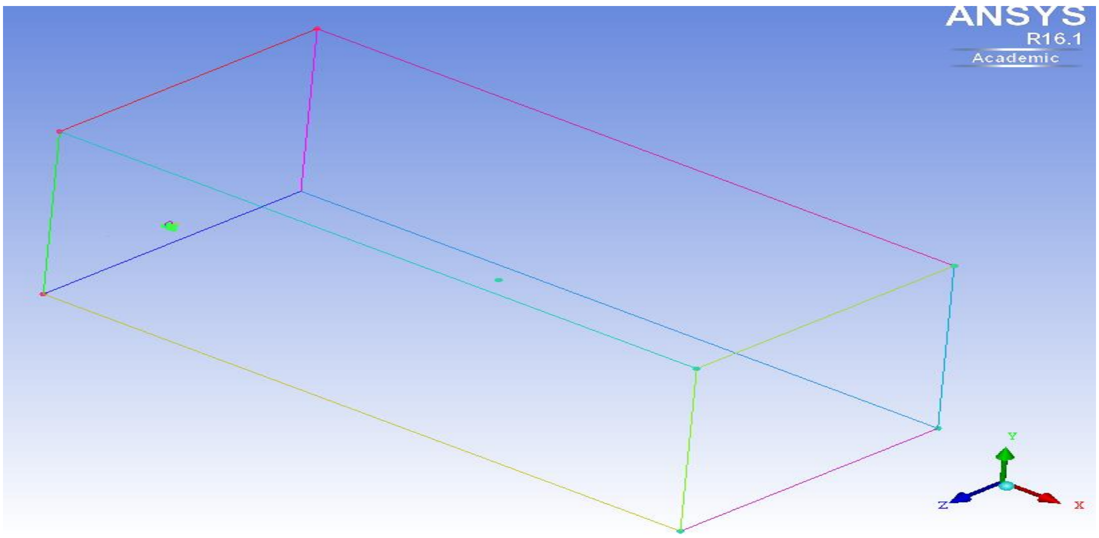


Figure 6-1: Top, front, back and bottom surfaces of the geometric CFD design.

The physical models were meshed and built under the ICEM 16.1 to identify if the grid had a significant impact on the convergence rate, the accuracy of the solutions and CPU time. The triangular and tetrahedron-shaped cells of the nozzle were given careful consideration, and the solid body of the model resulted in 2 438 372 elements and 423 623 nodes. This provided accurate simulation conditions for calculating performance. Figure 6-2 shows the body mesh of the modelled cube domain.

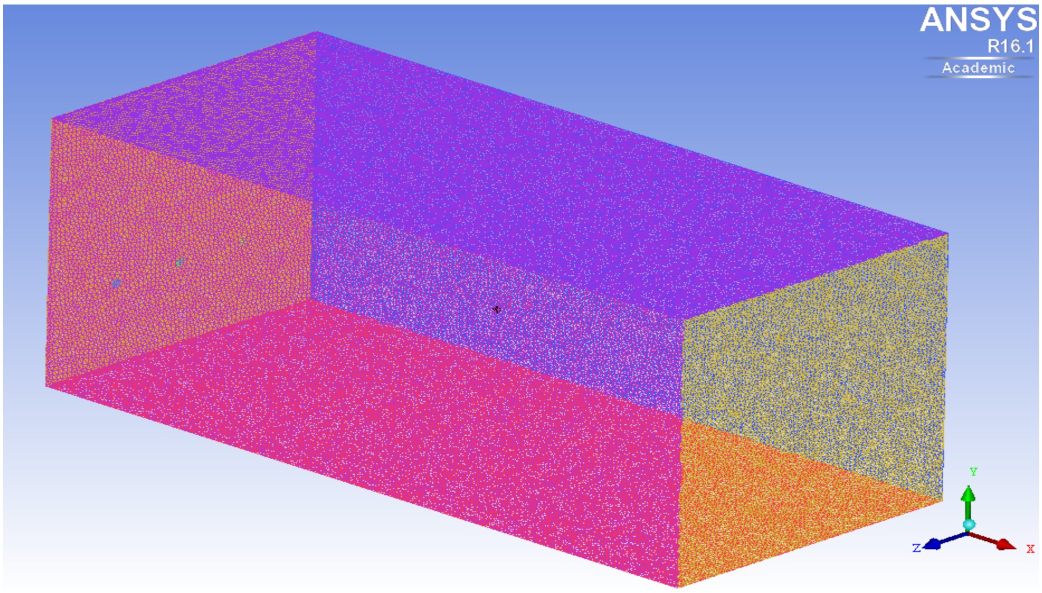


Figure 6-2: The generated grids for the PV model using CFD.

### 6.3.2 Simulation preparation

Grid calculations were conducted using Fluent 16.1, and the flexibility of the mesh supported both 3D tetrahedral and 2D triangular meshes. Fluent was then used to refine coarse mesh based on the flow solution. The pressure base solution was executed using a formulation for absolute velocity within a steady time, with an acceleration gravity of 9.81 m/s2 to facilitate real-world simulations. The mesh quality was determined based on orthogonal quality, which is equal to 4.16434e-01. Here, 1 represents high-quality mesh with acceptable values for fluid flow in a large space. Water vapour was used in the jet outlets, with water vapour density ρ expressed as

$$\rho = \frac{m}{V} = \frac{\dot{m}}{A * v} \tag{6-1}$$

Where *m* is the mass rate of the outlet, V is the water vapour volume, A is the outlet area and v is the speed of the nozzle. Nozzle outlet area A is $\pi * (d2)^{2}$. =0.000254 $m^3$.

$\rho = \dot{m}/A * v = 0.02140.000254 * 72.42 = 1.16338\ kg/m3$

Multiple tests of the water vapour did not reveal significant fluctuations, however, a value of 1.16 kg/m3 was linked to the simulated water vapour.

### 6.3.3 Boundary conditions

There were certain boundary conditions for each type, as shown in Figure 6-3. The descriptive information is listed in Table 6-3.

Table 6-3 Summary of boundary conditions.

| Zone Name | Type of Boundary |
|---|---|
| Total mass flow rate | Velocity inlet |
| Bottom surface domain | Wall of the adiabatic |
| Front, top and back domain surfaces | Outlet pressure |
| Water vapour outlet surface | Outlet pressure |

The surface of the PV was solid, and the mass flow rate velocity inlet had a set velocity which is coming from the result of total mass flow rate velocity outlet of jet pump from Chapter 5. Other surfaces are defined under outlet pressure. Three velocities were selected for the simulated flow: 72.42 m/s for test A, 222.7 m/s for test C and 447.2 m/s for test F. Simulated turbulence was indicated numerically, and the accuracy of the CFD simulation was adequate when the flow was affected by modelled turbulence, especially complexity inflow features. For this, k− ε was the standard solution used.

The viscous fluid model was set as a k-epsilon with significant standards to enhance the treatment of wall functions towards the execution of a near-wall treatment. The solutions were based on the least square and spatial discretisation. In the above changes, the settings of others were left unchanged to obtain significant outcomes. In addition, simulations were carried out to obtain a pressure-based solution. The parameters of the relaxed defaults for all variables were identified as near optimal for the largest number of possible cases, and calculations were begun.

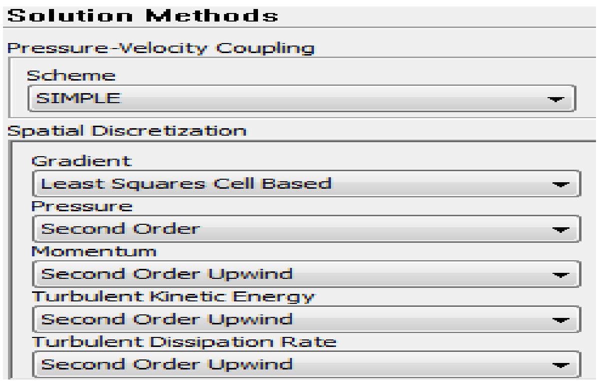


Figure 6-3: The solution methods.

Thus, calculate the velocity of the 2D mesh surface was used to model nozzle impingement by plotting the velocity values on the centre line and the velocity of X values through the axis of Z. In addition, numerical values gave the low-, medium- and high-velocity levels for different variations of PV surface jets.

## 6.4 Simulation Results and Discussion

The process was monitored to ensure it was run normally, and the level of default residuals decreased drastically once the convergence process was reached to $10^{-3}$. Thus, the solution was identified, and values were calculated.

The purpose of this research was to design an impingement of jet on a PV panel system. The height of the nozzles was important because they had to be level with the bottom surface and determination of the conjunction had to be performed carefully. The most suitable and accurate samples were chosen for testing, and nine different conditions were selected as suggested for optimal design of each model, which are described in detail.

Table 6-4 Variation between the cases

| Case Numbering | Nozzle Height Above the PV surface (mm) | Inlet Velocity |
|---|---|---|
| A-1 | 150.00 | 72.420 m/s |
| A-2 | 150.00 | 222.70 m/s |
| A-3 | 150.00 | 447.20 m/s |
| B-1 | 100.00 | 72.420 m/s |
| B-2 | 100.00 | 222.70 m/s |
| B-3 | 100.00 | 447.20 m/s |
| C-1 | 50.00 | 72.420 m/s |
| C-2 | 50.00 | 222.70 m/s |
| C-3 | 50.0 | 447.20 m/s |

### 6.4.1 The position of the four planes on the surface level

The CFD post adequately imports data and graphs and creates plots to simulate results. Figure 6-4 shows two yellow lines are located in the centre of the PV surface along the X axis. The Z axis is required to determine outlet velocity on the PV surface.

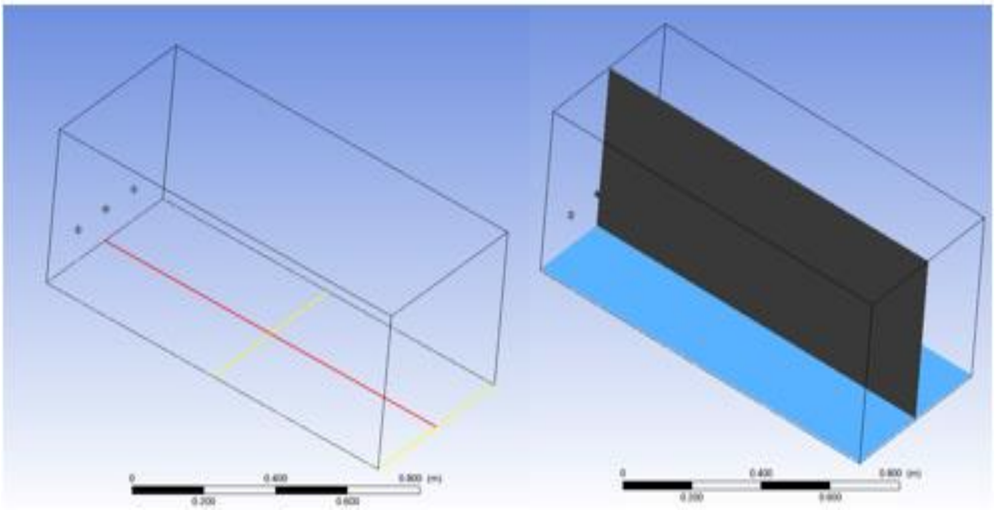

Figure 6-4: The positions of both axis.

### 6.4.2 Case A: Nozzle Height above the PV surface 150 mm.

For Case A, the nozzle axis was placed at the bottom surface at a height of 150 mm. As a result, velocity values were maintained at 72.42 m/s, which became Case A-1. Figure 6-5 shows the velocity distribution for this case.

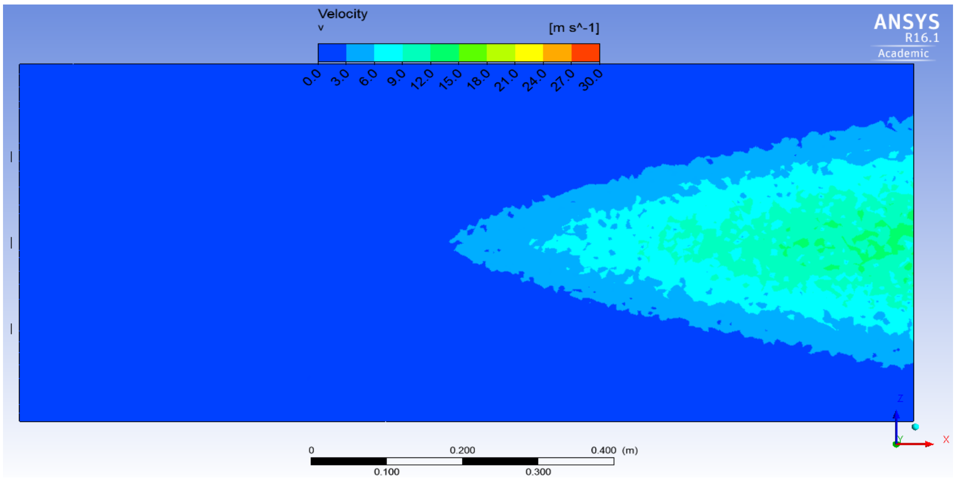


Figure 6-5: Case A-1: The level of velocity is equal to the contour, which is equal to jet impingement. The value is v = 72.42 m/s with a height of 150 mm.

A cross section of the PV surface is provided within the calculation domain. The velocity distribution image was obtained at speeds less than 12 m/s. The fan-shaped distribution started with the jet propulsion and was even distributed. Flow turbulence was as expected and was determined at a quarter of the zero flow velocity. The flow velocity is shown on the left side of the image, and nozzle output velocity was 72.4200 m/s. This illustrates that is provided and always present for comparison to compute the level of contour velocity. This range level was restricted to 0–30 m/s.

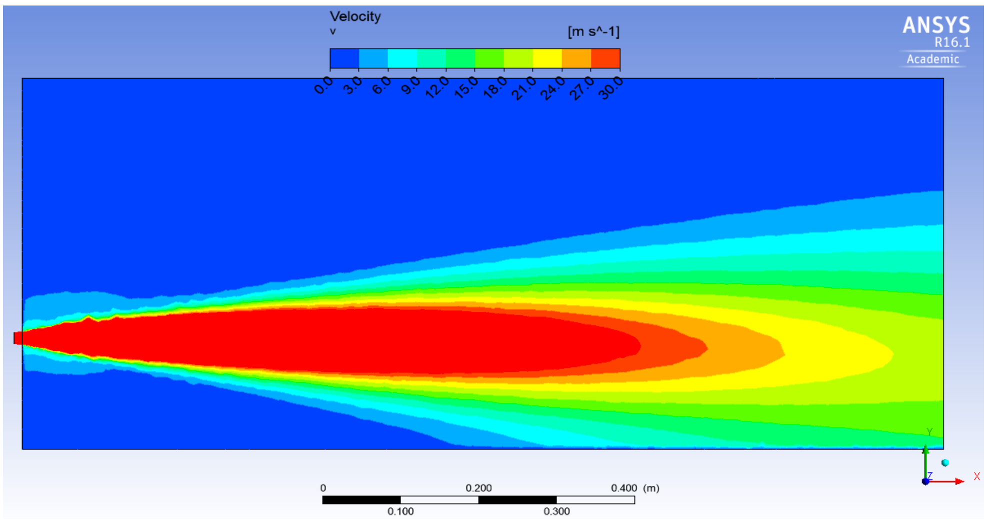

Figure 6-6: Case A-1: The contour of velocity distribution on the X axis (front view) when v = 72.42 m/s at a height of 150 mm.

Case A-2 had a significantly higher velocity compared to Case A-1. All other settings remained the same.

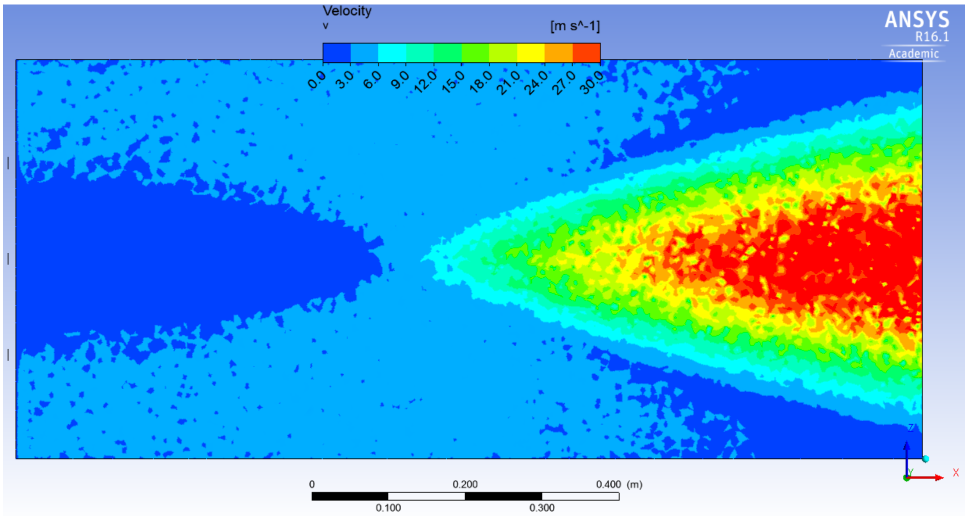


Figure 6-7: Case A-2: The velocity contour of jet impingement on the PV surface when v = 222.7 m/s at a height of 150 mm.

The flow patterns changed position significantly between the two cases because of different degrees of propulsion and expansion. The area reached and the level of the flow pattern was adopted to ensure that the correct range was provided (5–20 m/s) during observations.

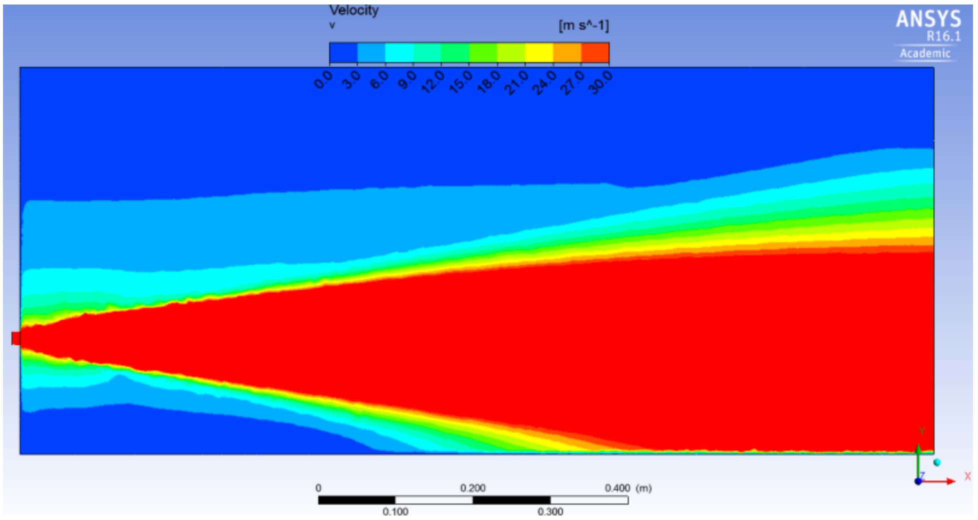


Figure 6-8: Case A-2: The distribution in the contour of the velocity on the X axis (front view) when v = 222.7 m/s at a height of 150 mm.

These cases were then compared to Case A-3, for which the impingement of jet speed was 447.2 m/s at the level of pointing, which was two-timed larger than the case on the front panel.

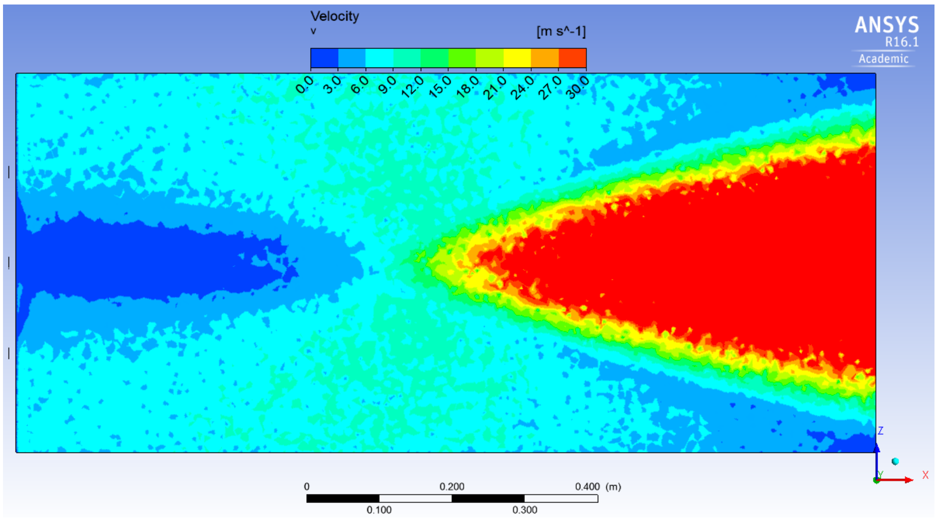


Figure 6-9: Case A-3: The jet impingement velocity contour on the surface of the PV when v = 447.2 m/s at a height of 150 mm.

Figure 6-9 shows excessive outlet velocity of 30 m/s for the PV panel. Observations were taken at the left corner, which produced outlet at a speed 6m/s, the outlet rate is provided up to the level of 8m/s to 20 m/s approximately for each corner.

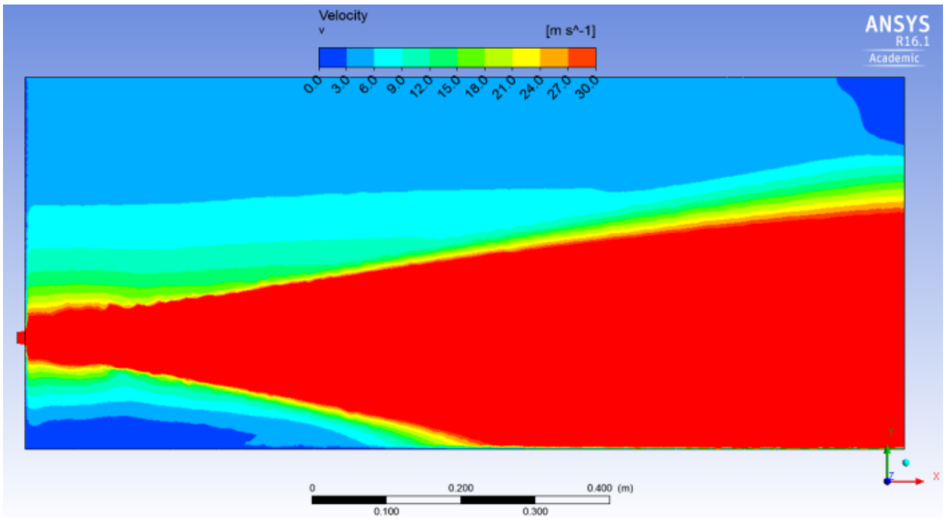


Figure 6-10: Case A-3: The distribution contour of the velocity on the X axis (front view) when v = 447.2 m/s at a height of 150 mm.

### 6.4.3 Case B: Nozzle Height above the PV surface 100 mm

In Case B, the axis nozzle was placed 100 mm from the bottom surface and the contour velocity of the impingement of jet on the PV surface was maintained under specific conditions to get a velocity value of 72.42 m/s (Case B-1). Figure 6-12 shows the velocity distribution of this case.

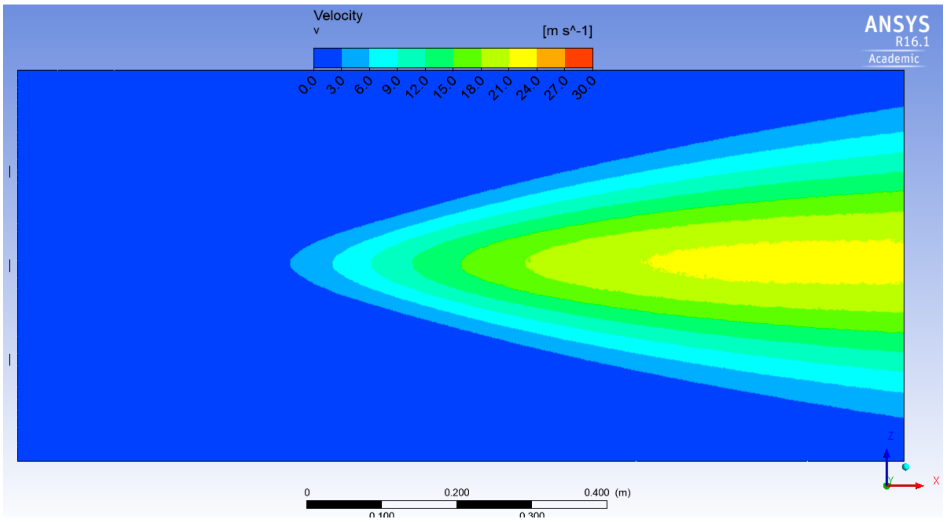


Figure 6-11: Case B-1: The impingement of jet contour velocity on the PV surface when v = 72.42 m/s at a height of 100 mm.

A comparison of Cases A-1 and B-1 found that speed was less than 24 m/s. On the surface of the PV, velocity was 72.42 m/s at 100 mm, which is shown in Figure 6-11. In contrast, the Case A-1 velocity was 72.42 m/s at 150 mm, with a fan-shaped distribution. Accurate values reveal that the lower quarter of the panel had a fairly even distribution, which indicates that three-quarters of the panel in Case A-1 compared to Case B-1.

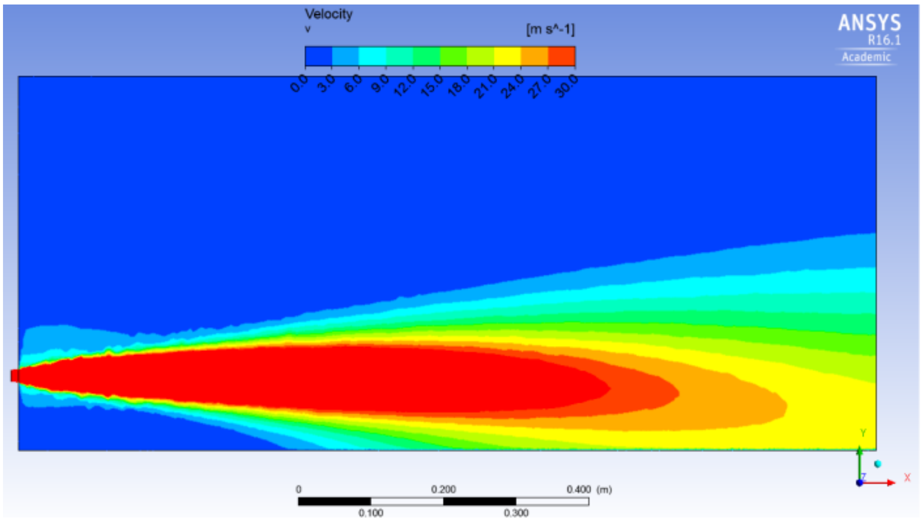


Figure 6-12: Case B-1: The velocity contour for the X distribution axis (front view) when v = 72.42 m/s at a height of 100 mm.

Case B-2 had a higher velocity than Case B-1, despite the settings being the same. The velocity of the outlet towards the nozzle in Case B-2 was at a subsonic speed.

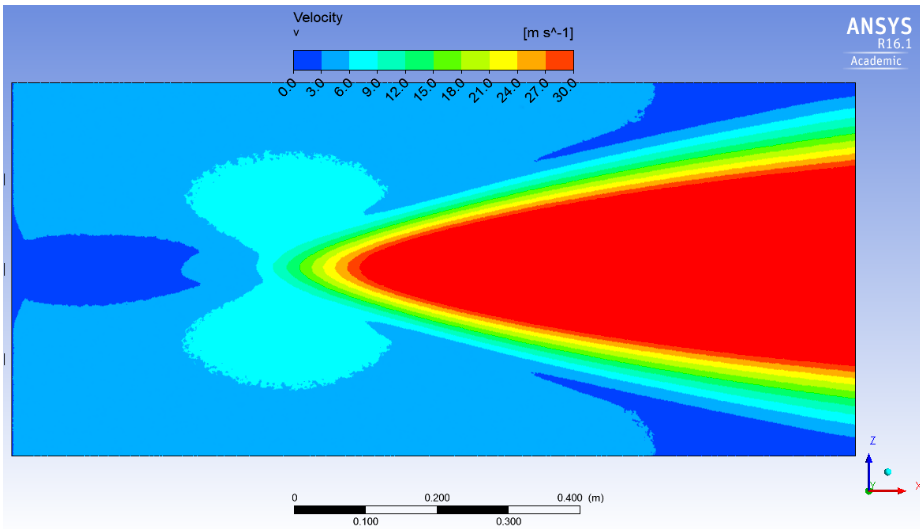


Figure 6-13: Case B-2: The jet impingement velocity contour on the PV surface when v = 222.7 m/s at a height of 100 mm.

Compared to Case B-1, Case B-2 had a different contour velocity for the impingement of jet on the surface of the PV, with values ranging from 6–22 m/s. Compared to Case A-2, different velocity descriptions were obtained. Case A-2 provided more significant descriptions of velocity outcomes, with a fan-shaped impingement. The main difference was that distribution ranged from 5–20 m/s. This revealed how Case A-1 differed from A-2 and how to determine differences between Cases B-1 and B-2, which is the objective of this research.

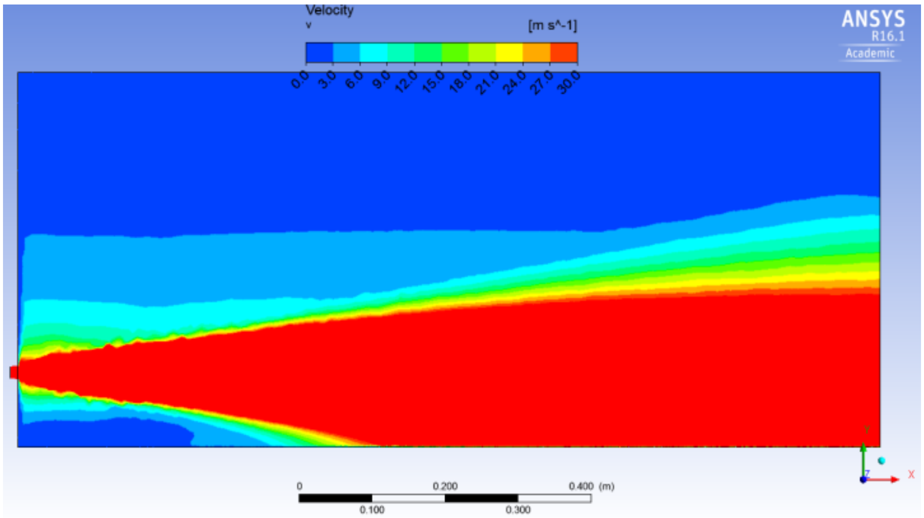


Figure 6-14: Case B-2: The distribution of the contour velocity on the X axis (front view) when v = 222.7m/s at a height of 100 mm (left).

For Case B-3, the speed of the impingement of jet from the nozzle was 447.2 m/s, which was two times faster than in Case B-2 and six times faster than Case B-1. The contour velocity is presented from different perspectives in figure 6-15.

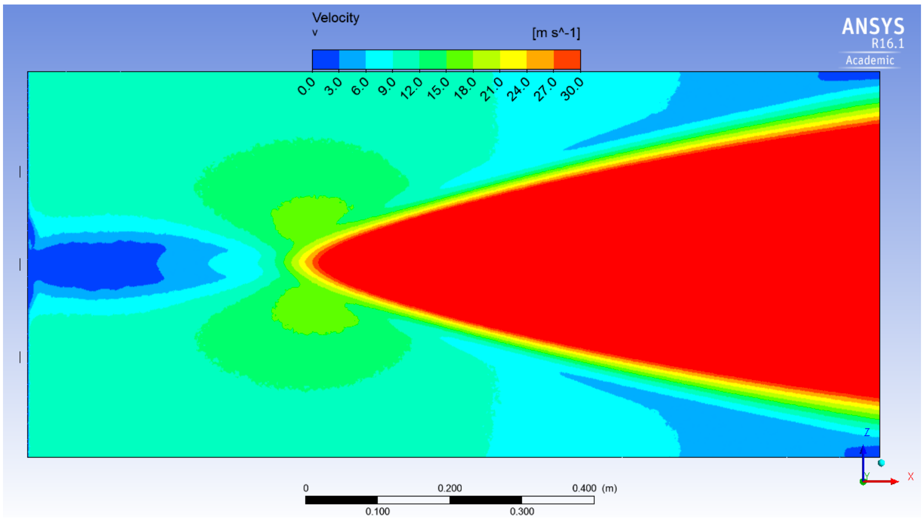


Figure 6-15: Case B-3: The impingement of jet velocity contour on the PV surface when v = 447.2 m/s at a height of 100 mm.

The description of the contour velocity on the surface of the PV includes certain characteristics. First, velocity was 447.2 m/s at a height of 100 mm, which shows how the explorative framework was able to recognise the PV surface and ensure significant outcomes.

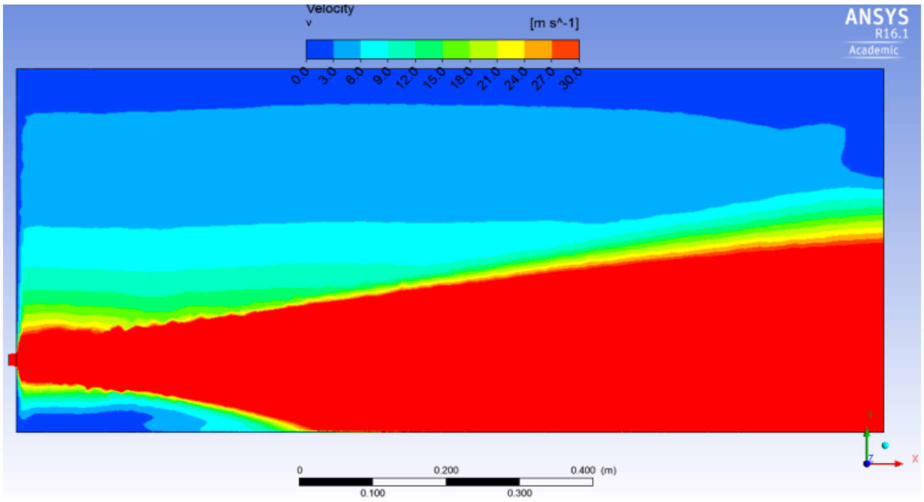


Figure 6-16: Case B-3: The distribution of counter velocity on the X axis (front view) when v = 447.2 m/s at a height of 100 mm.

### 6.4.4 Case C: Nozzle Height above the PV surface 50 mm

Case C began at a velocity of 72.42 m/s at a nozzle axis height of 50 mm. The distribution velocity for Case C-1 is shown in Figure 6-17.

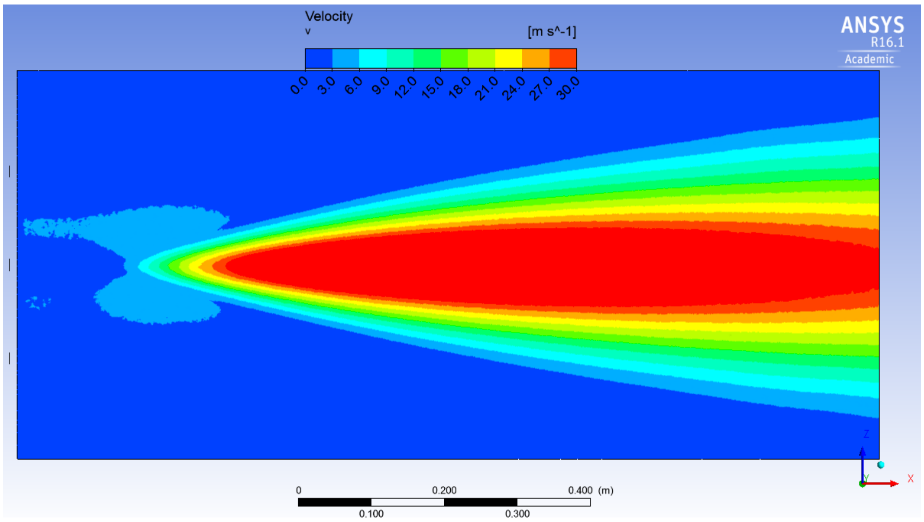


Figure 6-17: Case C-1: The impingement of jet contour velocity on the PV surface when v = 72.42 m/s at a height of 50 mm.

This study provides the information about the execution of contour velocity to obtain significant outcomes and demonstrations. Comparisons are based on speeds less than 24 m/s to obtain the best results. The A-1 contour velocity was 72.42 m/s at 150 mm with a fan-shaped distribution. The shape differences between A-1 and B-1 are due to the difference in speeds and the surface of the PV, which generate different outcomes. Analysis of the contour velocity of the impingement of jet was used to determine a velocity value of 72.42 m/s at a height of 50 mm. Different measurements were used for the calculations at different heights to determine how different attributes affect fluid system development.

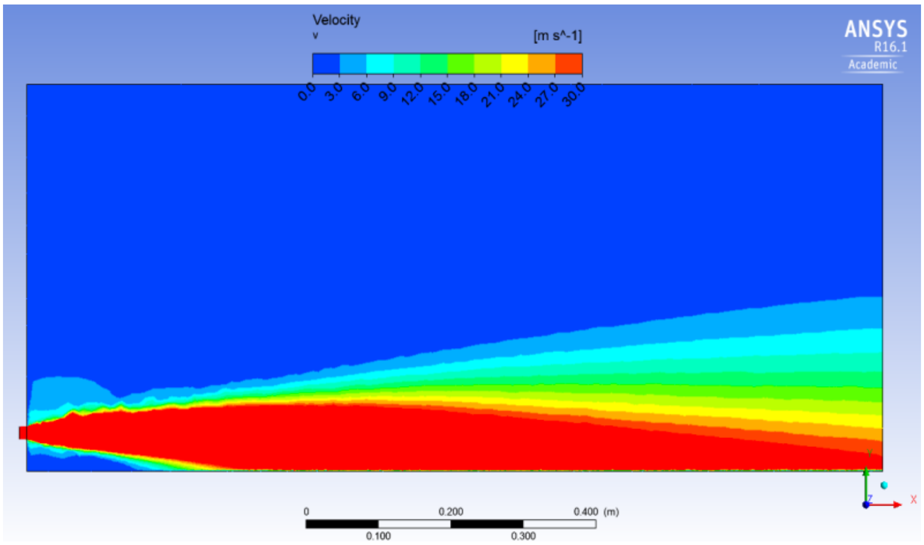


Figure 6-18: Case C-1: The contour velocity distribution on the X axis (front view) when v = 72.42 m/s at a height of 50 mm.

For Case C-2, higher velocities were observed compared to C-1 for the same simulation conditions, which agrees with the previous case descriptions. The velocity of the outlet was used for the explorative framework for Case C-2 in accordance with subsonic speed.

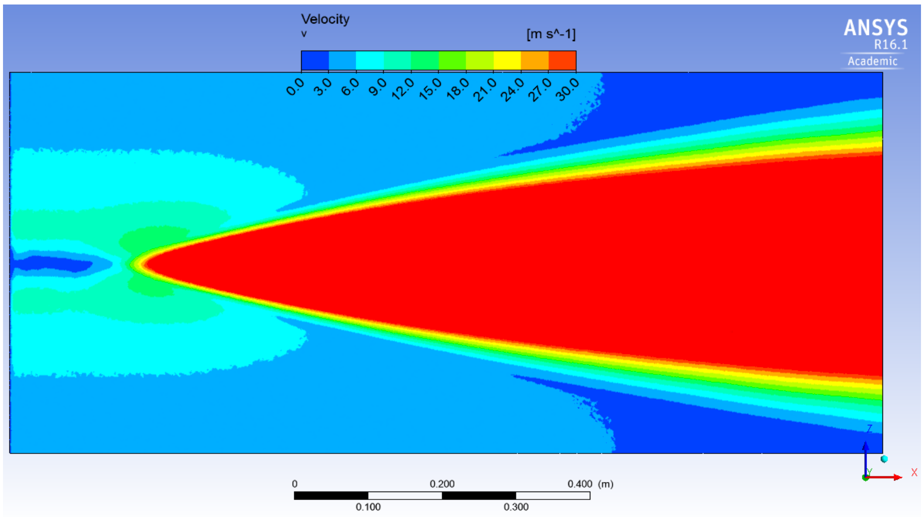


Figure 6-19: Case C-2: The velocity contour of the impingement of jet on the PV surface when v = 222.7 m/s at a height of 50 mm.

Comparisons of the contour velocity of the impingement of jet on the surface of the PV reveal significant differences in the shape and speed of the jet significant. Case B-1 had consistent speeds ranging from 6–22 m/s. A comparison between Cases A-2 and B-2 found differing values certain characteristics.

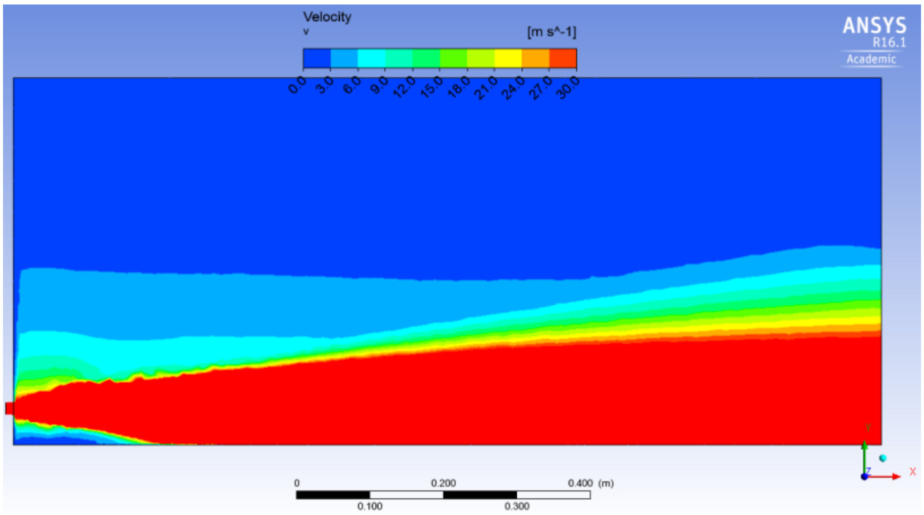


Figure 6-20: Case C-2: The distribution of contour velocity on the X axis (front view) when v = 222.7 m/s at a height of 50 mm.

The previous two cases illustrated outlet flow with subsonic velocity; in Case B-3, the impingement of jet had a speed of 447.2 m/s, which is two-timed faster than in Case B-2, six-times faster than in Case B-1, and two-times faster than Case A-2 (front) The velocity contour is presented below from both front and sectional views. The explorations of the contour velocity show how it is distributed and developed. Speed and height change certain variables, such as shape.

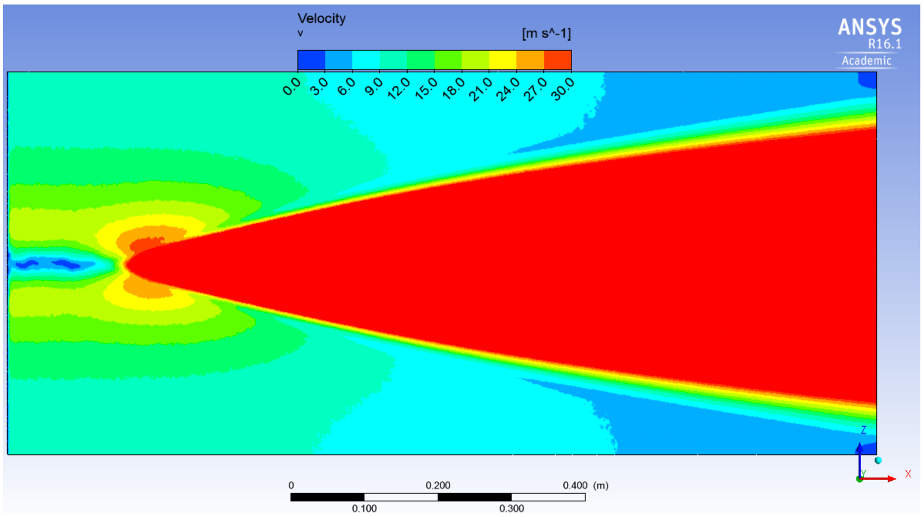


Figure 6-21: Case C-3: The impingement of jet velocity contour on the PV surface when v = 447.2 m/s at a height of 50 mm.

The diagram 7-21 shows velocity development of the impingement of jet on the surface of the PV at a velocity of 447.2 m/s. Observations of speed and distribution of velocity were analysed to generate data for Case C-3, including the fan-shaped distribution. These data provide accurate values for selected conditions.

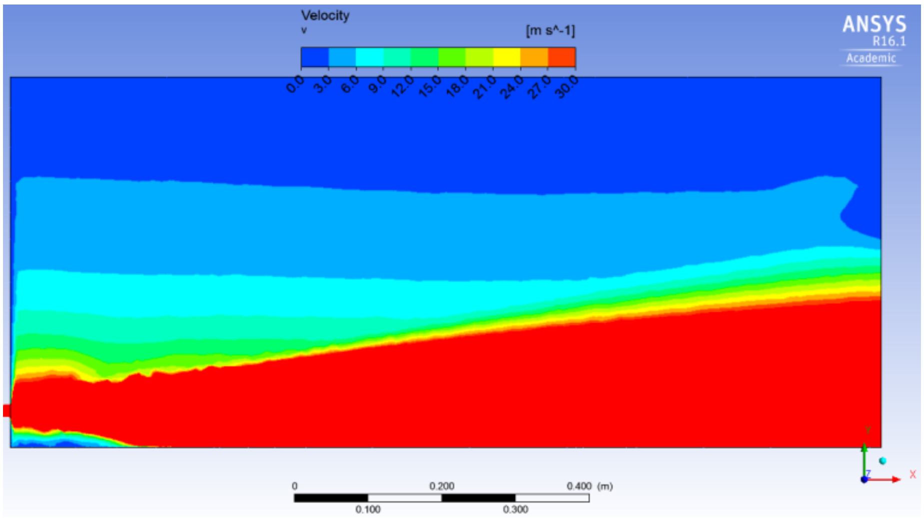


Figure 6-22: Case C-3: the distribution contour velocity in X axis (front view) when v = 447.2 m/s at a height of 50 mm.

A comparison of all results revealed that the speed of the jet from the nozzle ranged from 72.42–447.2 m/s, with certain variables resulting in certain characteristics. First, the movement of the outlet was concentrated on the pressurised impingement of jet, which created limitations for expansion. The outlet flow was primarily forced into the middle zone of the space, causing the lower left- and right-hand sides of the panel to not be reached by jet and leading to dust accumulation in both of these corners. When outlet flow was directed to these two areas, it caused yields of electricity on the PV panel that decreased sharply.

At the outlet of 444.7 m/s, the jet flows continuously over the in entire the surface of PV panel. Increased, leading to the impingement outlet flow covering the PV surface entirely and cleaning the dust. This method required high pressure in the jet pump, which wasted both electricity and water. Damages to the glass coating on the PV surface due to the sand moving at high-speeds must be explored in more detail.

In addition, the jet concentration in the middle zone of the cube domain only resulted in dust being removed from this area into the panel areas, which could not be reached by the outlet jet for cleaning, resulting in dust accumulation. This also required high electric costs. Thus, to fully and efficiently clean the PV surface, the number of nozzles should be increased.

## 6.5 The effects of the impingement of jet on PV surface design

The advanced PV surface cleaning system was designed according to the requirements. Optimization of the impingement of jet incorporated three effective suggestions: a current outlet jet, which is suitable for velocity ejection of water vapour, multiple nozzles to clean the surface of the PV panel and placement of the nozzle axis above the PV panel to effectively clean the entire panel.

### 6.5.1 Selecting the number of nozzles

After observing the conditions and results, it was determined that using a single jet to clean the entire system was not adequate because of uneven distribution. The velocity of the outlet in the middle and bottom of the panel are shown below.

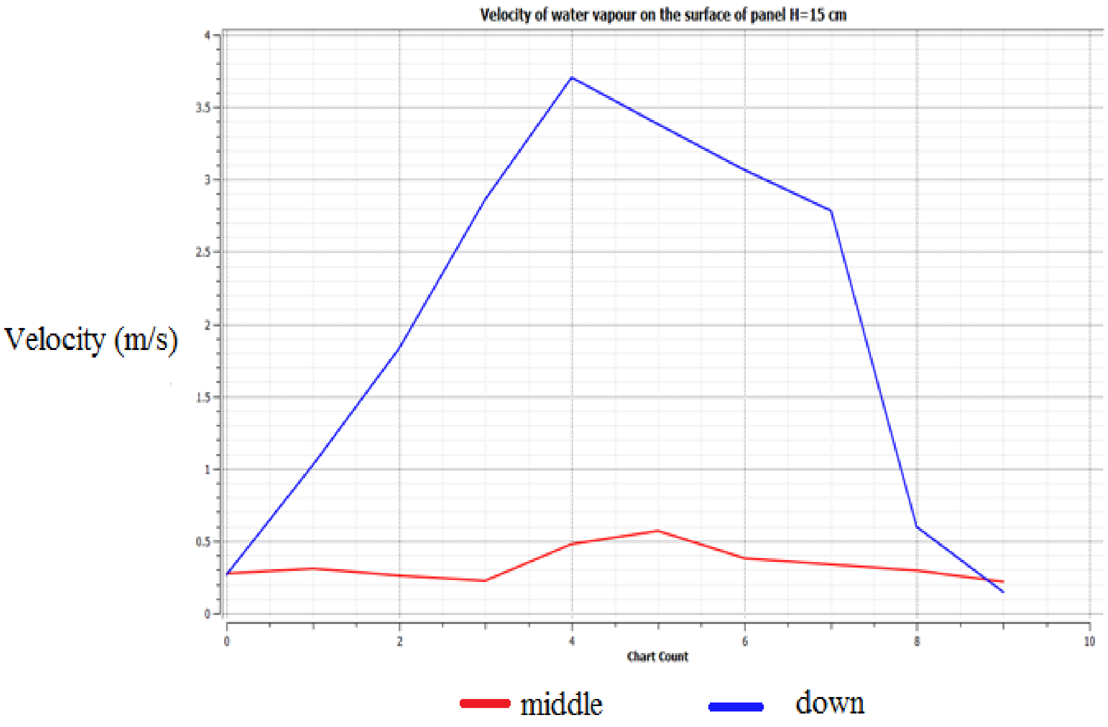


Figure 6-23: Case A-1: The velocity of the outlet on the surface of the panel at a height of 15 cm.

Figure 6-23 shows Case A-1, which had an outlet velocity on the surface of the panel at a height of 15.cm. The blue line shows the down chart count and the red line shows the middle chart count. The velocity was measured in meters per second.

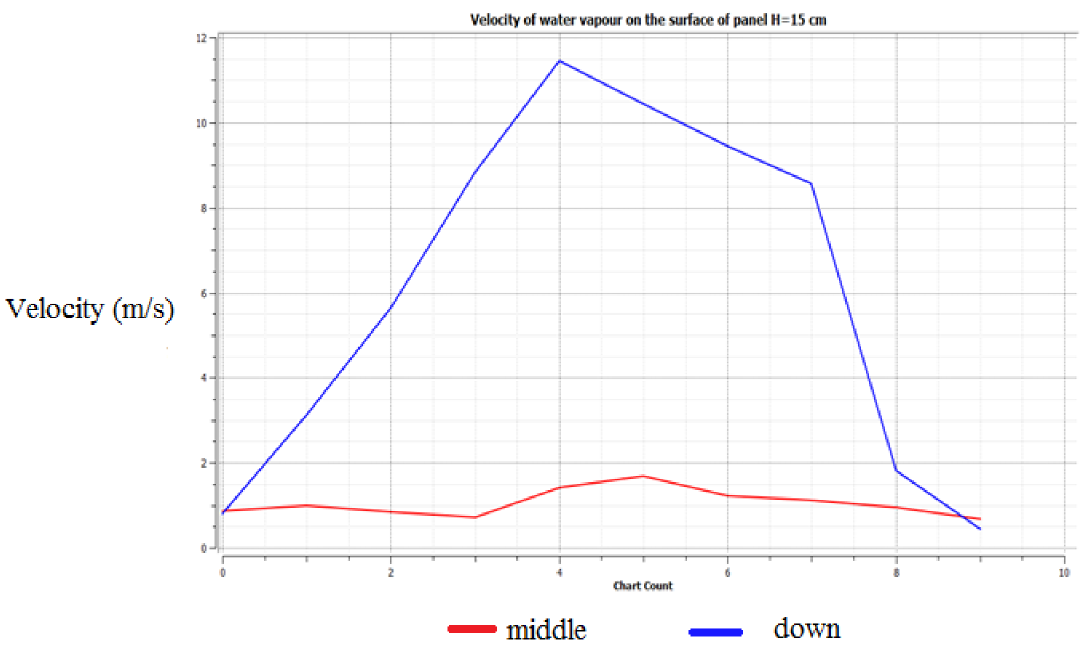


Figure 6-24: Case A-2: The velocity of the outlet on the surface of the panel at a height of 15 cm.

Figure 6-24 shows Case A-2, which had an outlet velocity on the surface of the PV panel at a height of 15 cm. The graph differs slightly from the previous graph in that the red line shows different velocity points. The velocity was also measured in meters per second.

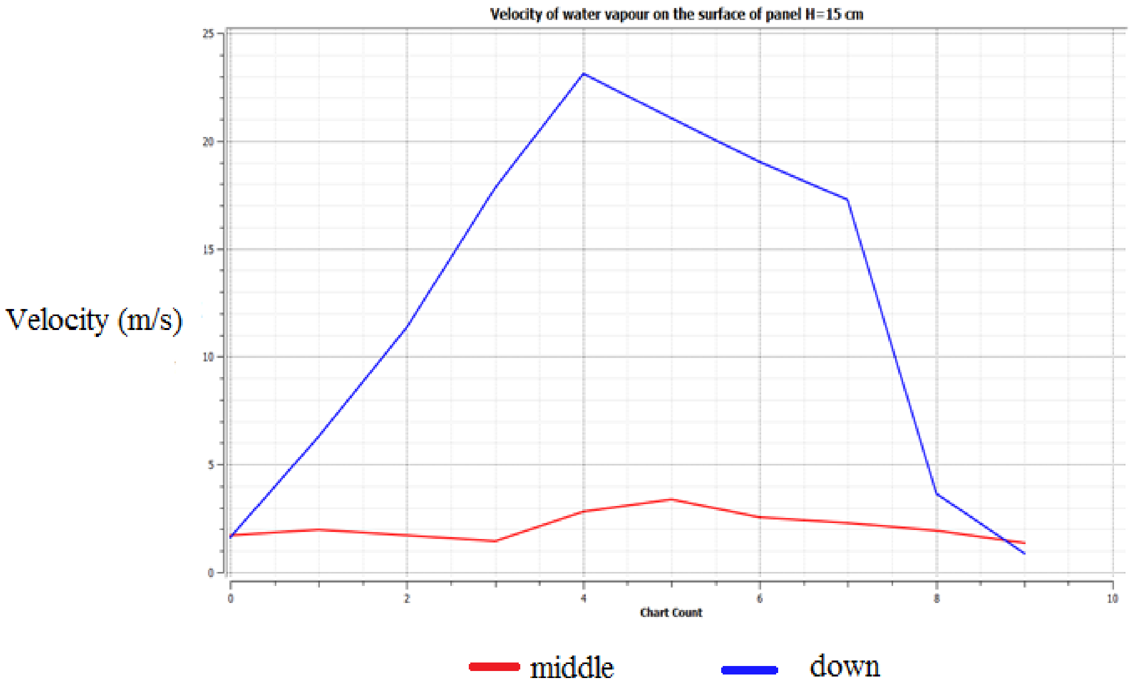


Figure 6-25: Case A-3: The velocity of the outlet on the surface of the panel at a height of 15 cm.

Figure 6-25 shows Case A-3, for which the red line differs considerably from the graphs for Cases A-1 and A-2 because of the velocity in the middle changes. The velocity shown in the graph is measured in meters per second.

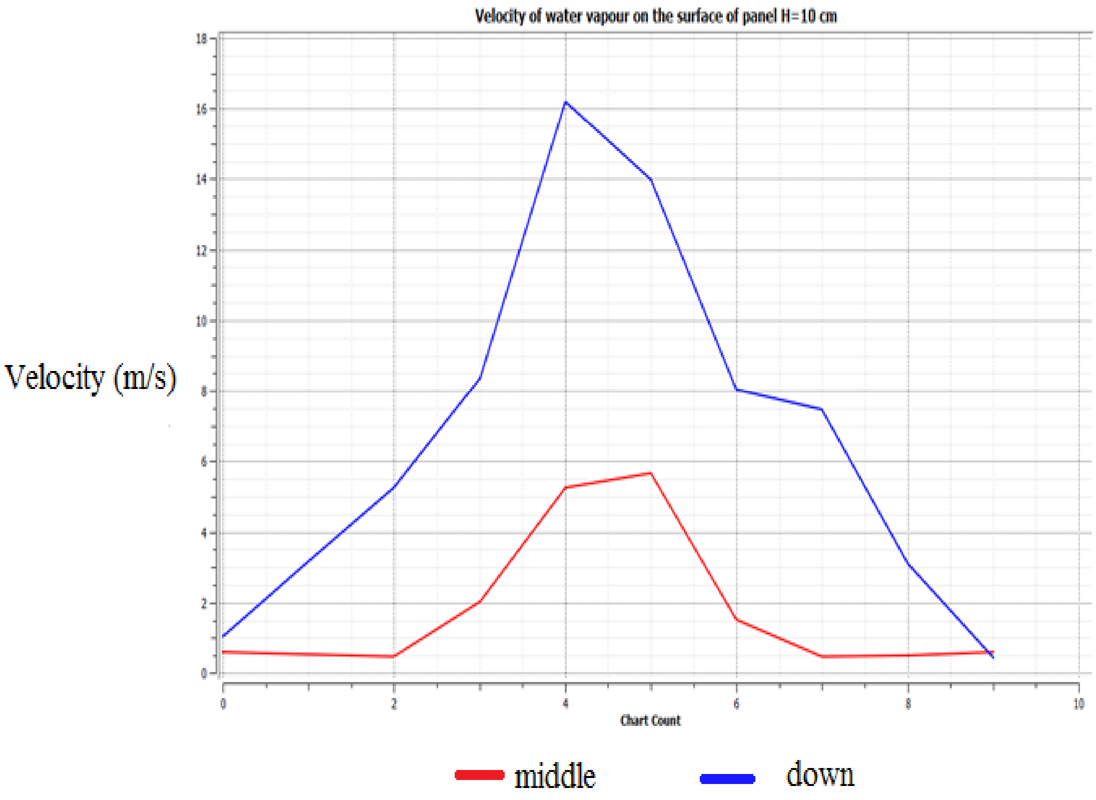


Figure 6-26: Case B-1: The velocity of the outlet on the surface of the panel at a height of 10 cm.

Figure 6-26 shows Case B-1 with different velocities for the different chart counts for the PV panel at a height of 10 cm. As the height changed, the velocity also changed. The velocity is measured in meters per second.

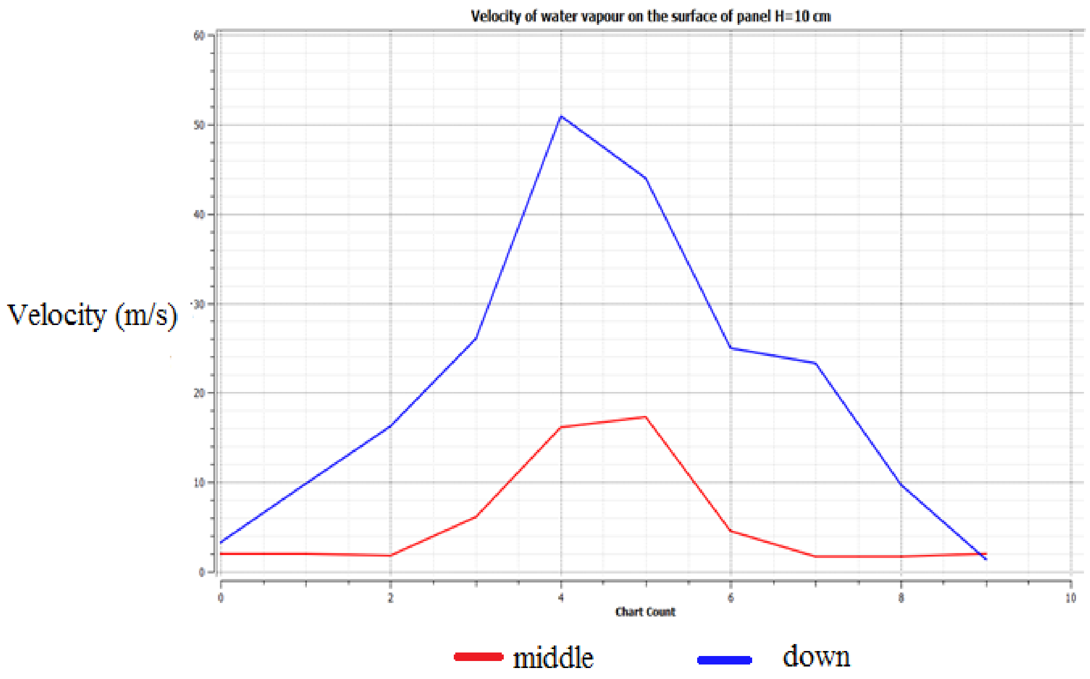


Figure 6-27: Case B-2: The velocity of the outlet on the surface of the panel at a height of 10 cm.

Figure 6-27 shows Case B-2, which has a velocity of the outlet on the surface at a height of 10 cm. The red line differs slightly and shows the peak values, which peak in graph B-1 and are much straighter in graph B-2, based on the different velocity values. The velocities are measured in meters per second.

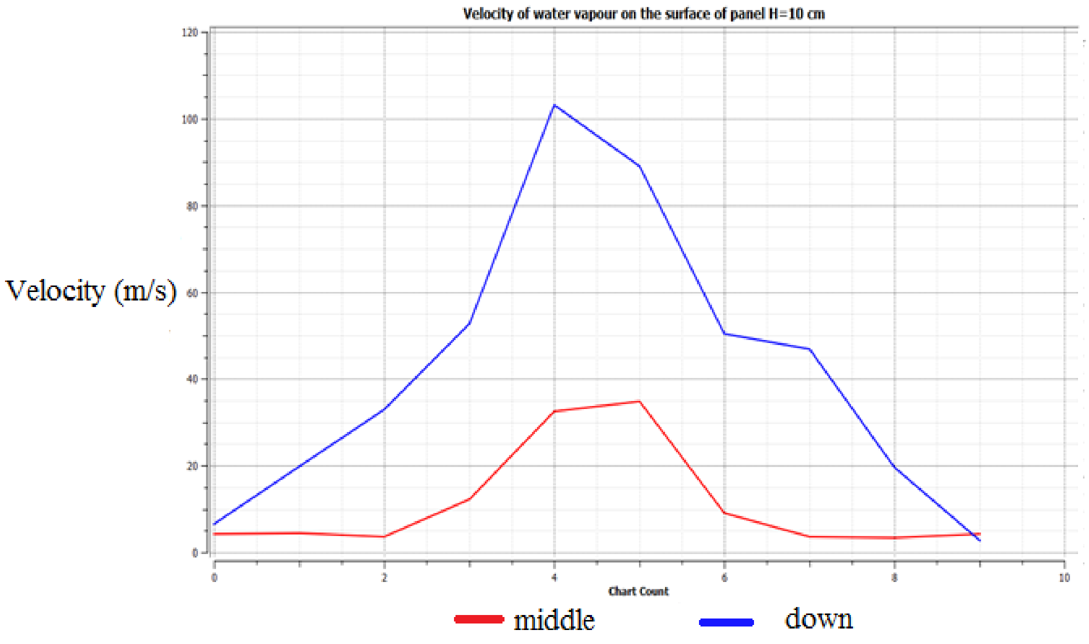


Figure 6-28: Case B-3: The velocity of the outlet on the surface of the panel at a height of 10 cm.

Figure 6-28 shows Case B-3, which had a velocity of the outlet on the surface of the panel at a height of 10 cm. The velocity chart count graph for an outlet on the surface of the PV panel was considerably different from the B-2 graph and the peak values of the B-1 graph.

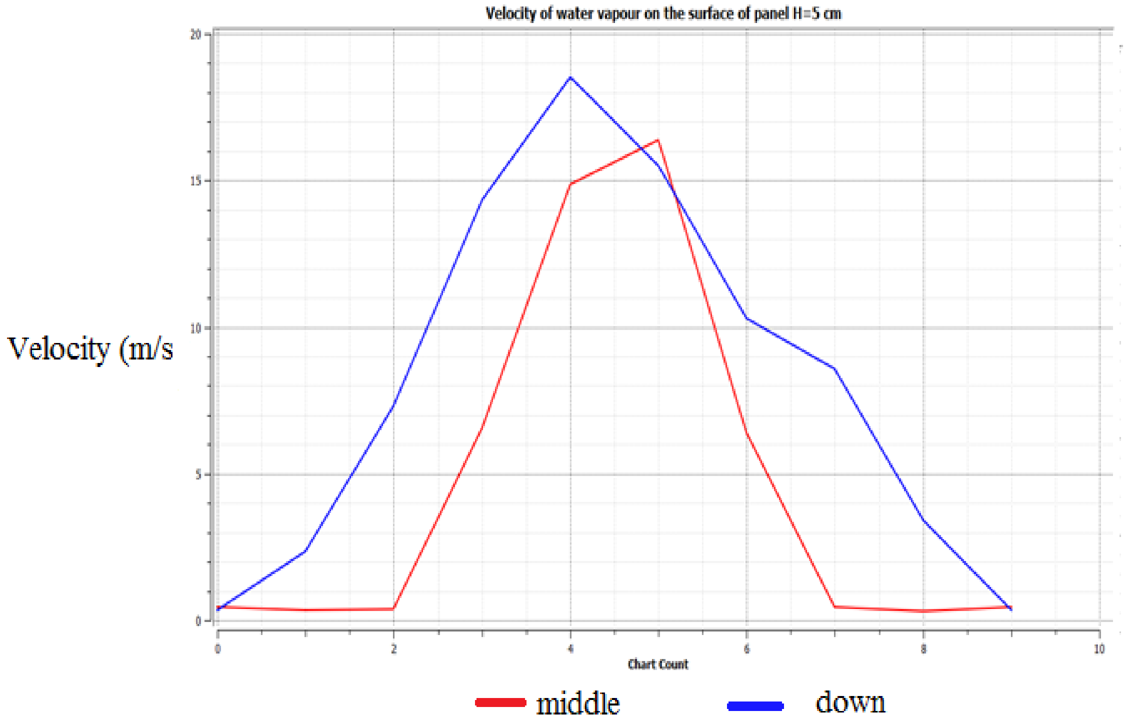


Figure 6-29: for Case C-1: The velocity of the outlet on the surface of the panel at a height of 5 cm.

Figure 6- 29 shows Case C-1, which had a velocity of the outlet on the surface of the panel at a height of 5 cm, which changes the velocity in comparison to the other cases. The peak values are different for the middle and the down chart counts. The velocity is measured in meters per second.

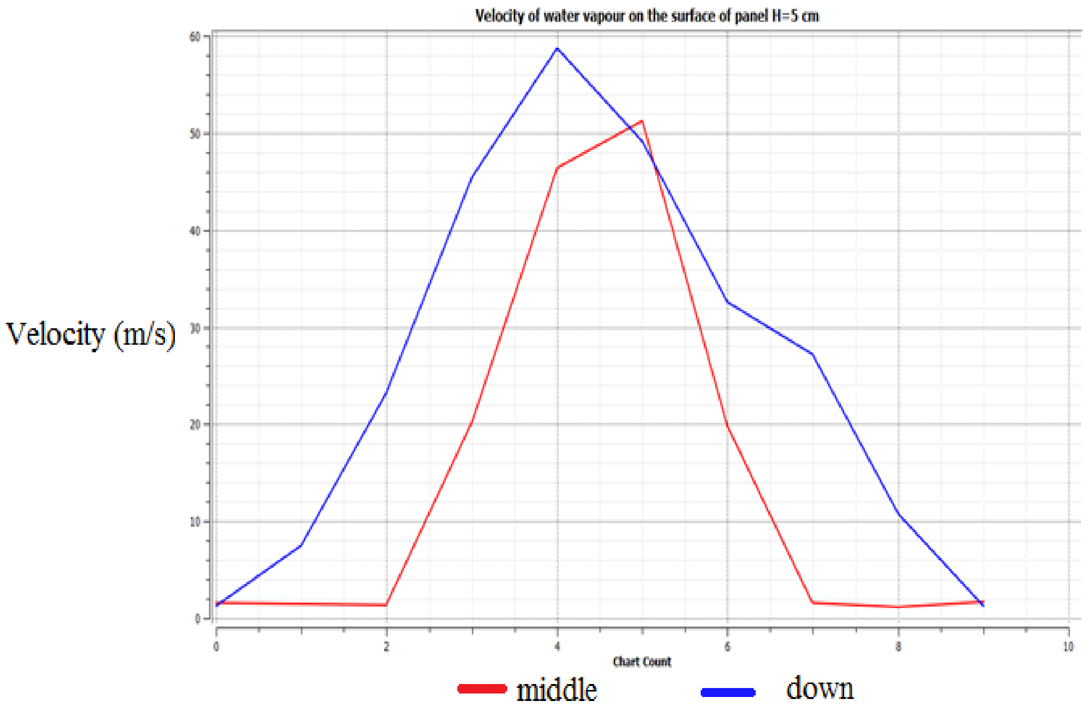


Figure 6-30: Case C-2: The velocity of the outlet on the surface of the panel at a height of 5 cm.

Figure 6-30 shows Case C-2, which had a velocity of the outlet on the surface of the panel at a height of 5 cm. This is slightly different from Case C-1. The peak values of both lines are almost the same; however, slightly different velocity values were obtained in this case.

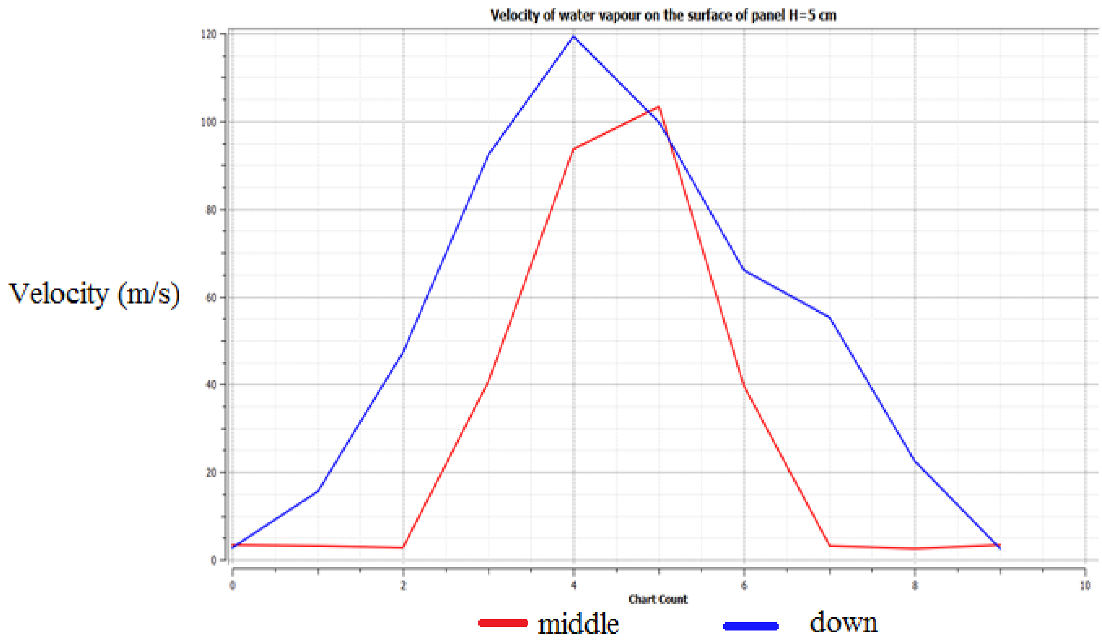


Figure 6-31: Case C-3: The velocity of outlet on the surface of the panel at a height of 5 cm.

Figure 6-31 shows Case C-3, which had a velocity of outlet on the surface of the panel at a height of 5 cm. The velocity versus chart count graph for the velocity of the outlet on the surface of PV panel was considerably different from the B-2 graph and different peak values than the B-1 graph.

The graphs for the different cases illustrate that the on the y-axis, the velocity of the steam vapour against the PV panel surface is shown, but on the x-axis, the two lines are red and blue. These two lines represent two impingement of jet velocities situated on the surface of the PV panel. The x-axis represents the width of the PV. Based on the graph, a single jet covers 1.06 m which is the exact width of the PV panel. A double jet covers 0.53 m, and a triple jet should cover 0.353 m. However, the results showed that the single jet could cover the entire width of the PV panel because of uneven distribution.

For Cases A-1, A-2, A-3, B-1, B-2, B-3 and C-1, the velocities graph show that velocity was zero or nearly zero, but when the distance reached the centreline, a sudden increase in velocity occurred. This significant variation indicates uneven distribution in the outlet at the PV panel surface, meaning that cleaning efficiency is not sufficient for the entire surface area of the PV panel.

From Cases C-2 and C-3, the velocities were 222.7 m/s and 447.2 m/s, respectively. The velocities indicate that these cases had the same behaviour of distribution and coverage for cleaning the panel as the other cases, but only reached 30 m/s with chart contour of 3.2–5-6. The graph 7-30 shows a chart contour of 2.20–6.5 at the bottom area of the PV panel surface.

Different nozzle heights provided different results, which is known as the Coanda effect (Allery et al. (2004)). When the jet was close to the surface of the PV panel or parallel to the x-axis, it can be deflected towards the PV panel surface and may reach a steady state. At this point, it is attached to the surface area of the PV panel. If there is a distance between the surface and the jet, the jet can move equally in all direction of the panel surface and will maintain its position or original state. However, when the jet is close to the surface area of the PV panel system, uneven distribution of the vapour over the surface of the panel occurs. When the jet is close to the surface, entrainment velocities increase, and when the outlet velocity increases, the static pressure decreases as described by Bernoulli's equation. Reduction in static pressure occurred between the jet and the surface area of the PV panel, forcing towards the surface (Allery et al., 2004). Additionally, when the jet is close to the surface of the panel, steady distribution of the outlet on the bottom surface occurs. The graphs show that when the nozzle is at a height of 50 mm, uniform distribution of the vapour in the direction of the nozzle is obtained at a speed of 222.7 m/s. When the nozzle was at a height of 100 mm, a high-velocity jet covered most of the bottom surface. The Coanda effect became relevant at nozzle heights of 150 mm, which reduced the attached jet effect on the surface of the panel. Therefore, a nozzle height of 50 mm was selected for the jet to ensure uniform and steady distribution of outlet over the surface of the PV panel.

The speed of the jet should be uniform to effectively clean the panel surface; thus, it is crucial to design or select an even jet speed. In this study, three velocities were chosen: 72.42 m/s, 222.7 m/s and 447.2 m/s (supersonic). The lowest-velocity nozzle gave an even distribution of outlet but was rejected because it did not cover the entire panel area and could not reach the left or right-hand corners of the system. This resulted in insufficient cleaning outside of the middle area of the panel. The low-velocity jet was capable of producing 5–10 m/s average values, which is within the same range of natural wind velocity.

The highest velocity of the outlet was 444.7m/s, which was also rejected because of the strong reactional forces of the impingement of jet, resulting in an added electric load to the outlet jet. The system has a support frame and a heavy load, consisting of three nozzles and the associated piping. Additionally, this velocity is too costly to employ in a three jet pump, which is an important production consideration. To generate an electrical load and water vapour, the air compressor must be work harder to expel more water. Furthermore, damage to solar arrays and wildlife can occur due to high-speed outlet jets, which are not environment friendly. During the cleaning process, undesired sound hazards must also be contained.

A nozzle height of 50 mm and a velocity of 222.7m/s provides outlet distribution. An average jet speed should not be less than 20 m/s because the average outlet jet speed is 30 m/s along the bottom panel area. To clean dust, a velocity of 30m/s is the stable provide adequate distribution of the water vapour. The width of the panel should be cover exactly by three jets with nozzle heights of 50 mm and a velocity of 222.7 m/s to clean dust on the panel surface with even distribution.

### 6.5.2 Analysis of triple jet performance

The CFD simulation proposed using triple nozzle impingement of jets at a height of 50 mm is the same as the design of Case C-2. A velocity of 222.7m/s for the outlet through three nozzles cleans the PV panel surface.

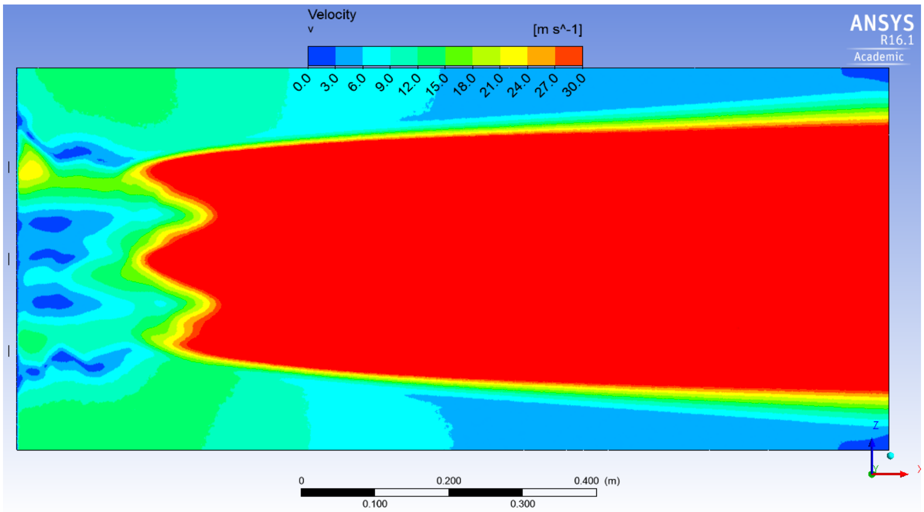


Figure 6-32: The velocity contour of the impingement of jet on the PV surface when v = 222.7 m/s at a height of 50 mm from three jets.

The velocity contour of the triple jet pump jets is illustrated in the following two diagrams. Compared to previous tests, the results differ significantly from the first contour. The outlet of jets cover the PV panels, and the two upper corners of the panel surface are reached because the outlet speed ranges from 9–15m/s. From the illustration, a jet velocity above 18m/s clean most of the panel surface, and the three jets interact in the middle of the panel, with two streams having velocities of approximately 30 m/s, which reaches the end of the panel from the lower top range. A higher velocity of outlet in the higher level occurs as the two jets join together. Figure 6-34 shows the contour of the velocity distribution on the X axis when v = 222.7 m/s at a height of 50 mm from three jets.

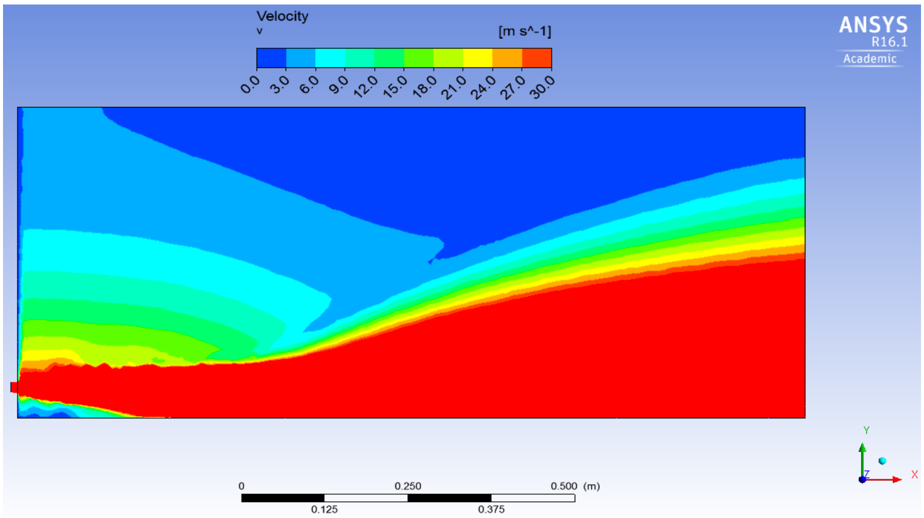


Figure 6-33: The contour of the velocity distribution on the X axis (front view) when v = 222.7 m/s at a height of 50 mm from three jets.

A comparison of single jet conditions reveals that jet conditions improved in the middle of the calculation domain where the section view is located. However, compared to the triple jet simulation, the area covered vertically significantly improved. The velocity of the steam, from the middle of the panel to the bottom was the same at 30m/s with small variations in the top area of this section. Consequently, the profile is significantly improved for vertical velocity. On the panel surface, the area influenced by the jets was amplified and covered by the jets, which enhances the process of dust cleaning.

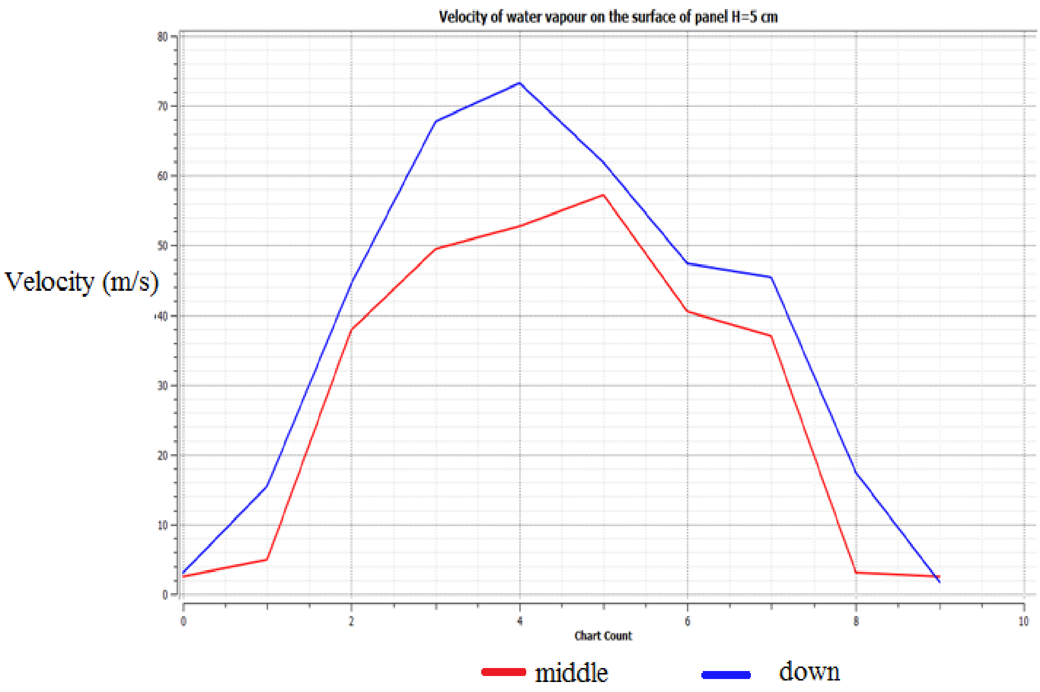


Figure 6-34: Velocity of the outlet impingement of jet on the panel top, middle and bottom for the triple jets.

In conclusion, the panel middle and bottom areas are sufficiently covered by the velocity distribution of the triple jets, which is illustrated in Figure 6-34. For a velocity of 222.7m/s, a three peak profile occurs for a single impingement of jet, which clean and covers three times the PV surface area or more than 80% of the panel surface. The velocity profile improves in the middle range with an average velocity of 25 m/s. Based on the single jet profile, there is no significant influence on the top area of the panel, meaning that this type of cleaning system is insufficient. There is a linear movement of the triple jet system, upwards along the surface, because of the high amount of coverage of the PV panel surface. This type of cleaning system evenly distributes the impingement of jet.

# Chapter 7: Experimental investigation of the Jet Pumps integrated with the PV Panel System

## 7.1 Introduction

Following the design, construction and development of the jet pump and PV panel experimental rig described in Chapter 2, a thorough test was conducted to examine the performance of the system under different operating conditions. These conditions include the air pressure inlet control, the air flow velocity and the water temperature inside the vessel. The jet pump used in the experimental rig was fabricated using aluminium for stability. The installation and results of these experimental tests are presented and discussed in this Chapter.

At the end of this Chapter, a conclusion on the performance of the system under different operational conditions is summarised; it is compared with the results in an attempt to illustrate the discrepancy of the experiment.

It is worth mentioning that the system performance assessments by CFD simulation through theoretical modelling alone cannot be a substitute for real empirical testing. Hence, the experimental investigations remain an essential stage for evaluating the overall performance of the fluid's behaviour inside and outside of the jet pump.

## 7.2 Laboratory rig set up and testing procedure

An experimental rig was designed and constructed to conduct the experimental study on the production of the air and water vapour jet pump. Experimental characteristics of the jet pump were assessed in the laboratory of SRB Engineering. The single jet pump was powered by a single phase, 220 Volts, 50Hz supply. A stopwatch and a water tank with a pressure gauge scale fitting a drain valve as well as a bend were provided to measure the actual flow rate Pitot tube contacted with measurements and all the measurement’s details will be shown in later Sections. Other standard accessories include a pressure control valve, a piping system to control the pressure and a vacuum gauge with a water vessel.

The tested jet pump with a variable primary nozzle cross section is presented in Figure 7-1. The jet pump operation is typically characterised by two inlets (high pressure and low pressure) and one outlet of (mixed) water vapour. The high pressure motive (primary) air coming from an air compressor generator (g) is led through the primary nozzle with the aim of increasing it's kinetic energy and significantly decreasing its static pressure at the exit location. This low pressure draws the secondary fluid from the water vessel. Due to the large velocity difference between the motive and secondary fluids, a shear layer develops. The secondary fluid accelerates under normal operating conditions to a sonic velocity. In addition, due to the relatively high temperature of the secondary fluid, this would enhance the evaporation rates of the water under entrainment of the air driven by the jet. Hence, enriches air-water vapour quality for dust removal from the photovoltaic panel surface.

The following steps show the laboratory rig testing procedure:

- The air compressor is first switched on and after that solar simulator on the PV panel.
- The overhead water tank of the system is filled with water.
- The data logger, computer and micromanometer are switched on. The Pitot tube and thermocouples are checked to ensure correct readings.

- The high pressure motive valve is opened to allow air through the jet until the system stabilises.
- Pressure and mass flow rate are observed and read for the high pressure motive.
- The secondary fluid valve was opened to reduce the pressure in the water tank and increase the evaporation rates.
- The pressure of the secondary fluid is observed and read by the pressure gauge.
- Velocity and mass flow rate are observed and read for the water vapour outlet.
- The pressure of the secondary fluid is observed and read by the pressure gauge.
- The photovoltaic current-voltage power is observed and read before and after cleaning.

Regarding materials and instruments, to ensure and establish thorough experiments for the aforementioned attributes pertaining to PV, different instruments, methods, utensils and materials have been used and are shown in the next Sections. Figure 7.1 shows schematic of laboratory rig setup.

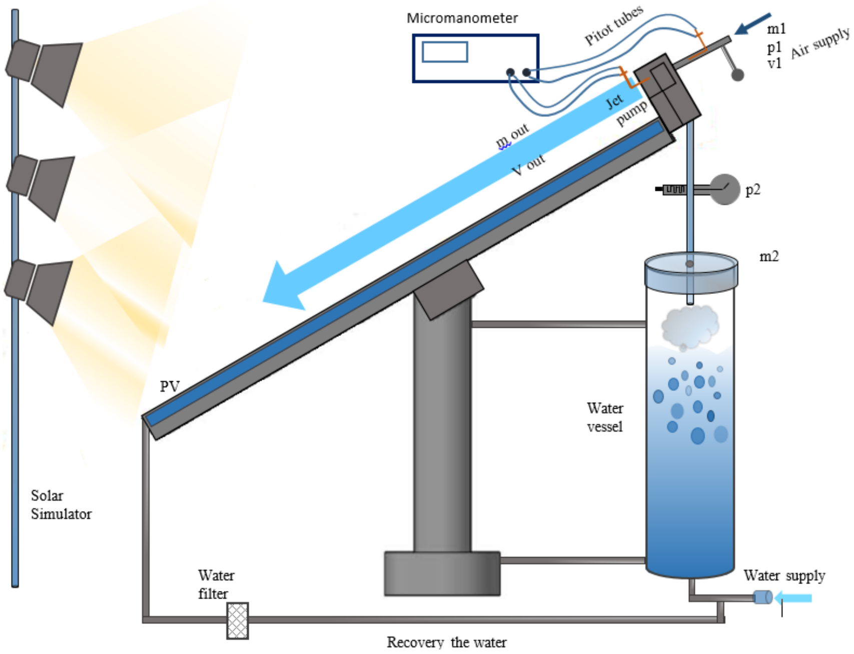


Figure 7-1. Schematic of laboratory rig setup.

## 7.3 Jet pump design and assembly

The jet pump was designed using a CFD program with various variables and conditions described in Chapter 6. This simulation attempted to obtain an accurate modelling of the nozzle of the jet pump assembly to achieve maximum performance. The three separate parts (nozzle, a suction chamber, and mixing throat and diffuser) were firstly drawn in AutoCAD. Then it was fabricated by aluminium inside the workshop of the engineering faculty. Figure 7-2 shows the jet pump dimensions and details of the design and geometry of the combined system.

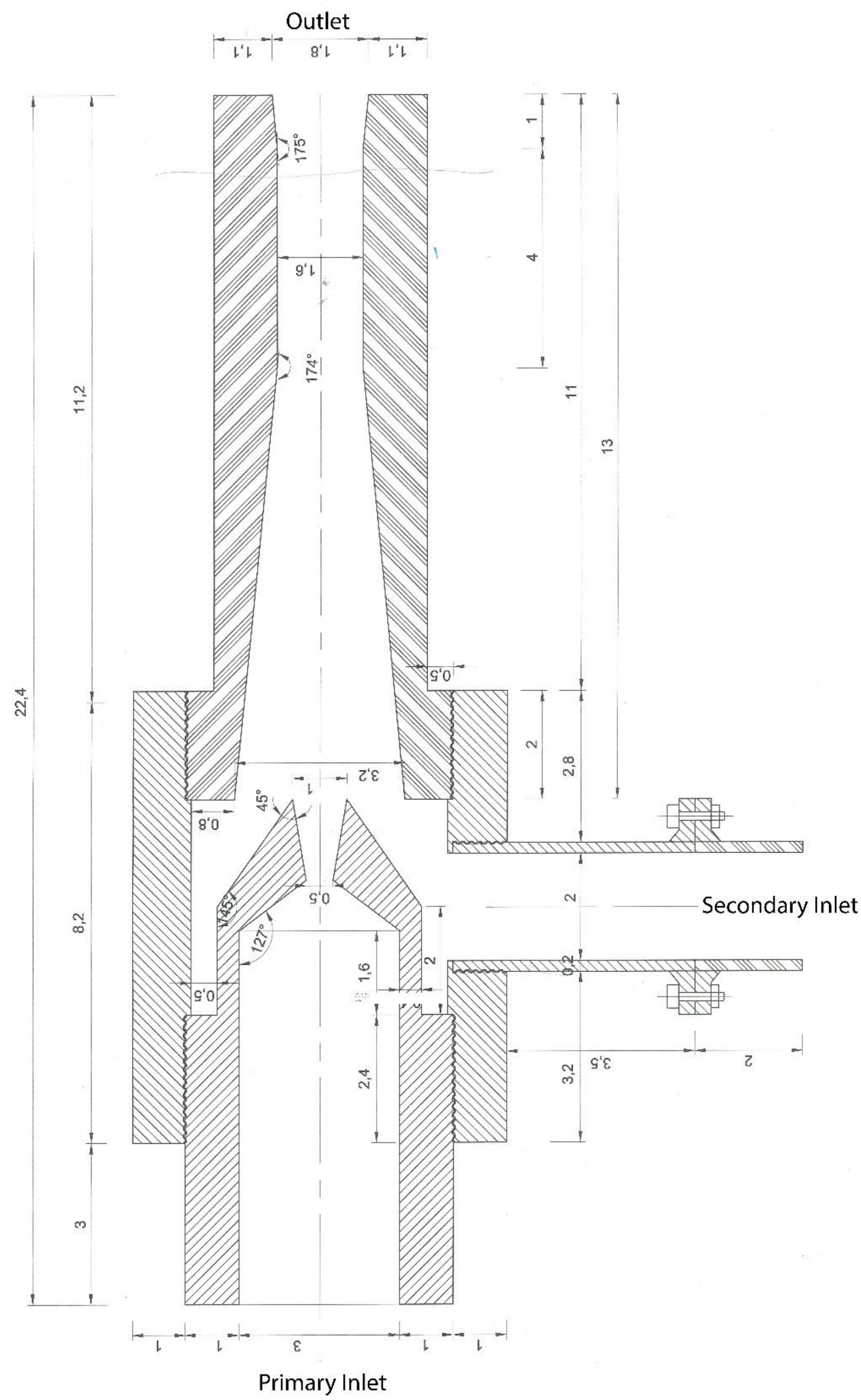


Figure 7-2: The jet pump details.

The first part of jet pump is the nozzle; the front part from 50mm aluminium, turned on a centre lathe into operating a flared inside diameters which allows expansion of pressurised cleaning fluid to achieve best spray pattern ,and threaded M40x1.5, this together with the rear part also machined with a mating M40x1.5mm thread allowed the nozzle to be changed easily and quickly, also considered the leak free in this process by using custom made ‘O’ rings one at the front of nozzle, and one to seal the rear part (air inlet) to end of the nozzle flange. Figure 7-3 shows three separate parts of the jet pump: nozzle, a suction chamber, and mixing throat and diffuser.

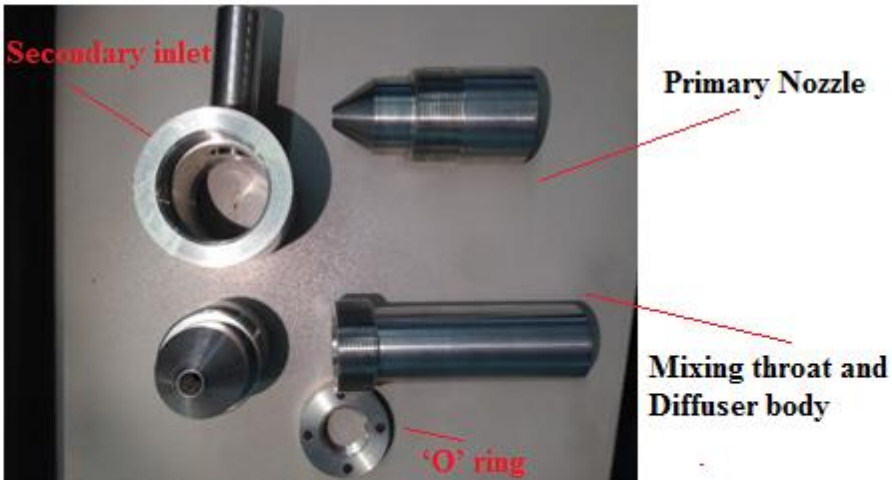


Figure 7-3: Three separate parts of the jet pump: nozzle, a suction chamber, and mixing throat and diffuser.

Table 7-1: Main prototype characteristics of the jet pump.

| Design parameters |
| --- |
| Part 1: Primary Nozzle |
| Part 2: Secondary Inlet |
| Part 3: Mixing throat and Diffuser |
| Aluminium Metal |
| Two ‘O’ Rings |
| Pressure1-25 bar |

However, the design for the jet impingement facility is similar to that designed in Chapter 2 and shown in Figure 2.1. The concept design of the air-water jet pump nozzle system is a single of the photovoltaic panel. The supersonic jet is supplied by high pressure air, which is contained in an air compressor and released through a 20 bar hose. Figure 7-4 shows the air compressor GX7FF used for this experiment.


Figure 7-4: Air compressor GX7FF (left) used for this experiment and Aircone® Model RVA501 Rotating Vane (right).

Also, a high pressure air compressor, which is equipped with a humidity elimination accessory at the outlet, charges the cylinder with roughly humidity-free air to 10 bar as the max pressure level, and all are kept at room temperature for the primary nozzle. The jet pump and the air compressor were connected by 1/4" BSPT male 7.9mm hose tail.

Moreover, a secondary flow comes from the water vessel after the water evaporates under the pressure inside the vessel. The flow rate of the steam entering the jet is provided through an orifice that is able to be controlled between experimental runs in order to adjust the vapour flow rate. Wind speed was measured to be 0.25m/s above the PV panel; this was read by the Aircone® Model RVA501 Rotating Vane with an accuracy ±1.0% of reading ±0.02m/s entirely based on digital technology. It can be regulated by digital technology. Figure 7-5 shows a photograph of experimental vapour jet impingement with a PV panel.

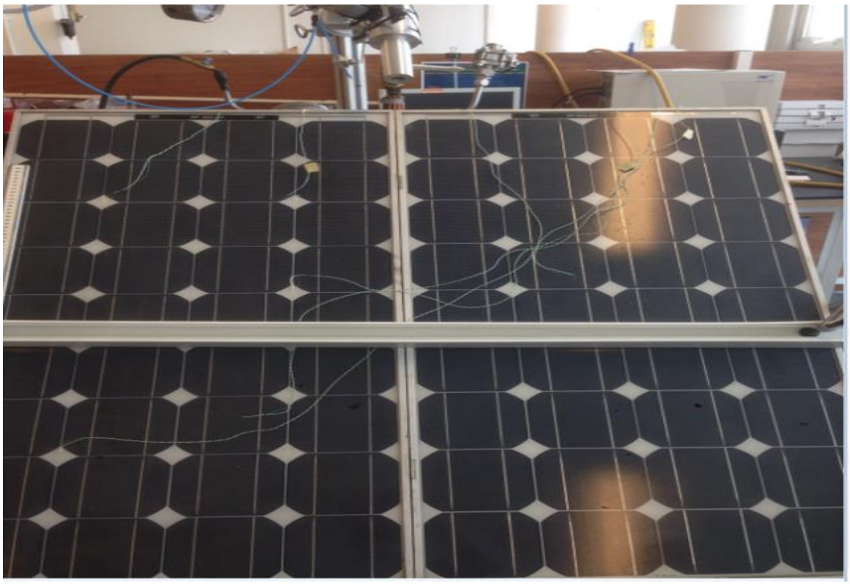

Figure 7-5: Photograph of experimental of vapour jet impingement with a PV panel.

## 7.4 Water tank assembly

For the water supply, a typical water vessel is made by a glass vessel under special conditions and by considering a cylinder design. The design and specifications allow the water vessel to be submerged in a vacuum without any damage to the walls of the water vessel. QVF® SUPRA-Line is shown in Figure 7-6. The flange ends-3” x 39.5” 75 mm made by glass tube vessel suitable for vacuum. It can also use a compatibility gasket in addition to (-1 bar). This vessel is capped at both ends with a conventional locking ring, eight nuts, and bolts with custom-made 8mm stainless steel 150mm flanges.

Figure 7-6: Basic water tank QVF® SUPRA-Line.

Figure 7-6 shows the schematic of the water vessel test setup. Lower flange: There are two holes (the housing drain valve and thermocouple) to measure the water temperature inside the vessel fit directly into. A type K thermocouple was used; it had a fixed process connection with a temperature range of -50 to +250 °C and an accuracy ±1.0 °C. The upper flange is shown in Figure 7-7. 25mm stainless steel outlet pipe with 105mm wall thickness of flanges to minimise vacuum loss during operational use, branching from that in one side.

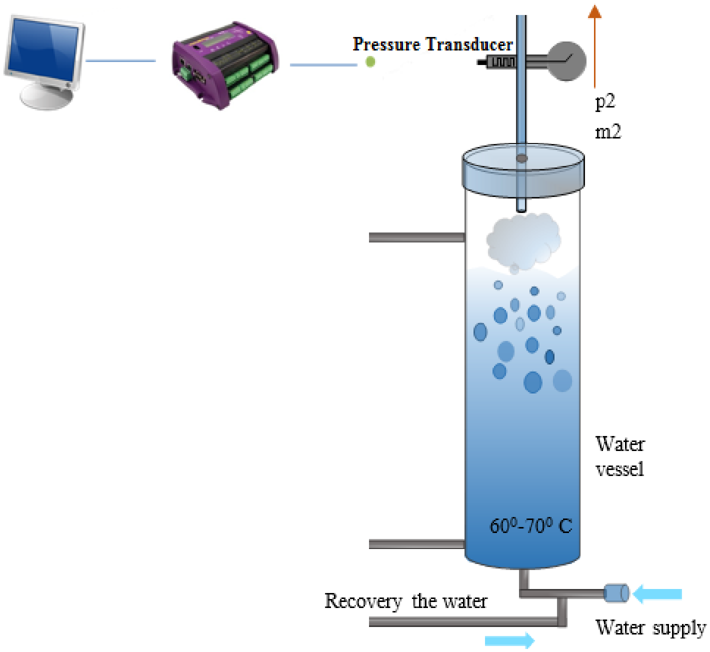


Figure 7-7: Schematic of the water vessel test setup.

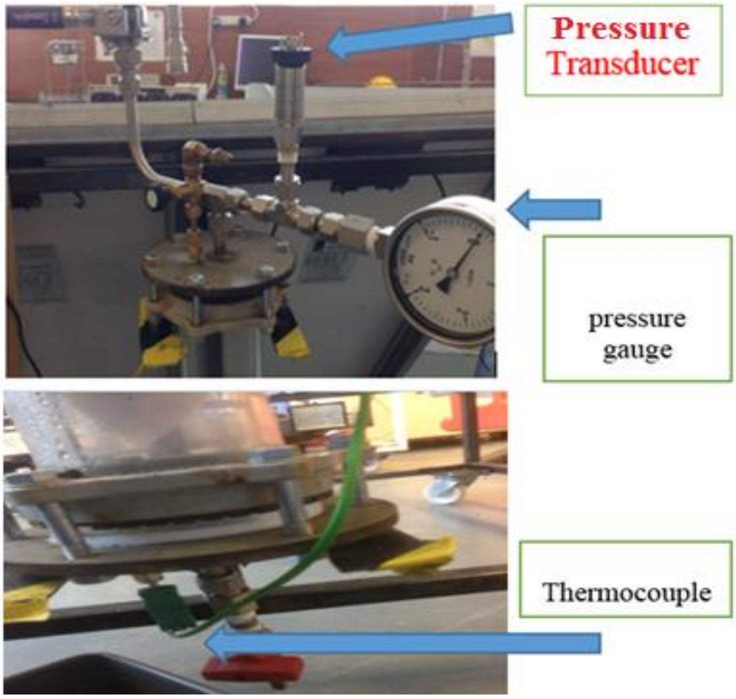


Figure 7-8: The upper and lower flanges of water tanks.

The pressure transducer is linked to a DT500 Data Taker which is, as already known, connected to a PC for data sorting. The pressure transducer is used to measure the inlet air pressure. In addition, estimations regarding the voltages and currents of the pressure transducer are conducted by employing a data logger (DT500 Data Taker). In this type of data logger, the transducer is connected to an inlet duct. The prime function of a data logger is to read the data with software.

Table 7-2: Transducer specification.

| |
|---|
| One piece stainless steel body |
| Multipurpose, high performance |
| Temperature compensated, strain gauge technology |
| +/-0.25%accuracy |
| -40 to +100/125 °C transmitter/ transducer range |
| 2x rated overpressure up to 250 mbar |

However, the other side of outlet pipe is a (-1 to 0 bar) atmospheric pressure gauge/manometer WIKA diameter 4"/100Mm connection 1/2" to show vacuum pressure close to the water tank. On the flange is a combined water filling loop and vacuum pump connection. This is made from a 12mm stainless steel tube and two ¼" turn vacuum suitable valves; this is meant to allow vacuum testing of the water tank and to see if the measured vacuum causes the water to boil at a different temperature. Figure 7-9 shows the vacuum pump connected to the top flange of the water tank for a vacuum test.


Figure 7-9: Vacuum pump connection with the top flange of the water tank for a vacuum test.

From the outlet pipe to the jet pump assembly is a reduced-length, large-diameter steam minimising 25mm ID hose with another ¼" turn ¾" valve. This allows pressure and flow conditions to be stabilised at the nozzle exit and develop in the water holding tank.

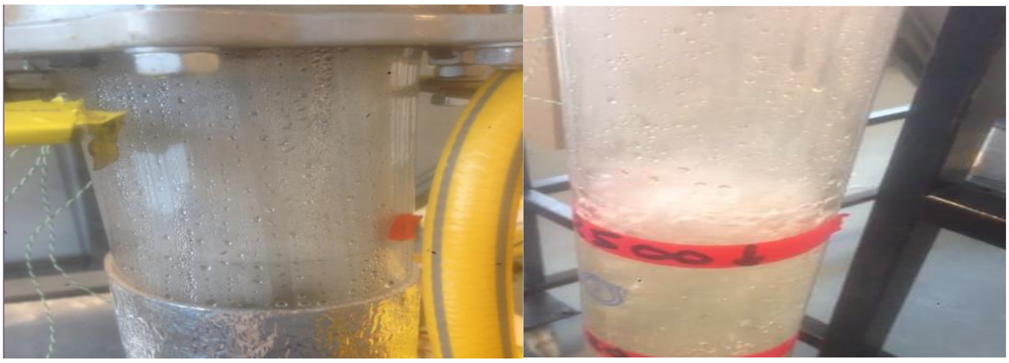

Figure 7-10: Water vaporization inside the water tank (left and right).

The objective is to move the water vapour from the water vessel and use this for cleaning as well as cooling the PV panel. After the process of cleaning and cooling, of the photovoltaic panel to vaporise cleaning fluid, the fluid is then made misty in the nozzle jet pump. The water evaporates at a pressure (0.2 – 0.5) bar with a temperature between 60 – 70$^{0}$C inside the tank. Figure 7-10 shows the vapour inside the water tank.

## 7.5 Pressure and flow measurements: micromanometer and pitot tube set up

The rig was fully instrumented to measure both the air flow and water vapour velocity along the dry and wet ducts. In this experiment, a micromanometer and a pitot tube are used for measurements of both the inlet flow and the outlet flow. Figure 7-11 shows a schematic of the FCO510 micromanometer integrated with a pitot tube.

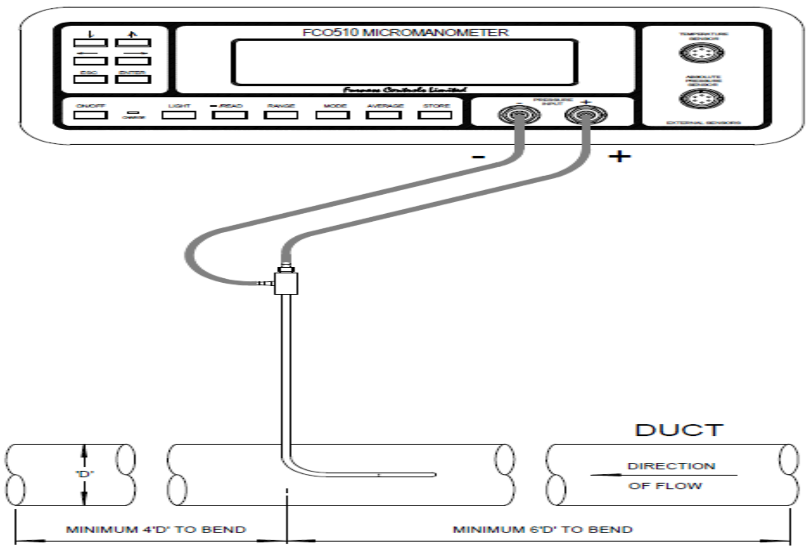


Figure 7-11: The FCO510 micromanometer integrated with a pitot tube.

The FCO510 micromanometer is an accurate differential pressure (D.P.) instrument that has two D.P. ranges, each with a resolution of 1:20000. It is a microprocessor-based instrument with a rich set of features, including 4½ digit main display with 15mm-high numeric characters for ease of viewing, with two smaller display windows to view auxiliary data simultaneously.

The parameters that have been measured include D.P., velocity, volumetric flow (or mass flow), flow calculations (based on either pitot tubes or laminar flow elements with corrections for temperature), pressure, viscosity and density.

Figure 7-12 illustrates that the simple Pitot tube is an L-shaped tube with two pressure docks set at the top of the tube assembly.

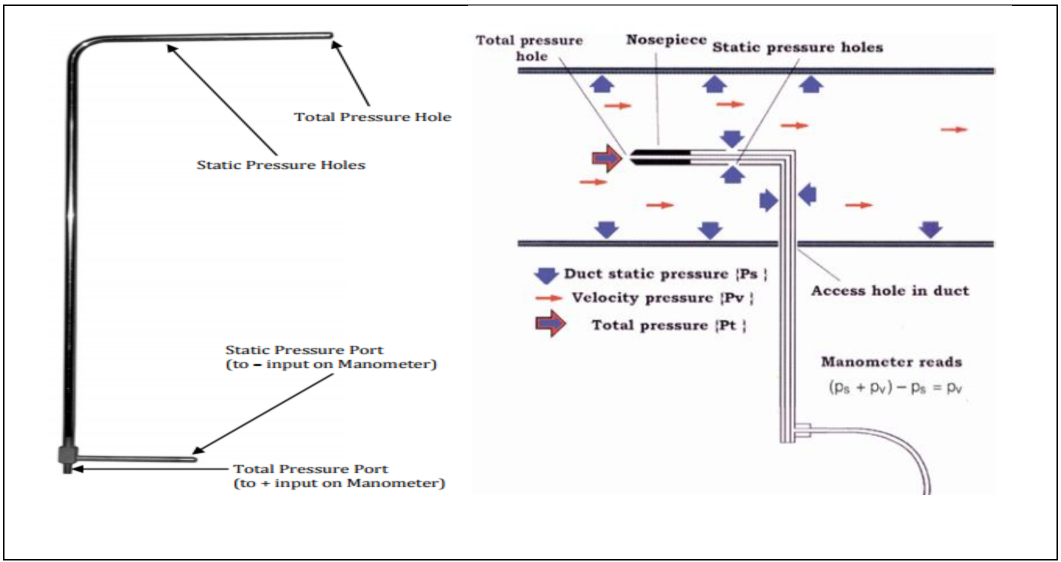


Figure 7-12: Simple pitot tube construction details (left) and measuring flow rates with a pitot tube (right).

The velocity head is estimated by extracting static pressure from the accumulated pressure. This can be presented as $P_v = P_t - P_s$. Standard equations help to translate the pressure related to velocity (m/s). After estimating the velocity and pressure, the rest of the formula can be employed for thee calculation of the velocity, following Klopfenstein Jr (1998).

$$V = 44.72136 \cdot K_{\text{pitot}} \cdot \Gamma_{\text{pitot}} \cdot \sqrt{\frac{h_{\text{kPa}}}{\rho}} \tag{7-1}$$

Where:

| | |
|---|---|
| V | air velocity (m/s) |
| $K_{Pitot}$ | Pitot tube constant |
| $\Gamma_{Pitot}$ | gas compression constant |
| $h_{kPa}$ | [total pressure−static pressure] (kPa) |
| $\rho$ | air density ($kg/m^3$) |

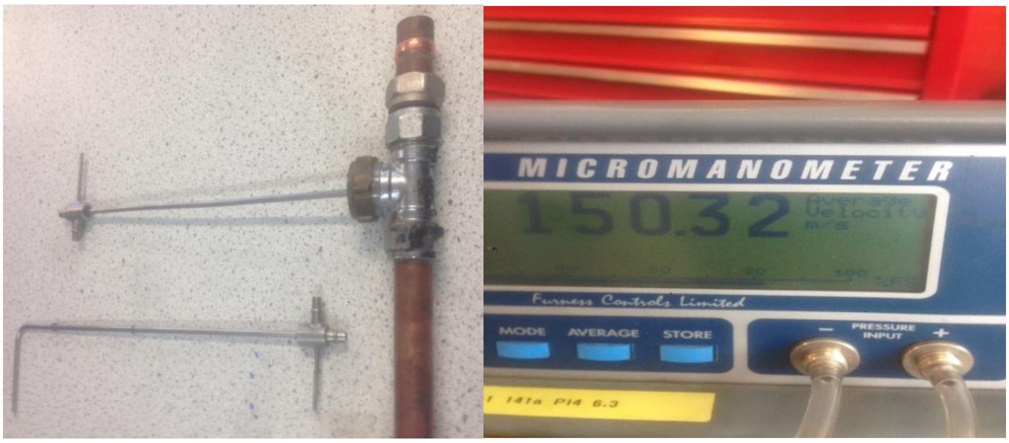


Figure 7-13: Micromanometer and pitot tube assembly in the lab.

## 7.6 Monitoring PC and data logger

A digital system, in the form of a PC, is used to connect (digitally) with other devices, such as the data logger. These are connected and configured to the devices, which are used for measurement, through specifying input data and frequency as per how statistical evidence would be collected. The data logger also allows monitoring of the performance and gathering the data in a more suitable format to allow graphical representation using computer software, such as Microsoft Excel. In this experiment, a data logger (Data Taker DT500) is used to collect and sort data.

## 7.7 PV panel assembly

The panel BP 275F, which has been employed, is depicted in Figure 7-14. The characteristics of these panels are presented in detail in Table 7-3. The IV characteristic curves of the panel figure 7-15. These data represent the performance of a typical BP 275F module as measured at their output terminals.

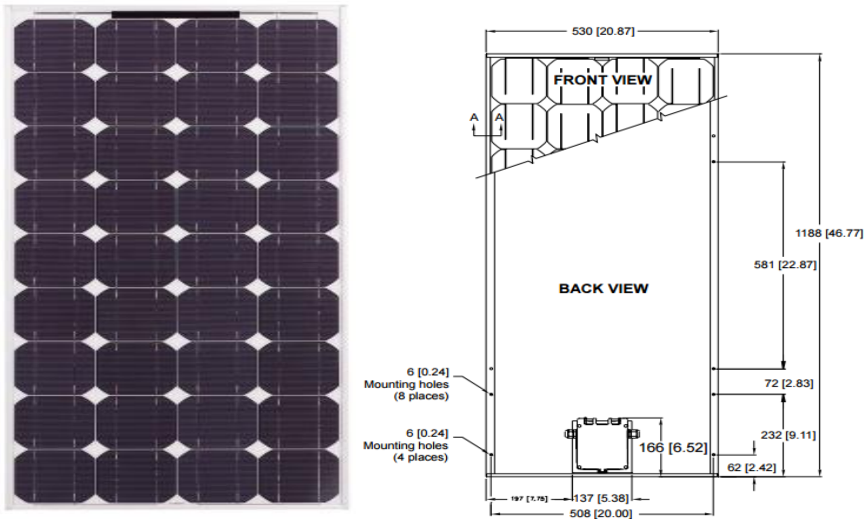


Figure 7-14: PV Panel BP Solar275F.

Table 7-3: PV Panel BP 275F module specifications.

| | |
|---|---|
| Type | BP Solar, BP 275F 75W |
| Cell | Monocrystalline silicon cells |
| No. of series connected cells | 36 |
| Size | 1188 x 530 x 44 mm |
| Weight | 7.5 Kg |
| Maximum Power ($P_{min}$) | 75 W |
| Maximum Power Voltage ($V_{mp}$) | 17 V |
| Maximum Power Current ($I_{mp}$) | 4.45 A |
| Open Circuit Voltage ($V_{oc}$) | 21.40 V |
| Short Circuit Current ($I_{sc}$) | 4.75 A |
| Minimum Power ($P_{min}$) | 70 W |
| Temperature Coefficient of $I_{sc}$ | (0.065±0.015)%/°C |
| Temperature Coefficient of $V_{oc}$ | –(80±10)mV/°C |
| Temperature Coefficient of Power | –(0.5±0.05)%/°C |
| Nominal Operating Cell Temperature | 47±2°C |
| Maximum System Voltage | 600 |

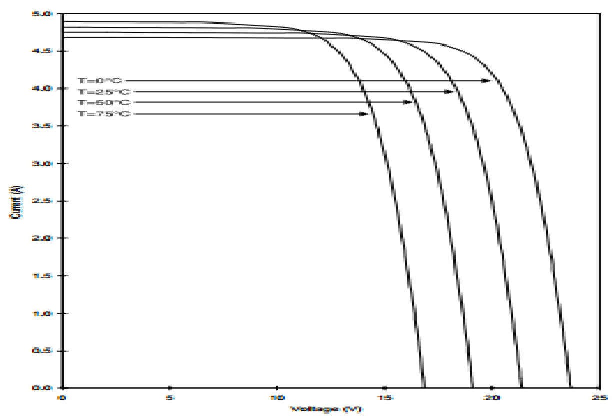


Figure 7-15: BP 275F I-V Curves.

The PV panel is fixed on a frame; that frame is fabricated from a 25mm stainless steel square hollow (box section) 25 x 25 x 1.6mm. The tubes are welded together with four wheels (one in each corner) to allow positioning in relation to the nozzle and solar simulator. Figure 7-16 shows the PV panel fixed on a frame.

Figure 7-16: The PV panel fixed on a frame.

In terms of the solar simulator, the simulator uses a number of metal halide lamps, which are used to give light to the photovoltaic panel. These types of devices are exploited for the production of artificial sunlight, which is used in various positions for different purposes, such as measuring irradiation levels.

However, the solar simulator was provided by 36.X 500w halogen lamps, which were held in a custom-made frame that was able to control the lamp intensity and tilt. Lamps were wired up in pairs (as shown in Figure7-17), which shows the solar simulator (left) with control sliders (right).


Figure 7-17: The solar simulator (left) with control sliders (right).

A pyranometer is used to measure the light intensity, points on the PV panel which is mapped out, to give an even spread of the lighting intensity with an accuracy of 5 – 10%.This particular device is employed to estimate the level of radiation on a global scale. Therefore, it can be said that it is used to measure the level of illumination, as can be seen in Figure 7-18, which shows a Pyrometer LP02 (left) and digital multimeter UT60A (right).

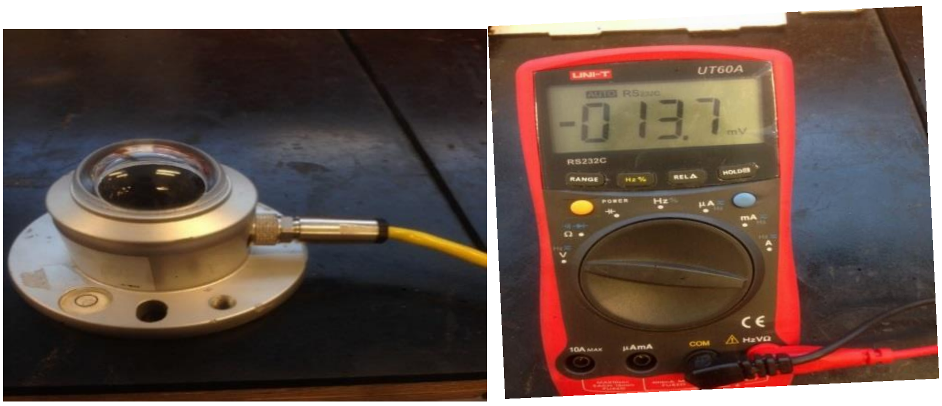


Figure 7-18: The Pyranometer LP02 (left) digital multimeter UT60A (right).

These devices have been specially designed to study the radiation on the panel, particularly on the surface of the panel. In addition, they can measure the radiation that is diffused from the surface. Therefore, the device (pyranometer) will be positioned on the solar panel to estimate radiation from the solar simulator.

Table 7-4: Specification of the Pyranometer LP02.

| DESCRIPTION | |
|---|---|
| Sensor type | Thermopile solar radiation sensor; ISO 9060 ‘Second Class’ compliant |
| Sensor range | $0W/m^2$ to $2000W/m^2$ |
| Spectral range | 305nm to 2800nm |
| Instrument compatibility | RNRG Symphonie loggers with Thermopile SCM (#6646) and Logger measurement range from $0W/m^2$ to $1500W/m^2$ |
| Calibration | Calibration sheet included with each sensor defines output in microvolts per Watt/square meter, traceable to World Radiometric Reference (WRR) calibration uncertainty <1.8% (k=2), as specified by Hukseflux. |
| Output signal range | -0.1 mV to +50 mV |
| Drift | Less than 1% per year |
| Operating temperature range | -40 °C to 80 °C (-40 °F to 176 °F) |
| Operating humidity range | 0 to 100% |

The device fits the criteria set by the ISO 9060, which defines parameters and criteria. In addition, it is also in accordance with standards set by the WMO Guide. It has been chosen because it performs better than silicon cells, which are in accordance with the parameters set by ISO 9060. Table 7-4 shows the description of pyranometer LP02.

To estimate the output voltage and the currents, a multimeter is used. All the devices are coupled with the data logger, which automatically measures the data and sorts to a computer. Figure 7-19. Shows the schematic of power test of PV panel.

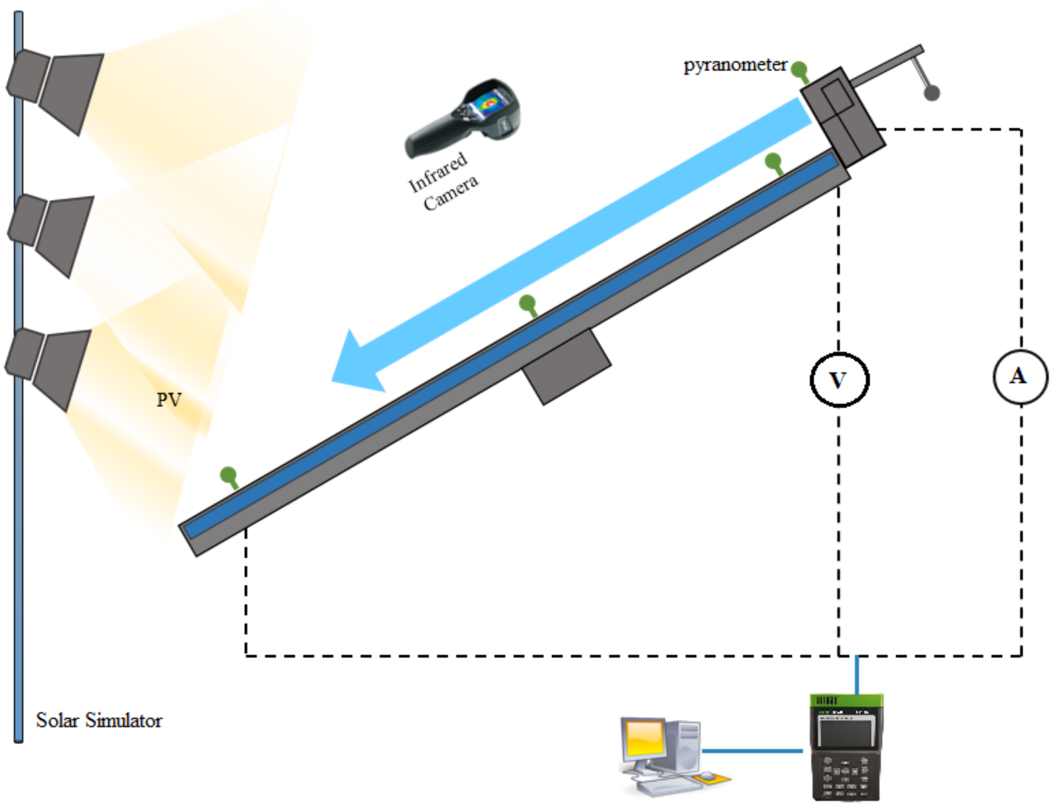


Figure 7-19: The schematic of power test of PV panel.

Moreover, for the instrument to measure radiated and transmitted solar power at an installation to determine the optimum positioning and alignment of solar panels. The ISM490 Solar Power Meter or Solar Module Analyser is shown in Figure 7-20.


Figure 7-20: ISM490 Solar Module Analyser.

## 7.8 The test procedure for the rig

However, the test allows monitoring of the influence of temperature and the solar radiation level on the operation of the PV panel by comparing the characteristic curves. After installing the last measuring device on the board, the user must turn on the solar simulator and read the performance of the PV panel before dust accumulation. After that, the user must place about 250 grams of the dust equally around the board on a glass plate tilted at 45°. Figure 7-21 shows the PV panel with accumulated dust. The user must then read the performance again for the current versus voltage (I-V) and power versus voltage (P-V) curves. The user should clean the surface with the jet pump under specific speeds and reread the board, comparing the results.

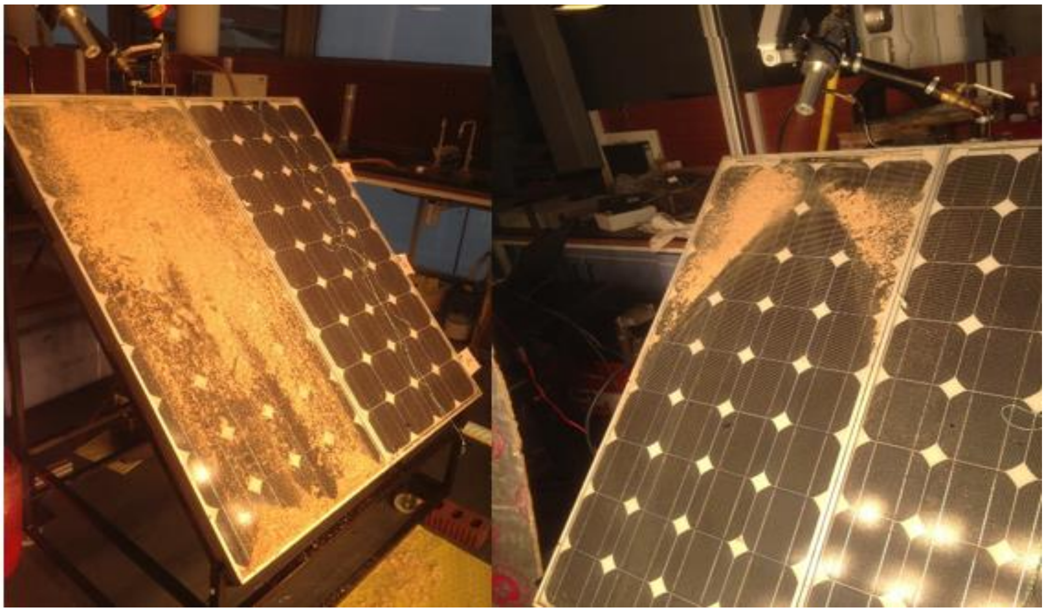

Figure 7-21: Experimental test PV panel with dust (left) and after jet pump cleaning (right).

It should be mentioned that this high pressure compressed air system was installed to produce 10 bar as a maximum pressure, which may be a hazard under lab conditions.

The pressure is controlled by the internal pressure gauge to manage the airflow inside the air supplier's pip, which feeds the jet as a primary inlet to avoid overpressure. The external gauge has been installed to ensure proper and continuous airflow.

An emergency shutdown button is located on the rig where it can be easily reached to shut it down. There is also a safety valve on the compressor and vessel to shut it down if the temperature at the outlet of the compressor element is too high and to protect the air outlet system if the outlet pressure exceeds the opening pressure of the valve. In the case of an emergency, the button is pressed to shut down the electromagnet's power supply. Figure 7-22 shows the safety button on the compressor (left) and the electromagnet's power supply (right)


Figure 7-22: Safety button on the compressor (left) and the electromagnet's power supply (right)

## 7.9 Comparing the experimental jet pump output with the CFD results

The experimental test has been found to be the actual result compared to the results of the CFD in the study of the jet pump system, which was shown in Chapter 5. In this thesis, the jet pump model was used with 5mm as the diameter of the nozzle throat.

When $d_1$=5 mm, $\dot{m}_{out}$ and $v_{out}$ might realise comparatively high values; the fluid's velocity, however, might be kept at a value that is safe for a jet pump.

The values of the total mass flow rate ($\dot{m}_{out}$) and the velocity outlet from the jet pump ($v_{out}$) are able to be realised as the clear value. The further rustle of simulation, like the entrainment ratio (ER), could be resolved regarding the results of the experiment:

ER=$\dot{m}_2/\dot{m}_1$. Figure 7-24 display the relationship between the primary pressure inlet P (bar) with all mass flow, the entrainment ratio and Figure 7-25 shows the velocity outlet from the jet pump $v_{out}$.

However, the following Section shows the previous results of the CFD modelling and the experimental testing compared to what has been done in similar operating conditions. These results are compared to show how accurate the experimental testing was. The accuracy for each case was calculated using:

$$\text{Discrepancy} = \frac{Xexp - Xcfd}{Xexp} \times 100 \qquad (7\text{-}2)$$

### 7.9.1 The experiment jet pump result

In Table 7-5 shows the mass flow rates and the entrainment ratio the velocity of the outlet with variation in the primary pressure inlet.

Table 7-5: The Experiment Jet pump output results.

| $P_{inlet}$ (bar ) | $\dot{m}_1$ (kg/s) | $\dot{m}_2$ (kg/s) | $\dot{m}_{out}$ (kg/s) | $v_{out}$ (m/s) | ER |
|---|---|---|---|---|---|
| 0.5 | 0.006945 | 0.006955 | 0.0139 | 47 | 1.001442 |
| 1 | 0.0098737 | 0.0099263 | 0.0198 | 68 | 1.005319 |
| 1.5 | 0.011298 | 0.011402 | 0.0227 | 76.5 | 1.00921 |
| 2 | 0.0136604 | 0.0138396 | 0.0275 | 97.8 | 1.013116 |
| 2.5 | 0.0153691 | 0.0156309 | 0.031 | 107 | 1.017038 |
| 3 | 0.0163782 | 0.0167218 | 0.0331 | 113.8 | 1.020974 |
| 3.5 | 0.0180253 | 0.0184747 | 0.0365 | 127.6 | 1.024927 |
| 4 | 0.0196511 | 0.0202189 | 0.03987 | 139.5 | 1.028894 |
| 4.5 | 0.0204144 | 0.0210856 | 0.0415 | 148.2 | 1.032878 |
| 5 | 0.0207671 | 0.0215329 | 0.0423 | 154.63 | 1.036877 |
| 5.5 | 0.0224902 | 0.0234098 | 0.0459 | 163.4 | 1.040891 |
| 6 | 0.0243041 | 0.0253959 | 0.0497 | 171.7 | 1.044922 |

However, for mass flow rates, mass inlet1, mass inlet2 and the total mass flow rate $\dot{m}_{out}$ (kg/s) in addition to the entrainment ration for the primary pressure inlet P (bar) form 0.5 bar to 6 bar for the same jet pump, in that case the mass flow rates are influenced by variation pressure, that an increase in pressure results in a rise in the total mass flow rate as well as the entrainment ratio for all tests with kept the same trend line. Figure 7-23 has shown the mass flow rates and the entrainment ratio with variation in the primary pressure inlet. Also, the velocity outlet (m/s) with variation in the primary pressure inlet as shown in Figure 7-24.

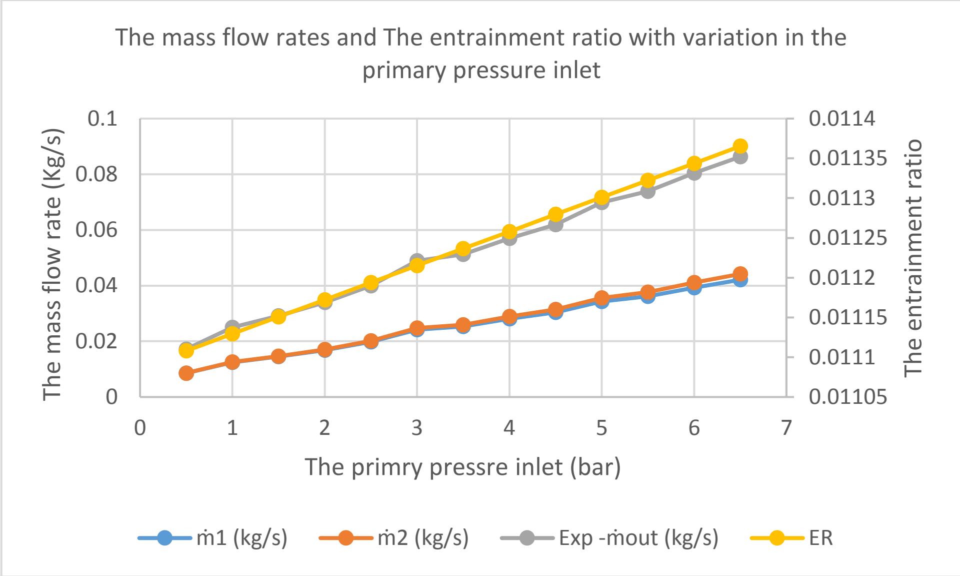


Figure 7-23: The mass flow rates and the entrainment ratio with variation in the primary pressure inlet.

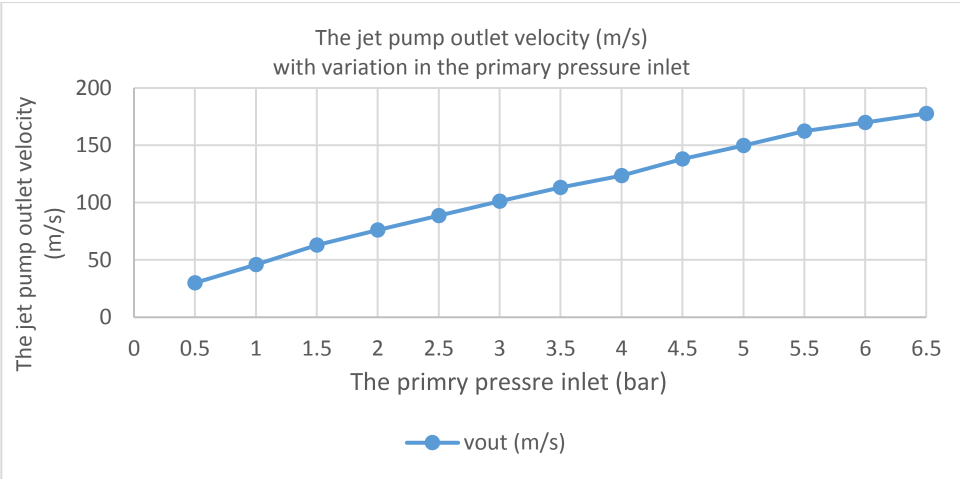


Figure 7-24: The jet pump outlet velocity (m/s) with variation in the primary pressure inlet.

### 7.9.2 Validation of CFD and experimental results for outlet mass flow rate for the jet pump

Figure 7-25 illustrates the CFD plot in comparison with the experimental plot of the total mass flow rate $\dot{m}_{out}$ (kg/s) for the primary pressure inlet P (bar) from 0.5 bar to 6 bar for the same jet pump. In that case, the mass flow was influenced by a variation in pressure. A pressure increase results in a rise in the total mass flow rate for all tests, which kept the same trend line.

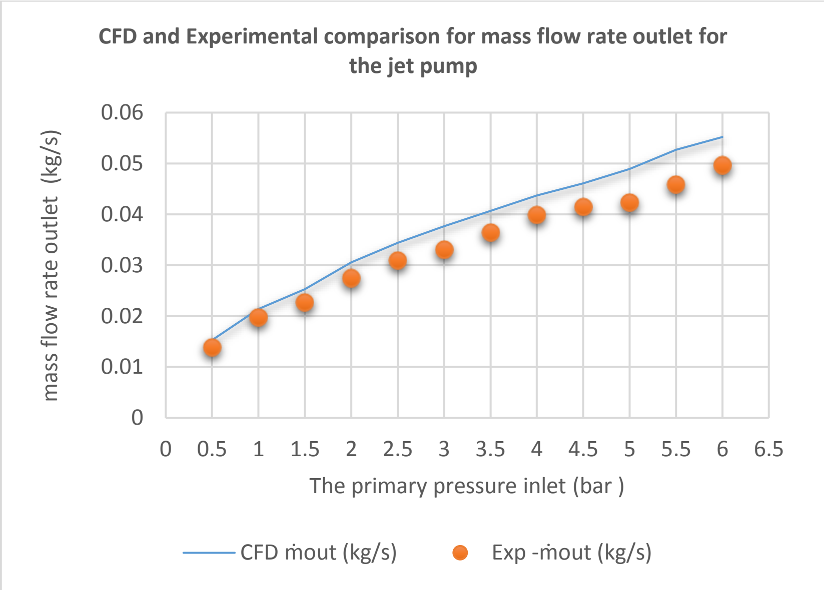


Figure 7-25: CFD and experimental results comparison for mass flow rate outlet for the jet pump.

The discrepancy has been calculated on a pressure-by-pressure basis. The discrepancy is often less than 15% at any point of the test. The accuracy has comparatively less at the start of the operation; before the pressure crosses the 2.5 bar limit, the discrepancy is often equal to 11%.

### 7.9.3 Validation of CFD and experimental results for the velocity outlet from the jet pump

Similarly, Figure 7-26 illustrates the CFD plot in comparison with the experimental plot of the velocity outlet from the jet pump for the primary pressure inlet P (bar) from 0.5 bar to 6 bar for the same jet pump. In that case, the velocity outlet was influenced by a variation in pressure. An increase in pressure leads to a rise in the velocity outlet for all tests, which kept the same direction as the trend line.

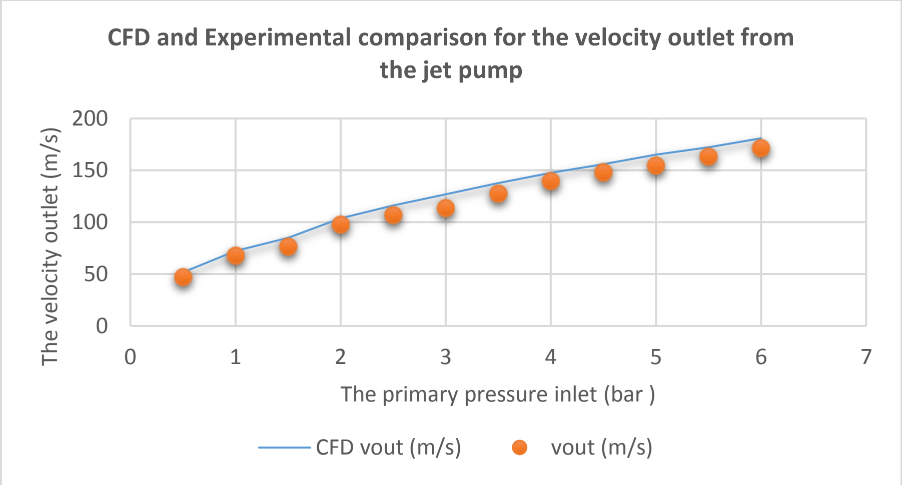


Figure 7-26: CFD and experimental results comparison for the velocity outlet from the jet pump.

The discrepancy has been calculated on a pressure-by-pressure basis, which is not more than 11.5% at any point in the tests. The discrepancy is slightly stable; after 3.5 bar, the discrepancy is often equal to 5.5%.

### 7.9.4 Validation of CFD and experimental result for the entrainment ratio

Finally, the ER influenced by pressure variation, which is an increase on the pressure results, leads to a slight increase on the ER for all tests, which kept the same direction as the trend line. Figure7-27 illustrated the CFD plot in comparison with the experimental plot of the ER of the jet pump for the primary pressure inlet P (bar) from 0.5 bar to 6 bar for the same jet pump.

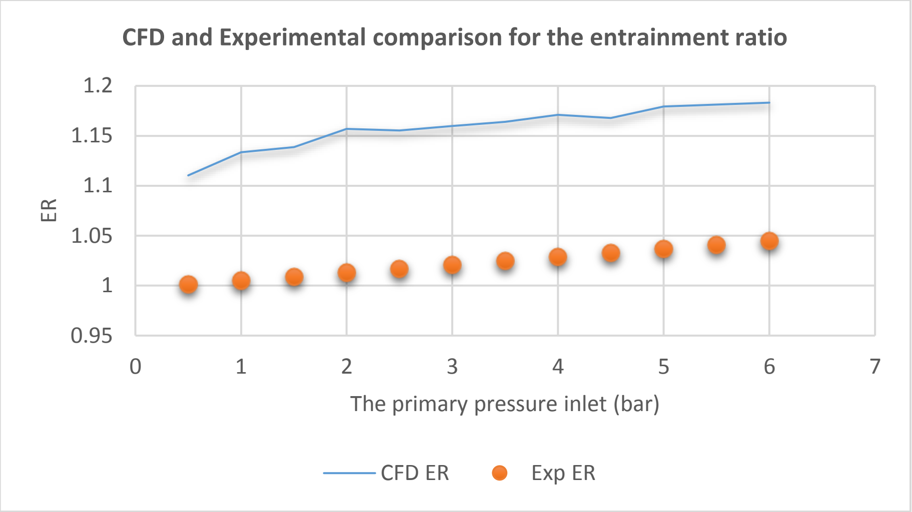


Figure 7-27: CFD and experimental results comparison for the entrainment ratio.

The result of the discrepancy shows that the trend line remained in the same direction. The percentage on discrepancy for a 0.5 bar pressure value reached no less than 8.5%; after this, the pressure started from 1 bar and remained stable, fluctuating no more than 12%.

## 7.10 Effect of dust on the output of power of a PV module

After measuring the light intensity level on the surface of the board, the power and voltage readings could be obtained for many load impedances. Primarily, PV characteristic curves of the panel for particular operating conditions relied on an ideal case, dust effect and after cleaning. Next to that the Solar Simulator read the variable performance of panel for all these situations. Figure 7-28 shows the (P-V) and (I-V) curves through testing a PV panel. A sample of the power and voltage measurements worksheet takes into consideration the various operating parameters given in Appendix C.

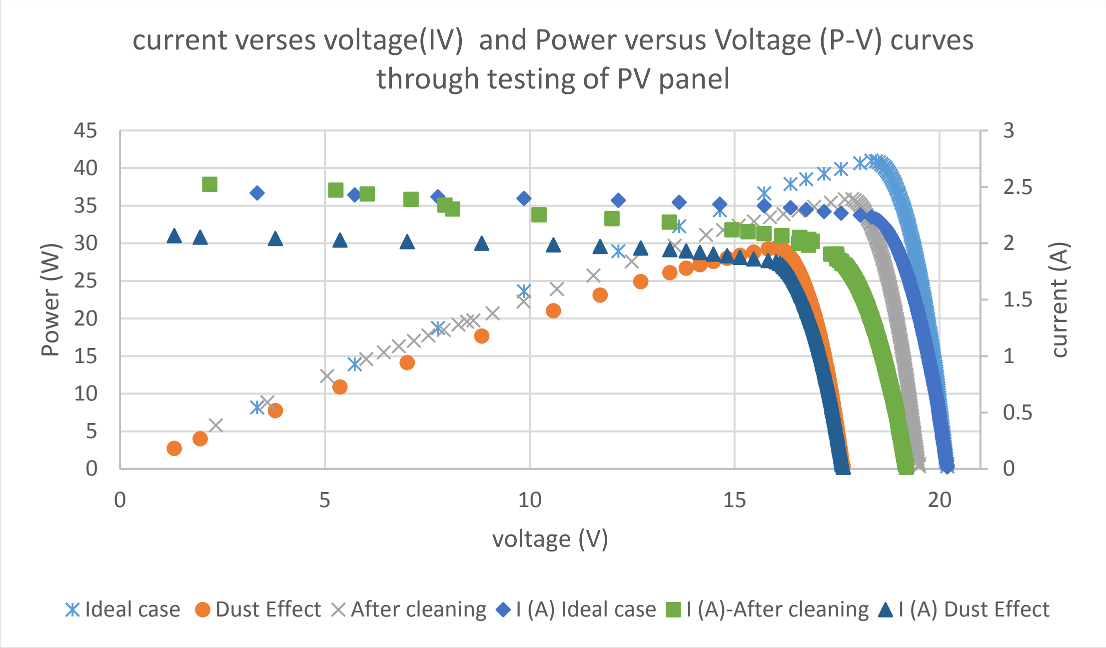


Figure 7-28: The Power versus Voltage (P-V) curves through testing of PV panel.

After analysing the experimental data, dust accumulation on a glass plate tilted at 45° was found, and it reduced the transmittance and power compared with the ideal case. This reduction happened because of the effect of the dust on the panel, which reduced the atmospheric radiation balance.

The voltage decreased from 20 V to 17.5 V, and the power decreased from 40 W to 26 W, which is about a 30% drop. The percentage of decreased energy depends on the amount of dust accumulation on the surface and the kind of dust particles.

However, after cleaning the PV surface by using the jet pump under specific conditions as the velocity of water vapour and the highest of the jet pump on the PV surface. Following of the recommendation of CFD analysis in Chapter 6 to obtain the excellent results to improve the performance of panel, with take a consideration of library condition and safety procedure. It provides a comparison of the different tests of velocities on the panel surface, which would power the linear movement of the jet for the efficient use of the surface of the PV. In Figure 7-28, the P-V curves (through testing of the PV panel) show the effect of cleaning on PV efficiency. By increasing the power and voltage of a panel in short time, the middle curve shows a change in the performance regarding the dust curve, which increased the power from 26W to about 35W after using one jet.

In addition, for a more accurate result, it used the InFrared Camera Fluke® TiS10 (9Hz) supplied with smartView® software to show the effect of the jet pump cleaning and cooling on the PV panel's surface. Figure 7-29 shows the photos of an Infrared Camera Fluke for a PV panel's surface before using the jet for cleaning and cooling (left), using one air jet (right) and using one air-water vapour jet pump.

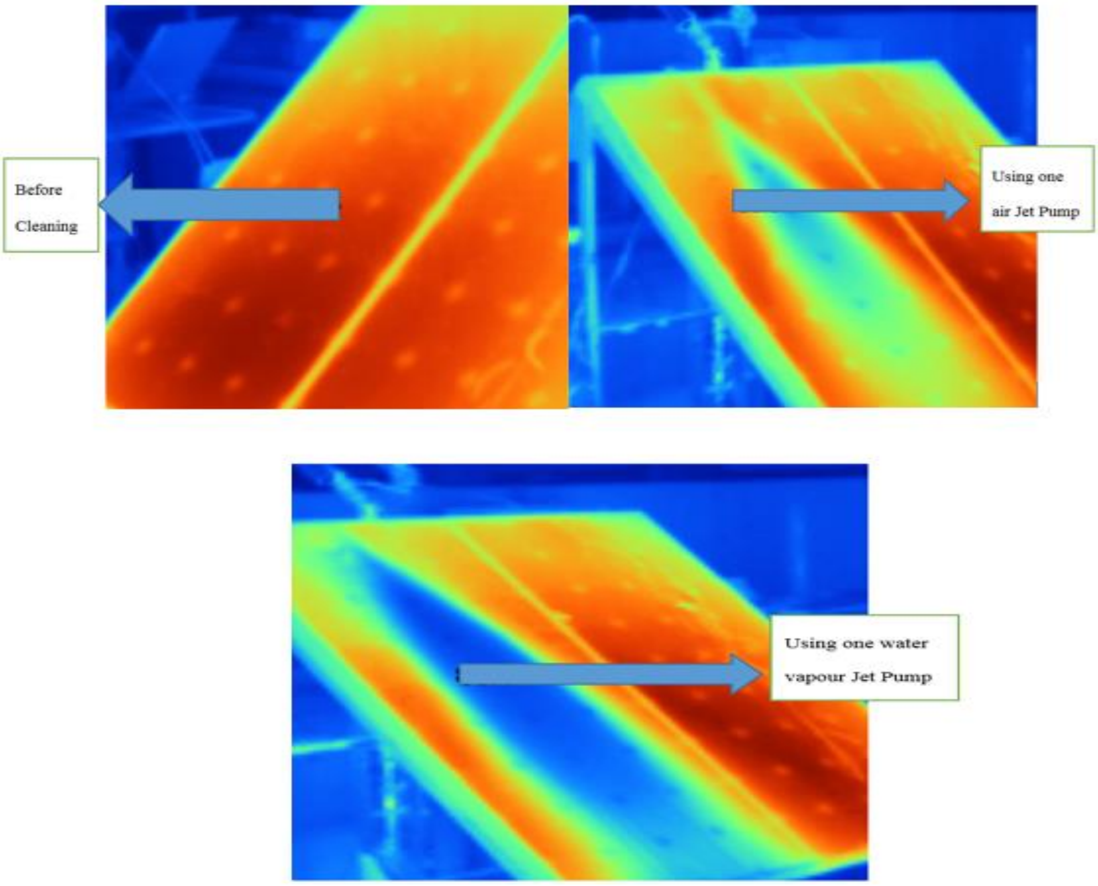


Figure 7-29: The photos by the Infrared Camera Fluke for a PV panel's surface before using the jet for cleaning and cooling (left), using one air jet (right) and using one air-water vapour jet pump.

Figure 7-29 shows a clear difference between the PV surface before and after using the air jet. Before using the air-water vapour jet pump, the left figure shows the red colour covering the board which covered by some dust. After that, the air jet pump cleaner was used, taking into consideration the optimum design in Chapter 5. As seen in Figure A-15 in Appendix A. The air-water vapour jet pump was the most effective option, resulting in the most blue on the panel. Comparison of the Figure 6-22 using one jet pump with the contour velocity of the impingement of jet on the surface of the PV case C-2 in Chapter 6 reveals insignificant differences in the fan-shape which enhances and validates the result in Chapter 6.

It is noteworthy that data recording has to be done as fast as possible because the solar source could heat up the PV panel, increasing the uncertainty in measuring the data. Additionally, to protect the surface of PV panel form any burning cells.

# Chapter 8: Conclusions and Future Work

## 8.1 Conclusions

This Chapter summarises the research done in this thesis, discusses its limitations and presents some recommendations for future work.

The use of renewable energy technologies is increasing worldwide. With abundant active research underway, especially in the area of solar energy, the performance of these technologies is predicted to advance considerably, supporting an increase in both their use and the amount of industry investment.

On the other hand, sustainable energy technologies are associated with some challenges and limitations. Their main weakness is periodic stopping, which disincentives their development in the energy industry.

In this work, a review was conducted of previous research on photovoltaic (PV) panels and jet pump systems. The review focused on the environmental factors affecting PV system performance, especially those related to weather conditions, such as dust, temperature and the sun’s position. Self-cleaning technologies can solve the issue of dust accumulation on PV panels which reduce the performance and energy output, addressing this major obstacle to the widespread adoption of solar energy. The literature review also identified the best methods for reducing waste energy.

As explained in Section 1.2, the major objective of this research was to design and construct a jet pump cleaning system that uses air-water vapour for the purposes of dust removal and cooling of PV panels in dusty, hot areas, such as Gulf region. The performance of the designed jet pump system was investigated through computational fluid dynamics (CFD) analysis, which enabled an assessment of the air-water vapour flow from the jet pump across the surface of the PV panels; testing was then performed in the laboratory to validate those results.

The jet pump design was created by modelling the governing equations of fluid dynamics, as discussed in Section 3.6. Section 5.6 mainly focused on selecting the most accurate model of the jet pump design to be imported into the CFD simulation in order to calculate the jet pump's effect on the PV panel and determine the most reasonable geometry for the system. The jet pump was then placed in the most successful simulated arrangement relative to the PV panel surface, and the number of jets and corresponding velocity changes were graphically shown in Section 6.5.2.

In summary, this thesis designed a jet pump system, performed experiments with a real jet pump apparatus (described in Section 7.8) and validated the CFD simulation results by comparison with the experimental results (discussed in Section 7.9).

## 8.2 Contribution

This study contributes to the body of knowledge about renewable energy technologies with a design for a jet pump system for both the cleaning and cooling of PV panel systems. By managing the velocity magnitude and mass flow rate of the water vapour, the quantity of water needed can be reduced to increase the efficiency of this system. This study has also presented a method for creating a CFD model for a jet pump design. A model dimension was defined for analysing a prototype with a simple FLUENT set-up with a jet pump integrated with a PV panel system. The details were given for the CFD methods adopted to simulate water vapour so that the jet pump could recognise impingement on the surface of the PV panels. Different velocities of the linear jet movement were tested and compared to ensure full coverage of the surface of the PV panels. Methods were also presented for validation and analysis of the CFD model based on comparison with the experimental data.

## 8.3 Future Work

Due to the limitations of this research, experimental results could not be obtained for more testing of the design. Further research should focus on improving the performance of the jet pump with the PV system. The PV panels and the jet pump were analysed under theoretically ideal conditions. This type of simplification decreases the mesh size of the CFD grid, reducing the complexity of the calculation and therefore the running time as well. Future work may initially concentrate on increasing the complexity of the CFD model for it to fully account for the effects on the PV panels of the mass transfer from the pressure inlet to the jet pump output of the system. Additionally, other parameters of the design, such as the nozzle diameter, should be considered and tested at various conditions.

Research work could also be focused on other kinds of jets like air and water, or adopts a deployable scissor-rod structure to perform a linear mechanical movement and analysis the load and control the movement.

Also, automated valves could be used for the suction line of the jet pump, to ensure the release of water vapour in stages. First, the jet pump will use air jet alone to blow off the dust, and when the primary air flow is stabilized, the suction valves will be opened to allow water into the suction chamber for mist production. Following the cleaning process, the water valve will be closed and allow drying of the PV panels using air jet alone to avoid the formation of dust cementation on the wet surface. The cleaning process could also be initiated by the temperature of the cooling water, to ensure that the extracted heat is dissipated immediately, through the jet pump to enable effective PV cooling as well as PV cleaning.

# References


ABD-ELHADY, M., ZAYED, S. & RINDT, C. Removal of dust particles from the surface of solar cells and solar collectors using surfactants. Proceedings of the Eurotherm international conference on heat exchanger fouling and cleaning IX, Crete, Greece, 2011. 5-10.

ABDULATEEF, J., SOPIAN, K., ALGHOUL, M. & SULAIMAN, M. 2009. Review on solar-driven ejector refrigeration technologies. *Renewable and Sustainable Energy Reviews,* 13**,** 1338-1349.

ADDY, A. & CHOW, W. 1964a. Interaction between primary and secondary streams of supersonic ejector systems and their performance characteristics. *AIAA journal,* 2**,** 686-695.

ADDY, A. & CHOW, W. 1964b. On the starting characteristics of supersonic ejector systems. *Journal of Basic Engineering,* 86**,** 861-868.

ALLERY, C., GUERIN, S., HAMDOUNI, A. & SAKOUT, A. 2004. Experimental and numerical POD study of the Coanda effect used to reduce self-sustained tones. *Mechanics Research Communications,* 31**,** 105-120.

ANDERSON, M., GRANDY, A., HASTIE, J., SWEEZEY, A., RANKY, R., MAVROIDIS, C. & MARKOPOULOS, Y. P. 2010. ROBOTIC DEVICE FOR CLEANING PHOTOVOLTAIC PANEL ARRAYS.

AOYOMA, M. & MASUDA, S. Characteristics of electric dust collector based on electric curtain. Proceedings of the General Conference of the Institute of Electronic Engineers in Japan, 1971.

ATTEN, P., PANG, H. L. & REBOUD, J.-L. 2009. Study of dust removal by standing-wave electric curtain for application to solar cells on mars. *Industry Applications, IEEE Transactions on,* 45**,** 75-86.

BARTOSIEWICZ, Y., AIDOUN, Z., DESEVAUX, P. & MERCADIER, Y. 2005. Numerical and experimental investigations on supersonic ejectors. *International Journal of Heat and Fluid Flow,* 26**,** 56-70.

BARTOSIEWICZ, Y., AIDOUN, Z. & MERCADIER, Y. 2006. Numerical assessment of ejector operation for refrigeration applications based on CFD. *Applied Thermal Engineering,* 26**,** 604-612.

BIRIS, A., SAINI, D., SRIRAMA, P., MAZUMDER, M., SIMS, R., CALLE, C. & BUHLER, C. Electrodynamic removal of contaminant particles and its applications. Industry Applications Conference, 2004. 39th IAS Annual Meeting. Conference Record of the 2004 IEEE, 2004. IEEE, 1283-1286.

BLANCO, M. I. 2009. The economics of wind energy. *Renewable and Sustainable Energy Reviews,* 13**,** 1372-1382.

BOCK, J. P., ROBINSON, J., SHARMA, R., ZHANG, J. & MAZUMDER, K. An efficient power management approach for self-cleaning solar panels with integrated electrodynamic screens. Proc. ESA Annual Meeting on Electrostatics, 2008.

BOLLINGER, J. 2007. *APPLICATIONS OF SOLAR ENERGY TO POWER STAND-ALONE AREA AND STREET LIGHTING.* MASTER OF SCIENCE IN ELECTRICAL ENGINEERING, UNIVERSITY OF MISSOURI-ROLLA.

BONNINGTON, S. T., KING, A. L. & HEMMINGS, J. 1976. *Jet pumps and ejectors: A state of the art review and bibliography*, BHRA Fluid Engineering.

CALLE, C., MCFALL, J., BUHLER, C., SNYDER, S., ARENS, E., CHEN, A., RITZ, M., CLEMENTS, J., FORTIER, C. & TRIGWELL, S. Dust particle removal by electrostatic and dielectrophoretic forces with applications to NASA exploration missions. Proceedings of the electrostatics society of America Annual meeting, Minneapolis, 2008. 17-19.

CHAIWONGSA, P. & WONGWISES, S. 2008. Experimental study on R-134a refrigeration system using a two-phase ejector as an expansion device. *Applied Thermal Engineering,* 28**,** 467-477.

CHEN, X., OMER, S., WORALL, M. & RIFFAT, S. 2013. Recent developments in ejector refrigeration technologies. *Renewable and Sustainable Energy Reviews,* 19**,** 629-651.

CHOU, S., YANG, P. & YAP, C. 2001. Maximum mass flow ratio due to secondary flow choking in an ejector refrigeration system. *International journal of refrigeration,* 24**,** 486-499.

CHUNNANOND, K. & APHORNRATANA, S. 2004. Ejectors: applications in refrigeration technology. *Renewable and sustainable energy reviews,* 8**,** 129-155.

CUDDIHY, E. & WILLIS, P. B. 1984. *Antisoiling technology: theories of surface soiling and performance of antisoiling surface coatings*, The Administration.

CUDDIHY, E. F. 1980. Theoretical considerations of soil retention. *Solar energy materials,* 3**,** 21-33.

CUDDIHY, E. F. Surface soiling: theoretical mechanisms and evaluation of low-soiling coatings. Proceedings of the Flat-Plate Solar Array Project Research Forum, 1983. 379-396.

DEFRATE, L. & HOERL, A. Optimum design of ejectors using digital computers. Computer Techniques, Chemical Engineering Progress Symposium Series, 55(21), pp. 43-51., 1959.

DODO, A., HERNANDEZ-PEREZ, V., ZHU, J. & RIFFAT, S. 2012. Interrogating the Flow Behavior in a Novel Magnetic Desiccant Ventilation System using Computational Fluid Dynamics (CFD).

DUTTON, J. & CARROLL, B. 1986. Optimal supersonic ejector designs. *Journal of Fluids Engineering,* 108**,** 414-420.

EAMES, I. W., APHORNRATANA, S. & HAIDER, H. 1995. A theoretical and experimental study of a small-scale steam jet refrigerator. *International Journal of Refrigeration,* 18**,** 378-386.

EASOM, G. 2000. *Improved turbulence models for computational wind engineering.* University of Nottingham.

EL-SHOBOKSHY, M. S. & HUSSEIN, F. M. 1993. Effect of dust with different physical properties on the performance of photovoltaic cells. *Solar Energy,* 51**,** 505-511.

ELMINIR, H. K., GHITAS, A. E., HAMID, R. H., EL-HUSSAINY, F., BEHEARY, M. M. & ABDEL-MONEIM, K. M. 2006. Effect of dust on the transparent cover of solar collectors. *Energy Conversion and Management,* 47**,** 3192-3203.

ELSHERIF, H. & KANDIL, H. Fully automated cleaning systems for Photovoltaic panels and reflectors. GUC Workshop on Renewable Energies and Smart Grid, 2011. 25-26.

EMANUEL, G. 1976. Optimum performance for a single-stage gaseous ejector. *AIAA journal,* 14**,** 1292-1296.

FABRI, J. & SIESTRUNCK, R. 1958. Supersonic air ejectors. *Advances in applied mechanics,* 5**,** 1-34.

FERNÁNDEZ, D., CABÁS, R. & MORENO, L. Dust wiper mechanism for operation in Mars. Proceedings of 12th European Space Mechanisms & Tribology Symposium (ESMATS), 2007.

FLETCHER, C. 2012. *Computational techniques for fluid dynamics 2: Specific techniques for different flow categories*, Springer Science & Business Media.

FOX, R. W., PRITCHARD, P. J. & MCDONALD, A. T. 2011. *Introduction to Fluid Mechanics,* Wiley.

GARG, H. 1974. Effect of dirt on transparent covers in flat-plate solar energy collectors. *Solar Energy,* 15**,** 299-302.

GILBERT, G. B. & HILL, P. G. 1975. Analysis and testing of two-dimensional slot nozzle ejectors with variable area mixing sections, NASA contractor report

CR-2251.

GOFF & COOGAN 1942. Some Two Dimensional Aspects of the Ejector Problem. *Journal of Applied Mechanics* Trans ASME, 9(4), pp. A151-A154.

GUO, J. & SHEN, H. 2009. Modeling solar-driven ejector refrigeration system offering air conditioning for office buildings. *Energy and Buildings,* 41**,** 175-181.

HASSAN, A., RAHOMA, U., ELMINIR, H. & FATHY, A. 2005. Effect of airborne dust concentration on the performance of PV modules. *J Astron Soc Egypt,* 13**,** 24-38.

HE, G., ZHOU, C. & LI, Z. 2011. Review of Self-Cleaning Method for Solar Cell Array. *Procedia Engineering,* 16**,** 640-645.

HEDGES, K. & HILL, P. 1974. Compressible Flow Ejectors: Part I—Development of a Finite-Difference Flow Model. *Journal of Fluids Engineering,* 96**,** 272-281.

HUANG, B. J., CHANG, J. M., WANG, C. P. & PETRENKO, V. A. 1999. A 1-D analysis of ejector performance. *International Journal of Refrigeration,* 22**,** 354-364.

INTUSOFT NEWSLETTER, 2005 *Newsletter Issue 78* [Online]. Available: http://www.intusoft.com/nlhtm/nl78.htm [Accessed 25/03 2014].

ISHENGOMA, F. M. & NORUM, L. E. Design and implementation of a digitally controlled stand-alone photovoltaic power supply. Nordic Workshop on Power and Industrial Electronics, 2002. 12-14.

JI, M., UTOMO, T., WOO, J., LEE, Y., JEONG, H. & CHUNG, H. 2010. CFD investigation on the flow structure inside thermo vapor compressor. *Energy,* 35**,** 2694-2702.

KEENAN, J. & NEUMANN, E. 1942. A simple air ejector. *ASME Journal of Applied Mechanics,* 64**,** 75-82.

KEENAN, J. H. 1950. An investigation of ejector design by analysis and experiment. *Journal of Applied Mechanics,* 17**,** 299.

KLOPFENSTEIN JR, R. 1998. Air velocity and flow measurement using a Pitot tube. *ISA Transactions,* 37**,** 257-263.

LIAO, C. 2008. *Gas ejector modeling for design and analysis.* Texas A&M University.

LIU, G. & MARSHALL, J. 2010. Effect of particle adhesion and interactions on motion by traveling waves on an electric curtain. *Journal of Electrostatics,* 68**,** 179-189.

MANI, M. & PILLAI, R. 2010. Impact of dust on solar photovoltaic (PV) performance: Research status, challenges and recommendations. *Renewable and Sustainable Energy Reviews,* 14**,** 3124-3131.

MESSENGER, R. A. & VENTRE, J. 2002. *Photovoltaic systems engineering,* New York, CRC press.

MIKHAIL, S. 1960. Mixing of coaxial streams inside a closed conduit. *Journal of Mechanical Engineering Science,* 2**,** 59-68.

MOHARRAM, K. A., ABD-ELHADY, M. S., KANDIL, H. A. & EL-SHERIF, H. 2013. Influence of cleaning using water and surfactants on the performance of photovoltaic panels. *Energy Conversion and Management,* 68**,** 266-272.

MUNDAY, J. T. & BAGSTER, D. F. 1977. A New Ejector Theory Applied to Steam Jet Refrigeration. *Industrial & Engineering Chemistry Process Design and Development,* 16**,** 442-449.

NAKAGAWA, M., MARASIGAN, A. R., MATSUKAWA, T. & KURASHINA, A. 2011. Experimental investigation on the effect of mixing length on the performance of two-phase ejector for CO2 refrigeration cycle with and without heat exchanger. *International Journal of Refrigeration,* 34**,** 1604-1613.

NEVE, R. 1993. Computational fluid dynamics analysis of diffuser performance in gas-powered jet pumps. *International Journal of Heat and Fluid Flow,* 14**,** 401-407.

NIU, J. J., WANG, J. N. & XU, Q. F. 2009. Synthesis of superhydrophobic silicon oxide nanowires surface on silicon wafer. *Journal of nanoscience and nanotechnology,* 9**,** 1819-1824.

PARK, Y.-B., IM, H., IM, M. & CHOI, Y.-K. 2011. Self-cleaning effect of highly water-repellent microshell structures for solar cell applications. *Journal of Materials Chemistry,* 21**,** 633-636.

PATANKAR, S. V. & SPALDING, D. B. 1972. A calculation procedure for heat, mass and momentum transfer in three-dimensional parabolic flows. *International journal of heat and mass transfer,* 15**,** 1787-1806.

PIANTHONG, K., SEEHANAM, W., BEHNIA, M., SRIVEERAKUL, T. & APHORNRATANA, S. 2007. Investigation and improvement of ejector refrigeration system using computational fluid dynamics technique. *Energy Conversion and Management,* 48**,** 2556-2564.

PILKINGTON. 2014. *Self cleaning glass* [Online]. Available: http://www.pilkingtonselfcleaningglass.co.uk/default1.htm [Accessed 10/03 2014].

RICE, P. & DANDACHI, J. 1991. Equation for the prediction of steam flowrate required in the design of ejectors. *Chemical Engineering Research and Design,* 69**,** 332-334.

RIFFAT, S., JIANG, L. & GAN, G. 2005. Recent development in ejector technology—a review. *International journal of ambient energy,* 26**,** 13-26.

RIFFAT, S. & OMER, S. 2001. CFD modelling and experimental investigation of an ejector refrigeration system using methanol as the working fluid. *International Journal of Energy Research,* 25**,** 115-128.

RIFFAT, S. B., GAN, G. & SMITH, S. 1996. Computational fluid dynamics applied to ejector heat pumps. *Applied Thermal Engineering,* 16**,** 291-297.

SALIM, A., HURAIB, F. & EUGENIO, N. PV power-study of system options and optimization. EC photovoltaic solar conference. 8, 1988. 688-692.

SARVER, T., AL-QARAGHULI, A. & KAZMERSKI, L. L. 2013. A comprehensive review of the impact of dust on the use of solar energy: History, investigations, results, literature, and mitigation approaches. *Renewable and Sustainable Energy Reviews,* 22**,** 698-733.

SAYIGH, A., AL-JANDAL, S. & AHMED, H. Dust effect on solar flat surfaces devices in Kuwait. Proceedings of the workshop on the physics of non-conventional energy sources and materials science for energy, 1985. 2-20.

SCHUMACHER, J., HANSEN, J. & NEVENZEL, J. 1979. Preliminary design report: New ideas for heliostat reflector cleaning systems. *NASA STI/Recon Technical Report N,* 80**,** 23809.

SHARMA, R., WYATT, C. A., ZHANG, J., CALLE, C. I., MARDESICH, N. & MAZUMDER, M. K. 2009. Experimental evaluation and analysis of electrodynamic screen as dust mitigation technology for future Mars missions. *Industry Applications, IEEE Transactions on,* 45**,** 591-596.

SIMS, R., BIRIS, A., WILSON, J., YURTERI, C., MAZUMDER, M., CALLE, C. & BUHLER, C. Development of a transparent self-cleaning dust shield for solar panels. Proceedings ESA-IEEE joint meeting on electrostatics, 2003. 814-821.

SUN, D.-W. & EAMES, I. W. 1995. Recent developments in the design theories and application of ejectors: a review. *Journal of the Institute of Energy,* 68**,** 65-79.

TANNER, L. & BLOWS, L. 1976. A study of the motion of oil films on surfaces in air flow, with application to the measurement of skin friction. *Journal of Physics E: Scientific Instruments,* 9**,** 194.

URBÁN, A., ZAREMBA, M., MALÝ, M., JÓZSA, V. & JEDELSKÝ, J. 2017. Droplet dynamics and size characterization of high-velocity airblast atomization. *International Journal of Multiphase Flow,* 95**,** 1-11.

VERSTEEG, H. K. & MALALASEKERA, W. 2007. *An introduction to computational fluid dynamics: the finite volume method,* Pearson Education.

WANG, H.-C. 1990. Effects of inceptive motion on particle detachment from surfaces. *Aerosol Science and Technology,* 13**,** 386-393.

WHEAL, R. 2005. *Photocatalytic solar chimney for pre-heating air and the removal of VOCs, Thesis (PhD),* University of Nottingham.

WILLIAMS, R. B., REBEKAH, T., ANDRANIK, S. & STEPHEN, F. 2007. Vibration Characterization of Self-Cleaning Solar Panels with Piezoceramic Actuation. *48th AIAA/ASME/ASCE/AHS/ASC Structures, Structural*

*Dynamics, and Materials Conference.* American Institute of Aeronautics and Astronautics.

2005. *Intusoft Newsletter, Newsletter Issue 78* [Online]. Available: http://www.intusoft.com/nlhtm/nl78.htm [Accessed 25/03 2014].

ABD-ELHADY, M., ZAYED, S. & RINDT, C. Removal of dust particles from the surface of solar cells and solar collectors using surfactants. Proceedings of the Eurotherm international conference on heat exchanger fouling and cleaning IX, Crete, Greece, 2011. 5-10.

ABDULATEEF, J., SOPIAN, K., ALGHOUL, M. & SULAIMAN, M. 2009. Review on solar-driven ejector refrigeration technologies. *Renewable and Sustainable Energy Reviews,* 13**,** 1338-1349.

ADDY, A. & CHOW, W. 1964a. Interaction between primary and secondary streams of supersonic ejector systems and their performance characteristics. *AIAA journal,* 2**,** 686-695.

ADDY, A. & CHOW, W. 1964b. On the starting characteristics of supersonic ejector systems. *Journal of Basic Engineering,* 86**,** 861-868.

ALLERY, C., GUERIN, S., HAMDOUNI, A. & SAKOUT, A. 2004. Experimental and numerical POD study of the Coanda effect used to reduce self-sustained tones. *Mechanics Research Communications,* 31**,** 105-120.

ANDERSON, M., GRANDY, A., HASTIE, J., SWEEZEY, A., RANKY, R., MAVROIDIS, C. & MARKOPOULOS, Y. P. 2010. ROBOTIC DEVICE FOR CLEANING PHOTOVOLTAIC PANEL ARRAYS.

AOYOMA, M. & MASUDA, S. Characteristics of electric dust collector based on electric curtain. Proceedings of the General Conference of the Institute of Electronic Engineers in Japan, 1971.

ATTEN, P., PANG, H. L. & REBOUD, J.-L. 2009. Study of dust removal by standing-wave electric curtain for application to solar cells on mars. *Industry Applications, IEEE Transactions on*, 45**,** 75-86.

BARTOSIEWICZ, Y., AIDOUN, Z., DESEVAUX, P. & MERCADIER, Y. 2005. Numerical and experimental investigations on supersonic ejectors. *International Journal of Heat and Fluid Flow,* 26**,** 56-70.

BARTOSIEWICZ, Y., AIDOUN, Z. & MERCADIER, Y. 2006. Numerical assessment of ejector operation for refrigeration applications based on CFD. *Applied Thermal Engineering,* 26**,** 604-612.

BIRIS, A., SAINI, D., SRIRAMA, P., MAZUMDER, M., SIMS, R., CALLE, C. & BUHLER, C. Electrodynamic removal of contaminant particles and its applications. Industry Applications Conference, 2004. 39th IAS Annual Meeting. Conference Record of the 2004 IEEE, 2004. IEEE, 1283-1286.

BOCK, J. P., ROBINSON, J., SHARMA, R., ZHANG, J. & MAZUMDER, K. An efficient power management approach for self-cleaning solar panels with integrated electrodynamic screens. Proc. ESA Annual Meeting on Electrostatics, 2008.

BOLLINGER, J. 2007. *APPLICATIONS OF SOLAR ENERGY TO POWER STAND-ALONE AREA AND STREET LIGHTING.* MASTER OF SCIENCE IN ELECTRICAL ENGINEERING, UNIVERSITY OF MISSOURI-ROLLA.

BONNINGTON, S. T., KING, A. L. & HEMMINGS, J. 1976. *Jet pumps and ejectors: A state of the art review and bibliography*, BHRA Fluid Engineering.

CALLE, C., MCFALL, J., BUHLER, C., SNYDER, S., ARENS, E., CHEN, A., RITZ, M., CLEMENTS, J., FORTIER, C. & TRIGWELL, S. Dust particle removal by electrostatic and dielectrophoretic forces with applications to NASA exploration missions. Proceedings of the electrostatics society of America Annual meeting, Minneapolis, 2008. 17-19.

CHAIWONGSA, P. & WONGWISES, S. 2008. Experimental study on R-134a refrigeration system using a two-phase ejector as an expansion device. *Applied Thermal Engineering,* 28**,** 467-477.

CHEN, X., OMER, S., WORALL, M. & RIFFAT, S. 2013. Recent developments in ejector refrigeration technologies. *Renewable and Sustainable Energy Reviews,* 19**,** 629-651.

CHOU, S., YANG, P. & YAP, C. 2001. Maximum mass flow ratio due to secondary flow choking in an ejector refrigeration system. *International journal of refrigeration,* 24**,** 486-499.

CHUNNANOND, K. & APHORNRATANA, S. 2004. Ejectors: applications in refrigeration technology. *Renewable and sustainable energy reviews,* 8**,** 129-155.

CUDDIHY, E. & WILLIS, P. B. 1984. *Antisoiling technology: theories of surface soiling and performance of antisoiling surface coatings*, The Administration.

CUDDIHY, E. F. 1980. Theoretical considerations of soil retention. *Solar energy materials,* 3**,** 21-33.

CUDDIHY, E. F. Surface soiling: theoretical mechanisms and evaluation of low-soiling coatings. Proceedings of the Flat-Plate Solar Array Project Research Forum, 1983. 379-396.

DEFRATE, L. & HOERL, A. Optimum design of ejectors using digital computers. Computer Techniques, Chemical Engineering Progress Symposium Series, 55(21), pp. 43-51., 1959.

DODO, A., HERNANDEZ-PEREZ, V., ZHU, J. & RIFFAT, S. 2012. Interrogating the Flow Behavior in a Novel Magnetic Desiccant Ventilation System using Computational Fluid Dynamics (CFD).

DUTTON, J. & CARROLL, B. 1986. Optimal supersonic ejector designs. *Journal of Fluids Engineering,* 108**,** 414-420.

EAMES, I. W., APHORNRATANA, S. & HAIDER, H. 1995. A theoretical and experimental study of a small-scale steam jet refrigerator. *International Journal of Refrigeration,* 18**,** 378-386.

EASOM, G. 2000. *Improved turbulence models for computational wind engineering.* University of Nottingham.

EL-SHOBOKSHY, M. S. & HUSSEIN, F. M. 1993. Effect of dust with different physical properties on the performance of photovoltaic cells. *Solar Energy,* 51**,** 505-511.

ELMINIR, H. K., GHITAS, A. E., HAMID, R. H., EL-HUSSAINY, F., BEHEARY, M. M. & ABDEL-MONEIM, K. M. 2006. Effect of dust on the transparent cover of solar collectors. *Energy Conversion and Management,* 47**,** 3192-3203.

ELSHERIF, H. & KANDIL, H. Fully automated cleaning systems for Photovoltaic panels and reflectors. GUC Workshop on Renewable Energies and Smart Grid, 2011. 25-26.

EMANUEL, G. 1976. Optimum performance for a single-stage gaseous ejector. *AIAA journal,* 14**,** 1292-1296.

FABRI, J. & SIESTRUNCK, R. 1958. Supersonic air ejectors. *Advances in applied mechanics,* 5**,** 1-34.

FERNÁNDEZ, D., CABÁS, R. & MORENO, L. Dust wiper mechanism for operation in Mars. Proceedings of 12th European Space Mechanisms & Tribology Symposium (ESMATS), 2007.

FLETCHER, C. 2012. *Computational techniques for fluid dynamics 2: Specific techniques for different flow categories*, Springer Science & Business Media.

FOX, R. W., PRITCHARD, P. J. & MCDONALD, A. T. 2011. *Introduction to Fluid Mechanics,* Wiley.

GARG, H. 1974. Effect of dirt on transparent covers in flat-plate solar energy collectors. *Solar Energy,* 15**,** 299-302.

GILBERT, G. B. & HILL, P. G. 1975. Analysis and testing of two-dimensional slot nozzle ejectors with variable area mixing sections, NASA contractor report

CR-2251.

GOFF & COOGAN 1942. Some Two Dimensional Aspects of the Ejector Problem. *Journal of Applied Mechanics* Trans ASME, 9(4), pp. A151-A154.

GUO, J. & SHEN, H. 2009. Modeling solar-driven ejector refrigeration system offering air conditioning for office buildings. *Energy and Buildings,* 41**,** 175-181.

HASSAN, A., RAHOMA, U., ELMINIR, H. & FATHY, A. 2005. Effect of airborne dust concentration on the performance of PV modules. *J Astron Soc Egypt,* 13**,** 24-38.

HE, G., ZHOU, C. & LI, Z. 2011. Review of Self-Cleaning Method for Solar Cell Array. *Procedia Engineering,* 16**,** 640-645.

HEDGES, K. & HILL, P. 1974. Compressible Flow Ejectors: Part I—Development of a Finite-Difference Flow Model. *Journal of Fluids Engineering,* 96**,** 272-281.

HUANG, B. J., CHANG, J. M., WANG, C. P. & PETRENKO, V. A. 1999. A 1-D analysis of ejector performance. *International Journal of Refrigeration,* 22**,** 354-364.

ISHENGOMA, F. M. & NORUM, L. E. Design and implementation of a digitally controlled stand-alone photovoltaic power supply. Nordic Workshop on Power and Industrial Electronics, 2002. 12-14.

JI, M., UTOMO, T., WOO, J., LEE, Y., JEONG, H. & CHUNG, H. 2010. CFD investigation on the flow structure inside thermo vapor compressor. *Energy,* 35**,** 2694-2702.

KEENAN, J. & NEUMANN, E. 1942. A simple air ejector. *ASME Journal of Applied Mechanics,* 64**,** 75-82.

KEENAN, J. H. 1950. An investigation of ejector design by analysis and experiment. *Journal of Applied Mechanics,* 17**,** 299.

KLOPFENSTEIN JR, R. 1998. Air velocity and flow measurement using a Pitot tube. *ISA Transactions,* 37**,** 257-263.

LIAO, C. 2008. *Gas ejector modeling for design and analysis.* Texas A&M University.

LIU, G. & MARSHALL, J. 2010. Effect of particle adhesion and interactions on motion by traveling waves on an electric curtain. *Journal of Electrostatics,* 68**,** 179-189.

MANI, M. & PILLAI, R. 2010. Impact of dust on solar photovoltaic (PV) performance: Research status, challenges and recommendations. *Renewable and Sustainable Energy Reviews,* 14**,** 3124-3131.

MESSENGER, R. A. & VENTRE, J. 2002. *Photovoltaic systems engineering,* New York, CRC press.

MIKHAIL, S. 1960. Mixing of coaxial streams inside a closed conduit. *Journal of Mechanical Engineering Science,* 2**,** 59-68.

MOHARRAM, K. A., ABD-ELHADY, M. S., KANDIL, H. A. & EL-SHERIF, H. 2013. Influence of cleaning using water and surfactants on the performance of photovoltaic panels. *Energy Conversion and Management,* 68**,** 266-272.

MUNDAY, J. T. & BAGSTER, D. F. 1977. A New Ejector Theory Applied to Steam Jet Refrigeration. *Industrial & Engineering Chemistry Process Design and Development,* 16**,** 442-449.

NAKAGAWA, M., MARASIGAN, A. R., MATSUKAWA, T. & KURASHINA, A. 2011. Experimental investigation on the effect of mixing length on the performance of two-phase ejector for CO2 refrigeration cycle with and without heat exchanger. *International Journal of Refrigeration,* 34**,** 1604-1613.

NEVE, R. 1993. Computational fluid dynamics analysis of diffuser performance in gas-powered jet pumps. *International Journal of Heat and Fluid Flow,* 14**,** 401-407.

NIU, J. J., WANG, J. N. & XU, Q. F. 2009. Synthesis of superhydrophobic silicon oxide nanowires surface on silicon wafer. *Journal of nanoscience and nanotechnology,* 9**,** 1819-1824.

PARK, Y.-B., IM, H., IM, M. & CHOI, Y.-K. 2011. Self-cleaning effect of highly water-repellent microshell structures for solar cell applications. *Journal of Materials Chemistry,* 21**,** 633-636.

PATANKAR, S. V. & SPALDING, D. B. 1972. A calculation procedure for heat, mass and momentum transfer in three-dimensional parabolic flows. *International journal of heat and mass transfer,* 15**,** 1787-1806.

PIANTHONG, K., SEEHANAM, W., BEHNIA, M., SRIVEERAKUL, T. & APHORNRATANA, S. 2007. Investigation and improvement of ejector refrigeration system using computational fluid dynamics technique. *Energy Conversion and Management,* 48**,** 2556-2564.

PILKINGTON. 2014. *Self cleaning glass* [Online]. Available: http://www.pilkingtonselfcleaningglass.co.uk/default1.htm [Accessed 10/03 2014].

RICE, P. & DANDACHI, J. 1991. Equation for the prediction of steam flowrate required in the design of ejectors. *Chemical Engineering Research and Design,* 69**,** 332-334.

RIFFAT, S., JIANG, L. & GAN, G. 2005. Recent development in ejector technology—a review. *International journal of ambient energy,* 26**,** 13-26.

RIFFAT, S. & OMER, S. 2001. CFD modelling and experimental investigation of an ejector refrigeration system using methanol as the working fluid. *International Journal of Energy Research,* 25**,** 115-128.

RIFFAT, S. B., GAN, G. & SMITH, S. 1996. Computational fluid dynamics applied to ejector heat pumps. *Applied Thermal Engineering,* 16**,** 291-297.

SALIM, A., HURAIB, F. & EUGENIO, N. PV power-study of system options and optimization. EC photovoltaic solar conference. 8, 1988. 688-692.

SARVER, T., AL-QARAGHULI, A. & KAZMERSKI, L. L. 2013. A comprehensive review of the impact of dust on the use of solar energy: History, investigations, results, literature, and mitigation approaches. *Renewable and Sustainable Energy Reviews,* 22**,** 698-733.

SAYIGH, A., AL-JANDAL, S. & AHMED, H. Dust effect on solar flat surfaces devices in Kuwait. Proceedings of the workshop on the physics of non-conventional energy sources and materials science for energy, 1985. 2-20.

SCHUMACHER, J., HANSEN, J. & NEVENZEL, J. 1979. Preliminary design report: New ideas for heliostat reflector cleaning systems. *NASA STI/Recon Technical Report N,* 80**,** 23809.

SHARMA, R., WYATT, C. A., ZHANG, J., CALLE, C. I., MARDESICH, N. & MAZUMDER, M. K. 2009. Experimental evaluation and analysis of electrodynamic screen as dust mitigation technology for future Mars missions. *Industry Applications, IEEE Transactions on,* 45**,** 591-596.

SIMS, R., BIRIS, A., WILSON, J., YURTERI, C., MAZUMDER, M., CALLE, C. & BUHLER, C. Development of a transparent self-cleaning dust shield for solar panels. Proceedings ESA-IEEE joint meeting on electrostatics, 2003. 814-821.

SUN, D.-W. & EAMES, I. W. 1995. Recent developments in the design theories and application of ejectors: a review. *Journal of the Institute of Energy,* 68**,** 65-79.

TANNER, L. & BLOWS, L. 1976. A study of the motion of oil films on surfaces in air flow, with application to the measurement of skin friction. *Journal of Physics E: Scientific Instruments,* 9**,** 194.

URBÁN, A., ZAREMBA, M., MALÝ, M., JÓZSA, V. & JEDELSKÝ, J. 2017. Droplet dynamics and size characterization of high-velocity airblast atomization. *International Journal of Multiphase Flow,* 95**,** 1-11.

VERSTEEG, H. K. & MALALASEKERA, W. 2007. *An introduction to computational fluid dynamics: the finite volume method*, Pearson Education.

WANG, H.-C. 1990. Effects of inceptive motion on particle detachment from surfaces. *Aerosol Science and Technology,* 13**,** 386-393.

WHEAL, R. 2005. *Photocatalytic solar chimney for pre-heating air and the removal of VOCs, Thesis (PhD),* University of Nottingham.

WILLIAMS, R. B., REBEKAH, T., ANDRANIK, S. & STEPHEN, F. 2007. Vibration Characterization of Self-Cleaning Solar Panels with Piezoceramic Actuation. *48th AIAA/ASME/ASCE/AHS/ASC Structures, Structural Dynamics, and Materials Conference.* American Institute of Aeronautics and Astronautics.

XIA, Y., KHEZZAR, L., ALSHEHHI, M. & HARDALUPAS, Y. 2017. Droplet size and velocity characteristics of water-air impinging jet atomizer. *International Journal of Multiphase Flow,* 94**,** 31-43.

YADAV, R. L. & PATWARDHAN, A. W. 2008. Design aspects of ejectors: Effects of suction chamber geometry. *Chemical Engineering Science,* 63**,** 3886-3897.

YOUNG, R. M., HARGATHER, M. & SETTLES, G. 2013. Shear stress and particle removal measurements of a round turbulent air jet impinging normally upon a planar wall. *Journal of Aerosol Science,* 62**,** 15-25.

ZHANG, B. & SHEN, S. 2006. A theoretical study on a novel bi-ejector refrigeration cycle. *Applied thermal engineering,* 26**,** 622-626.

ZHANG, X., YAO, Z., HAO, P. & XU, H. 2002. Study on particle removal efficiency of an impinging jet by an image-processing method. *Experiments in fluids,* 32**,** 376-380.

ZHENG, B. & WENG, Y. 2010. A combined power and ejector refrigeration cycle for low temperature heat sources. *Solar Energy,* 84**,** 784-791.

ZHU, J., HSU, C.-M., YU, Z., FAN, S. & CUI, Y. 2009a. Nanodome Solar Cells with Efficient Light Management and Self-Cleaning. *Nano Letters,* 10**,** 1979-1984.

ZHU, Y., CAI, W., WEN, C. & LI, Y. 2009b. Numerical investigation of geometry parameters for design of high performance ejectors. *Applied Thermal Engineering,* 29**,** 898-905.

YADAV, R. L. & PATWARDHAN, A. W. 2008. Design aspects of ejectors: Effects of suction chamber geometry. *Chemical Engineering Science,* 63**,** 3886-3897.

YOUNG, R. M., HARGATHER, M. & SETTLES, G. 2013. Shear stress and particle removal measurements of a round turbulent air jet impinging normally upon a planar wall. *Journal of Aerosol Science,* 62**,** 15-25.

ZHANG, B. & SHEN, S. 2006. A theoretical study on a novel bi-ejector refrigeration cycle. *Applied thermal engineering,* 26**,** 622-626.

ZHANG, X., YAO, Z., HAO, P. & XU, H. 2002. Study on particle removal efficiency of an impinging jet by an image-processing method. *Experiments in fluids,* 32**,** 376-380.

ZHENG, B. & WENG, Y. 2010. A combined power and ejector refrigeration cycle for low temperature heat sources. *Solar Energy,* 84**,** 784-791.

ZHU, J., HSU, C.-M., YU, Z., FAN, S. & CUI, Y. 2009a. Nanodome Solar Cells with Efficient Light Management and Self-Cleaning. *Nano Letters,* 10**,** 1979-1984.

ZHU, Y., CAI, W., WEN, C. & LI, Y. 2009b. Numerical investigation of geometry parameters for design of high performance ejectors. *Applied Thermal Engineering*, 29**,** 898-905.

# Appendices

## Appendix A

**The plot diagram results of Group A simulations for $d_1$=2mm.**

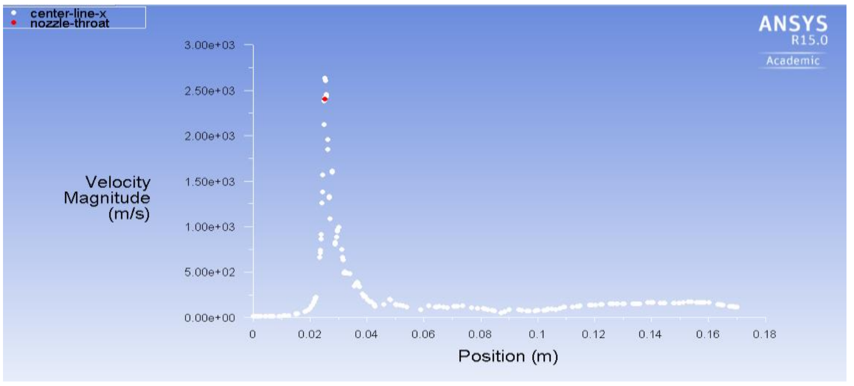


Figure A-1 diagram of a velocity Magnitude along the line of the centre in the Group A case d1= 2 mm ($\dot{m}_1$ = 0.01 kg/s).

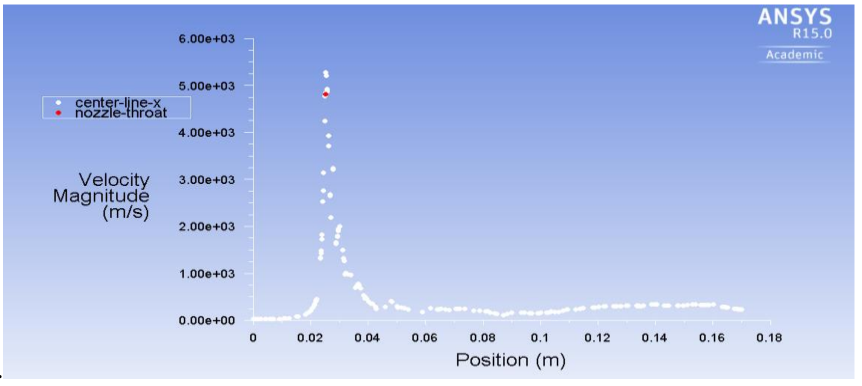


Figure A-2 Diagram of a velocity Magnitude along the line of the centre in the Group A case $d_1$= 2 mm ($\dot{m}_1$ = 0.02 kg/s).

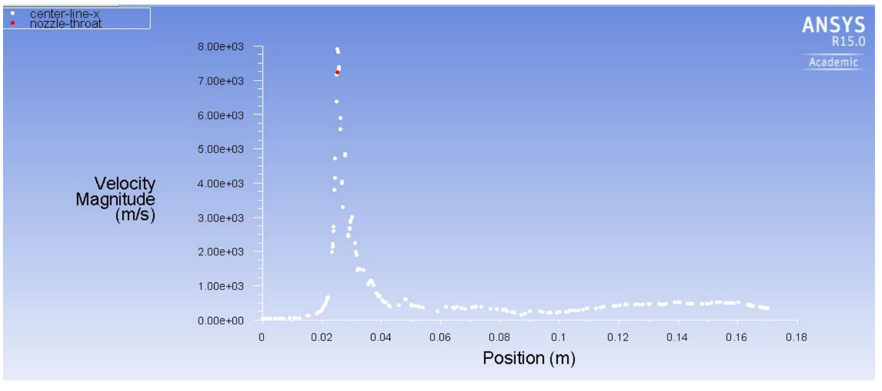


Figure 0A-3 Diagram of a velocity Magnitude along the line of the centre in the Group A case $d_1$= 2 mm ($\dot{m}_1$ = 0.03 kg/s).

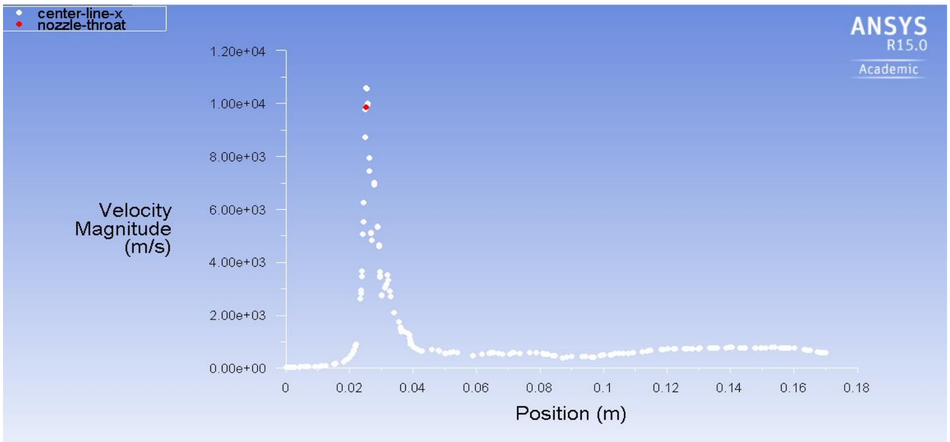


Figure A-4 Diagram of a velocity Magnitude along the line of the centre in the Group A case model $d_1$= 2 mm ($\dot{m}_1$ = 0.04 kg/s)

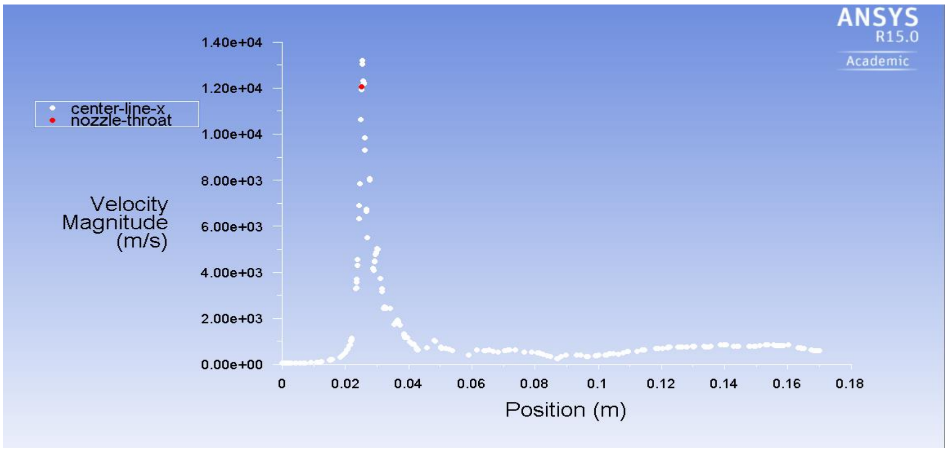


Figure A-5 Diagram of a velocity Magnitude along the line of the centre in the Group A case model $d_1$= 2 mm ($\dot{m}_1$ = 0.05 kg/s)

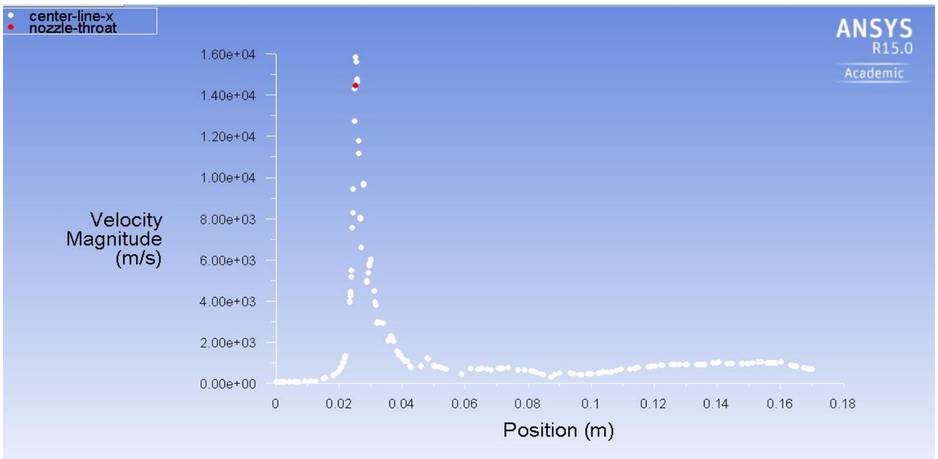


Figure 0A-6 Diagram of a velocity Magnitude along the line of the centre in the Group A case d1= 2 mm ($\dot{m}_1$= 0.06 kg/s)

**The plot diagram results of Group A simulations for $d_1$=3mm.**

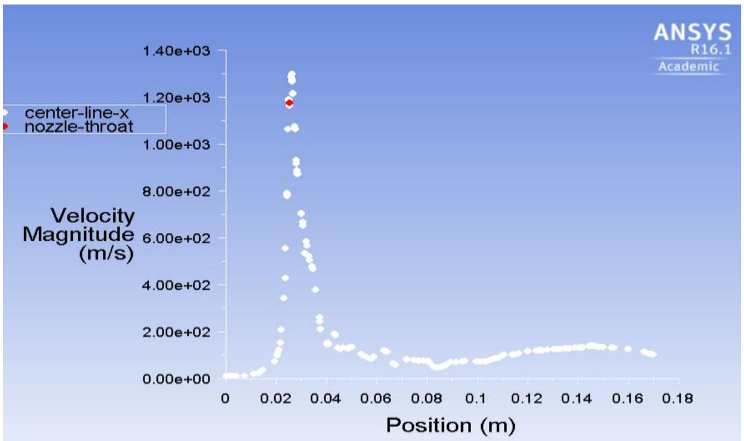


Figure A. 7 Diagram of a velocity Magnitude along the line of the centre in the Group A case d1=3 mm ($\dot{m}_1$ = 0.01 kg/s)

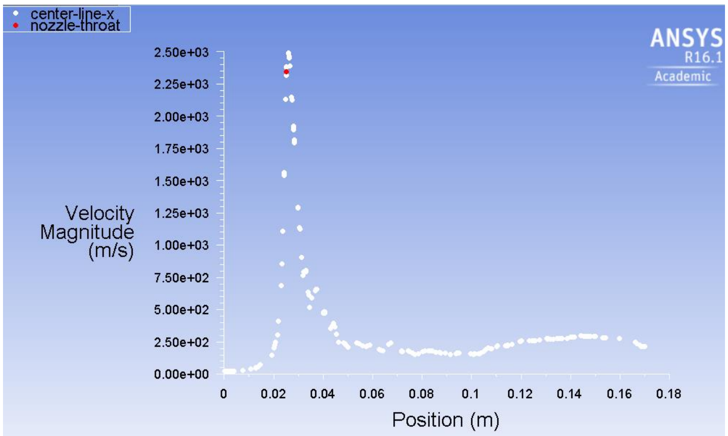


Figure A. 8 Diagram of a velocity Magnitude along the line of the centre in the Group A case d1=3 mm ($\dot{m}_1$ = 0.02 kg/s)

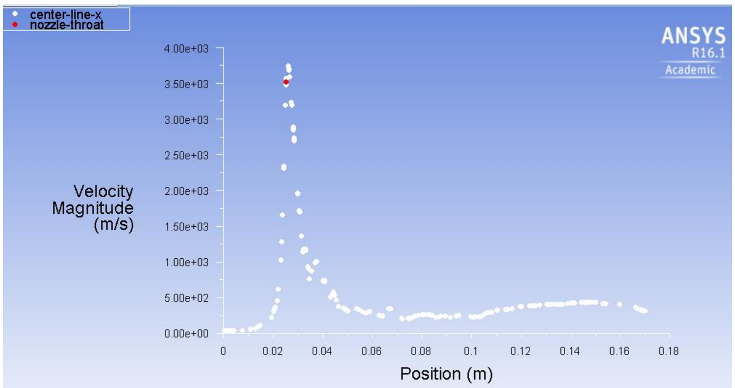


Figure A. 9 Diagram of a velocity Magnitude along the line of the centre in the Group A case model $d_1$=3 mm ($\dot{m}_1$ = 0.03 kg/s)

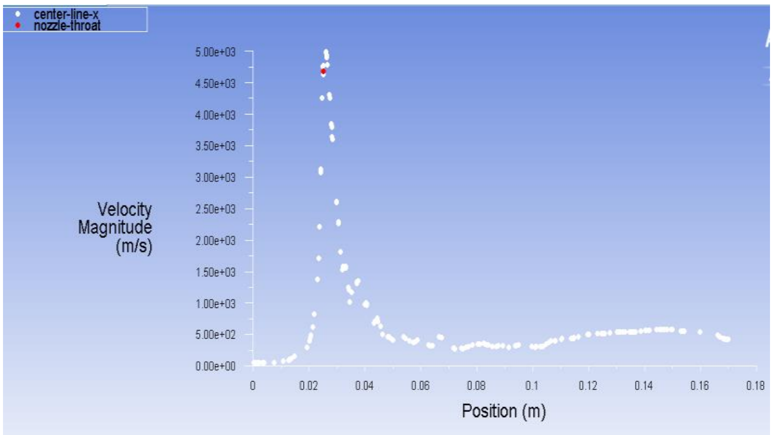


Figure A. 1 Diagram of a velocity Magnitude along the line of the centre in the Group A case $d_1$=3 mm ($\dot{m}_1$ = 0.04 kg/s)

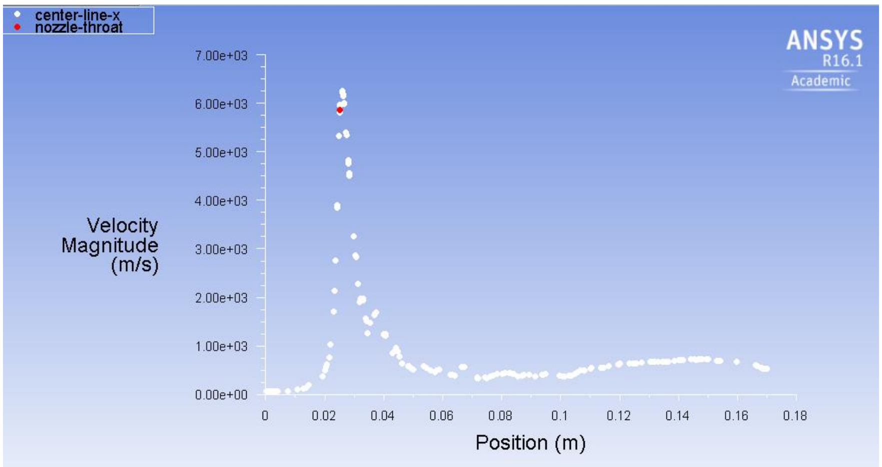


Figure A.11 Diagram of a velocity Magnitude along the line of the centre in the Group A case model $d_1$=3 mm ($\dot{m}_1$ = 0.05 kg/s)

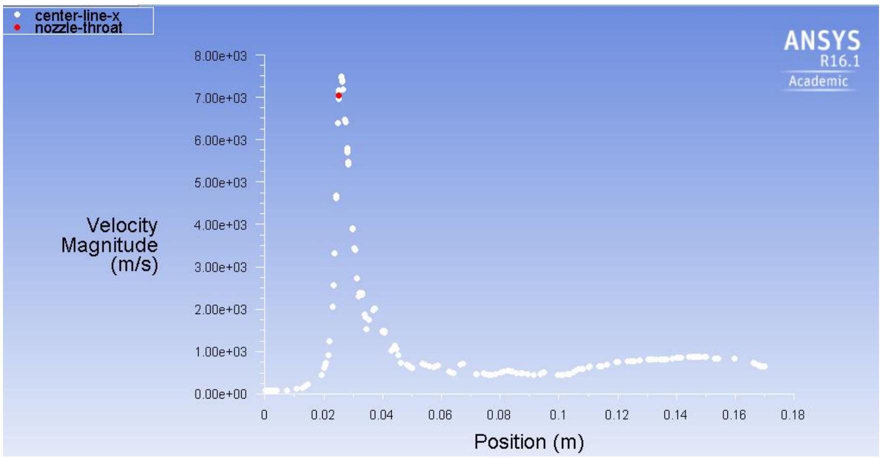


Figure A. 12 Diagram of a velocity Magnitude along the line of the centre in the Group A case $d_1$=3 mm ($\dot{m}_1$ = 0.06kg/s)

**The plot diagram results of Group A simulations for $d_1$=4mm.**

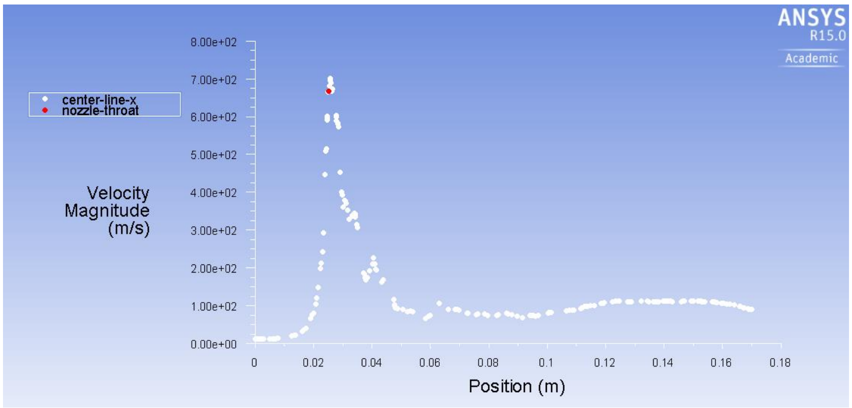


Figure A. 2 Diagram of a velocity Magnitude along the line of the centre in the Group A case $d_1$= 4 mm ($\dot{m}_1$ = 0.01 kg/s)

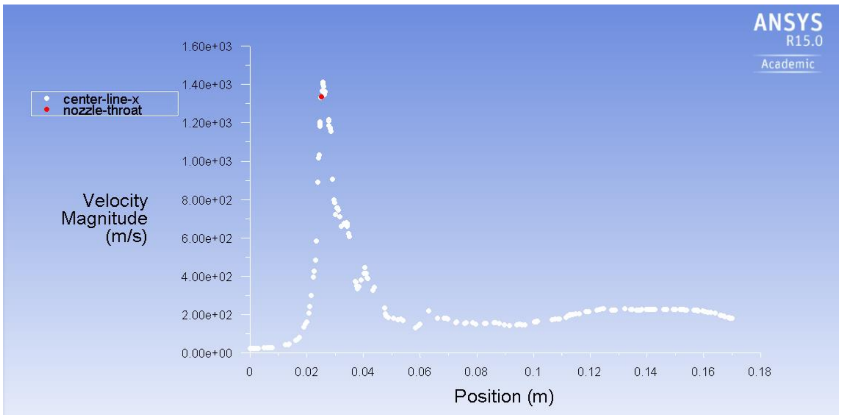


Figure A. 14 Diagram of a velocity Magnitude along the line of the centre in the Group A case $d_1$= 4 mm ($\dot{m}_1$ = 0.02 kg/s)

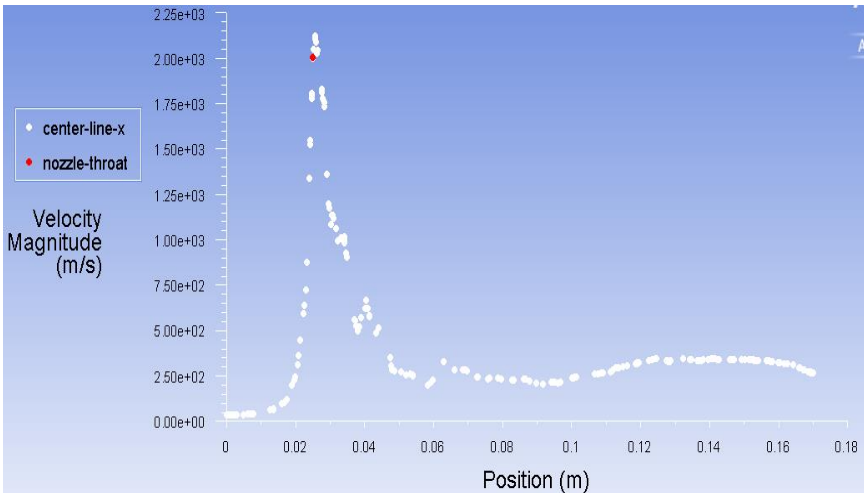


Figure A. 15 Diagram of a velocity Magnitude along the line of the centre in the Group A case = 4 mm ($\dot{m}_1$ = 0.03 kg/s)

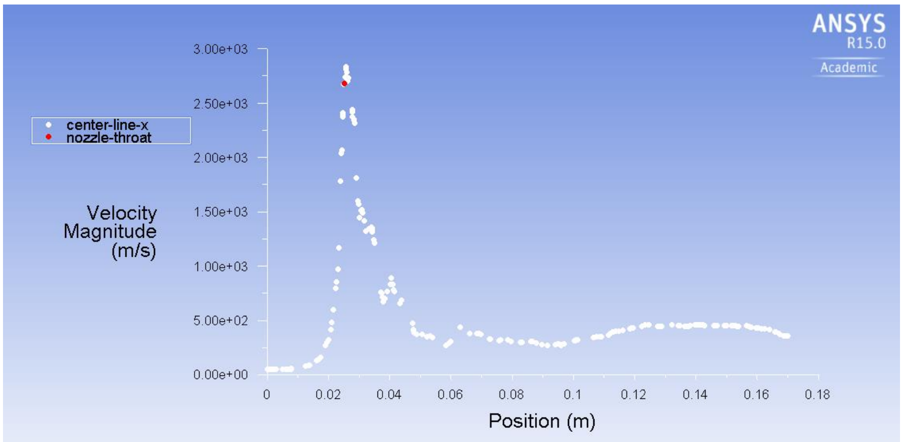


Figure A. 16 Diagram of a velocity Magnitude along the line of the centre in the Group A case $d_1$= 4 mm ($\dot{m}_1$ = 0.04 kg/s)

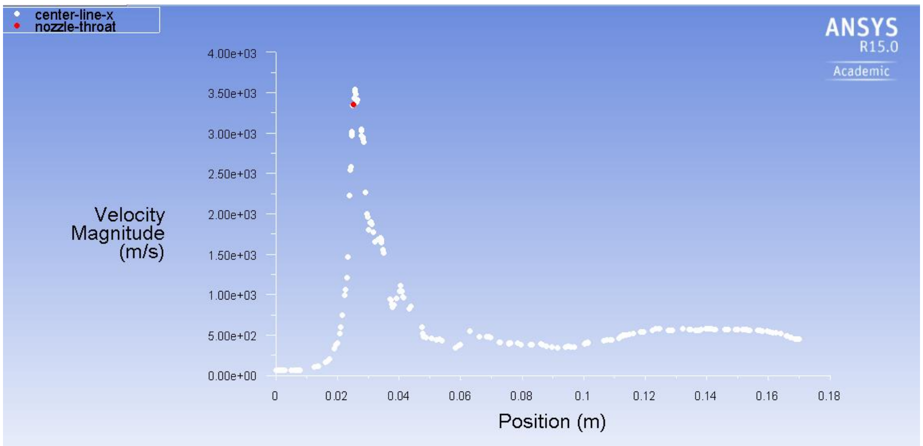


Figure A. 17 Diagram of a velocity Magnitude along the line of the centre in the Group A case $d_1$= 4 mm ($\dot{m}_1$ = 0.05 kg/s)

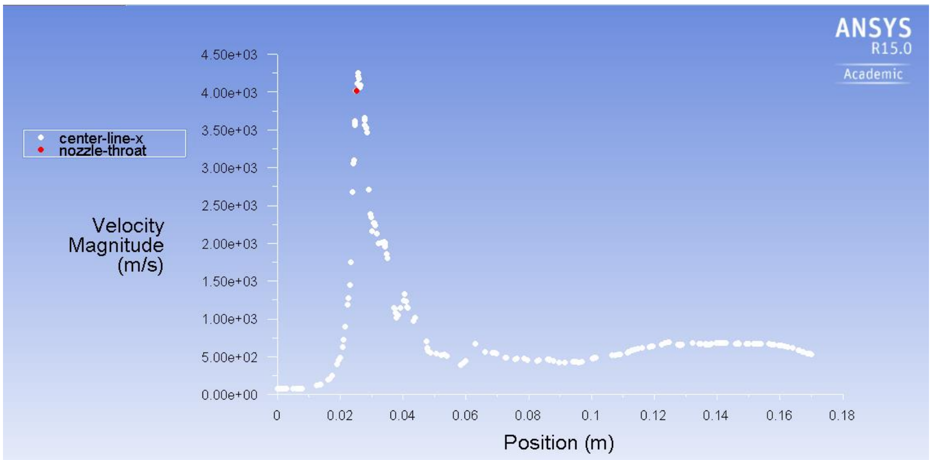


Figure A. 18 Diagram of a velocity Magnitude along the line of the centre in the Group A case $d_1$= 4 mm ($\dot{m}_1$ = 0.06 kg/s)

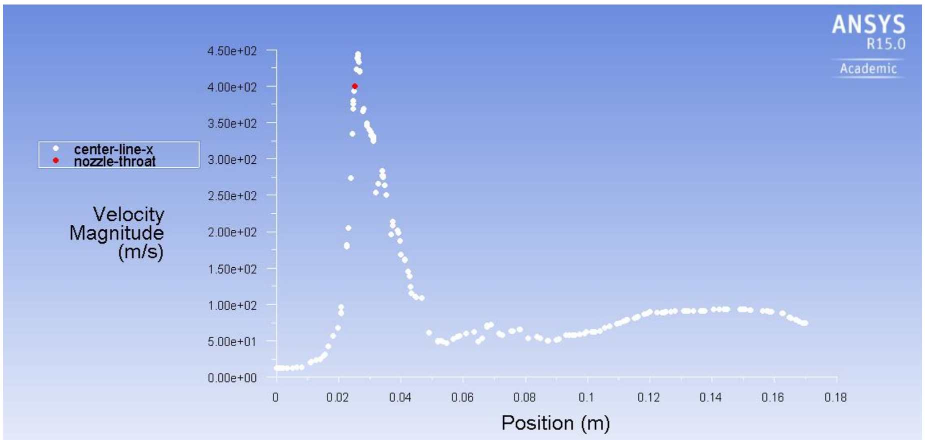


Figure 0A-19 Diagram of a velocity Magnitude along the line of the centre in the Group A case ($\dot{m}_1$ = 0.01 kg/s)

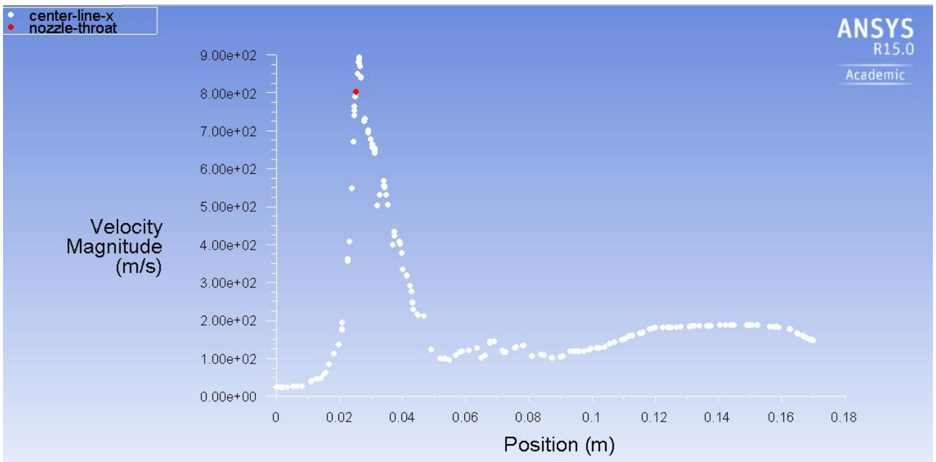


Figure A-20 Diagram of a velocity Magnitude along the line of the centre in the Group A case ($\dot{m}_1$ = 0.02 kg/s)

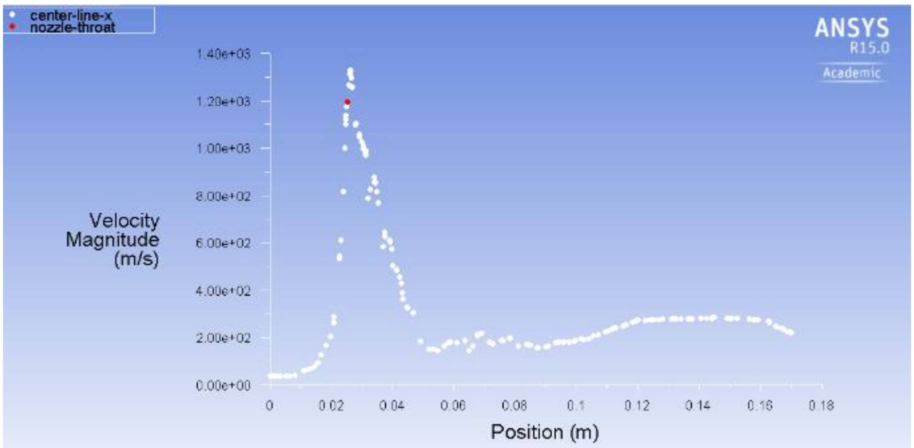


Figure A-21 Diagram of a velocity Magnitude along the line of the centre in the Group A case ($\dot{m}_1$ = 0.03 kg/s)

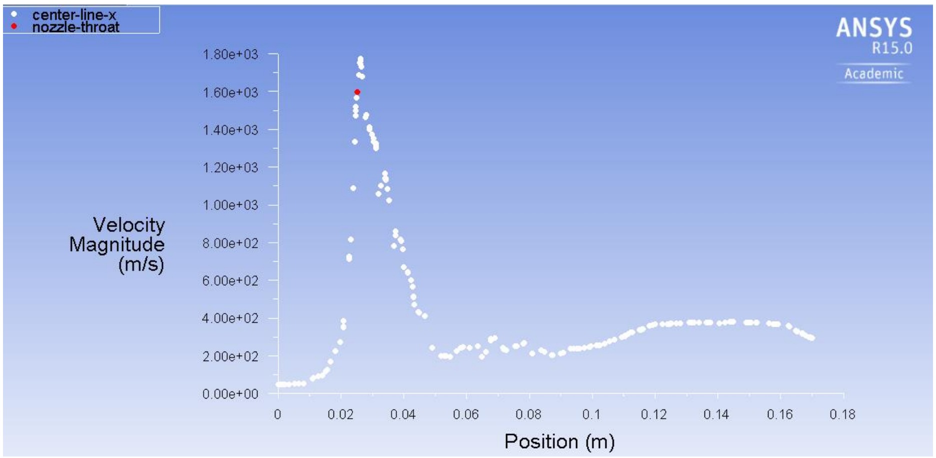


Figure A. 22 Diagram of a velocity Magnitude along the line of the centre in the Group A case ($\dot{m}_1$ = 0.04 kg/s)

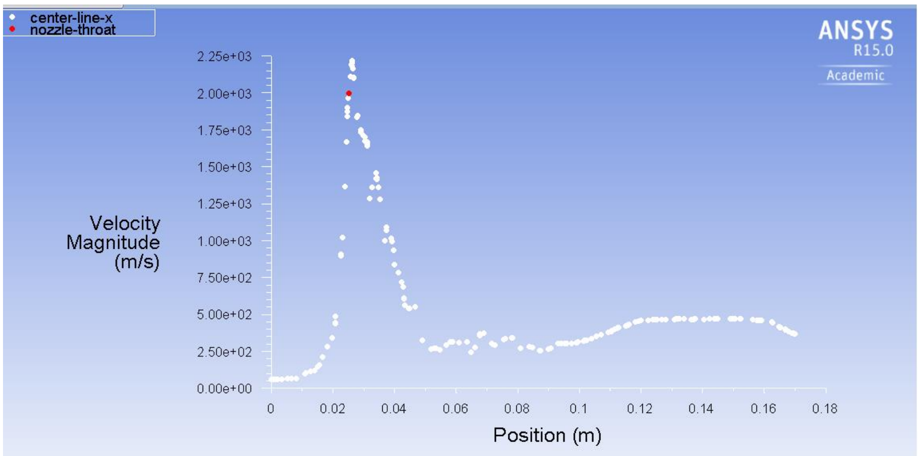


Figure A. 23 Diagram of a velocity Magnitude along the line of the centre in the Group A case ($\dot{m}1$ = 0.05 kg/s)

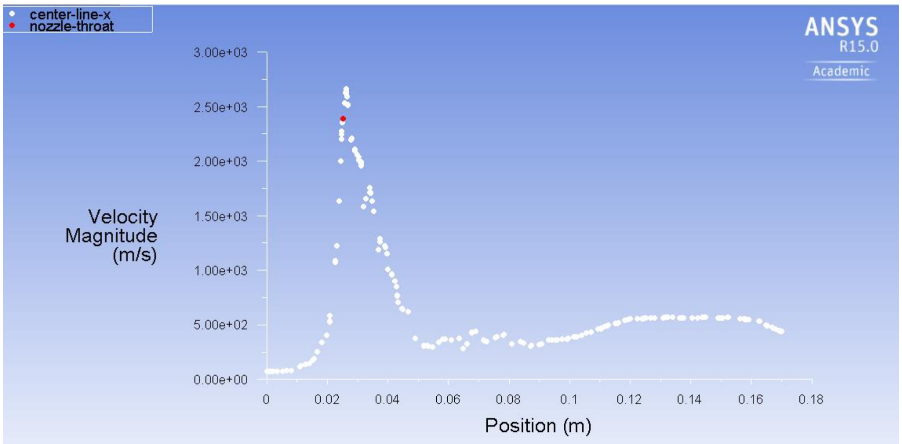


Figure A. 24 Diagram of a velocity Magnitude along the line of the centre in the Group A case model ($\dot{m}_1$ = 0.06 kg/s)

**The plot diagram results of Group A simulations for $d_1$=6mm.**

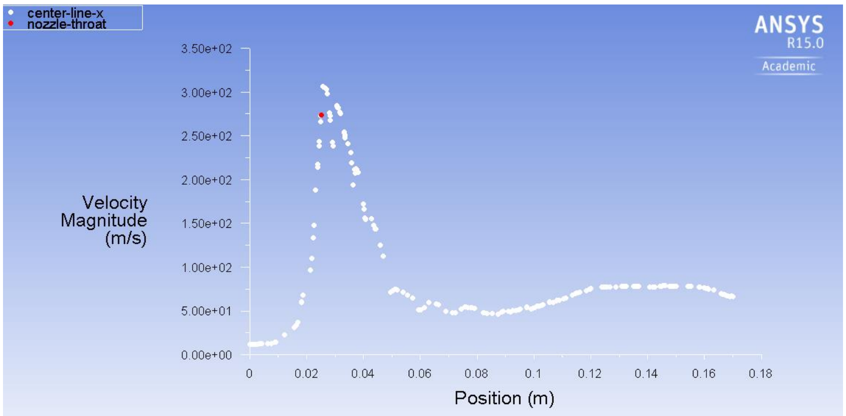


Figure A. 25 Diagram of a velocity Magnitude along the line of the centre in the Group A case $d_1$= 6 mm ($\dot{m}_1$ = 0.01 kg/s)

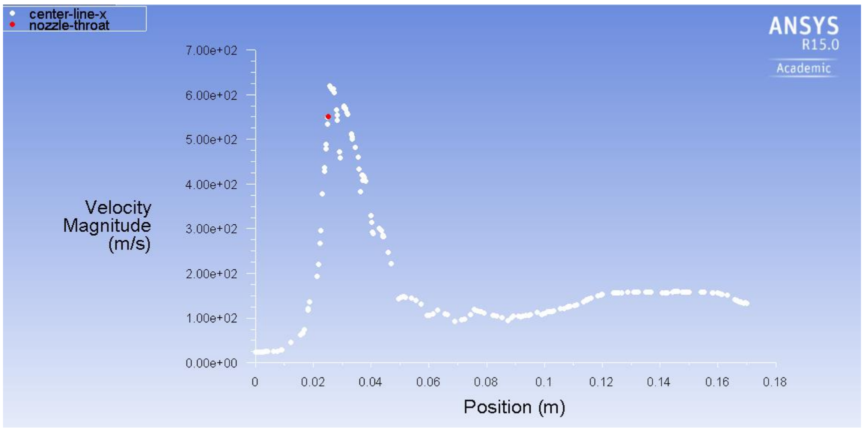


Figure A. 26 Diagram of a velocity Magnitude along the line of the centre in the Group A case $d_1$= 6 mm ($\dot{m}_1$ = 0.02 kg/s)

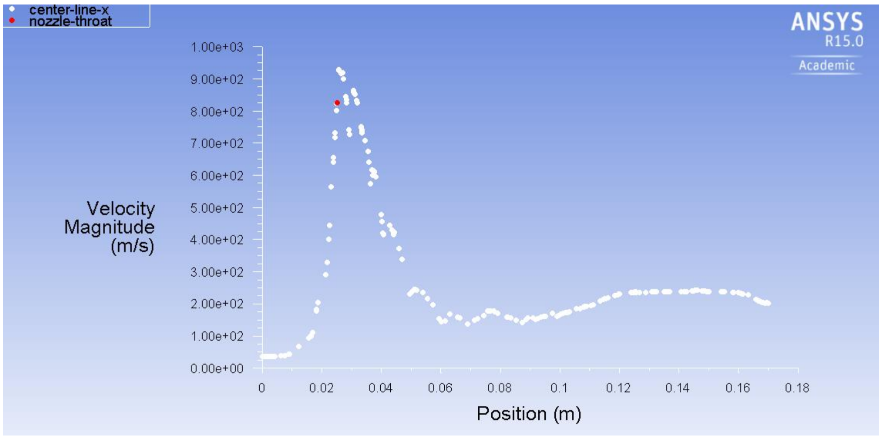


Figure A. 27 Diagram of a velocity Magnitude along the line of the centre in the Group A case $d_1$= 6 mm ($\dot{m}_1$ = 0.03 kg/s)

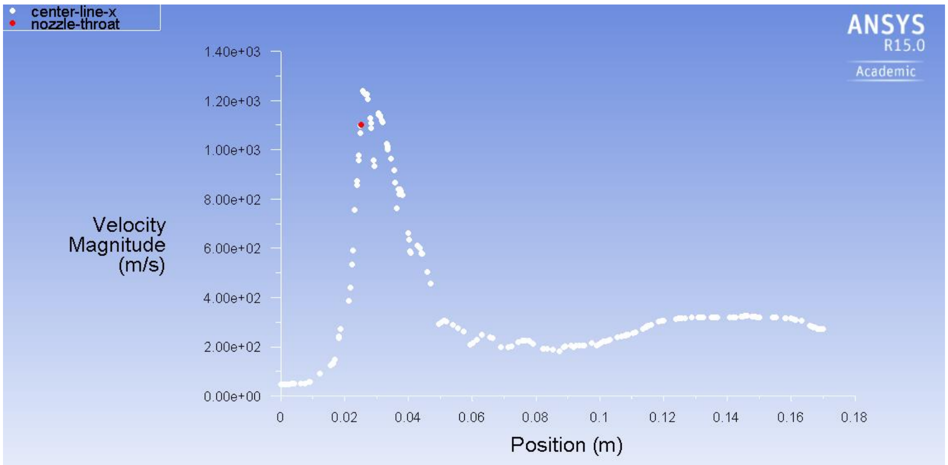


Figure A. 3 Diagram of a velocity Magnitude along the line of the centre in the Group A case $d_1$= 6 mm (ṁ1 = 0.04 kg/s)

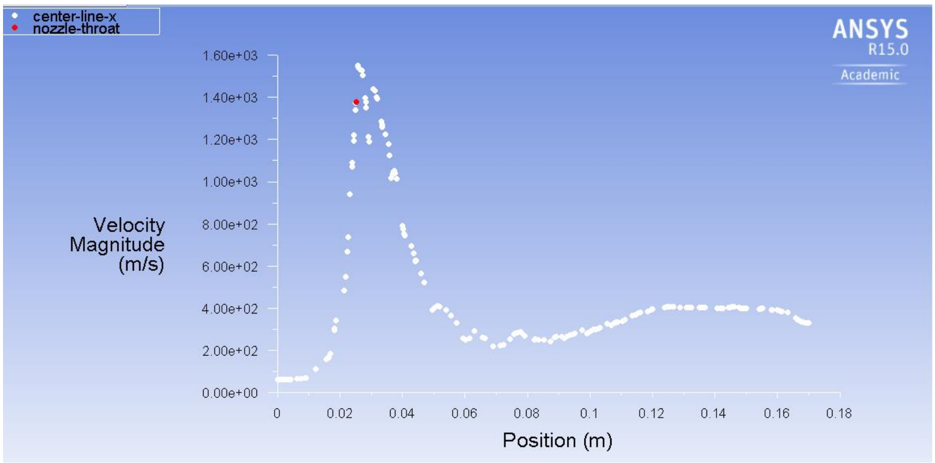


Figure A. 29 Diagram of a velocity Magnitude along the line of the centre in the Group A case $d_1$= 6 mm (ṁ1 = 0.05 kg/s)

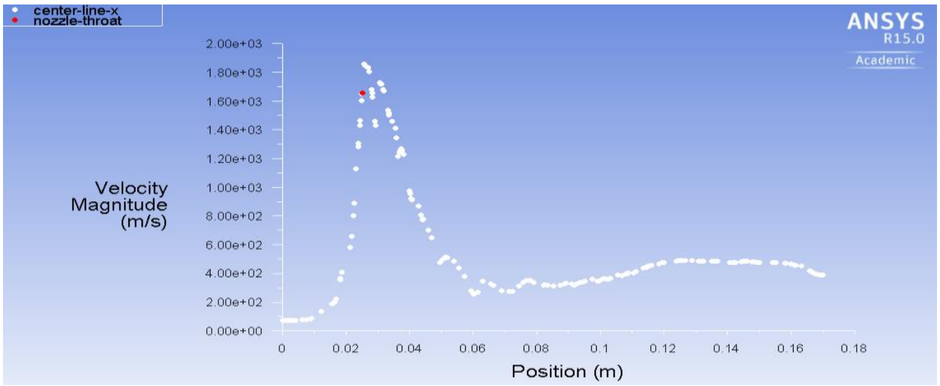


Figure A. 4 Diagram of a velocity Magnitude along the line of the centre in the Group A case $d_1$= 6 mm (ṁ1 = 0.06 kg/s)

**The plot diagram results of Group A simulations for $d_1$=7mm.**

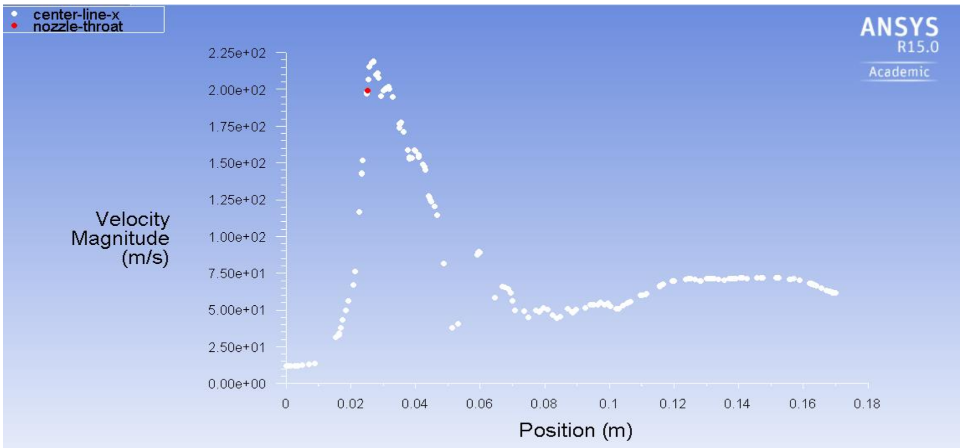


Figure A. 5 Diagram of a velocity Magnitude along the line of the centre in the Group A case $d_1$= 7 mm (ṁ1 = 0.01 kg/s)

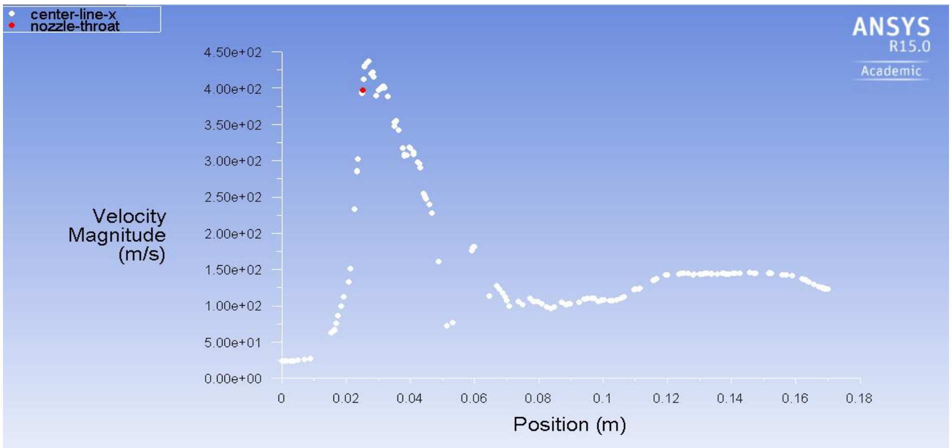


Figure A. 6 Diagram of a velocity Magnitude along the line of the centre in the Group A case $d_1$= 7 mm (ṁ1 = 0.02 kg/s)

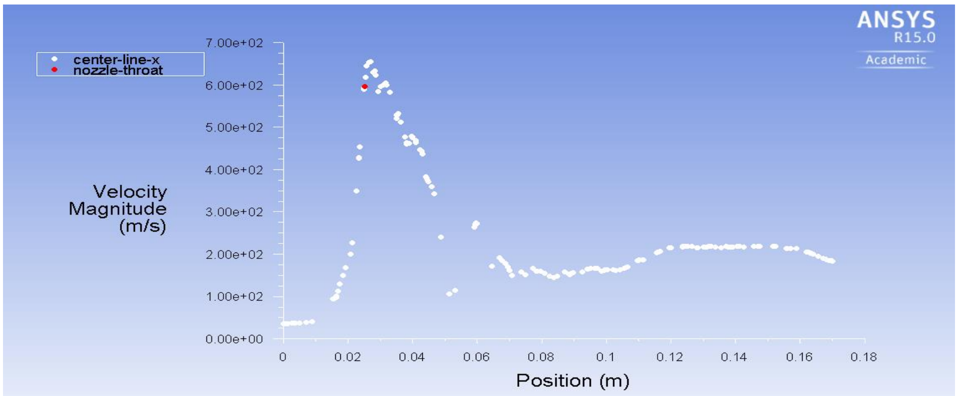


Figure A. 7 Diagram of a velocity Magnitude along the line of the centre in the Group A case $d_1$= 7 mm (ṁ1 = 0.03 kg/s)

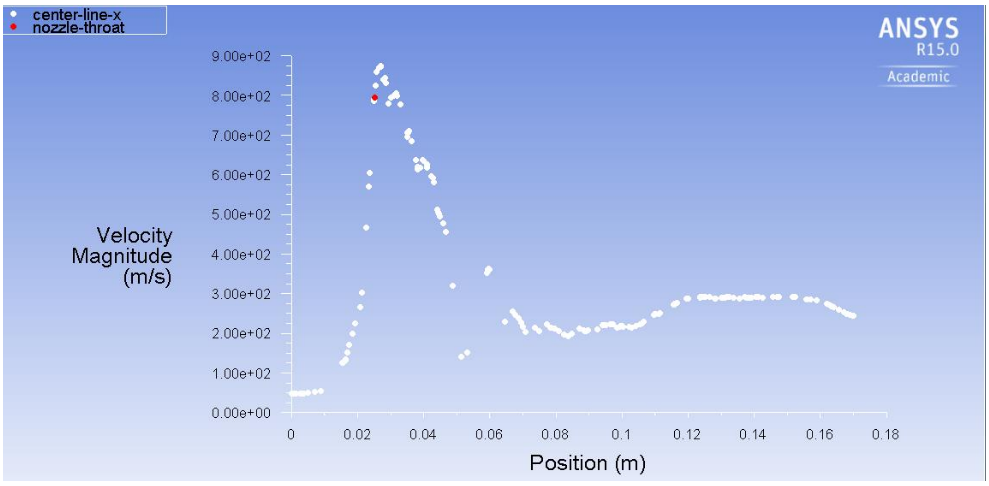


Figure A. 8 Diagram of a velocity Magnitude along the line of the centre in the Group A case $d_1$= 7 mm ($\dot{m}1$ = 0.04 kg/s)

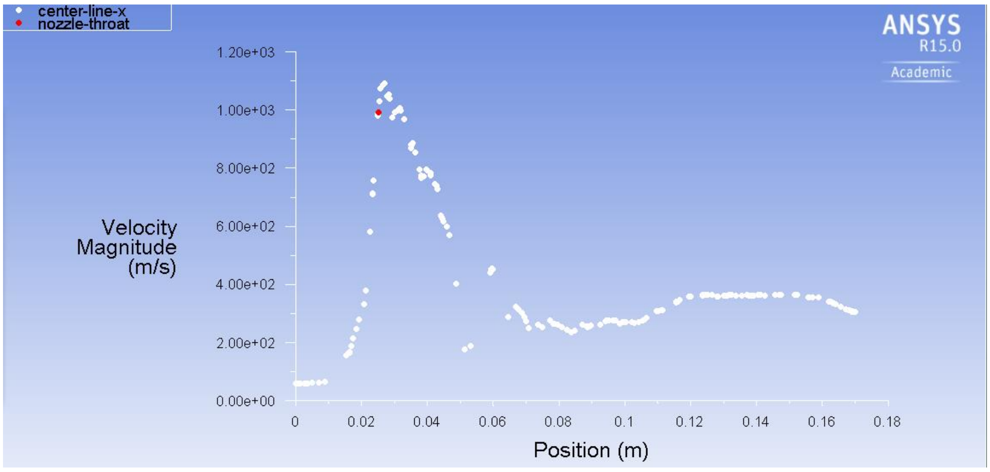


Figure A. 9 Diagram of a velocity Magnitude along the line of the centre in the Group A case d1= 7 mm ($\dot{m}1$ = 0.05 kg/s)

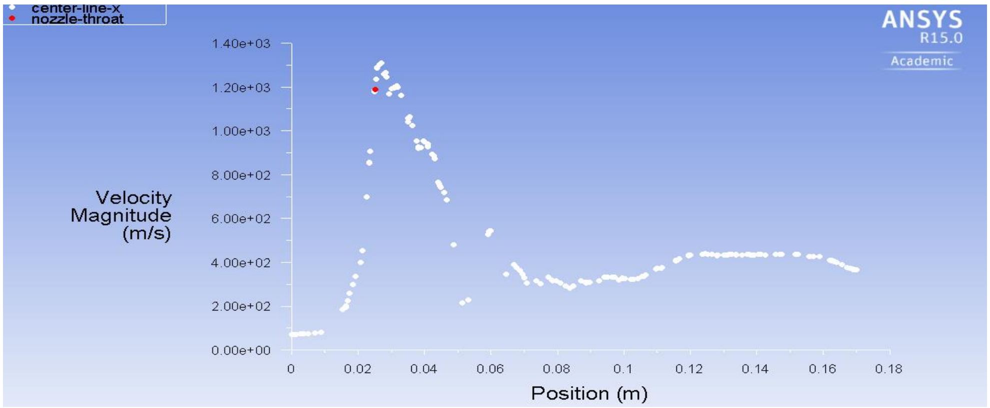


Figure A. 10 Diagram of a velocity Magnitude along the line of the centre in the Group A case $d_1$= 7 mm ($\dot{m}1$ = 0.06 kg/s)

**The plot for the velocity Magnitude diagram results of Group B simulations for the lengths of the mixing chamber $L_2$ =60mm.**

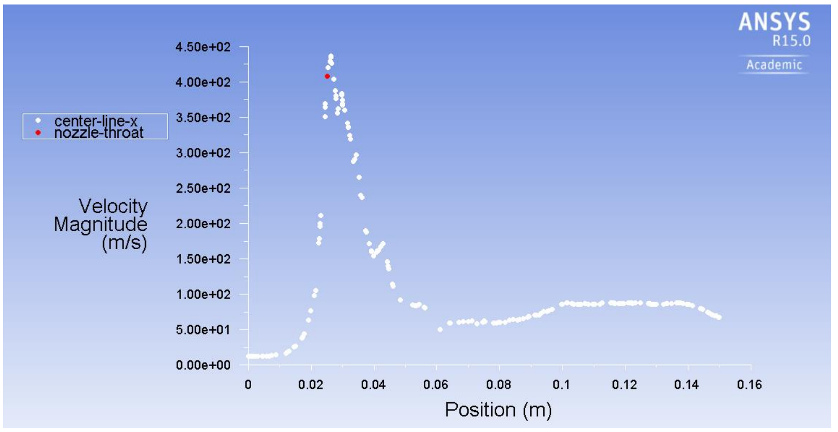


Figure A. 37 Diagram of a velocity Magnitude along the line of the centre in the Group B case L2= 60 mm (ṁ1 = 0.01 kg/s)

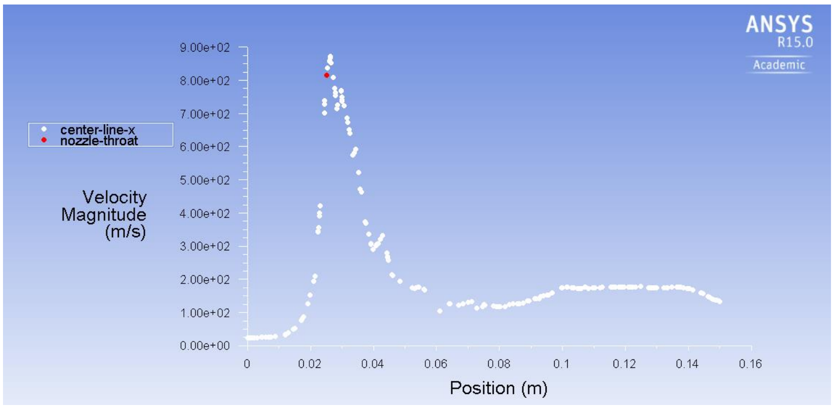


Figure A. 11 Diagram of a velocity Magnitude along the line of the centre in the Group B case $L_2$= 60 mm ($\dot{m}_1$ = 0.02 kg/s)

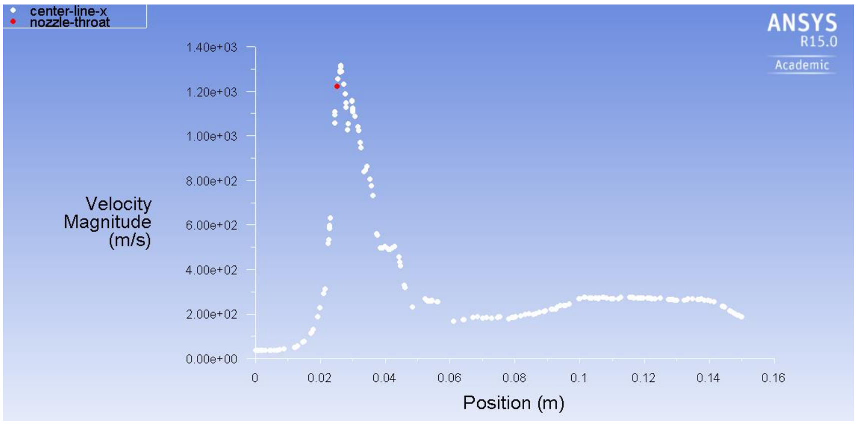


Figure A. 39 Diagram of a velocity Magnitude along the line of the centre in the Group B case $L_2$= 60 mm ($\dot{m}_1$ = 0.03 kg/s)

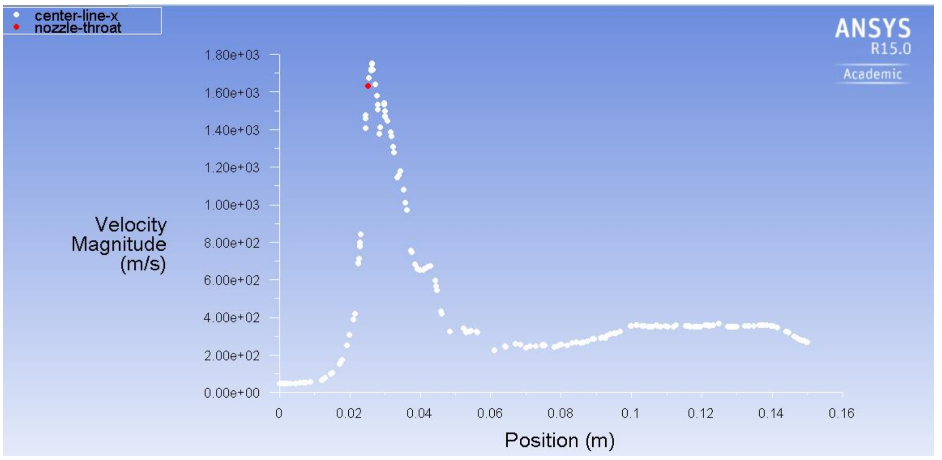


Figure A. 12 Diagram of a velocity Magnitude along the line of the centre in the Group B case $L_2$= 60 mm ($\dot{m}_1$ = 0.04 kg/s)

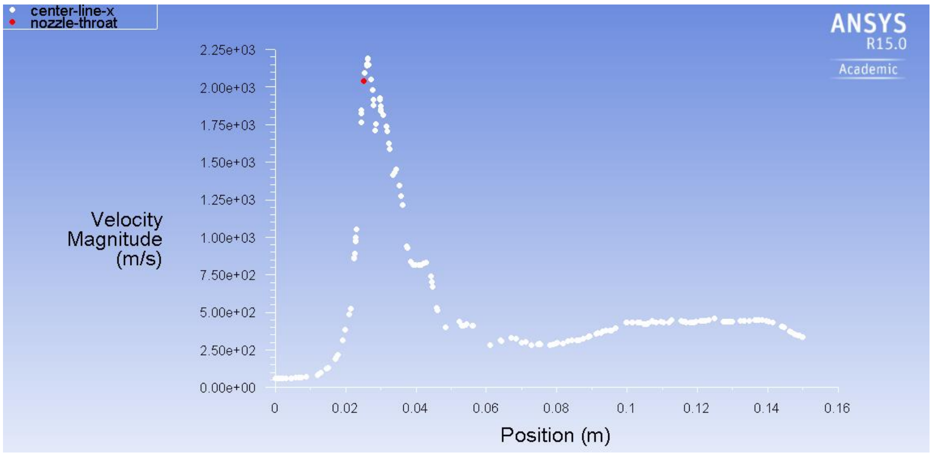


Figure A. 13 Diagram of a velocity Magnitude along the line of the centre in the Group B case $L_2$= 60 mm ($\dot{m}_1$ = 0.05 kg/s)

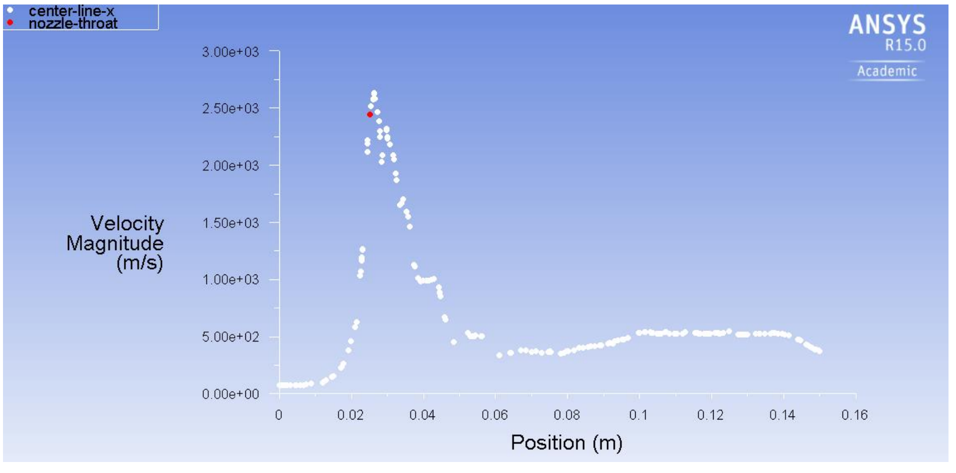


Figure A. 14 Diagram of a velocity Magnitude along the line of the centre in the Group B case L2= 60 mm ($\dot{m}1$ = 0.06 kg/s)

**The plot for the velocity Magnitude diagram results of Group B simulations for the lengths of the mixing chamber $L_2$ =70mm**

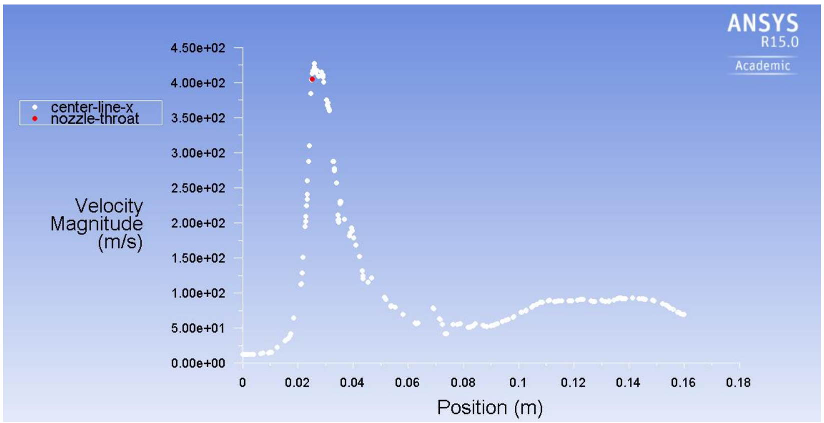


Figure A. 15 Diagram of a velocity Magnitude along the line of the centre in the Group B case L2= 70 mm (ṁ1 = 0.01 kg/s)

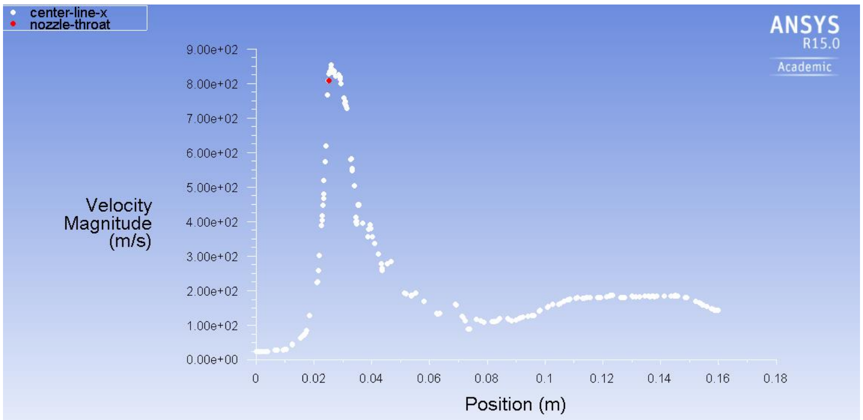


Figure A. 16 Diagram of a velocity Magnitude along the line of the centre in the Group B case L2= 70 mm (ṁ1 = 0.02 kg/s)

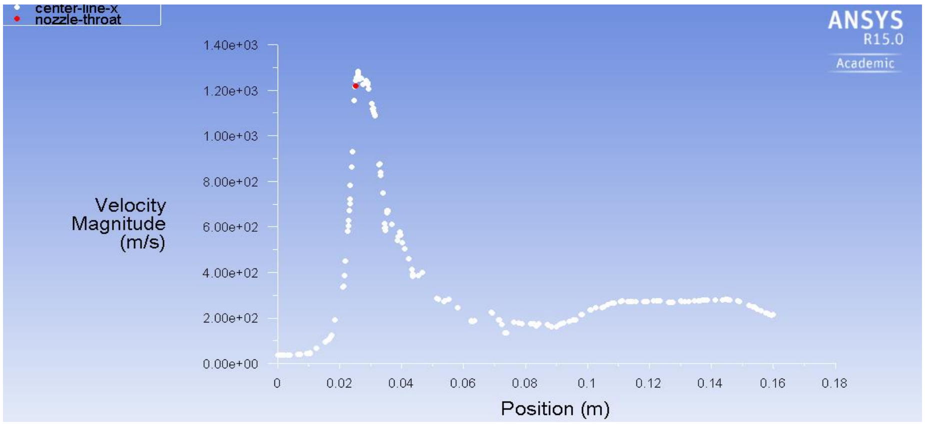


Figure A. 17 Diagram of a velocity Magnitude along the line of the centre in the Group B case L2= 70 mm (ṁ1 = 0.03 kg/s)

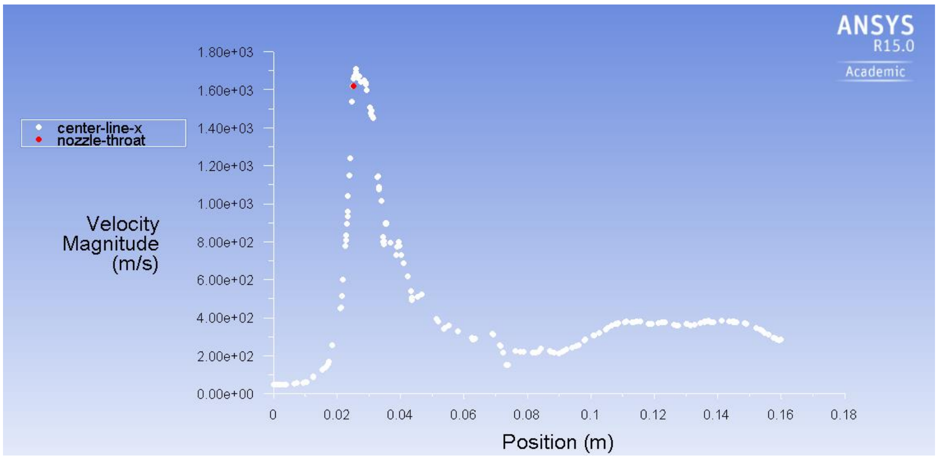


Figure A. 18 Diagram of a velocity Magnitude along the line of the centre in the Group B case L2= 70 mm (ṁ1 = 0.04 kg/s)

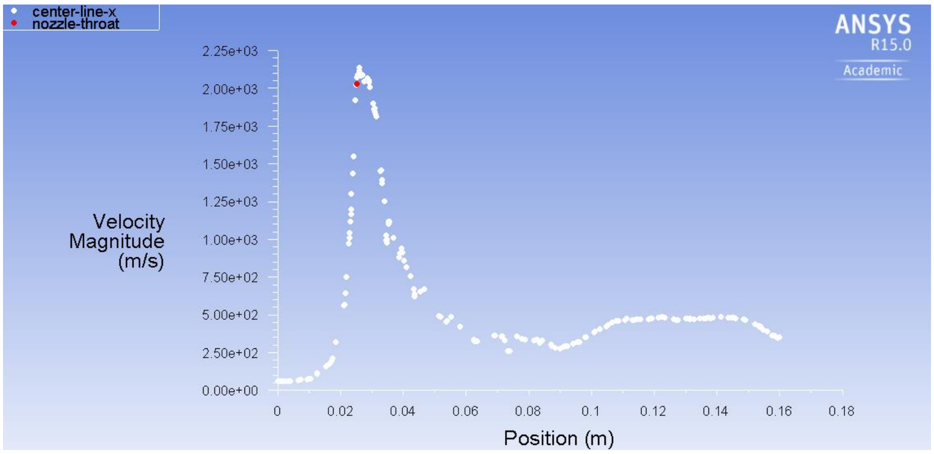


Figure A. 19 Diagram of a velocity Magnitude along the line of the centre in the Group B case L2= 70 mm (ṁ1 = 0.05 kg/s)

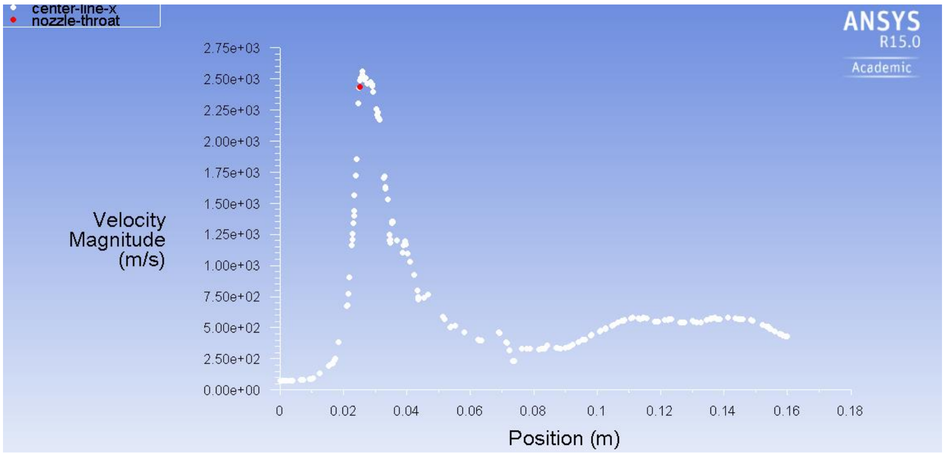


Figure A. 20 Diagram of a velocity Magnitude along the line of the centre in the Group B case L2= 70 mm (ṁ1 = 0.06 kg/s)

**The plot for the velocity Magnitude diagram results of Group B simulations for the lengths of the mixing chamber $L_2$ =90mm**

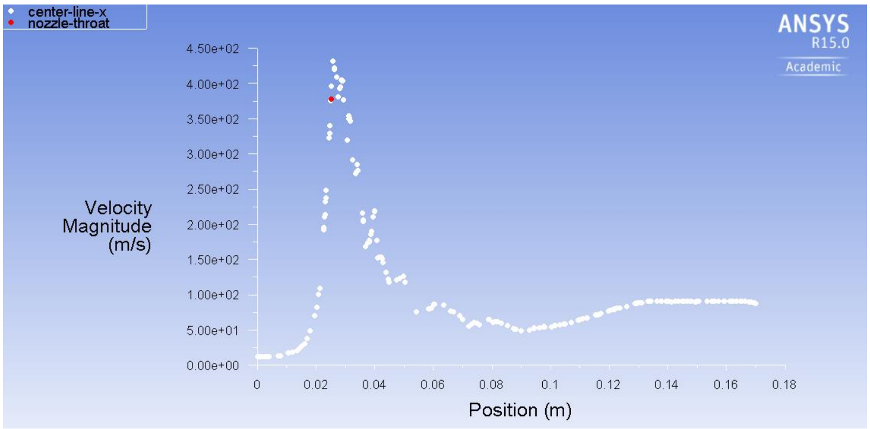


Figure A. 49 Diagram of a velocity Magnitude along the line of the centre in the Group B case L2= 90 mm (ṁ1 = 0.01 kg/s)

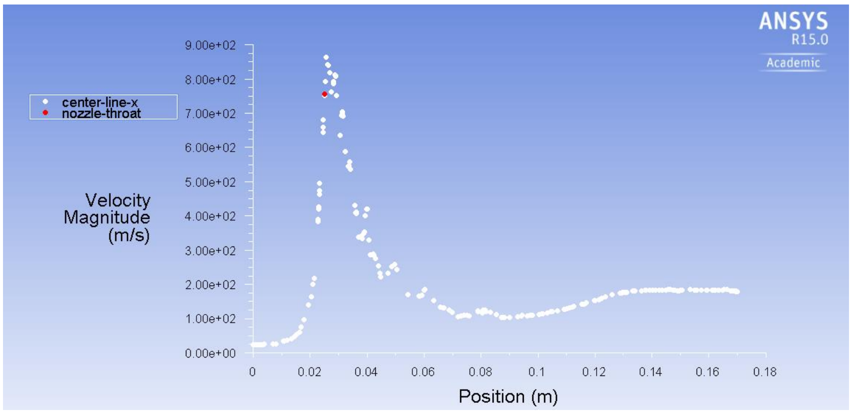


Figure A. 21 Diagram of a velocity Magnitude along the line of the centre in the Group B case L2= 90 mm (ṁ1 = 0.02 kg/s)

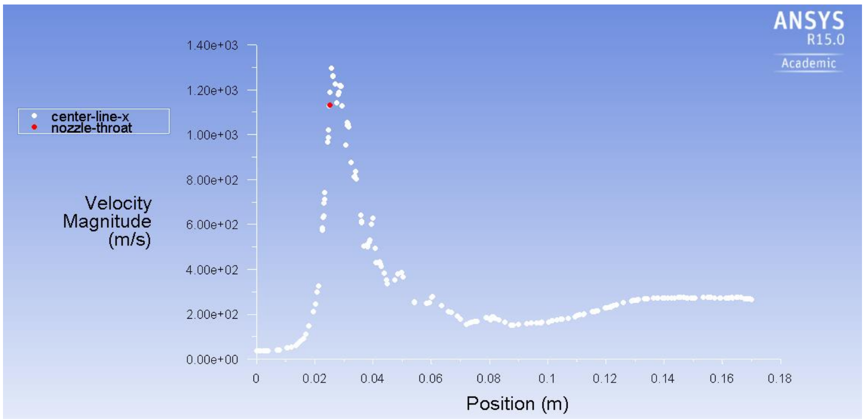


Figure A. 22 Diagram of a velocity Magnitude along the line of the centre in the Group B case L2= 90 mm (ṁ1 = 0.03 kg/s)

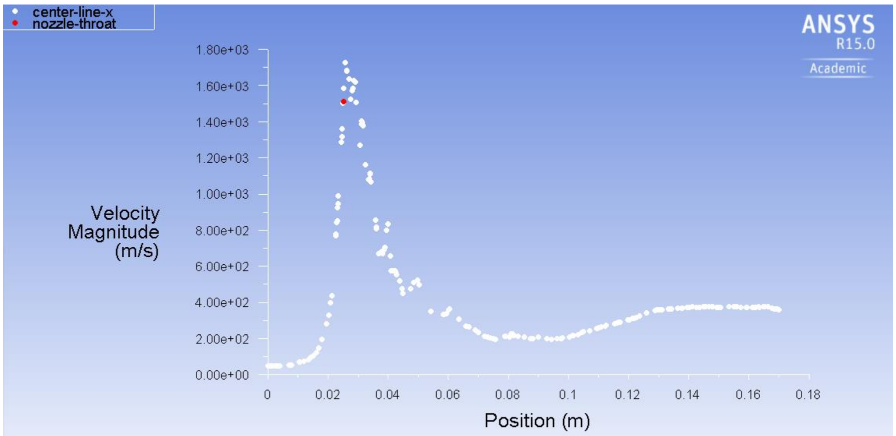


Figure A. 23 Diagram of a velocity Magnitude along the line of the centre in the Group B case L2= 90 mm (ṁ1 = 0.04 kg/s)

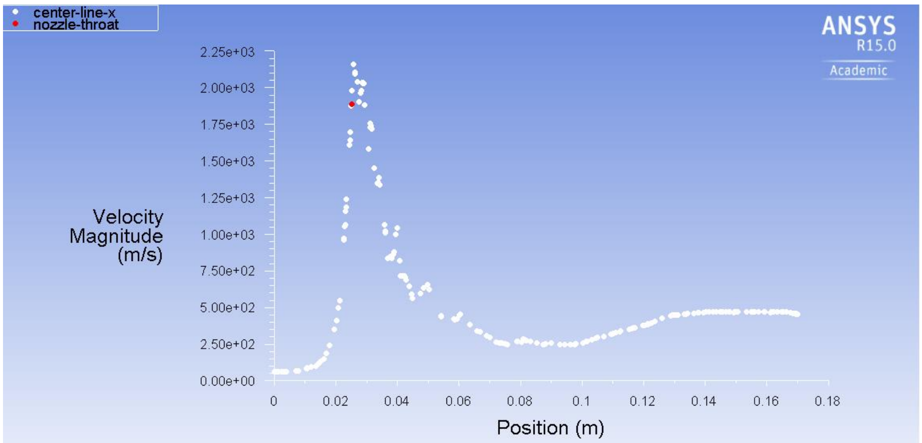


Figure A. 24 Diagram of a velocity Magnitude along the line of the centre in the Group B case L2= 90 mm (ṁ1 = 0.05 kg/s)

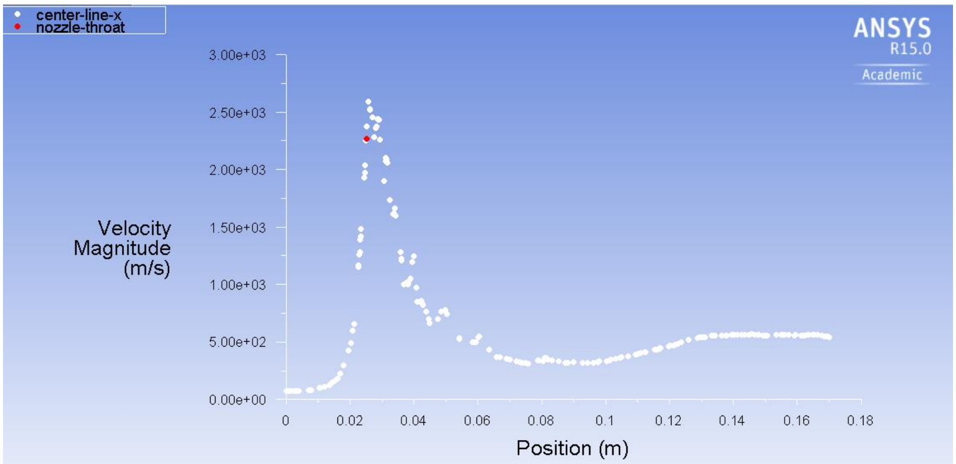


Figure A. 25 Diagram of a velocity Magnitude along the line of the centre in the Group B case L2= 90 mm (ṁ1 = 0.06 kg/s)

**The plot for the velocity Magnitude diagram results of Group B simulations for the lengths of the mixing chamber $L_2$ =1000mm**

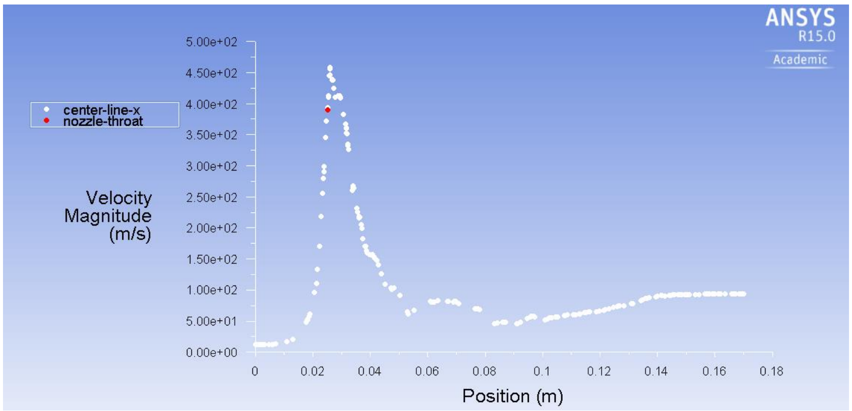


Figure A. 26 Diagram of a velocity Magnitude along the line of the centre in the Group B case L2= 100 mm (ṁ1 = 0.01 kg/s)

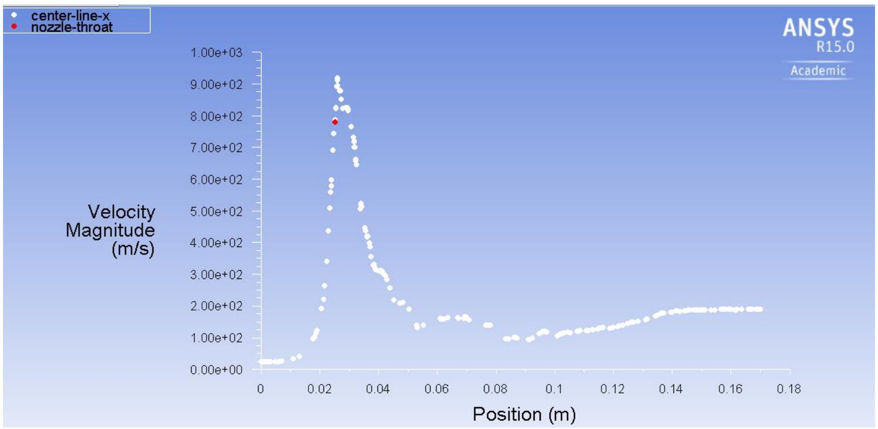


Figure A. 27 Diagram of a velocity Magnitude along the line of the centre in the Group B case L2= 100 mm (ṁ1 = 0.02 kg/s)

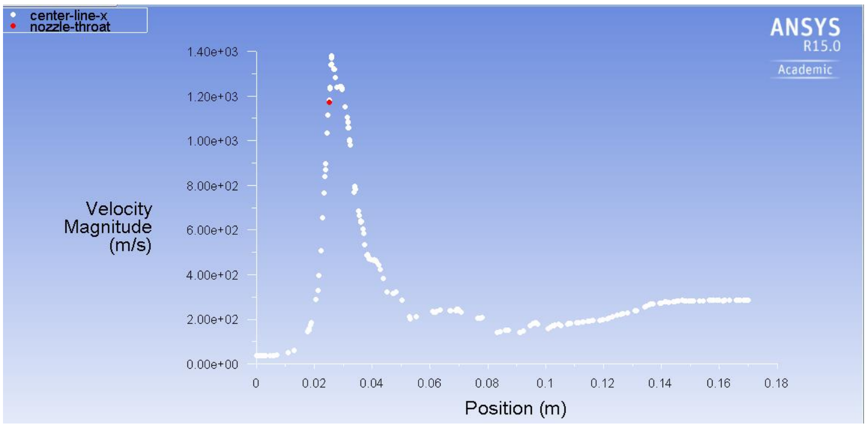


Figure A. 28 Diagram of a velocity Magnitude along the line of the centre in the Group B case L2= 100 mm (ṁ1 = 0.03 kg/s)

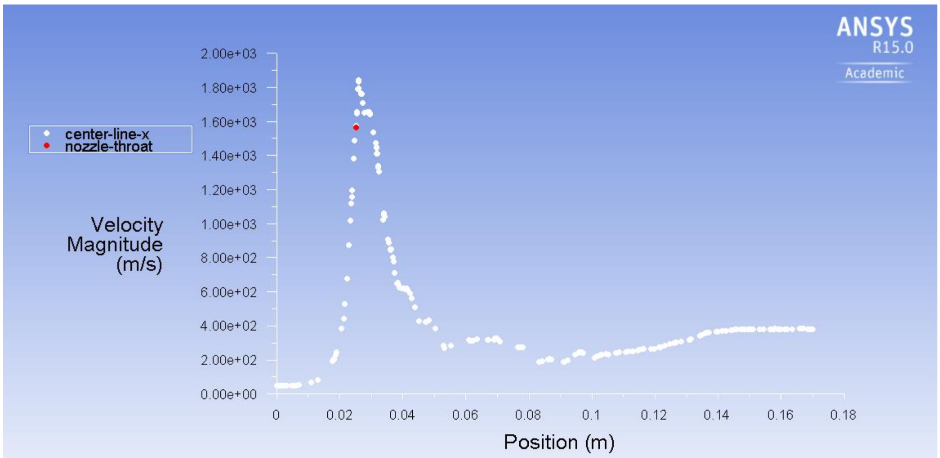


Figure A. 29 Diagram of a velocity Magnitude along the line of the centre in the Group B case L2= 100 mm (ṁ1 = 0.04 kg/s)

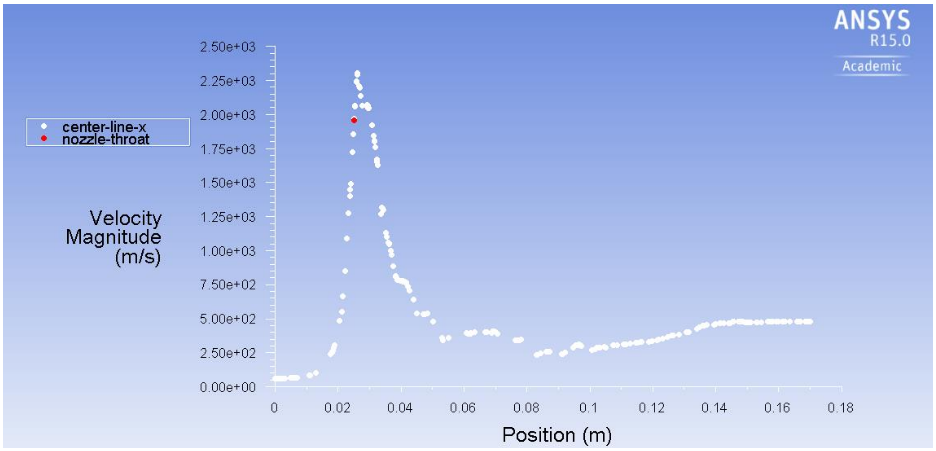


Figure A. 59 Diagram of a velocity Magnitude along the line of the centre in the Group B case L2= 100 mm (ṁ1 = 0.05 kg/s)

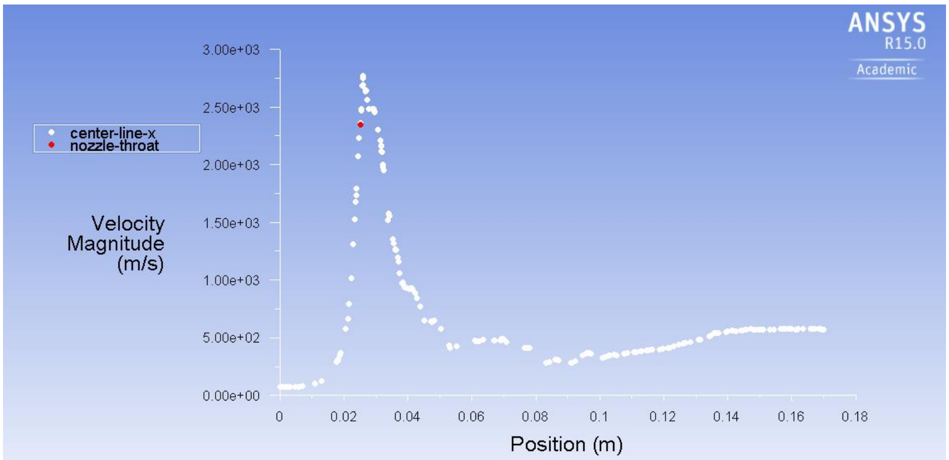


Figure A. 30 Diagram of a velocity Magnitude along the line of the centre in the Group B case $L_2$= 100 mm (ṁ1 = 0.06 kg/s)

**The plot for the velocity Magnitude diagram results of Group C simulations for the Jet pump throat L $_{throat}$ =20mm**

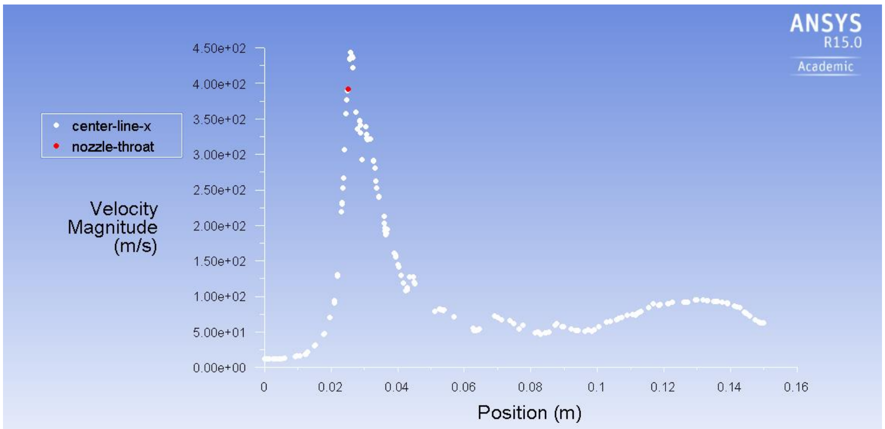


Figure A. 31 Diagram of a velocity Magnitude along the line of the centre in the Group C case L $_{throat}$ = 20 mm (ṁ1 = 0.01 kg/s

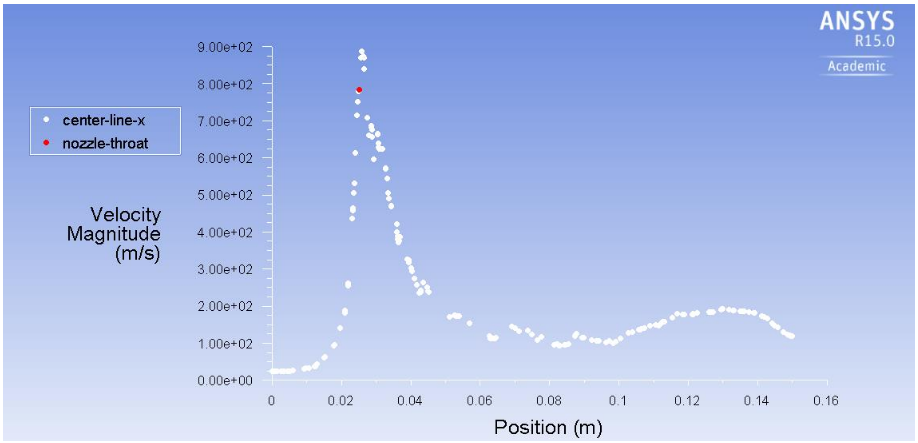


Figure A. 32 Diagram of a velocity Magnitude along the line of the centre in the Group C case L throat = 20 mm (ṁ1 = 0.02 kg/s)

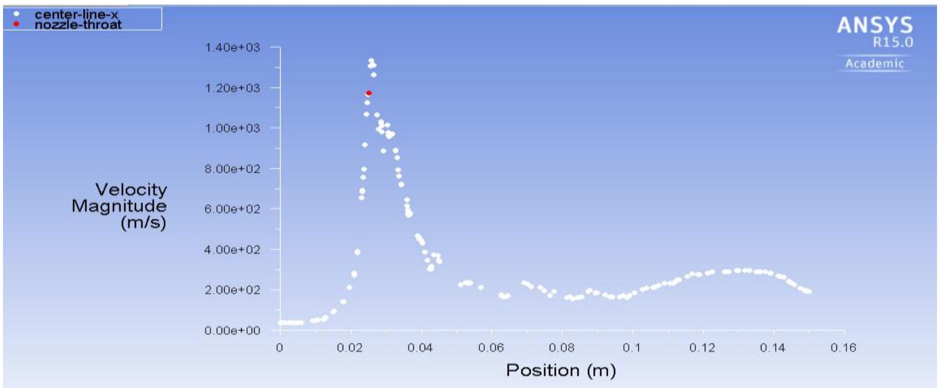


Figure A. 33 Diagram of a velocity Magnitude along the line of the centre in the Group C case L throat = 20 mm (ṁ1 = 0.03 kg/s)

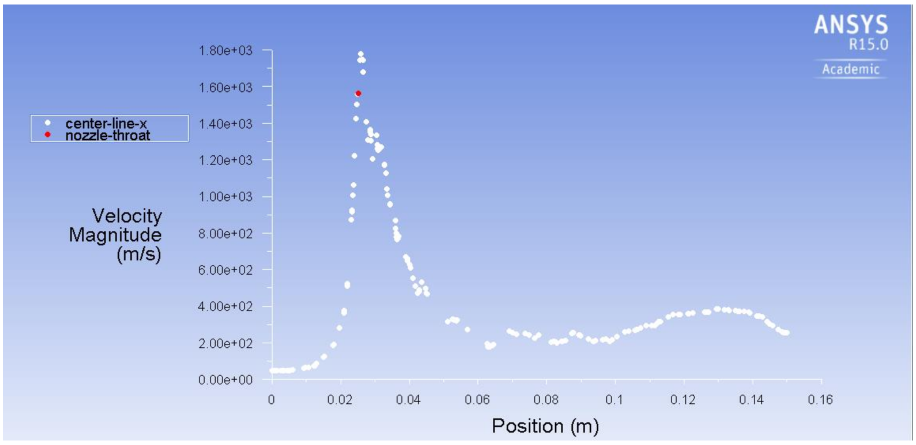


Figure A. 34 Diagram of a velocity Magnitude along the line of the centre in the Group C case L throat = 20 mm (ṁ1 = 0.04 kg/s)

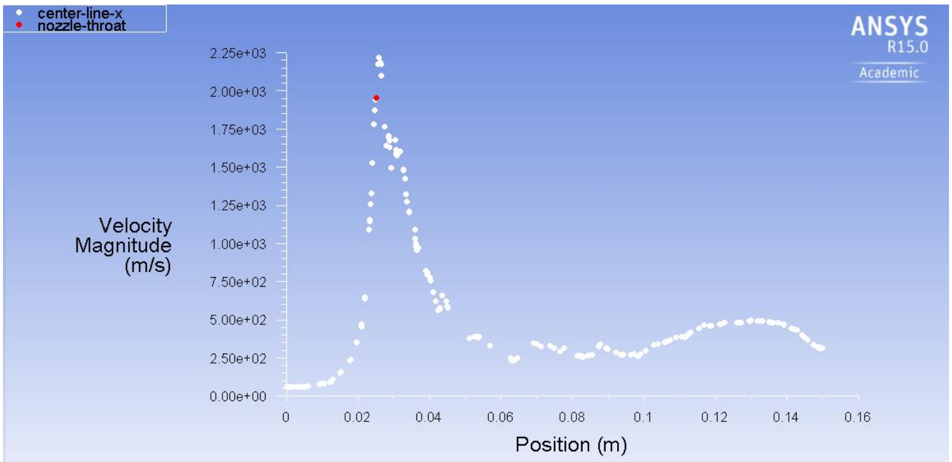


Figure A. 35 Diagram of a velocity Magnitude along the line of the centre in the Group C case L throat = 20 mm (ṁ1 = 0.05 kg/s)

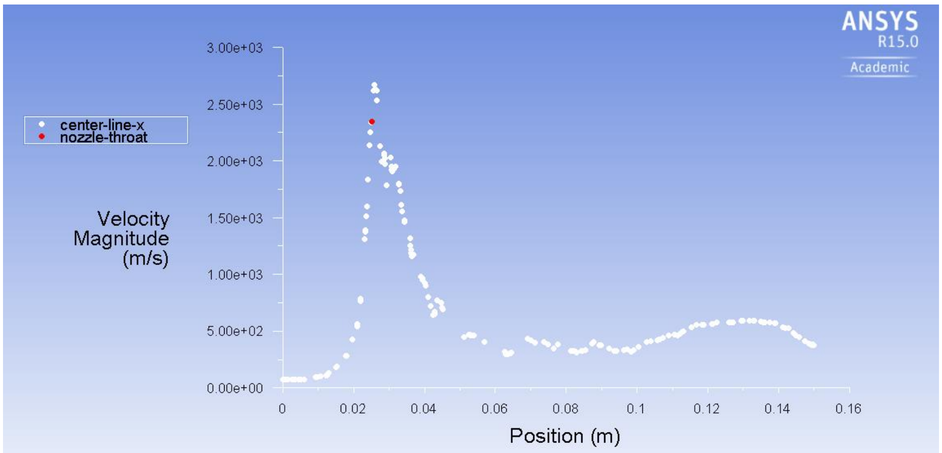


Figure A. 36 Diagram of a velocity Magnitude along the line of the centre in the Group C case L throat = 20 mm (ṁ1 = 0.06 kg/s)

**The plot for the velocity Magnitude diagram results of Group C simulations for the Jet pump throat L $_{throat}$ =30mm**

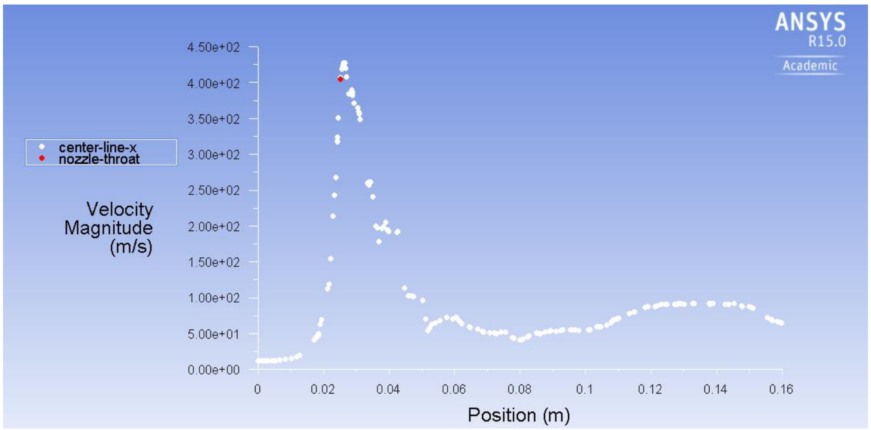


Figure A. 37 Diagram of a velocity Magnitude along the line of the centre in the Group C case L throat = 30 mm (ṁ1 = 0.01 kg/s)

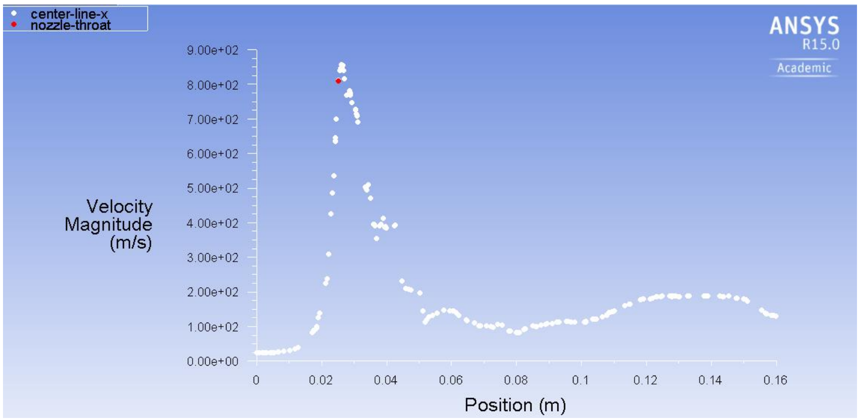


Figure A. 38 Diagram of a velocity Magnitude along the line of the centre in the Group C case L throat = 30 mm (ṁ1 = 0.02 kg/s)

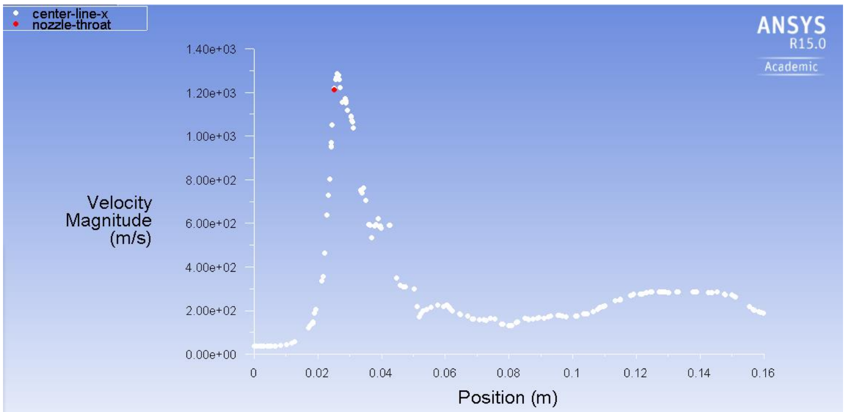


Figure A. 39 Diagram of a velocity Magnitude along the line of the centre in the Group C case L throat = 30 mm (ṁ1 = 0.03 kg/s)

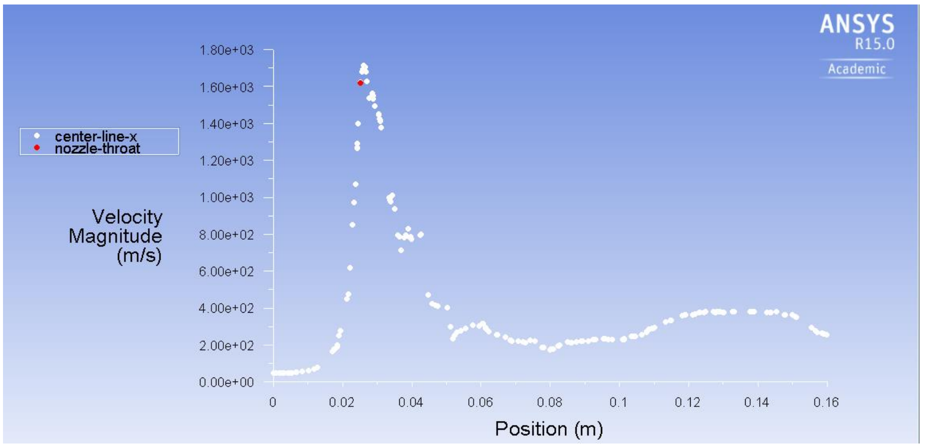


Figure A. 70 Diagram of a velocity Magnitude along the line of the centre in the Group C case L throat = 30 mm (ṁ1 = 0.04 kg/s)

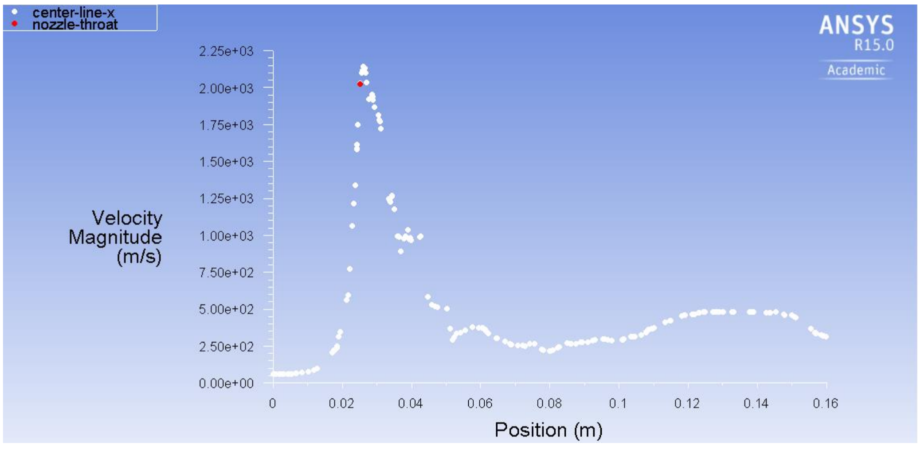


Figure A. 40 Diagram of a velocity Magnitude along the line of the centre in the Group C case L throat = 30 mm (ṁ1 = 0.05 kg/s)

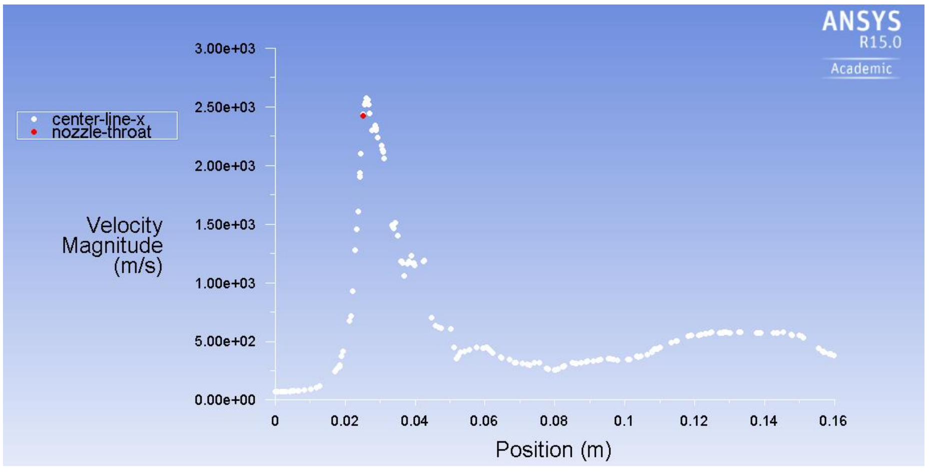


Figure A. 41 Diagram of a velocity Magnitude along the line of the centre in the Group C case L throat = 30 mm (ṁ1 = 0.06 kg/s)

**The plot for the velocity Magnitude diagram results of Group C simulations for the Jet pump throat L $_{throat}$ =50mm**

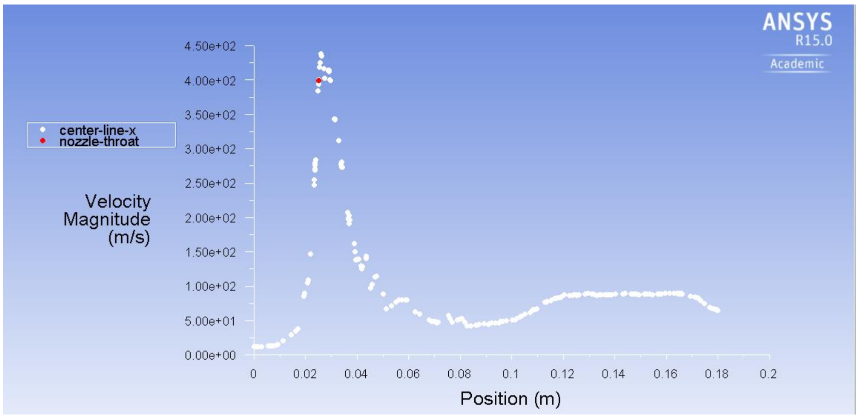


Figure A. 42 Diagram of a velocity Magnitude along the line of the centre in the Group C case L throat = 50 mm (ṁ1 = 0.01 kg/s)

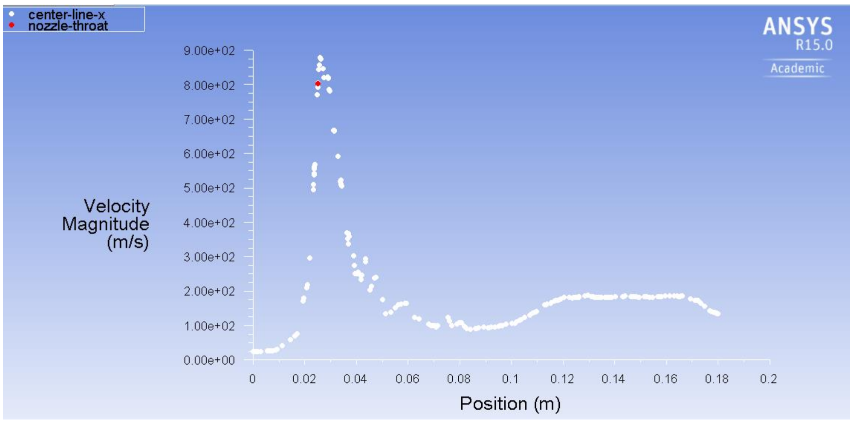


Figure A. 43 Diagram of a velocity Magnitude along the line of the centre in the Group C case L throat = 50 mm (ṁ1 = 0.02 kg/s)

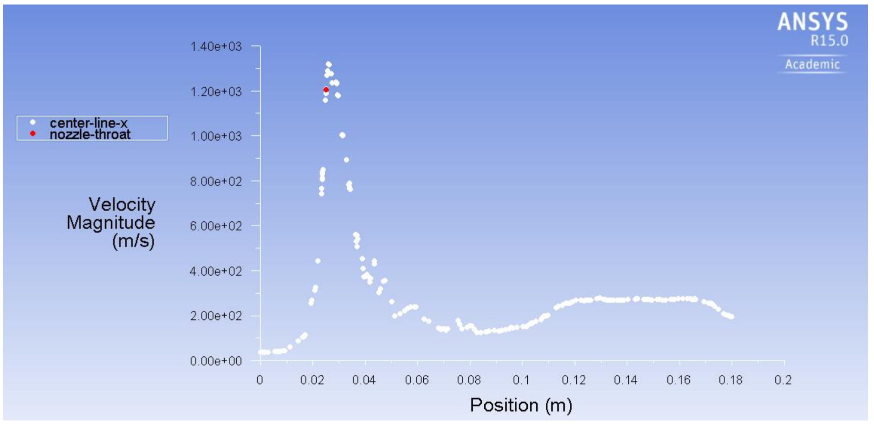


Figure A. 44 Diagram of a velocity Magnitude along the line of the centre in the Group C case L throat = 50 mm (ṁ1 = 0.03 kg/s)

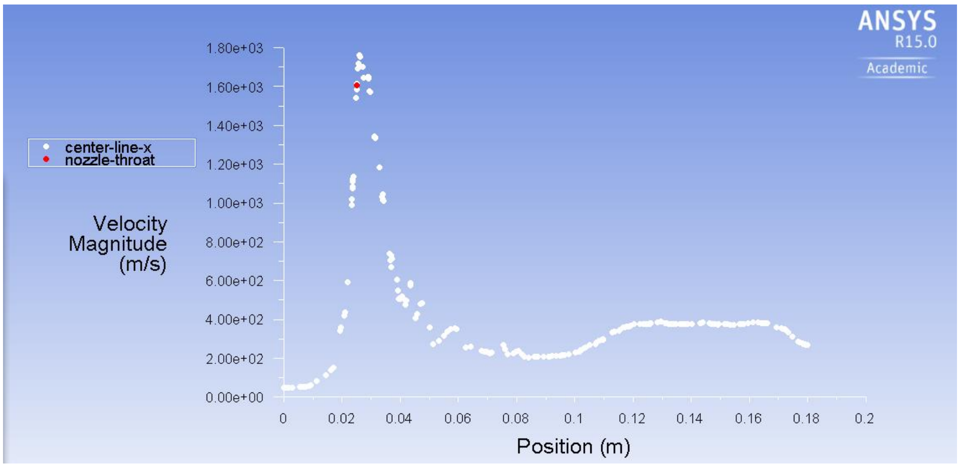


Figure A. 45 Diagram of a velocity Magnitude along the line of the centre in the Group C case L throat = 50 mm (ṁ1 = 0.04 kg/s)

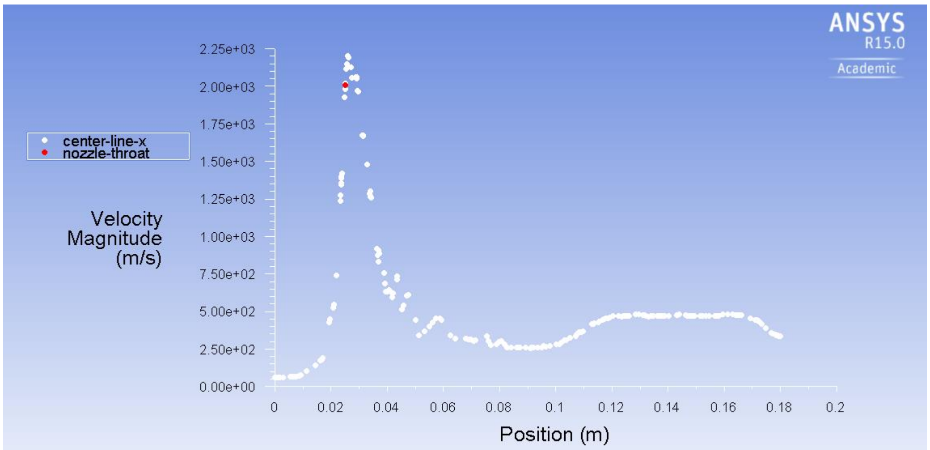


Figure A. 46 Diagram of a velocity Magnitude along the line of the centre in the Group C case L throat = 50 mm (ṁ1 = 0.05 kg/s)

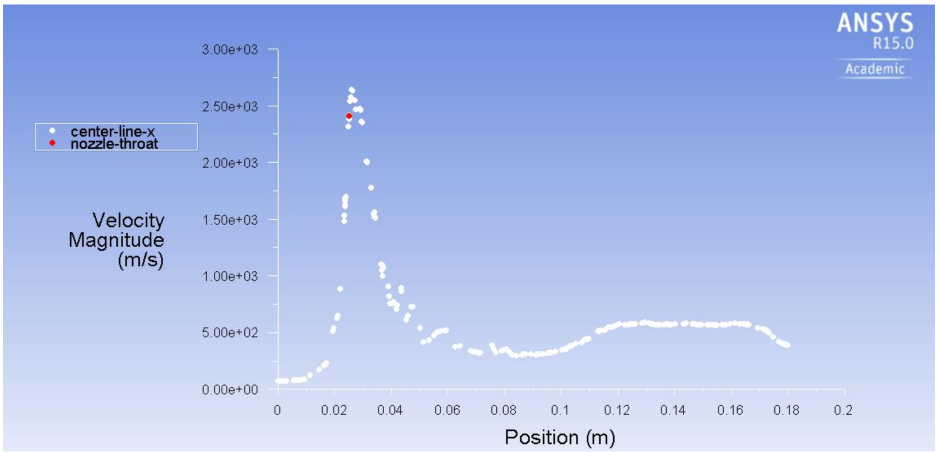


Figure A. 47 Diagram of a velocity Magnitude along the line of the centre in the Group C case L throat = 50 mm (ṁ1 = 0.06 kg/s)

**The plot for the velocity Magnitude diagram results of Group C simulations for the Jet pump throat L $_{throat}$ =60mm**

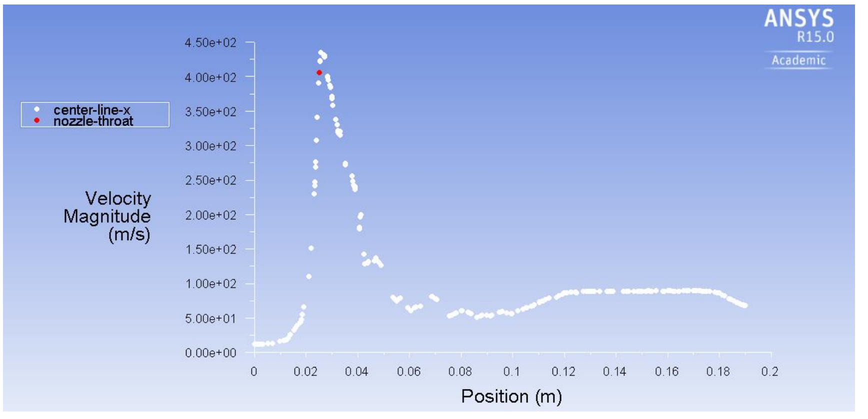


Figure A. 79 Diagram of a velocity Magnitude along the line of the centre in the Group C case L throat = 60 mm (ṁ1 = 0.01 kg/s)

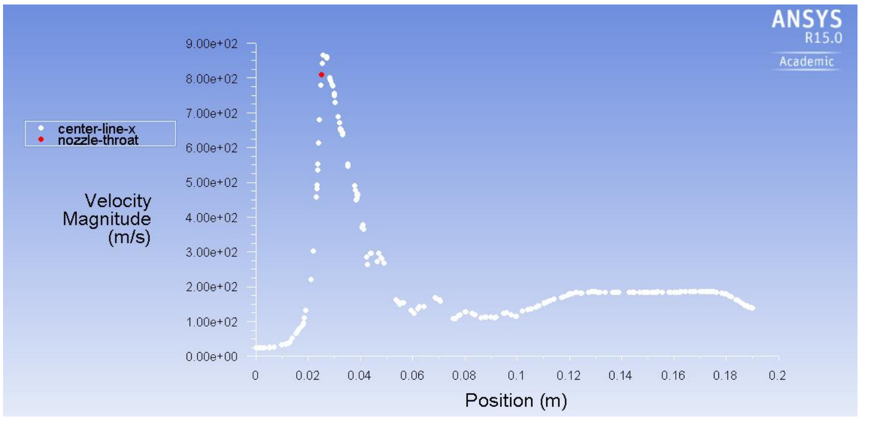


Figure A. 48 Diagram of a velocity Magnitude along the line of the centre in the Group C case L throat = 60 mm (ṁ1 = 0.02 kg/s)

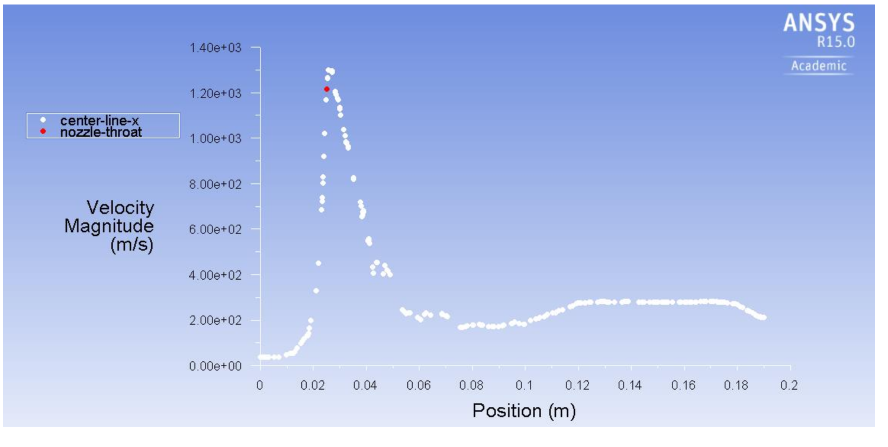


Figure A. 49 Diagram of a velocity Magnitude along the line of the centre in the Group C case L throat = 60 mm (ṁ1 = 0.03 kg/s)

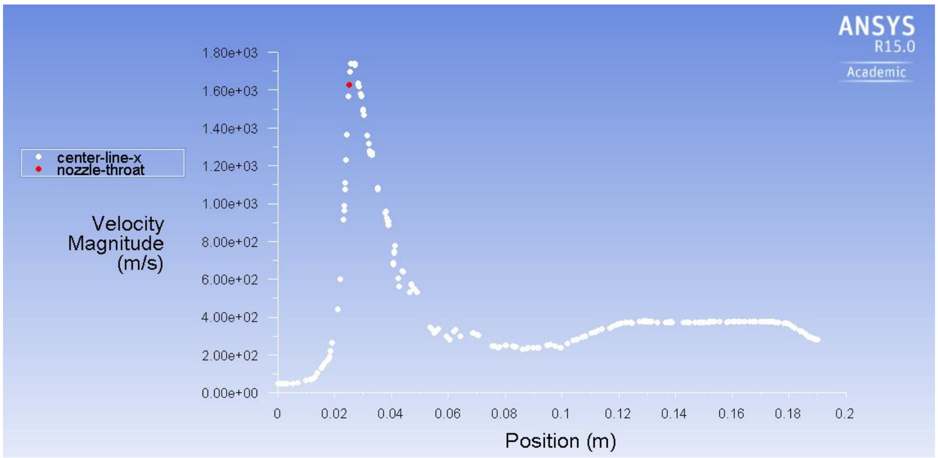


Figure A. 50 Diagram of a velocity Magnitude along the line of the centre in the Group C case L throat = 60 mm (ṁ1 = 0.04 kg/s)

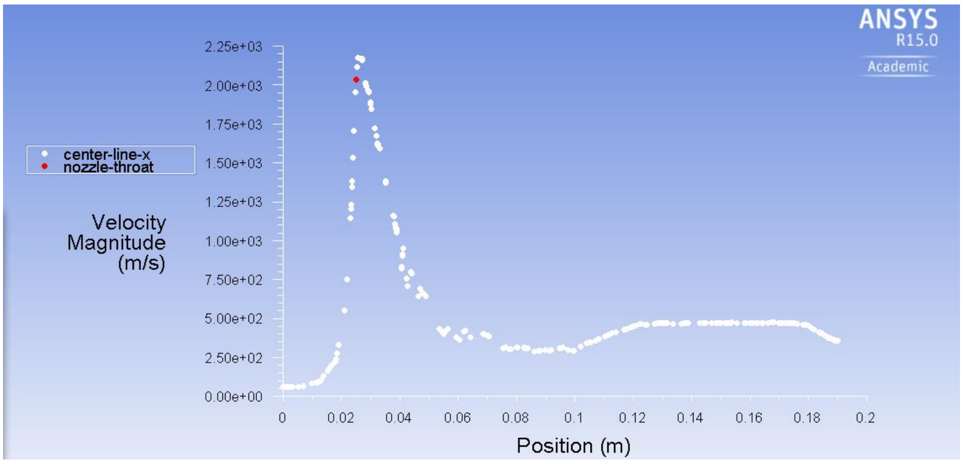


Figure A. 51 Diagram of a velocity Magnitude along the line of the centre in the Group C case L throat = 60 mm (ṁ1 = 0.05 kg/s)

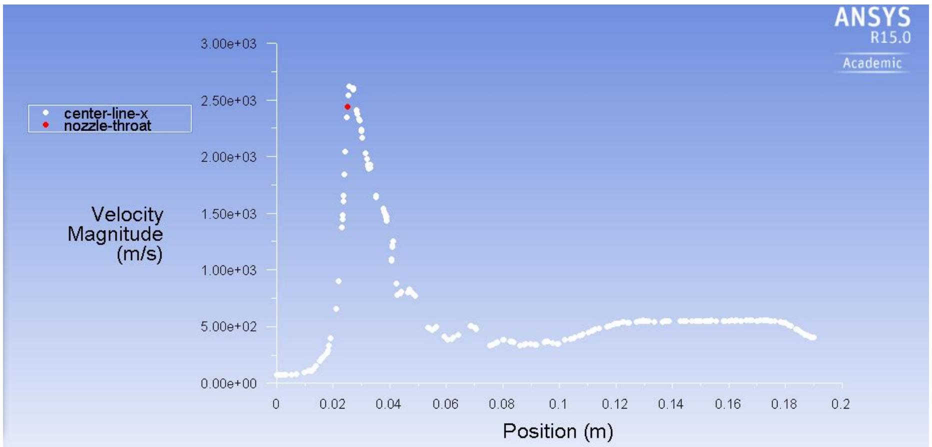


Figure A. 52 Diagram of a velocity Magnitude along the line of the centre in the Group C case $L_{throat}$ = 60 mm (ṁ1 = 0.06 kg/s)

# Appendix B

**Or-1st-30-2-10-80-40-0.01** | **Or-1st-30-2-10-80-40-0.02** | **Or-1st-30-2-10-80-40-0.03**

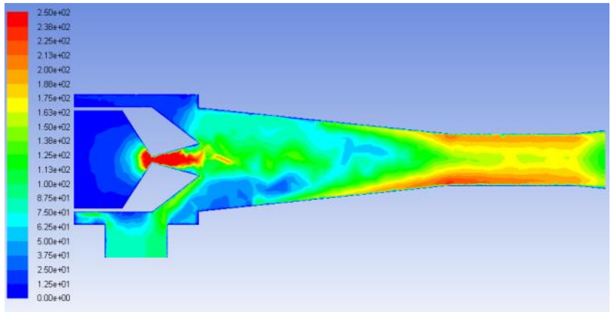

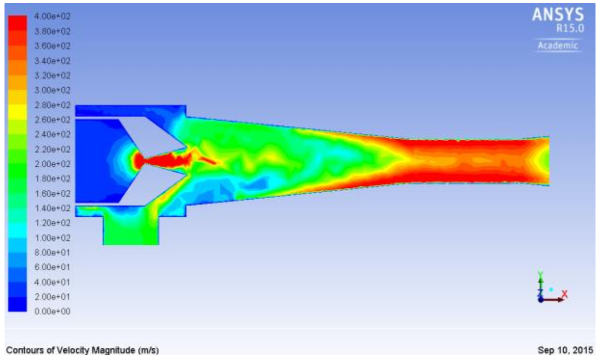


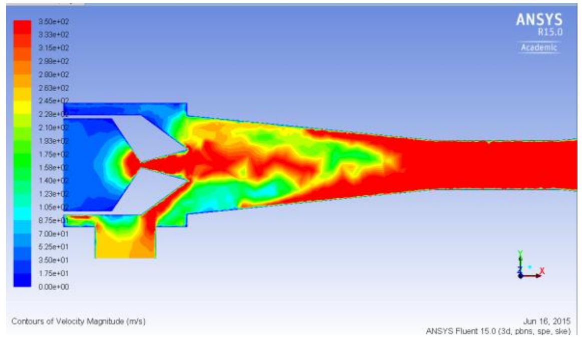


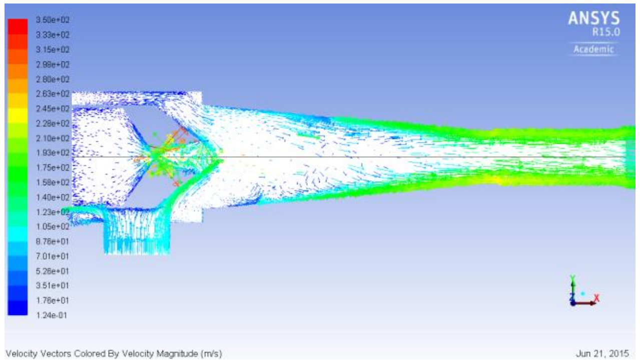


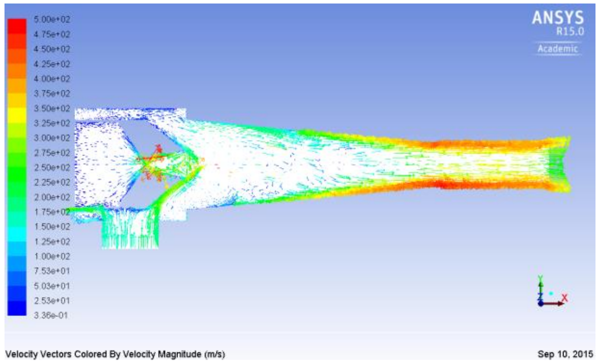


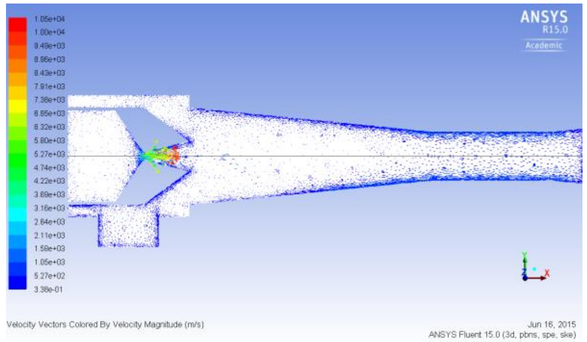

**Or-1st-30-2-10-80-40-0.04**

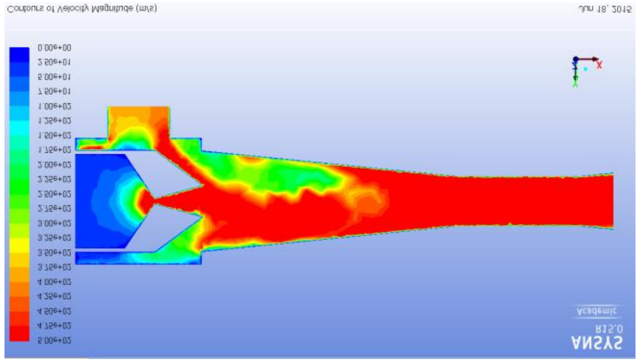


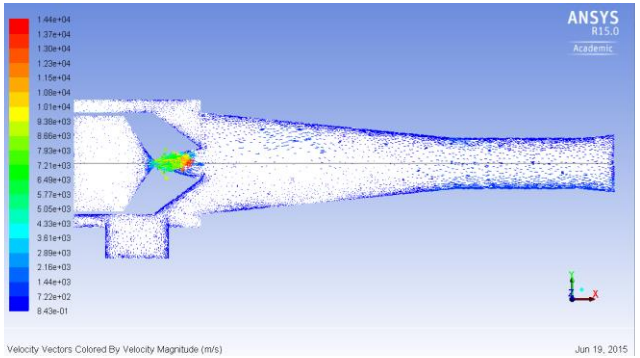


**Or-1st-30-2-10-80-40-0.05**

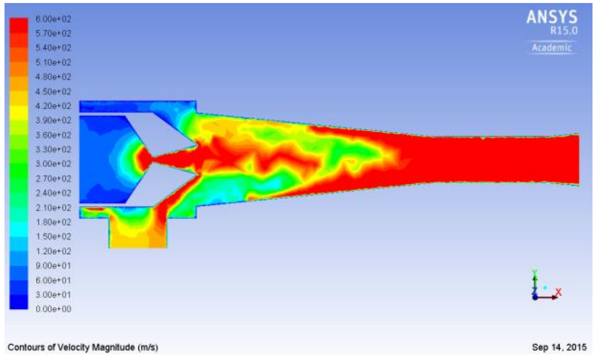


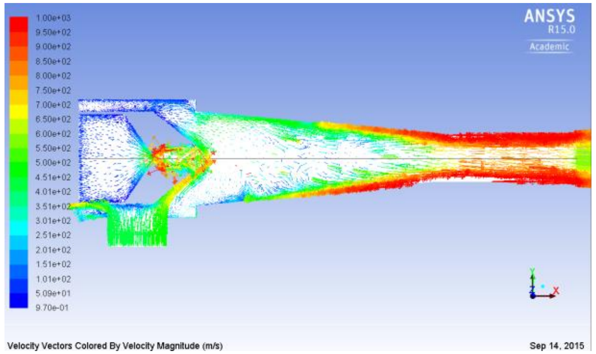


**Or-1st-30-2-10-80-40-0.06**

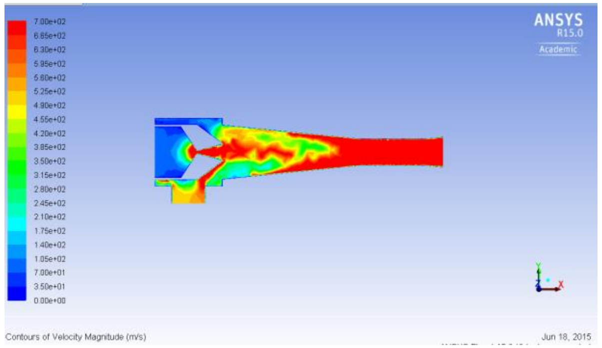


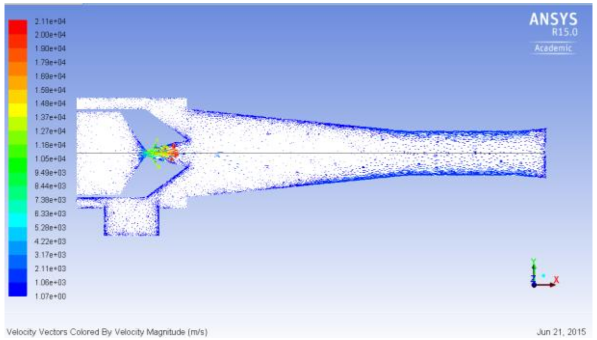

**Or-1st-30-3-10-80-40-0.01**

**Or-1st-30-3-10-80-40-0.02**

**Or-1st-30-3-10-80-40-0.03**

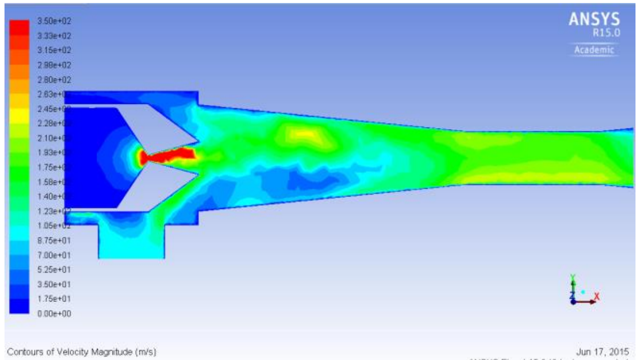


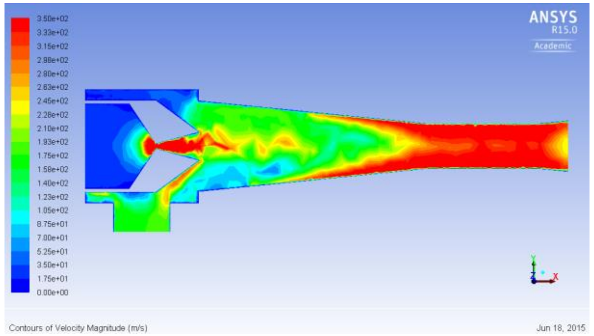


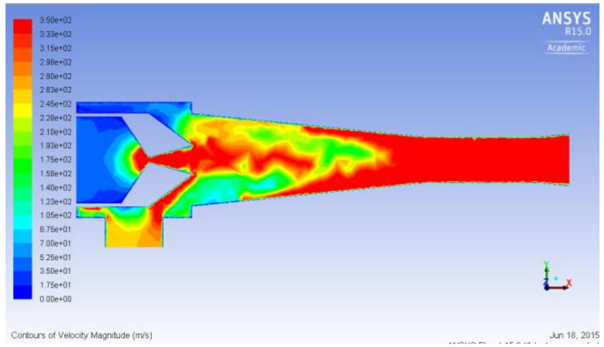


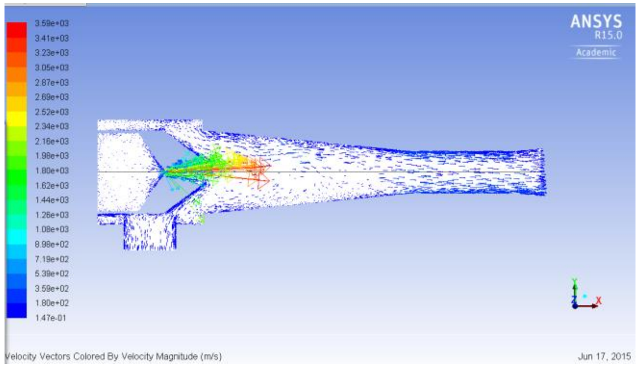


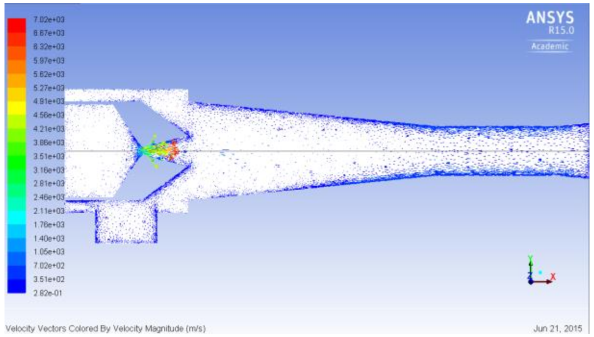


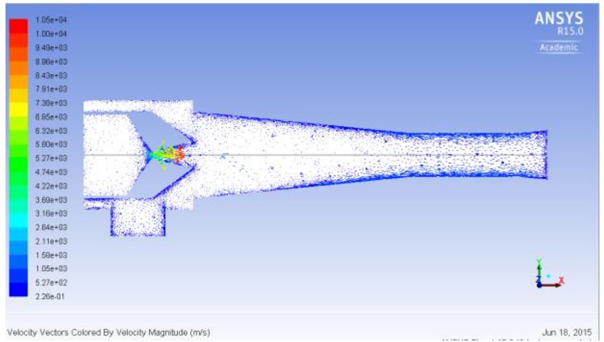

**Or-1st-30-3-10-80-40-0.04** **Or-1st-30-3-10-80-40-0.05** **Or-1st-30-3-10-80-40-0.06**

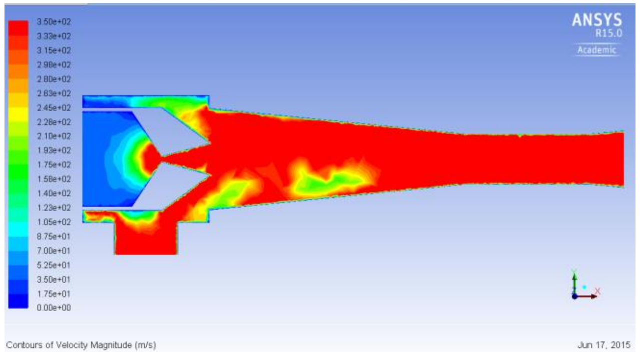


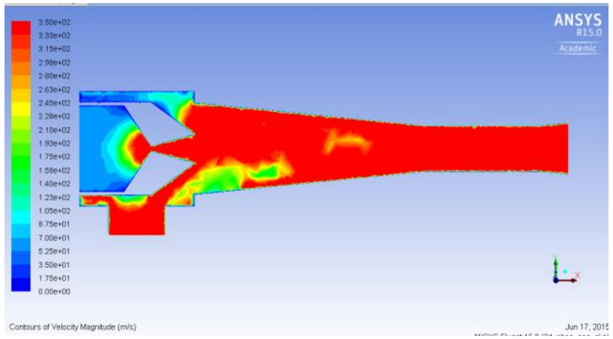


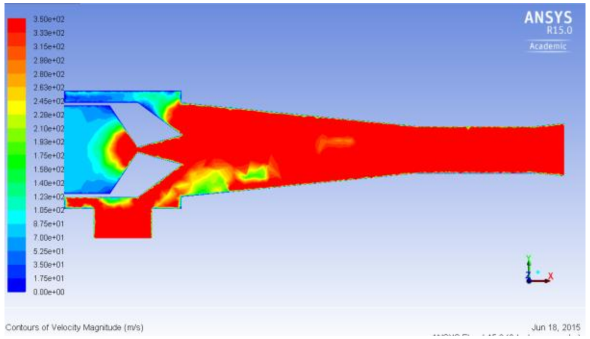


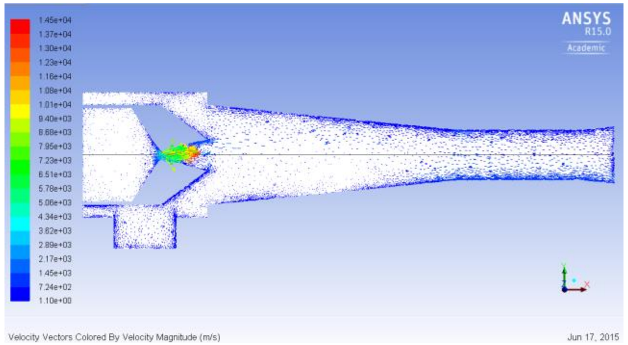


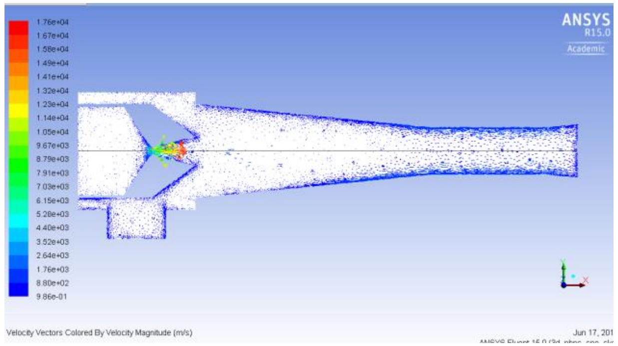


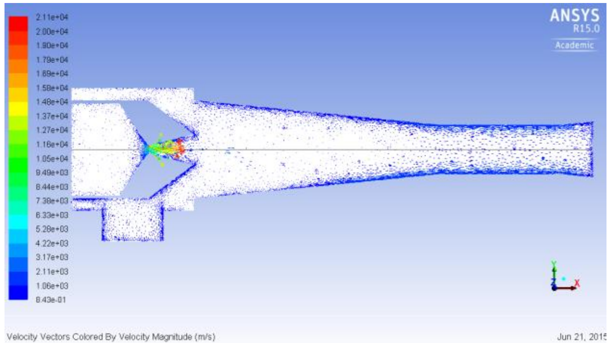

**Or-1st-30-3-10-80-40-small-new2016-0.01**

**Or-1st-30-3-10-80-40-small-new2016-0.02**

**Or-1st-30-3-10-80-40-small-new2016-0.03**

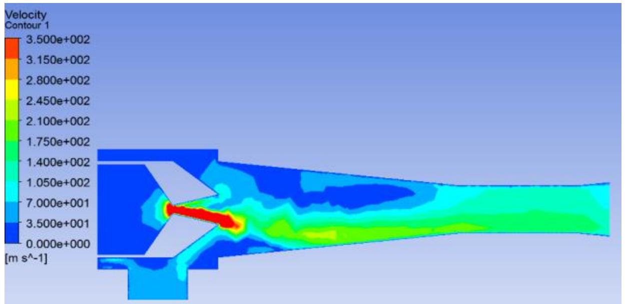


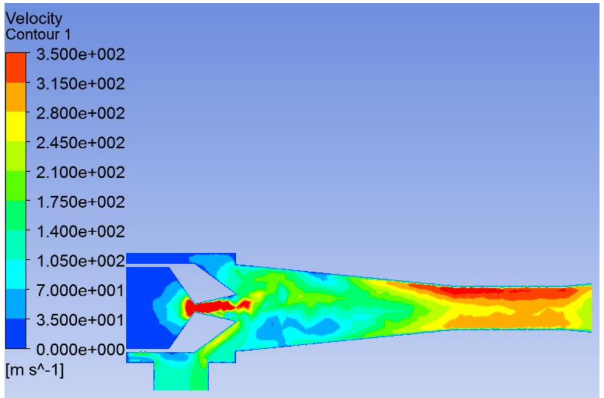


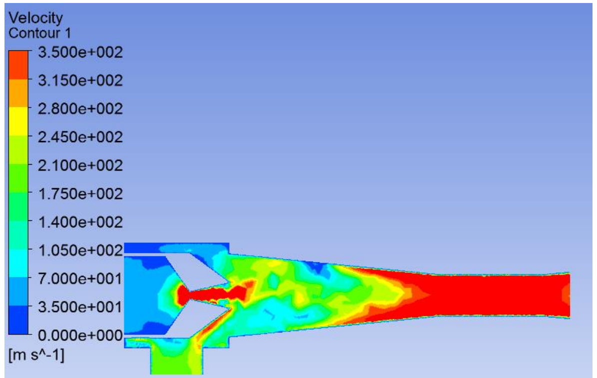


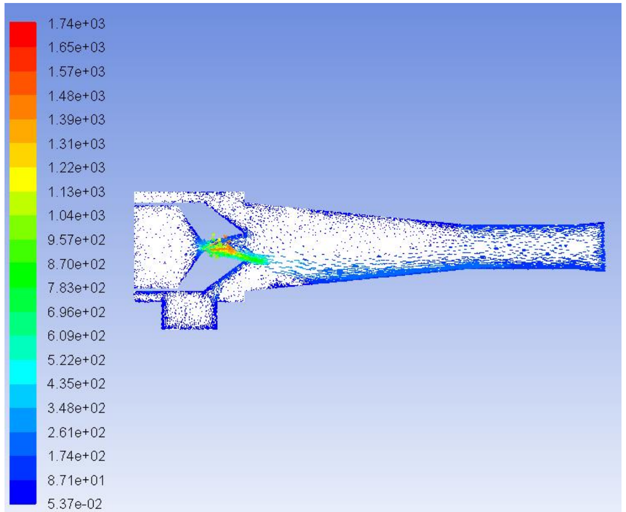


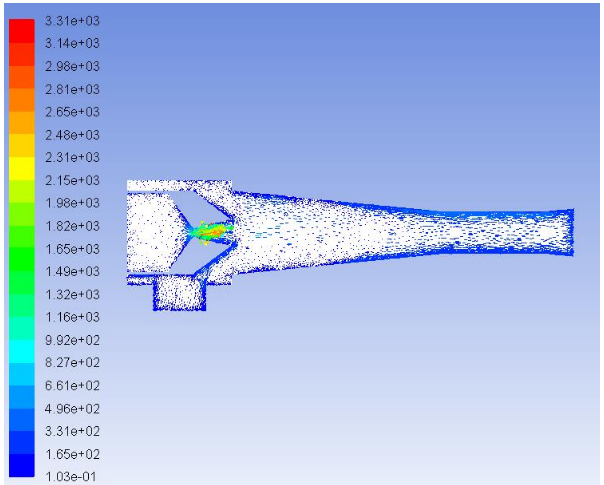


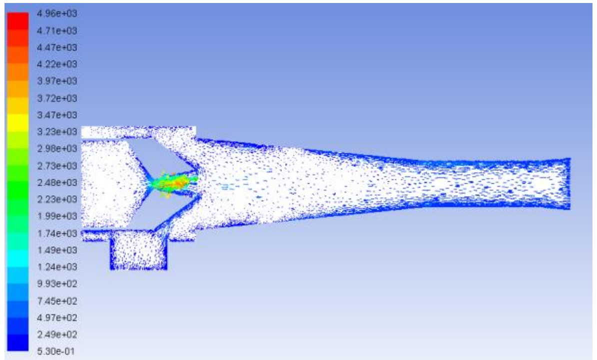

**Or-1st-30-3-10-80-40-small-new2016-0.04**

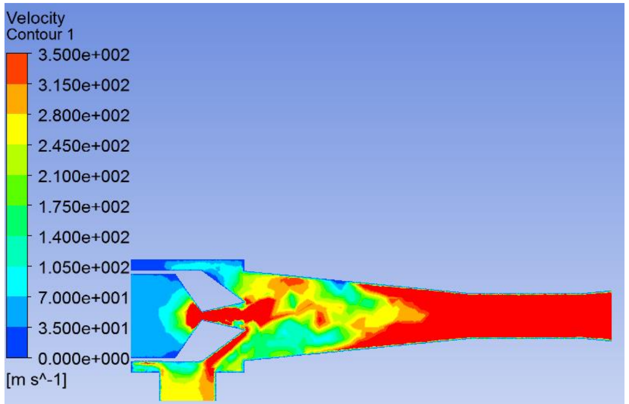


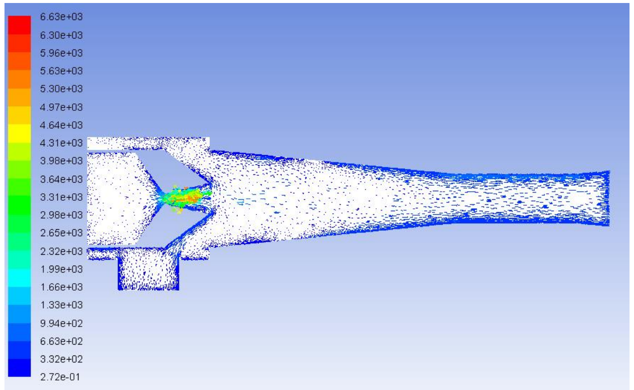


**Or-1st-30-3-10-80-40-small-new2016-0.05**

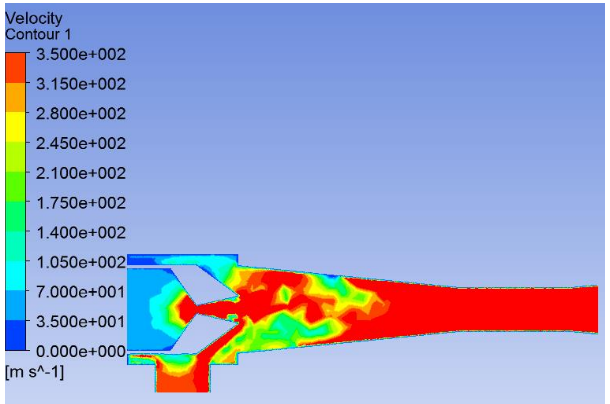


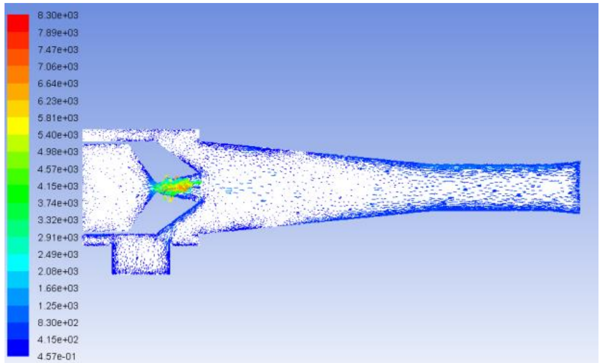


**Or-1st-30-3-10-80-40-small-new2016-0.06**

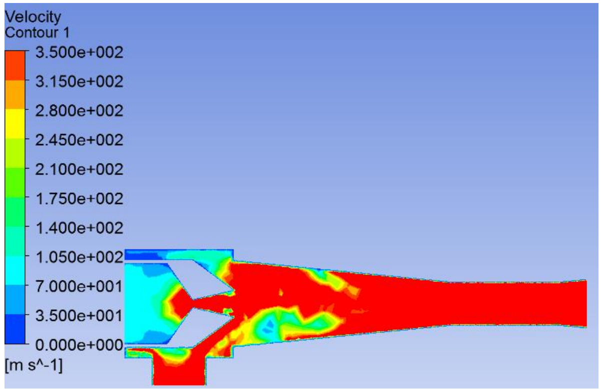


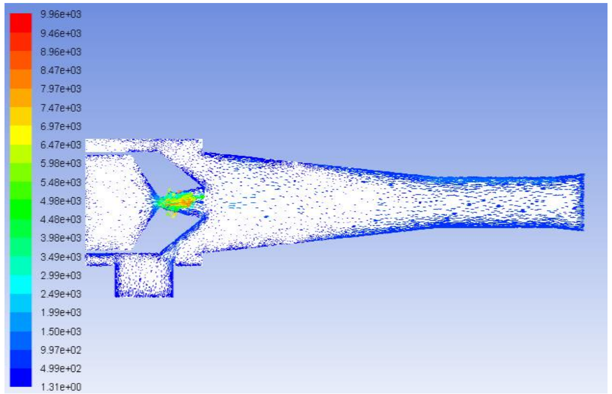

**Or-1st-30-4-10-80-40-0.01**

**Or-1st-30-4-10-80-40-0.02**

**Or-1st-30-4-10-80-40-0.03**

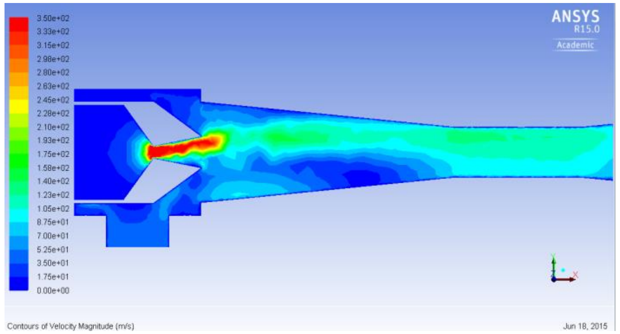


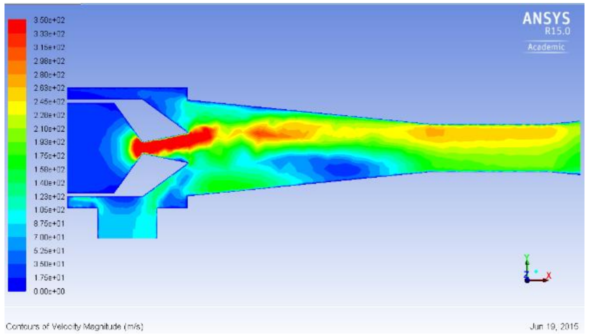


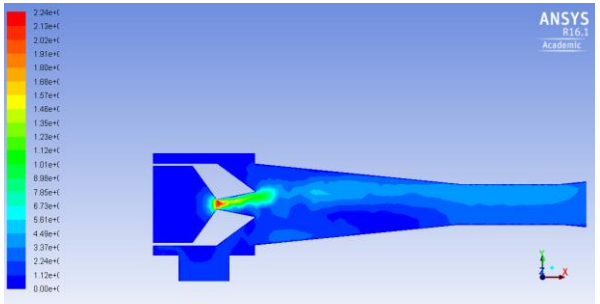


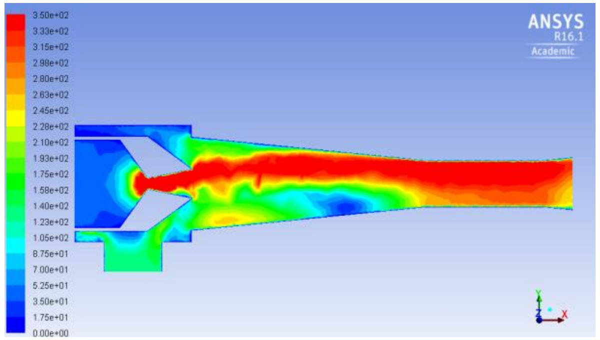


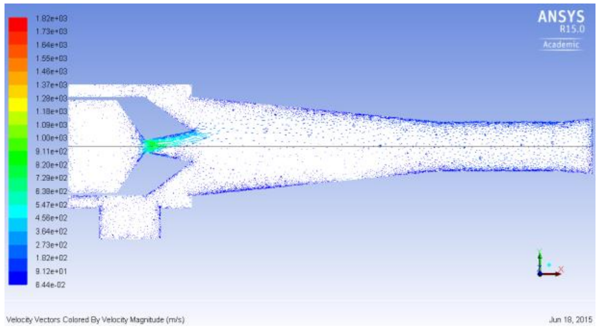


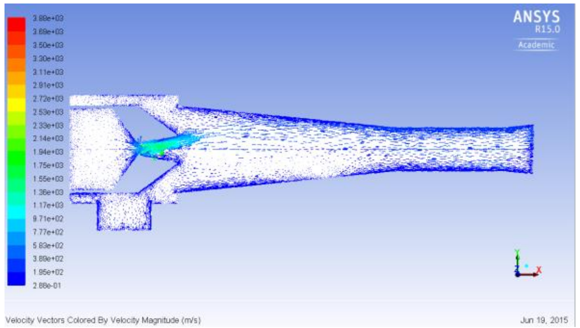


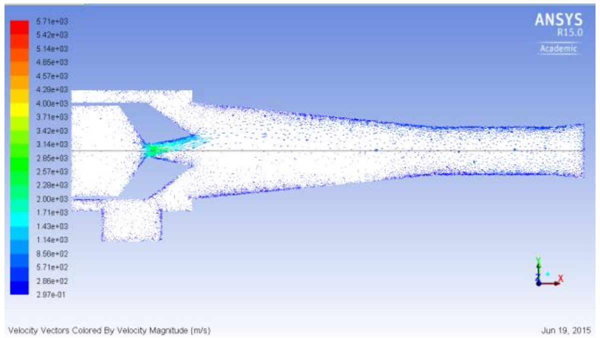

**Or-1st-30-4-10-80-40-0.04**

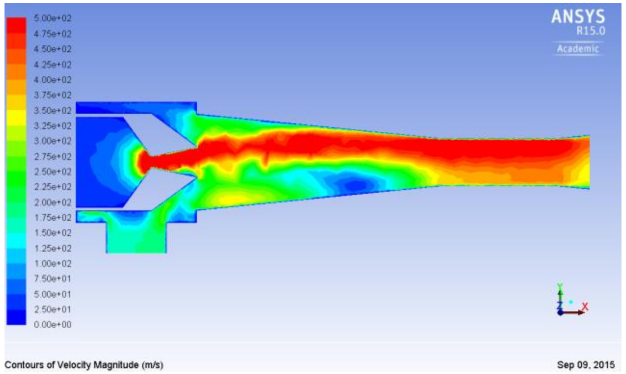


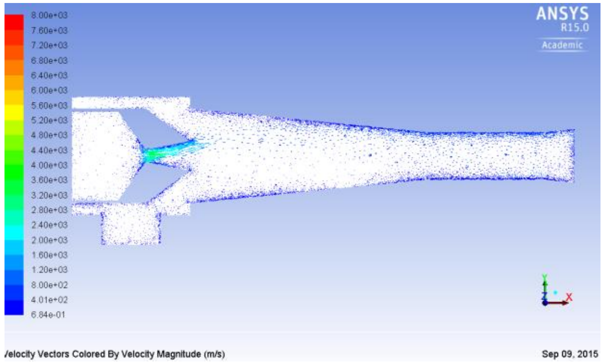


**Or-1st-30-4-10-80-40-0.05**

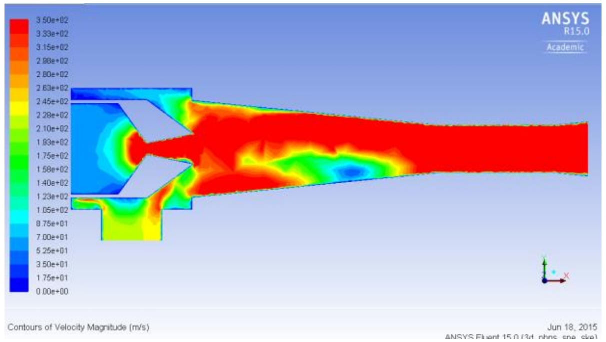


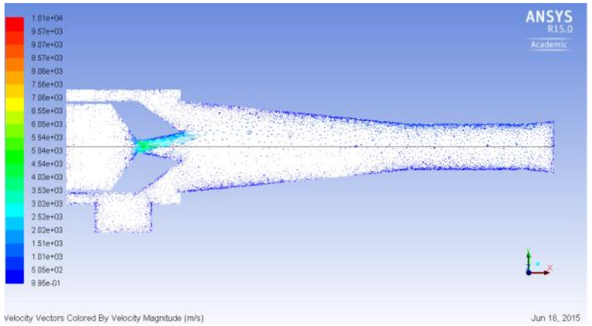


**Or-1st-30-4-10-80-40-0.06**

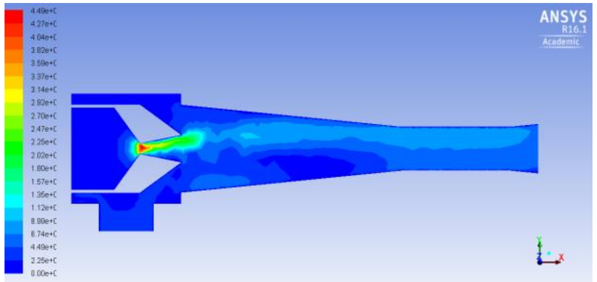


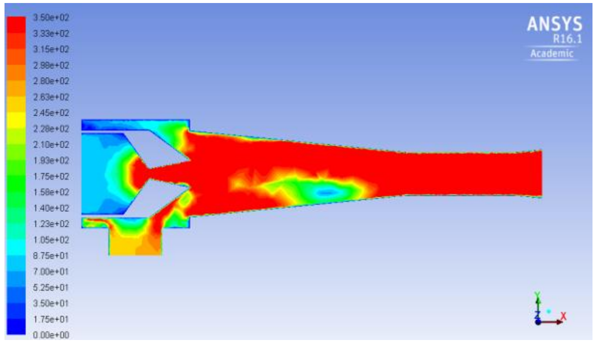


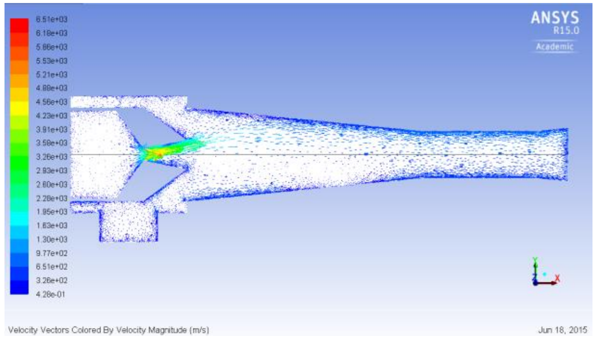

**Or-1st-30-5-10-80-40-0.01**

**Or-1st-30-5-10-80-40-0.02**

**Or-1st-30-5-10-80-40-0.03**

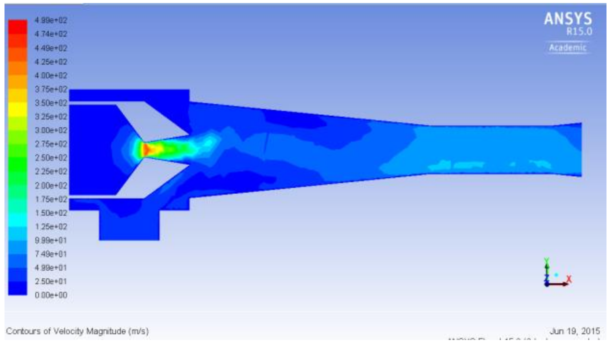


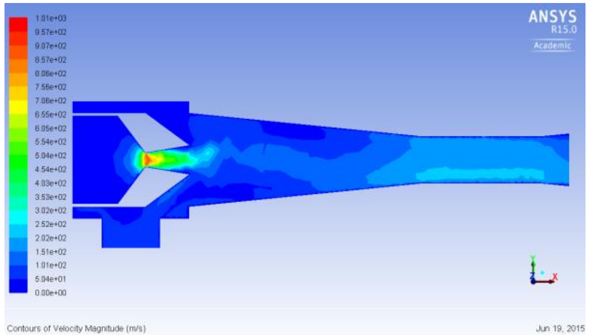


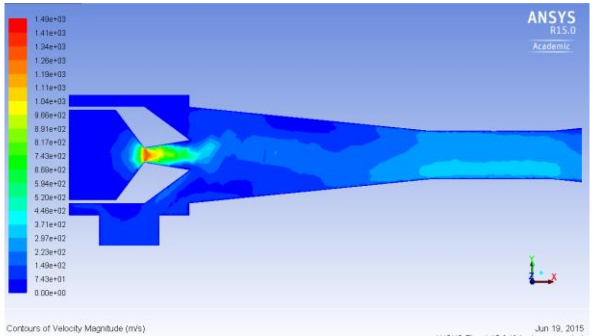


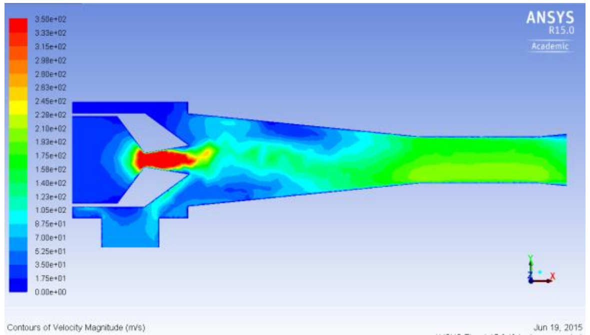


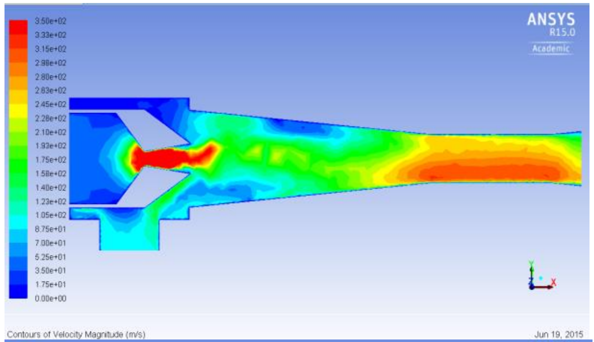


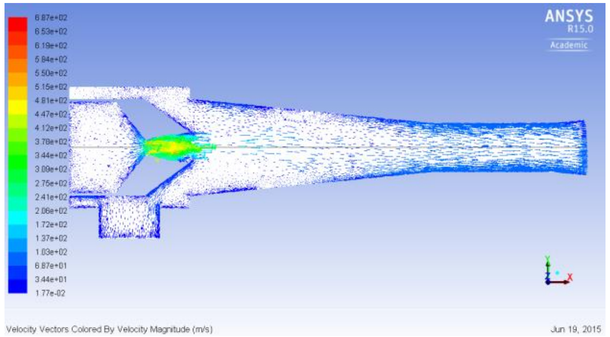


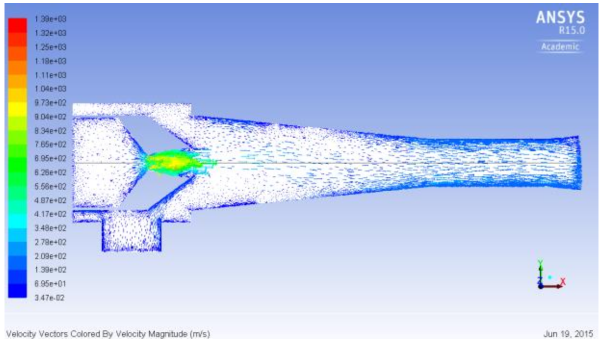


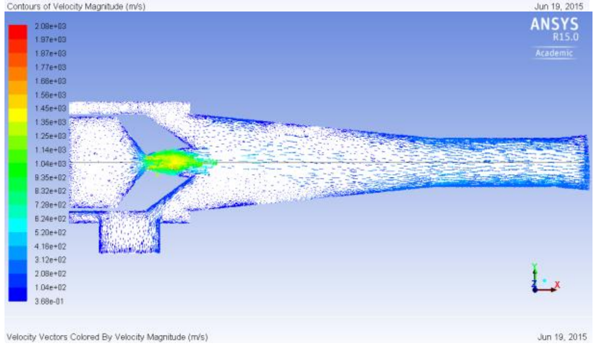

**Or-1st-30-5-10-80-40-0.04**

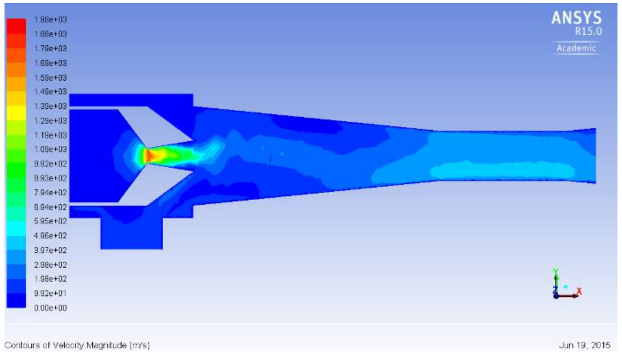


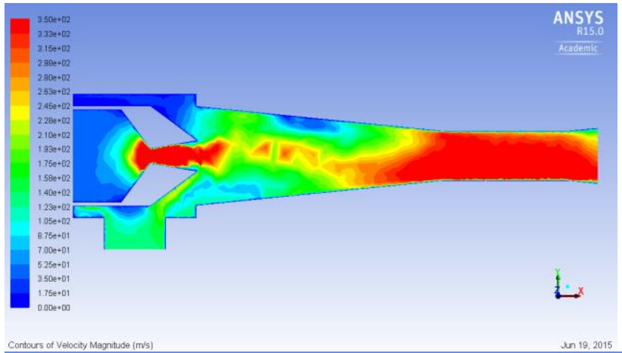


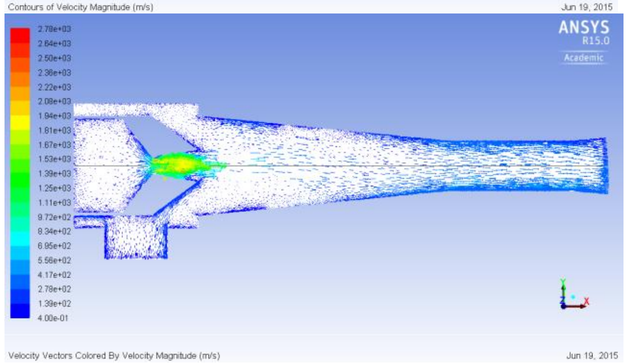


**Or-1st-30-5-10-80-40-0.05**

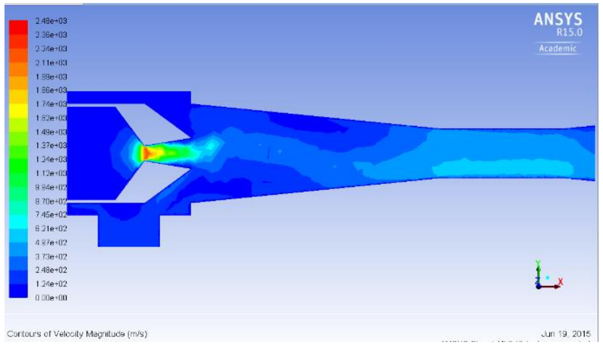


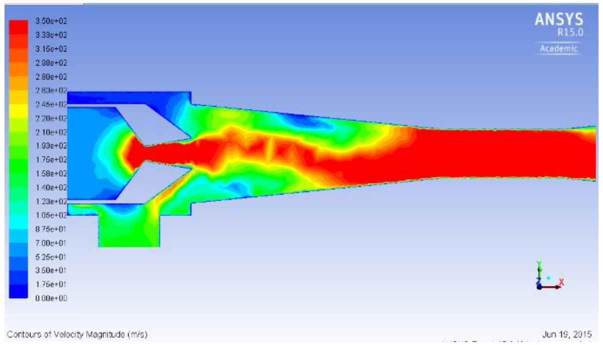


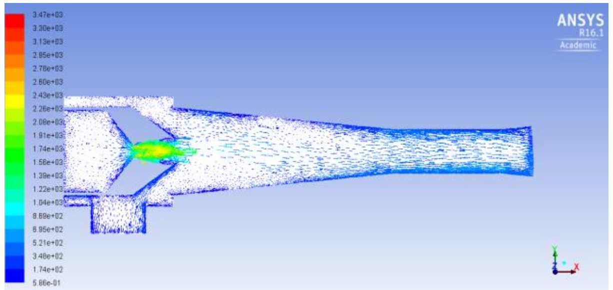


**Or-1st-30-5-10-80-40-0.06**

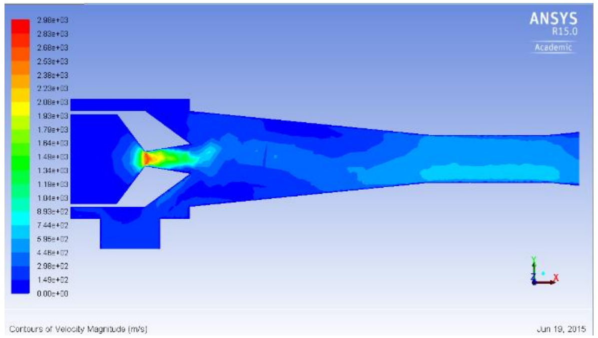


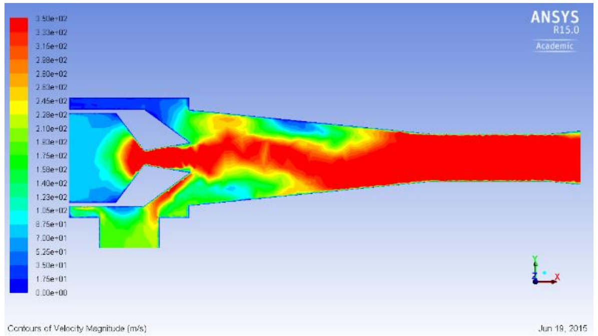


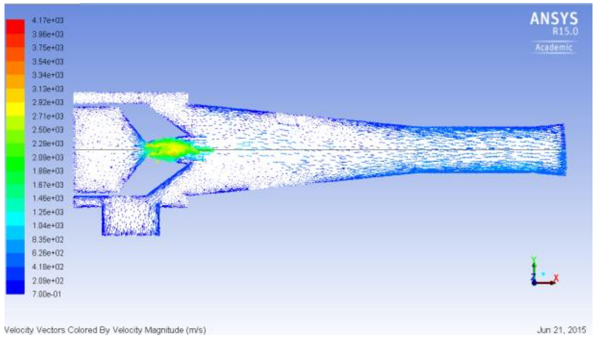

**Or-1st-30-6-10-80-40-0.01** **Or-1st-30-6-10-80-40-0.02** **Or-1st-30-6-10-80-40-0.03**

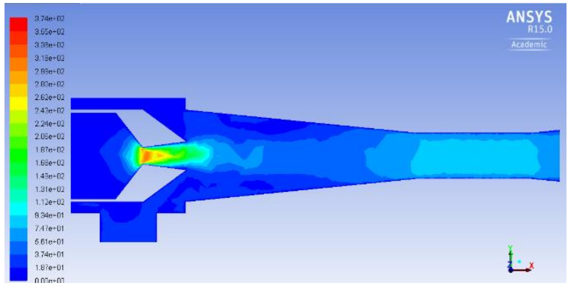


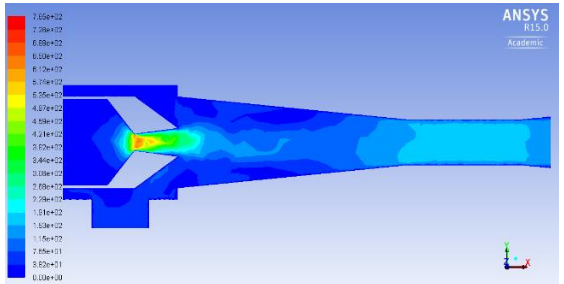


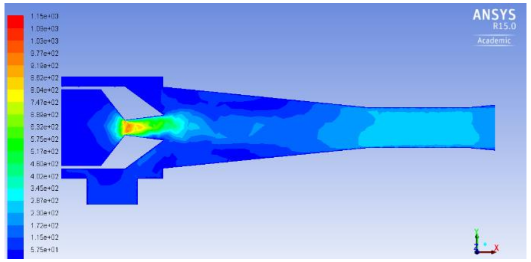


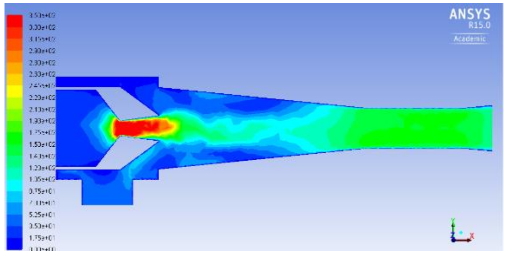


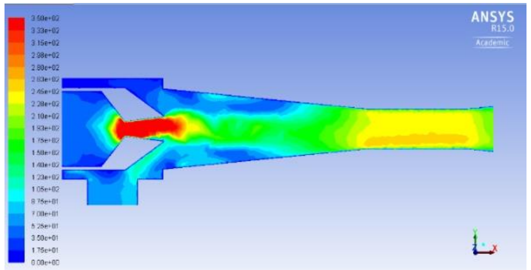


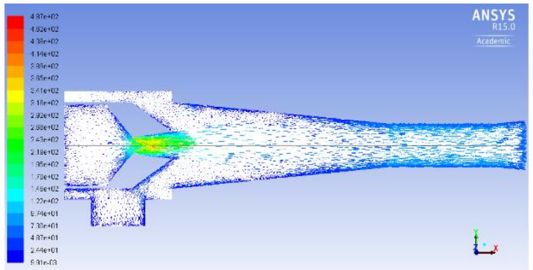


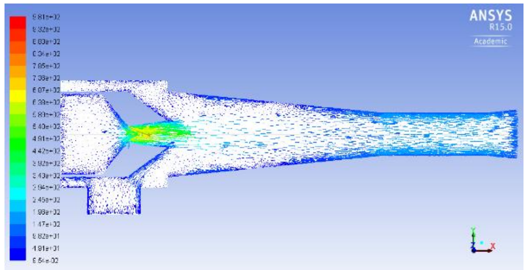


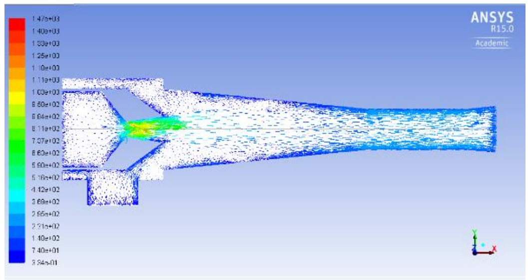

**Or-1st-30-6-10-80-40-0.04**

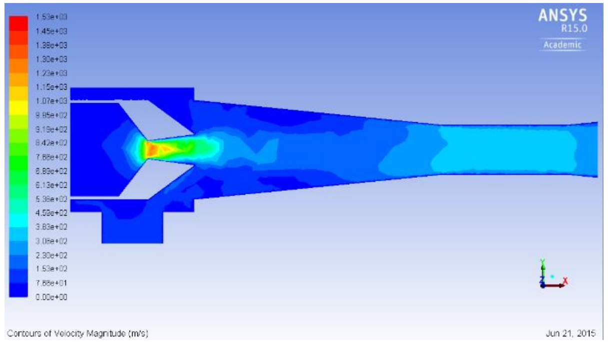


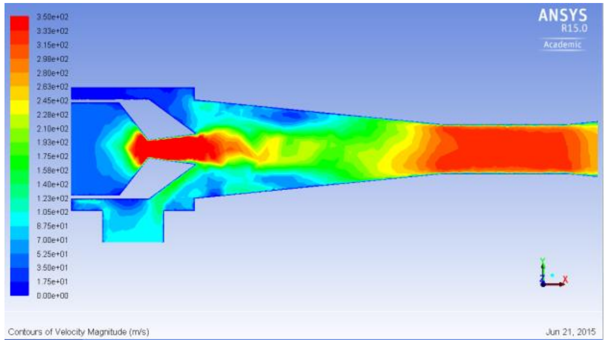


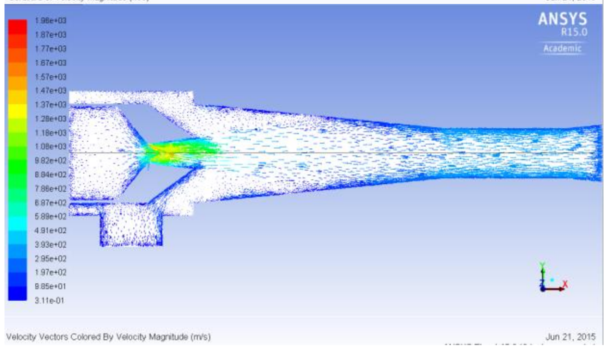


**Or-1st-30-6-10-80-40-0.05**

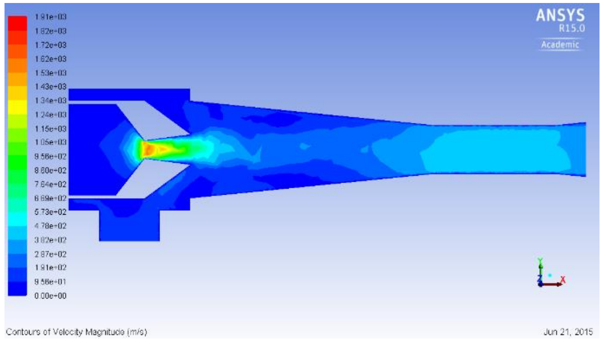


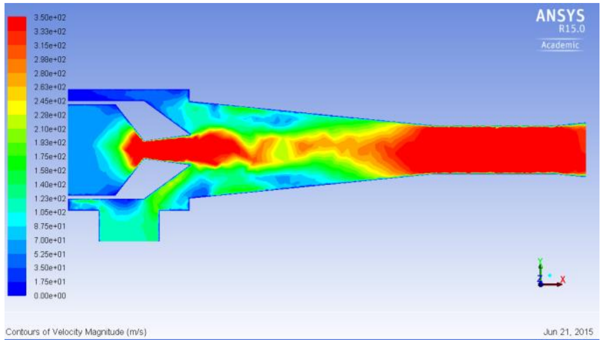


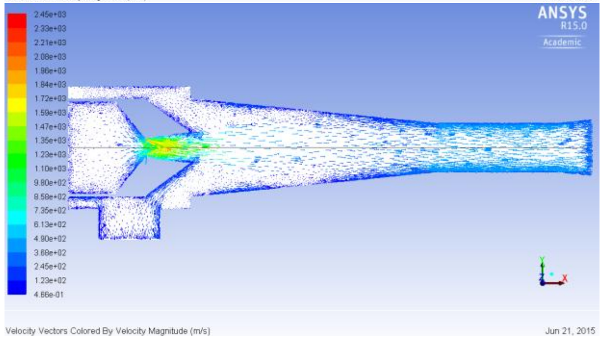


**Or-1st-30-6-10-80-40-0.06**

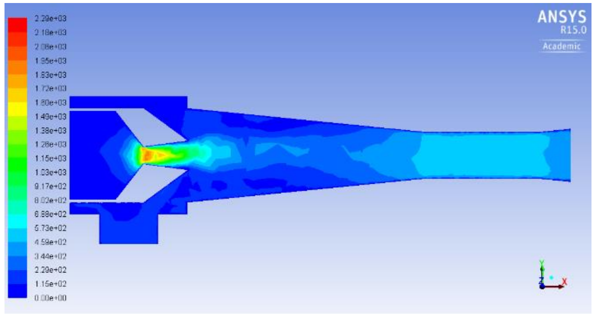


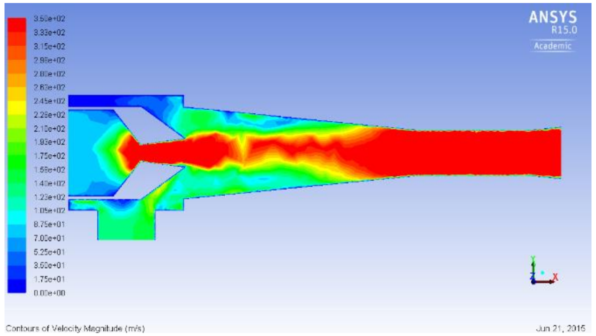


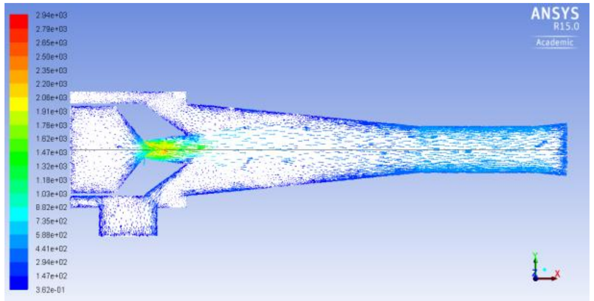

**Or-1st-30-7-10-80-40-0.01**

**Or-1st-30-7-10-80-40-0.02**

**Or-1st-30-7-10-80-40-0.03**

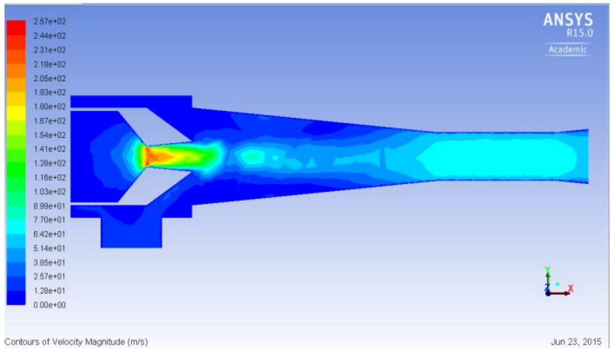


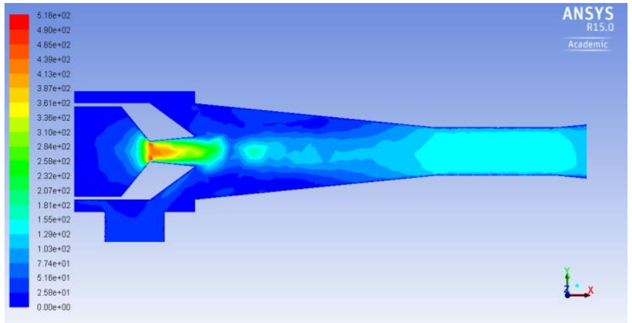


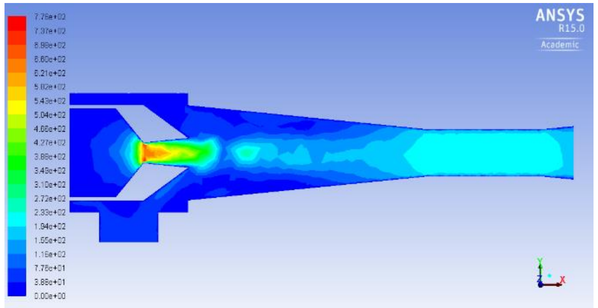


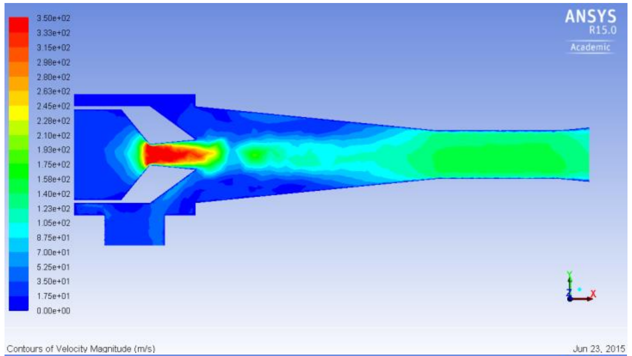


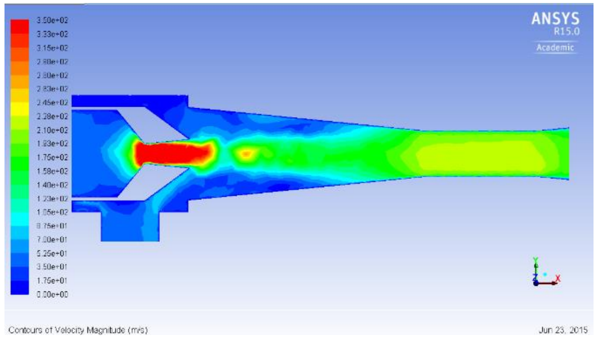


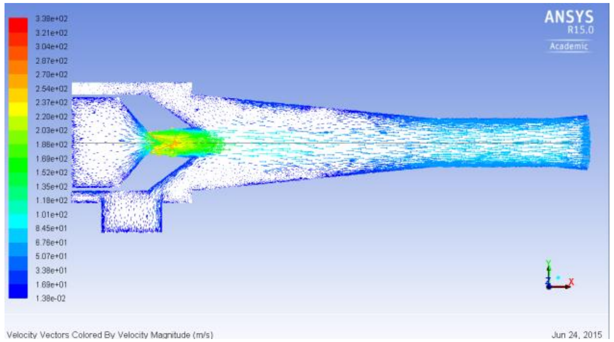


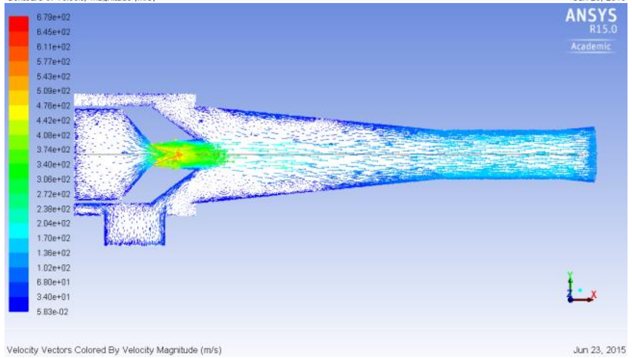


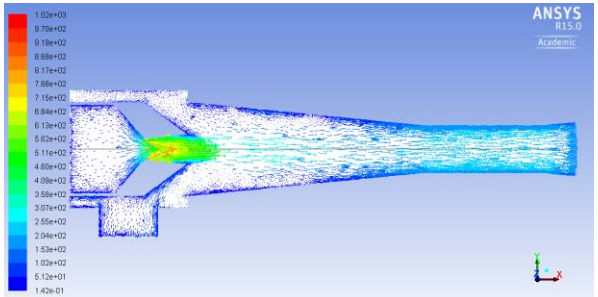

**Or-1st-30-7-10-80-40-0.04**

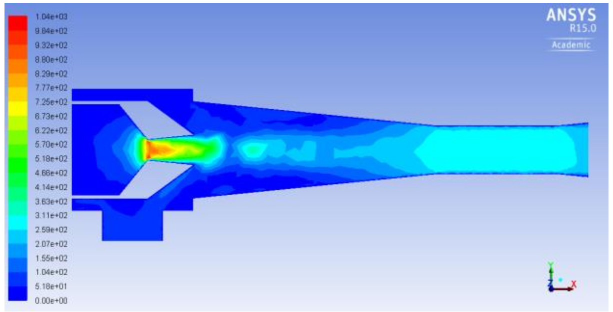


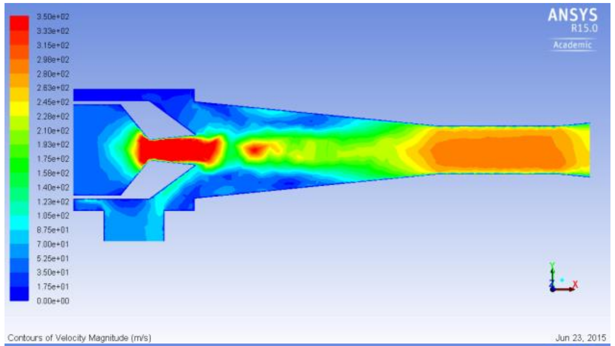


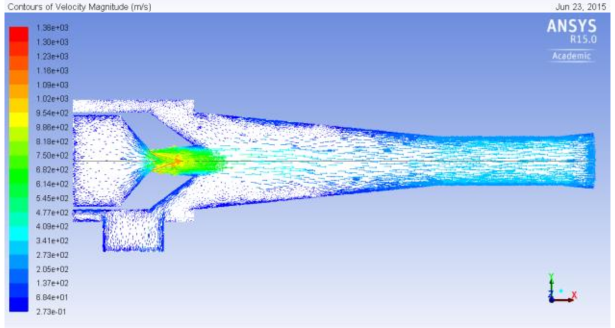


**Or-1st-30-7-10-80-40-0.05**

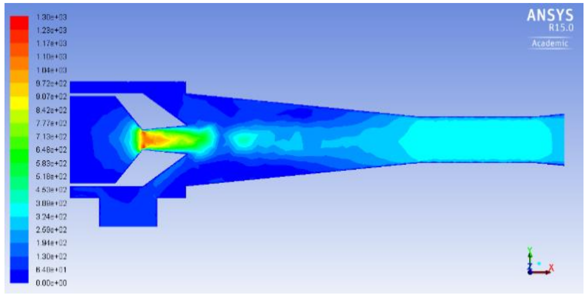


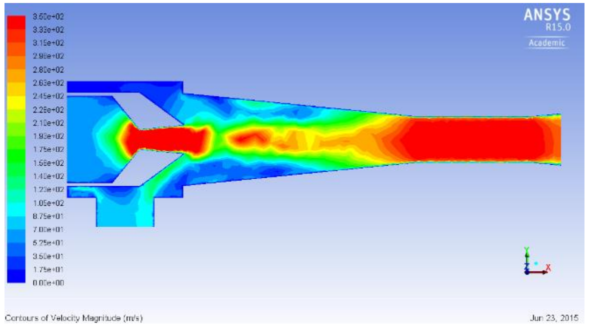


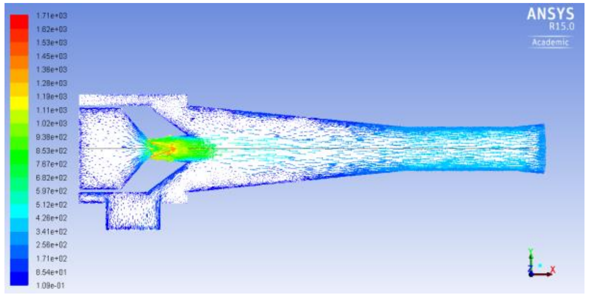


**Or-1st-30-7-10-80-40-0.06**

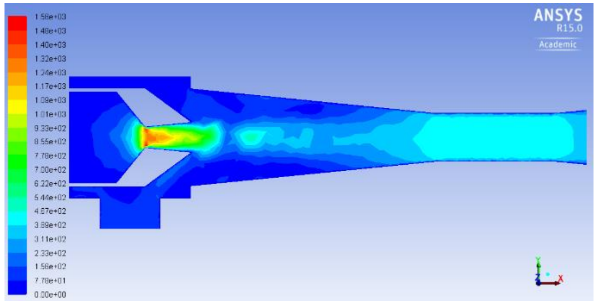


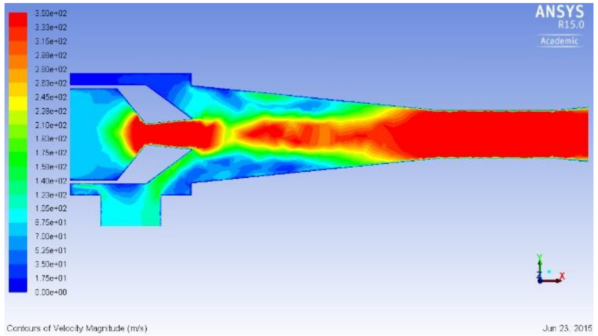


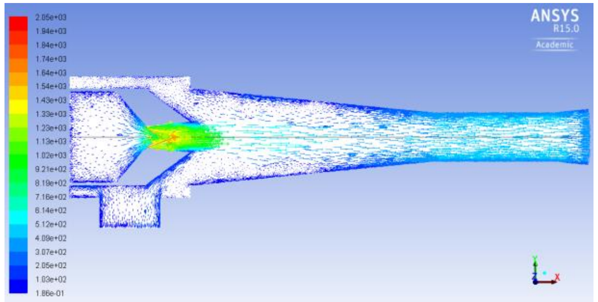

**Or-1st-30-5-10-60-40-0.01** **Or-1st-30-5-10-60-40-0.02** **Or-1st-30-5-10-60-40-0.03**

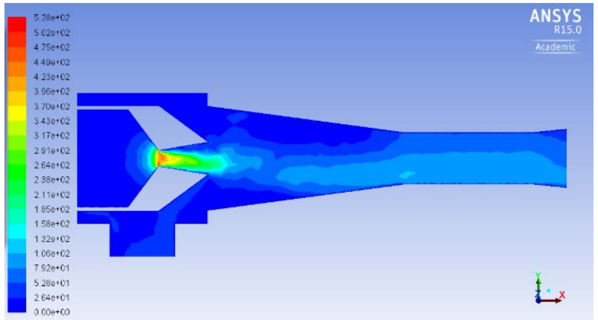


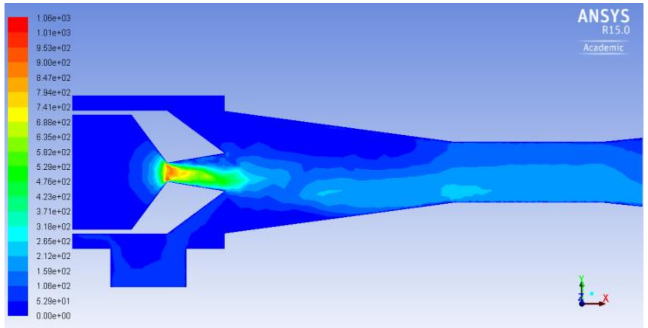


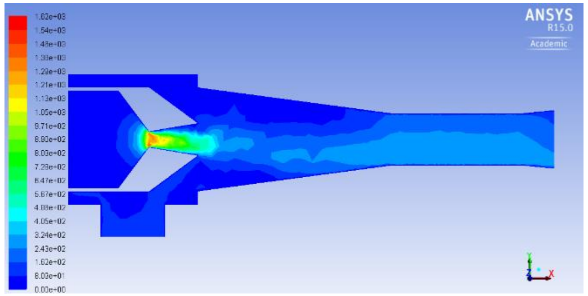


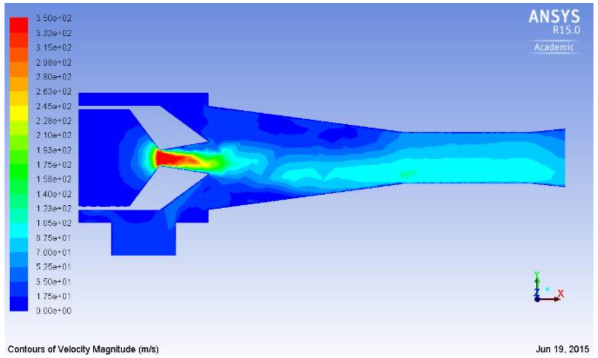


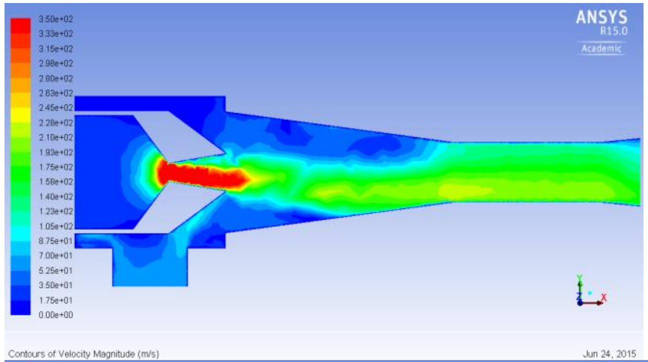


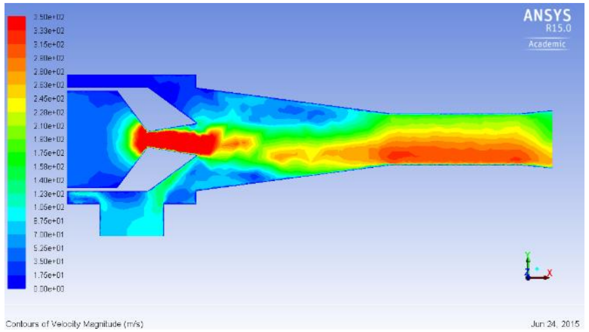


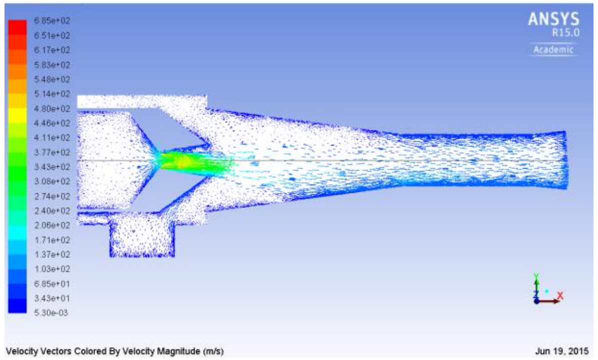


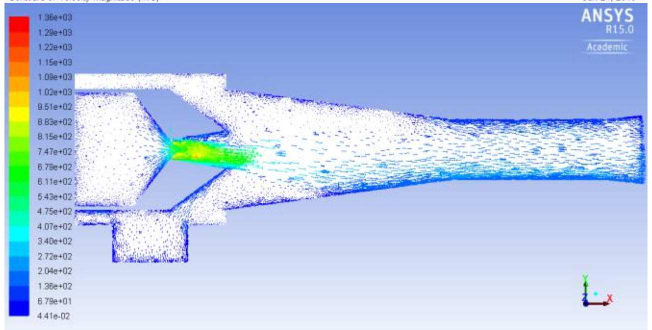


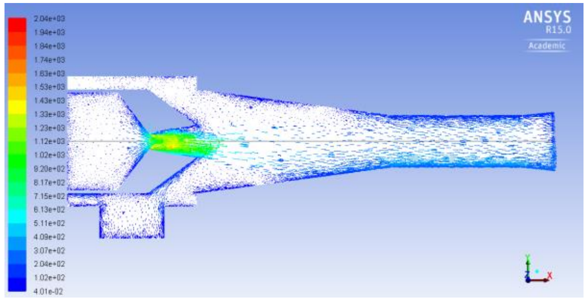

**Or-1st-30-5-10-60-40-0.04**

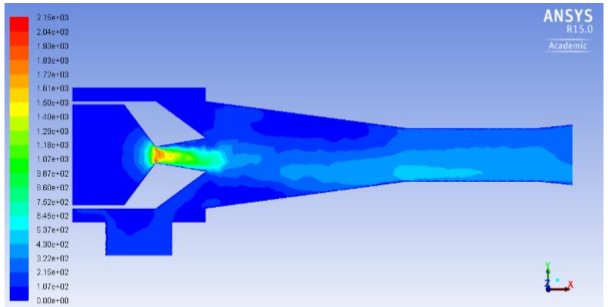


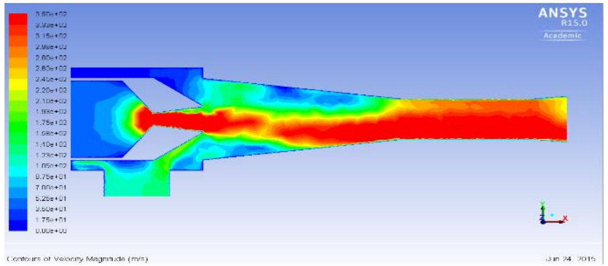


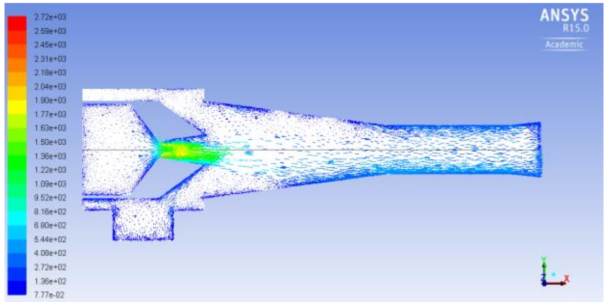


**Or-1st-30-5-10-60-40-0.05**

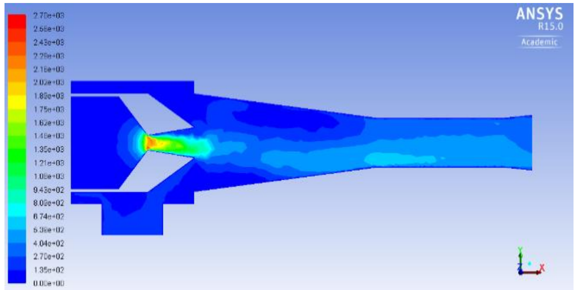


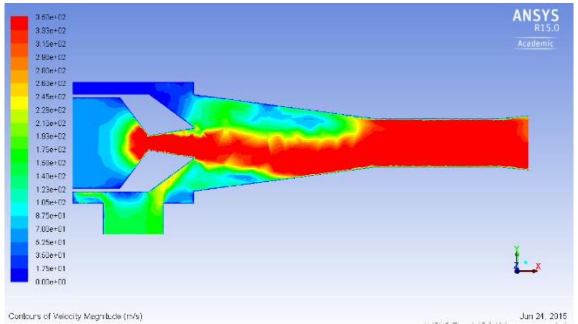


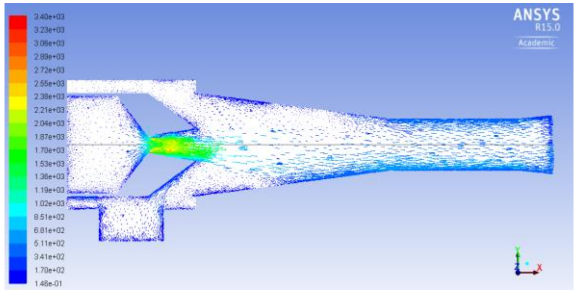


**Or-1st-30-5-10-60-40-0.06**

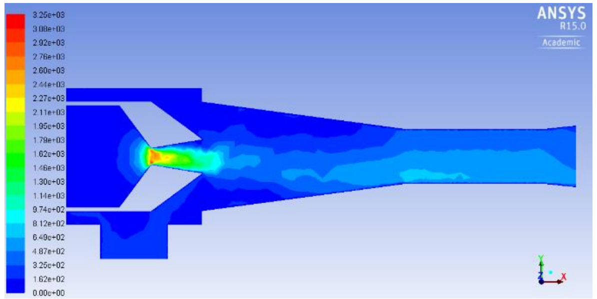


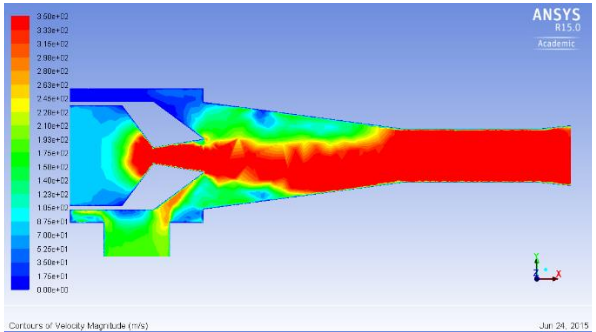


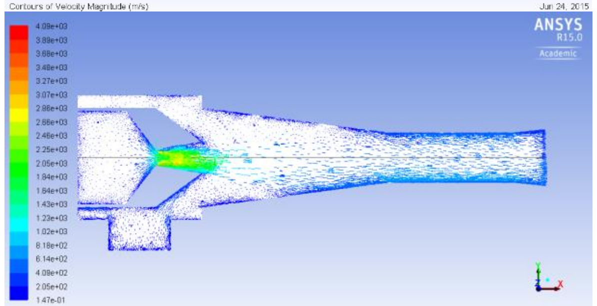

**Or-1st-30-5-10-70-40-0.01** **Or-1st-30-5-10-70-40-0.02** **Or-1st-30-5-10-70-40-0.03**

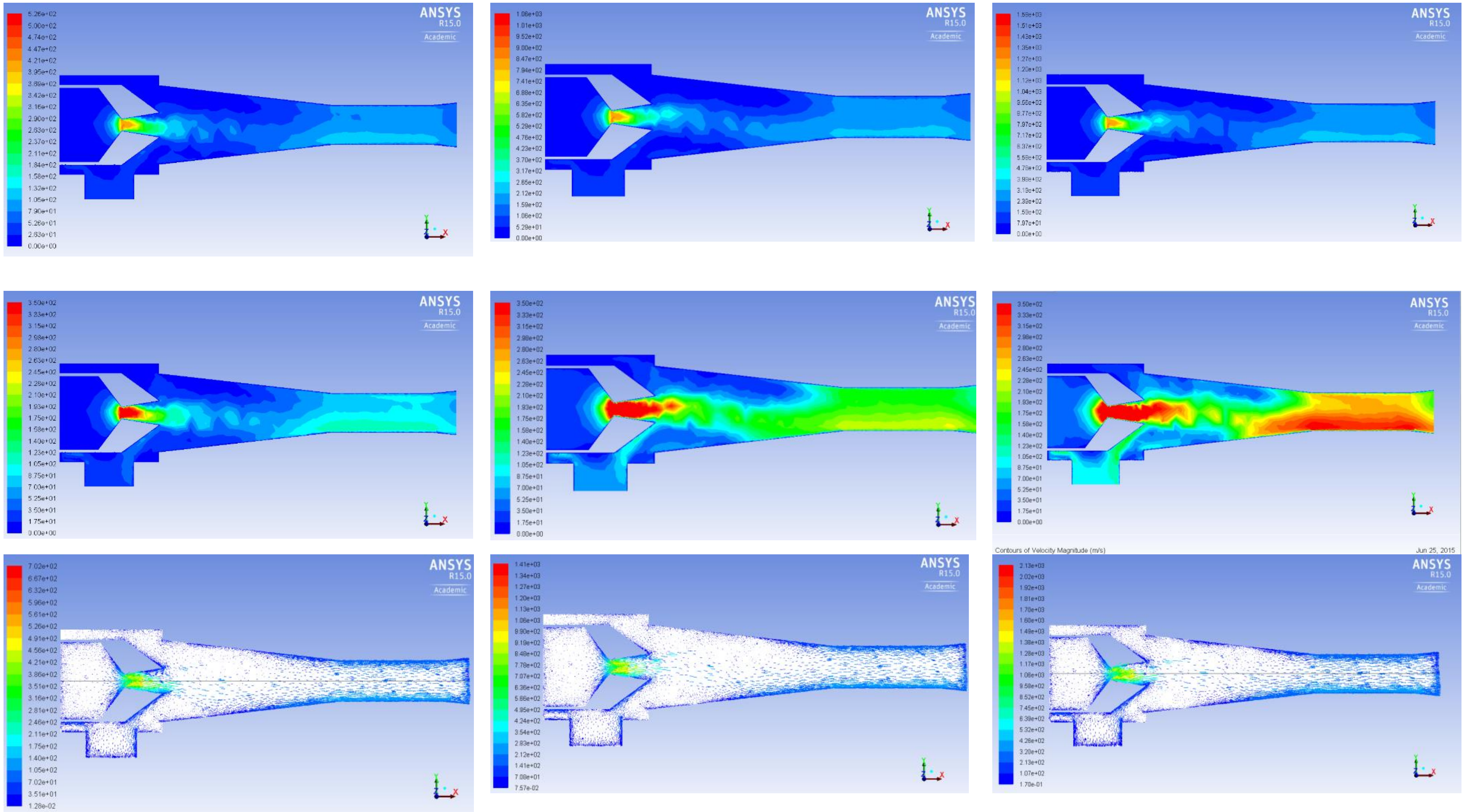

**Or-1st-30-5-10-70-40-0.04**

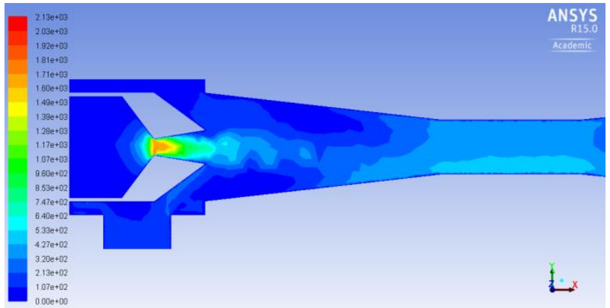


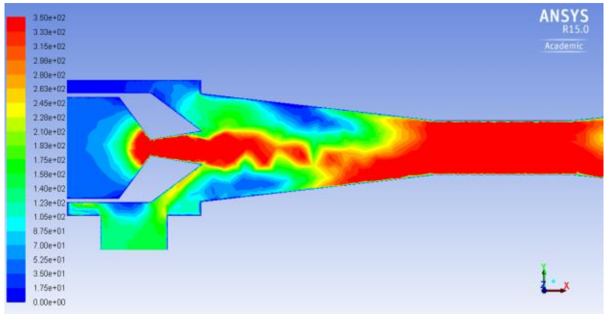


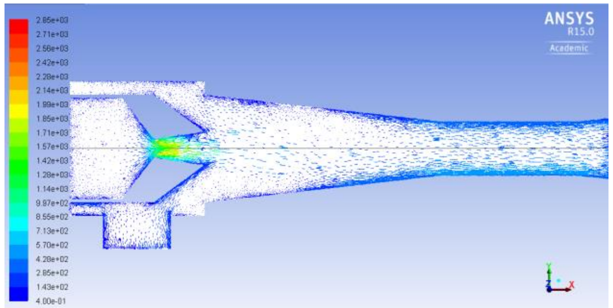


**Or-1st-30-5-10-70-40-0.05**

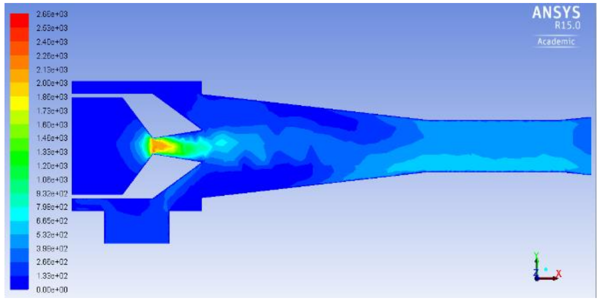


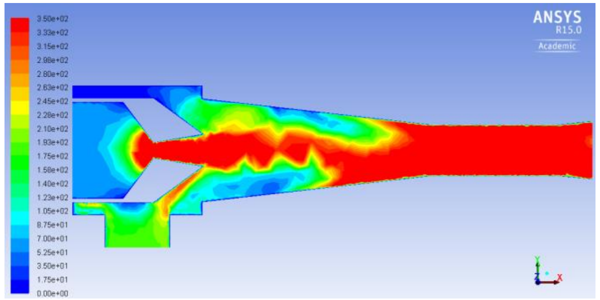


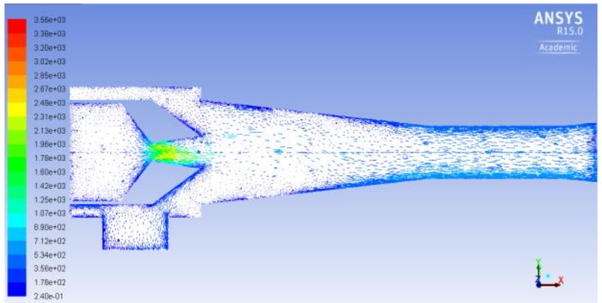


**Or-1st-30-5-10-70-40-0.06**

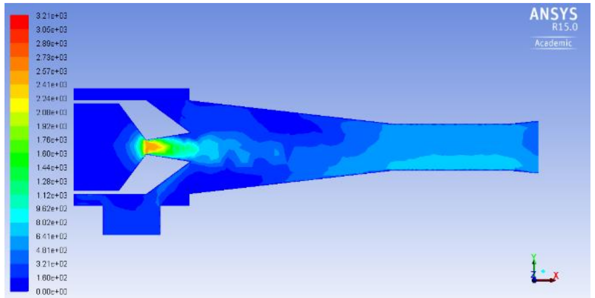


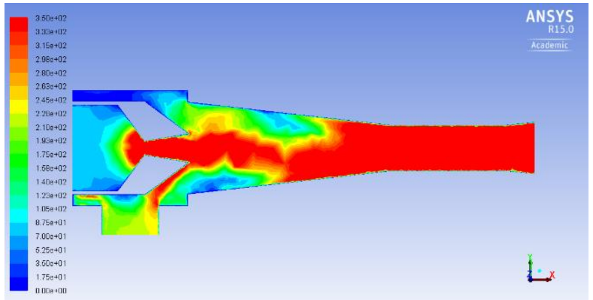


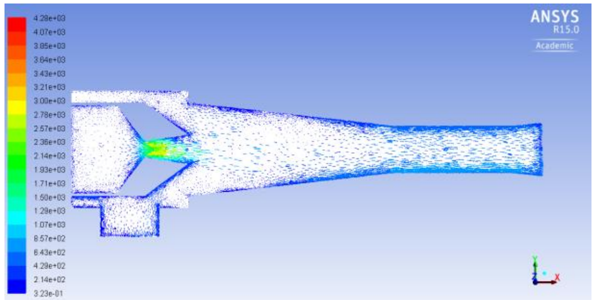

**Or-1st-30-5-10-90-40-0.01** **Or-1st-30-5-10-90-40-0.02** **Or-1st-30-5-10-90-40-0.03**

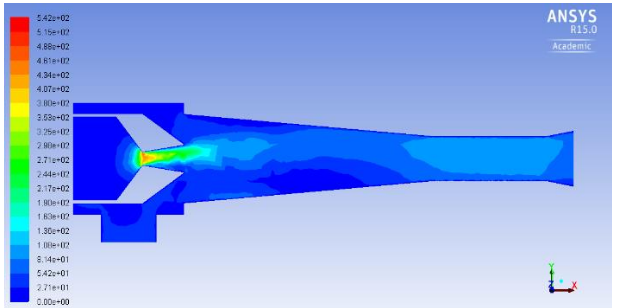


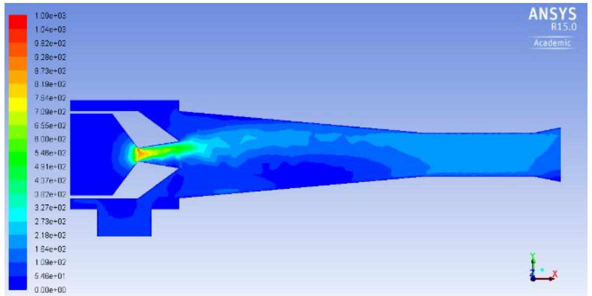


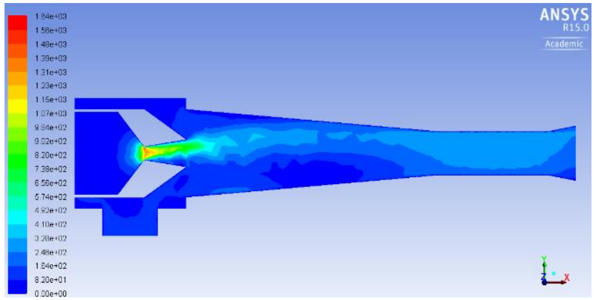


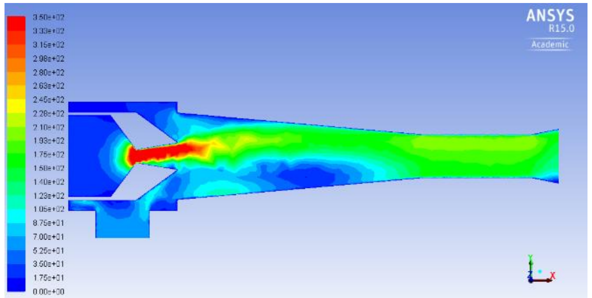


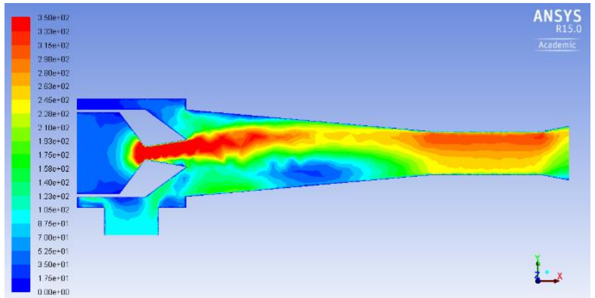


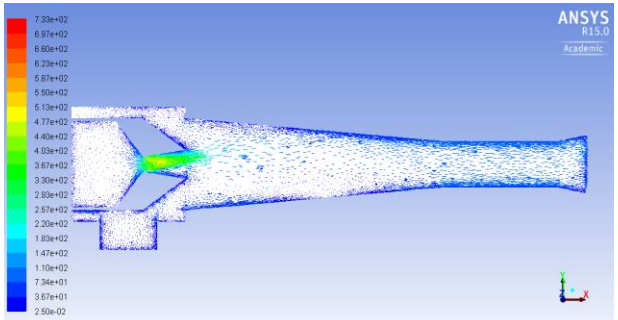


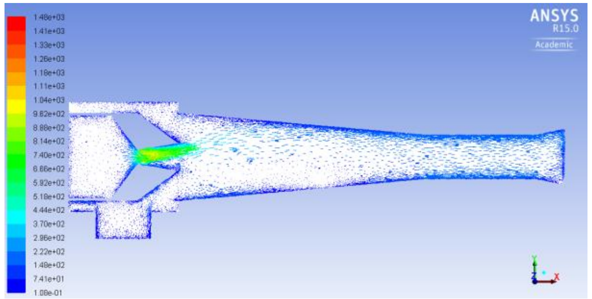


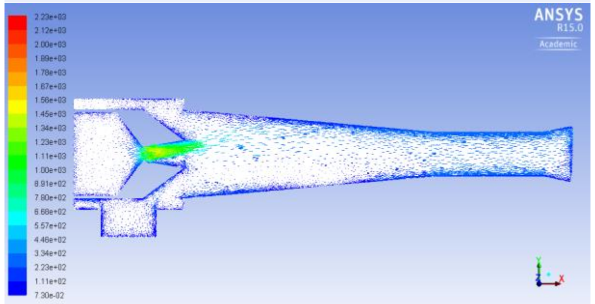

**Or-1st-30-5-10-90-40-0.04** | **Or-1st-30-5-10-90-40-0.05** | **Or-1st-30-5-10-90-40-0.06**

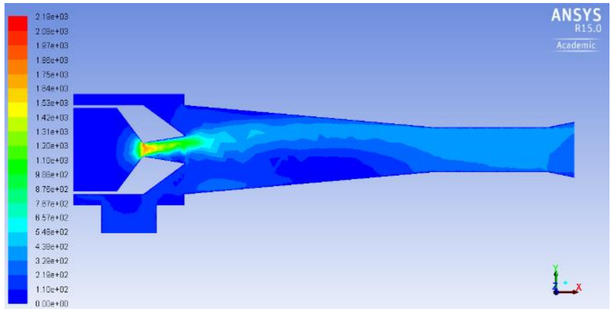


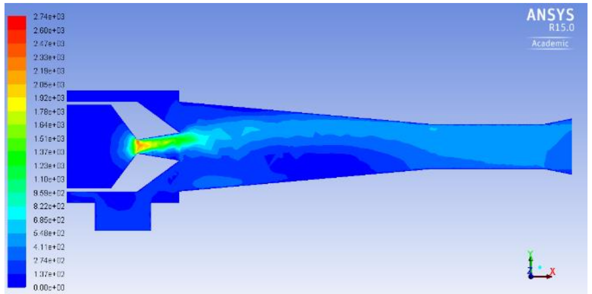


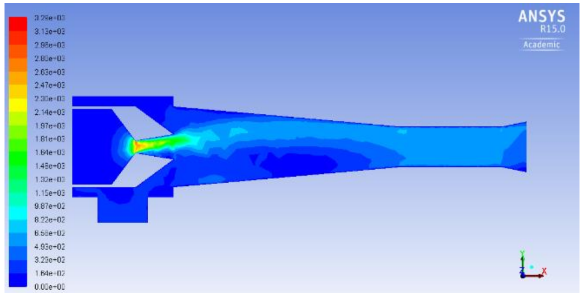


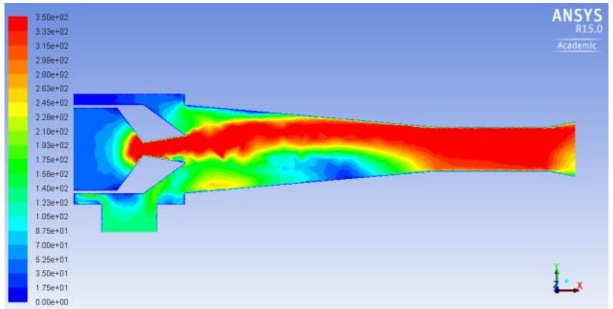


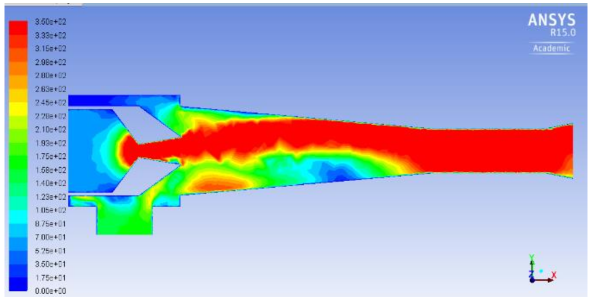


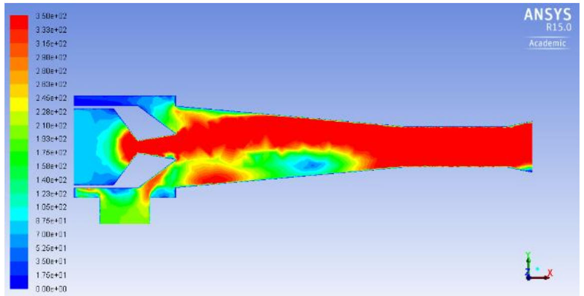


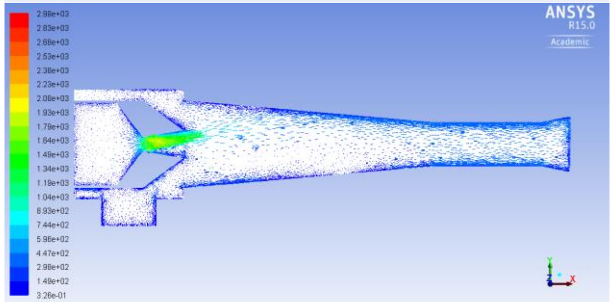


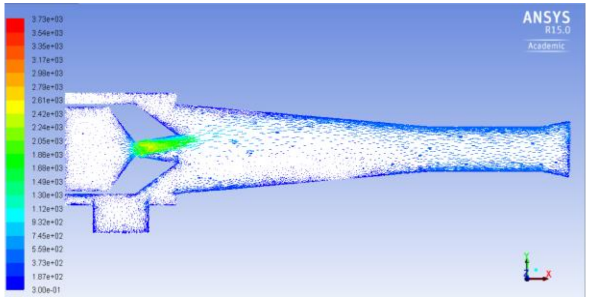


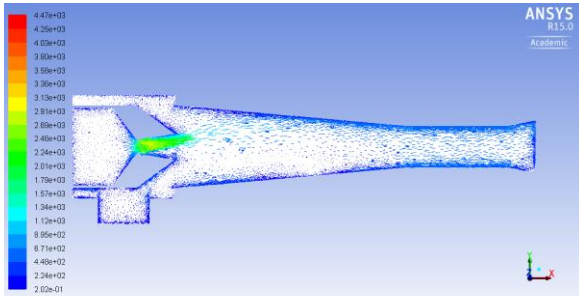

**Or-1st-30-5-10-100-40-0.01** | **Or-1st-30-5-10-100-40-0.02** | **Or-1st-30-5-10-100-40-0.03**

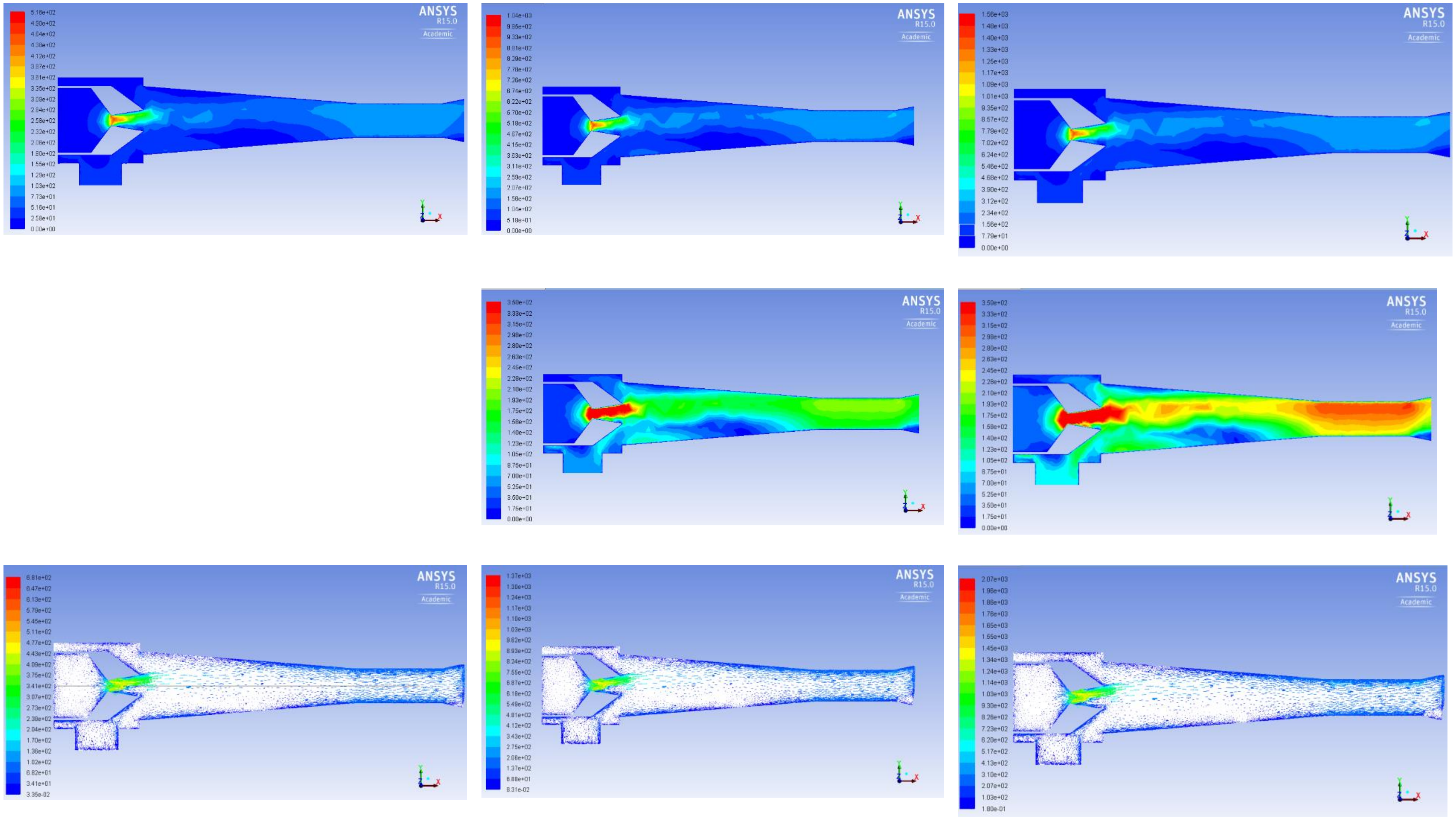

**Or-1st-30-5-10-100-40-0.04** **Or-1st-30-5-10-100-40-0.05** **Or-1st-30-5-10-100-40-0.06**

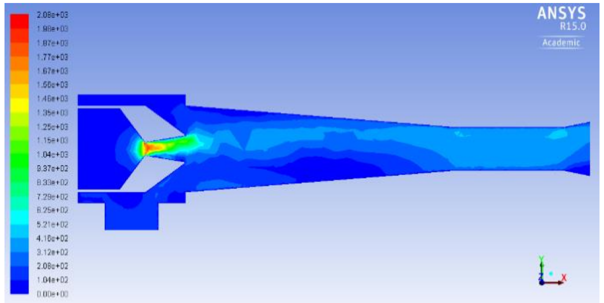


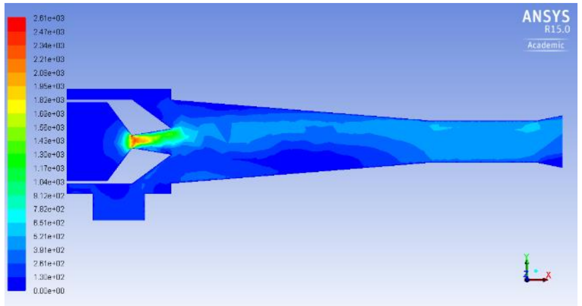


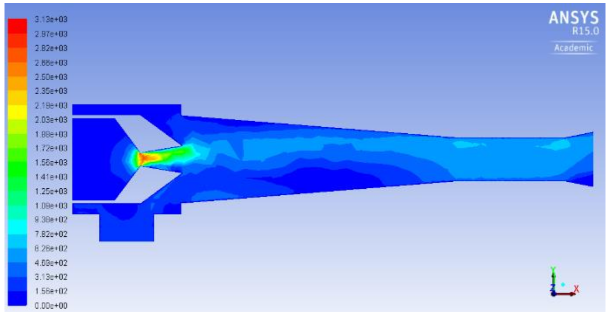


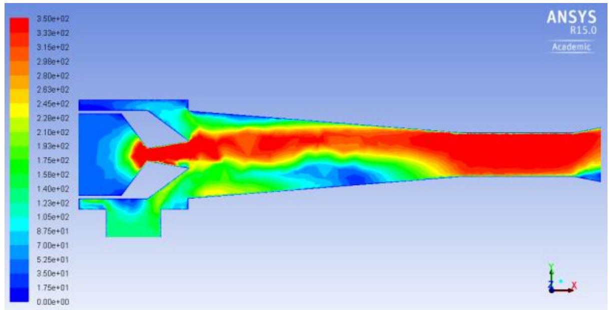


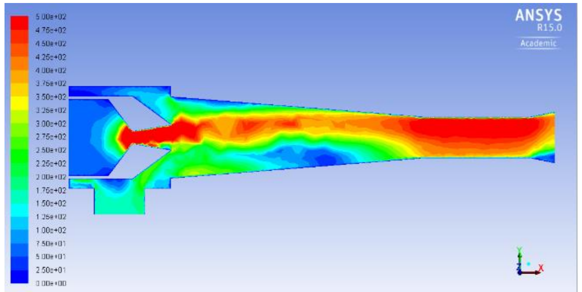


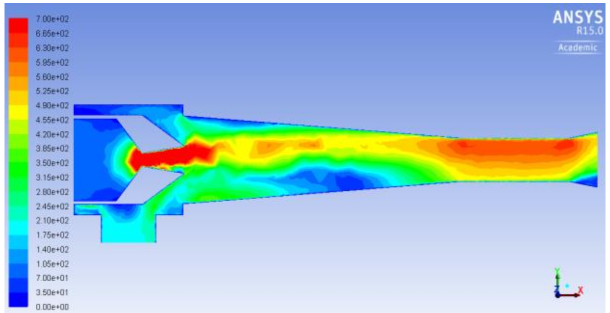


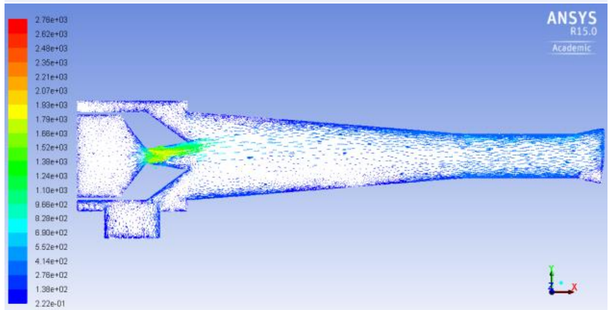


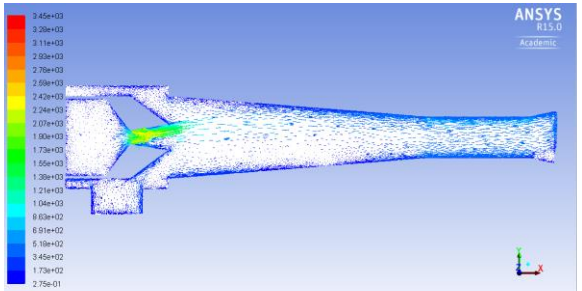


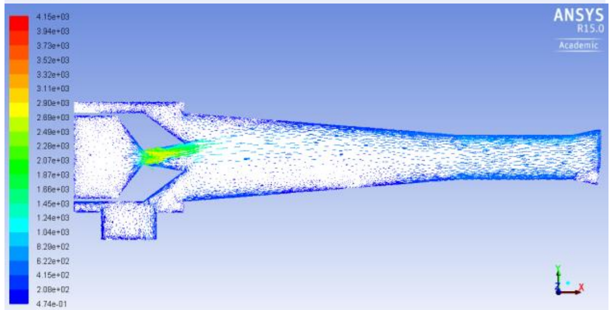

**Or-1st-30-5-10-80-20-0.01**

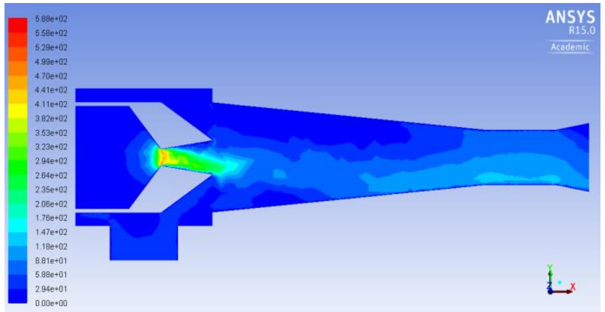


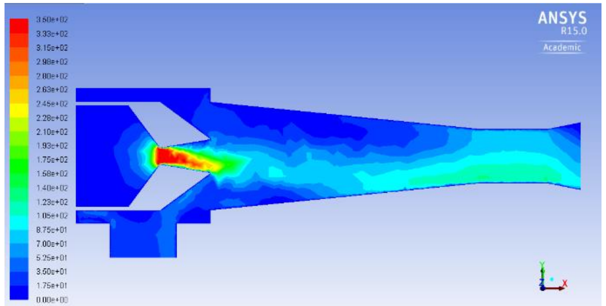


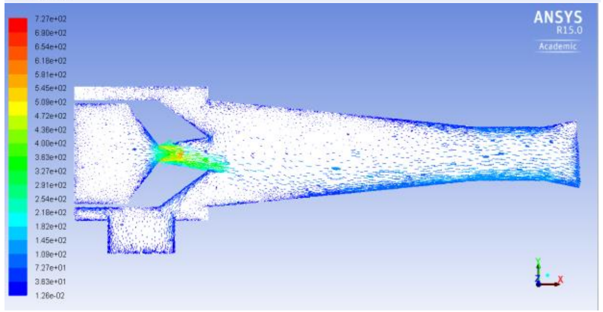


**Or-1st-30-5-10-80-20-0.02**

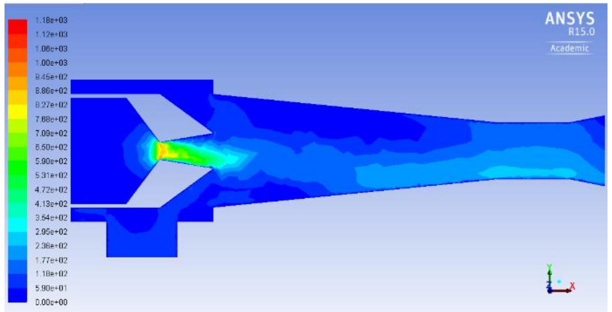


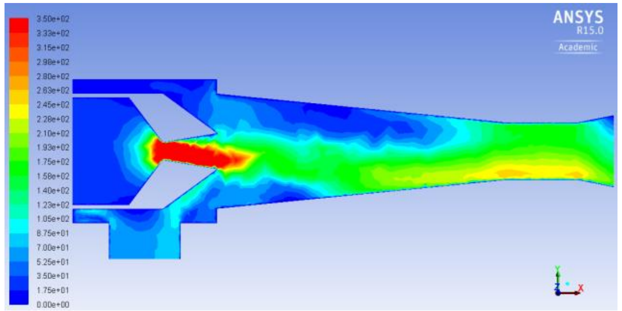


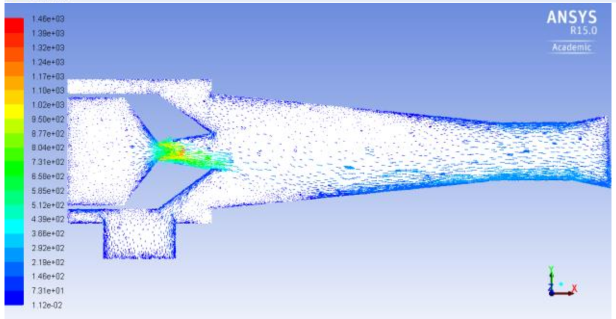


**Or-1st-30-5-10-80-20-0.03**

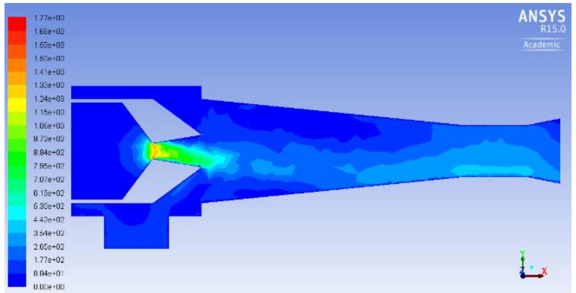


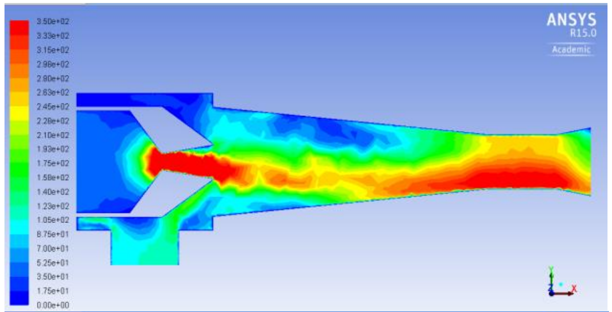


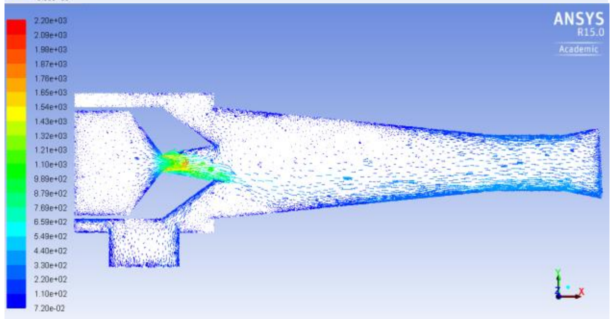

**Or-1st-30-5-10-80-20-0.04**

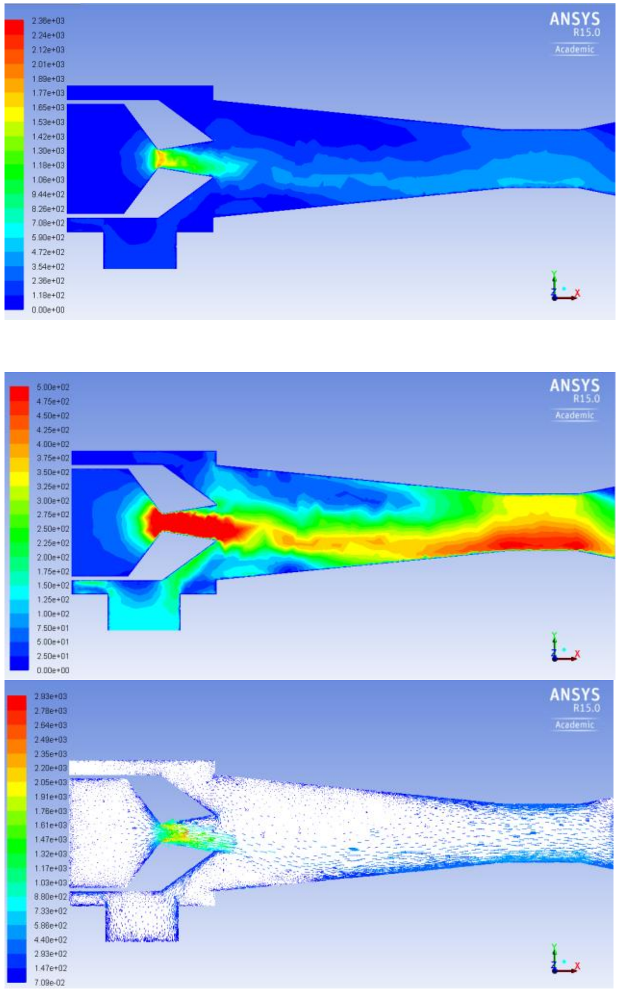


**Or-1st-30-5-10-80-20-0.05**

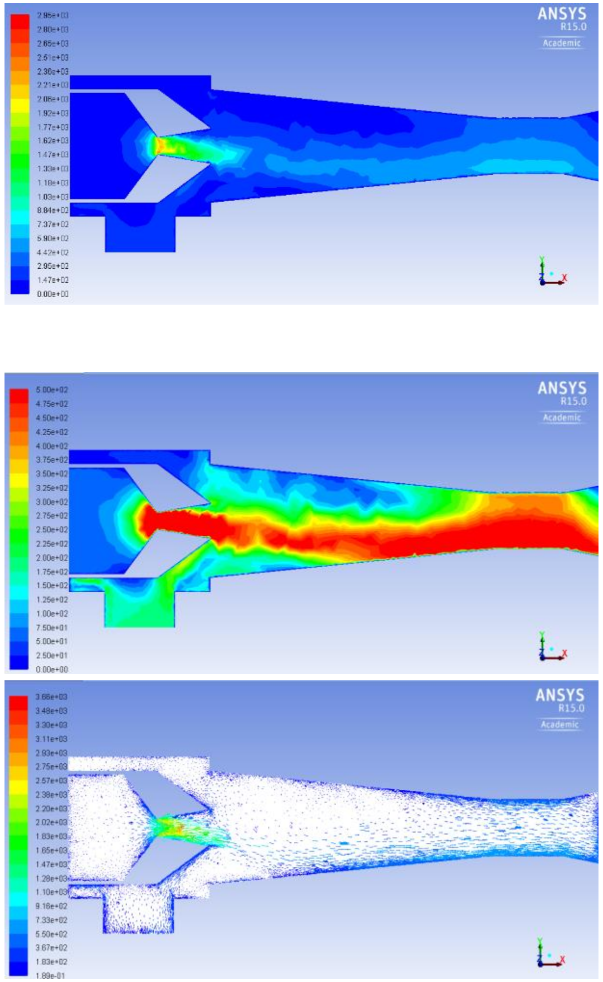


**Or-1st-30-5-10-80-20-0.06**

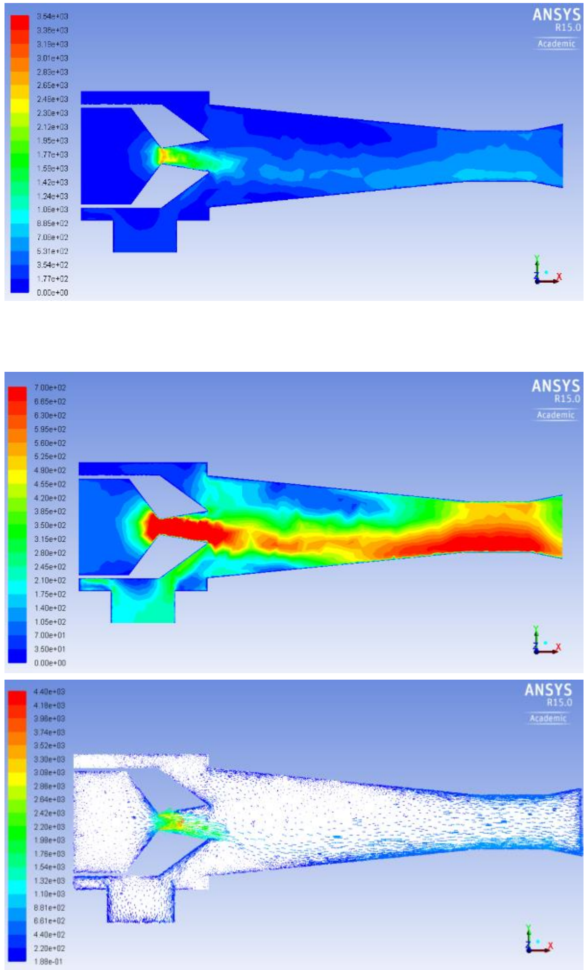

**Or-1st-30-5-10-80-30-0.01** **Or-1st-30-5-10-80-30-0.02** **Or-1st-30-5-10-80-30-0.03**

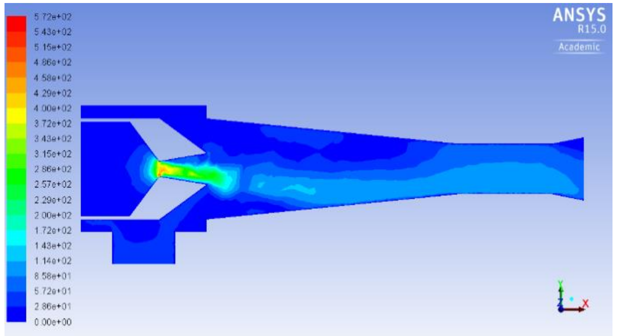
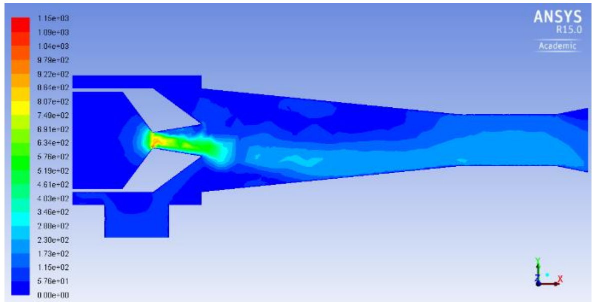
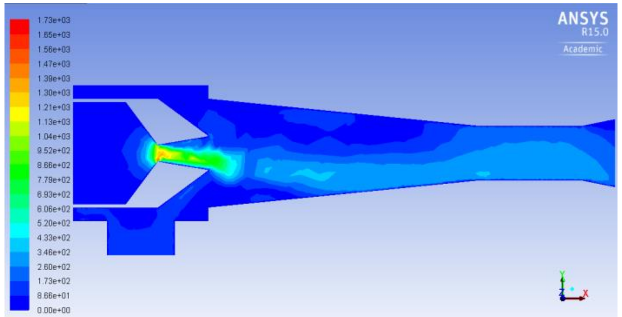

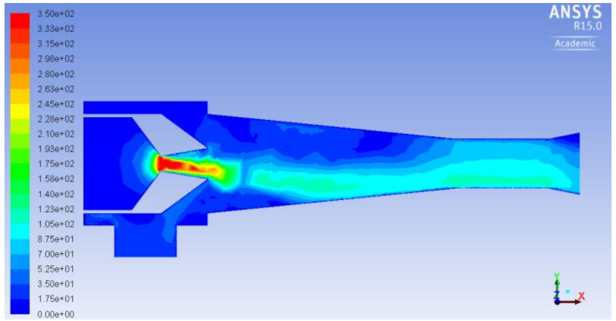
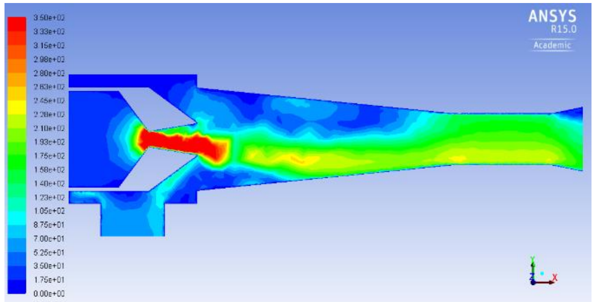
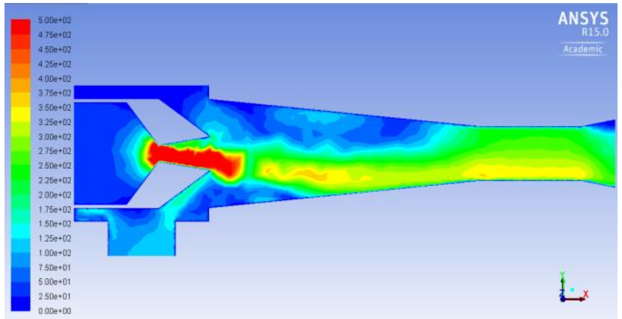

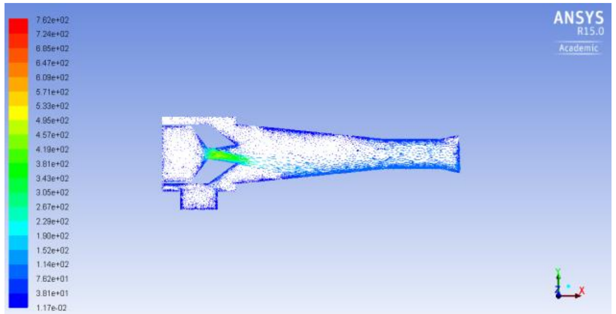
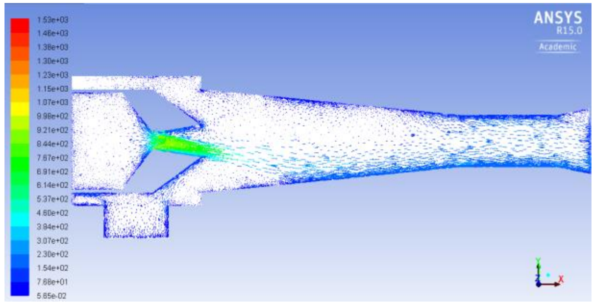
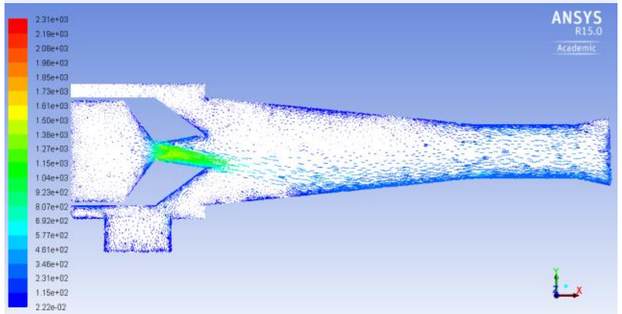

**Or-1st-30-5-10-80-30-0.04** | **Or-1st-30-5-10-80-30-0.05** | **Or-1st-30-5-10-80-30-0.06**

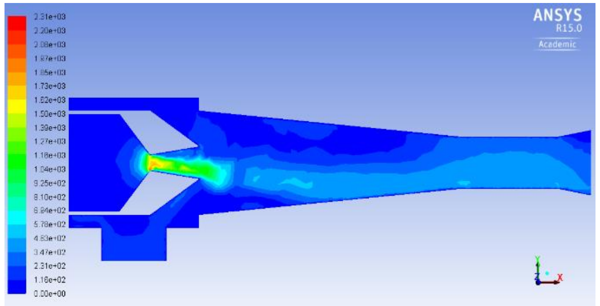


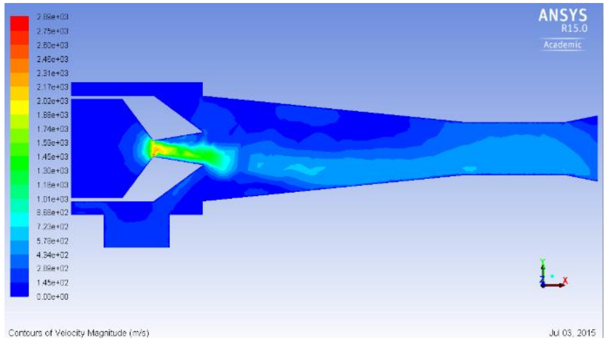


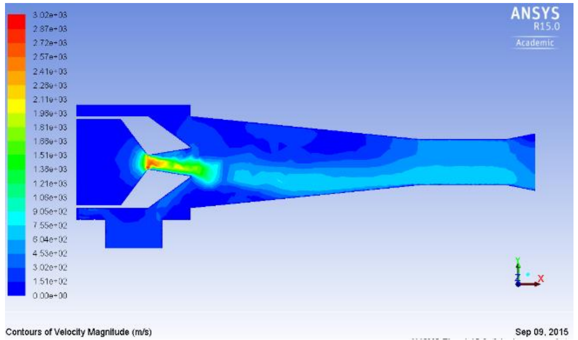


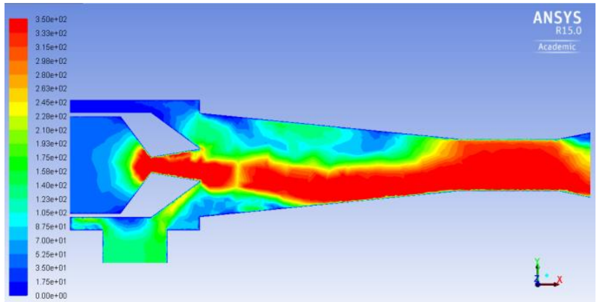


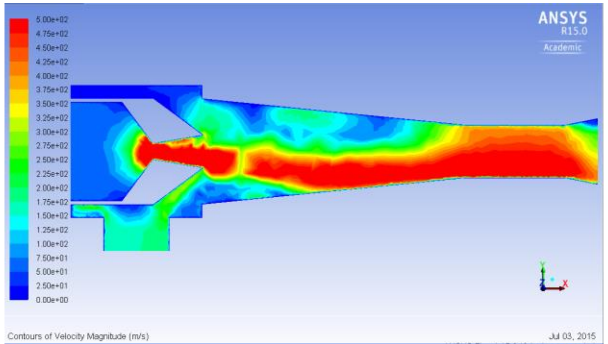


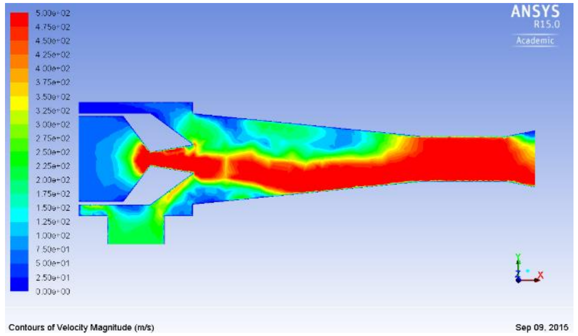


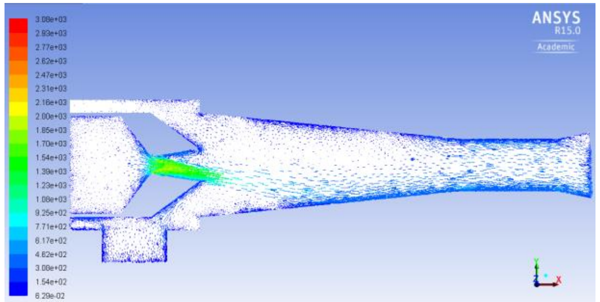


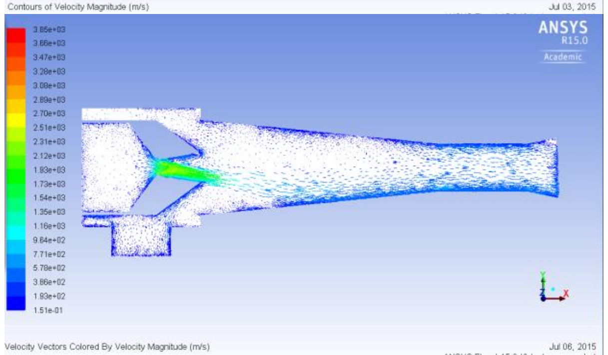


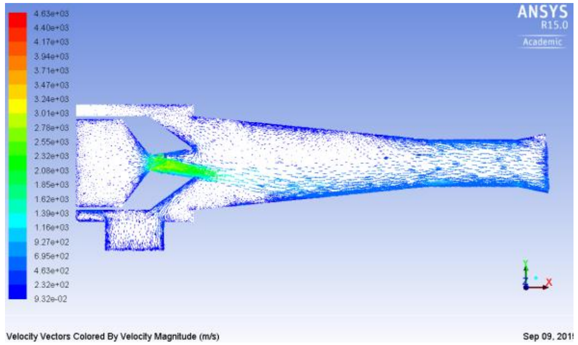

**Or-1st-30-5-10-80-50-0.01** **Or-1st-30-5-10-80-50-0.02** **Or-1st-30-5-10-80-50-0.03**

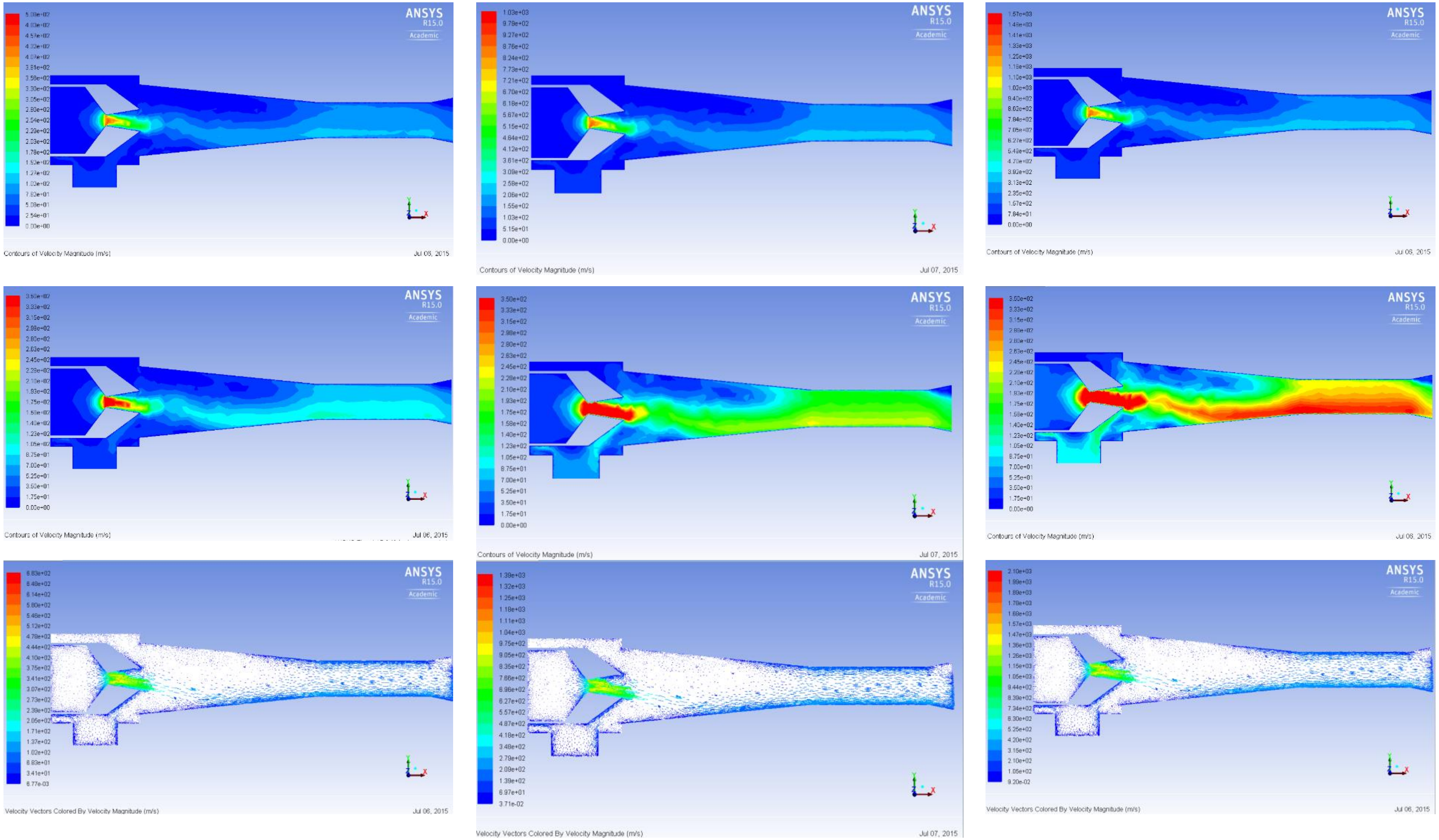

**Or-1st-30-5-10-80-50-0.04** **Or-1st-30-5-10-80-50-0.05** **Or-1st-30-5-10-80-50-0.06**

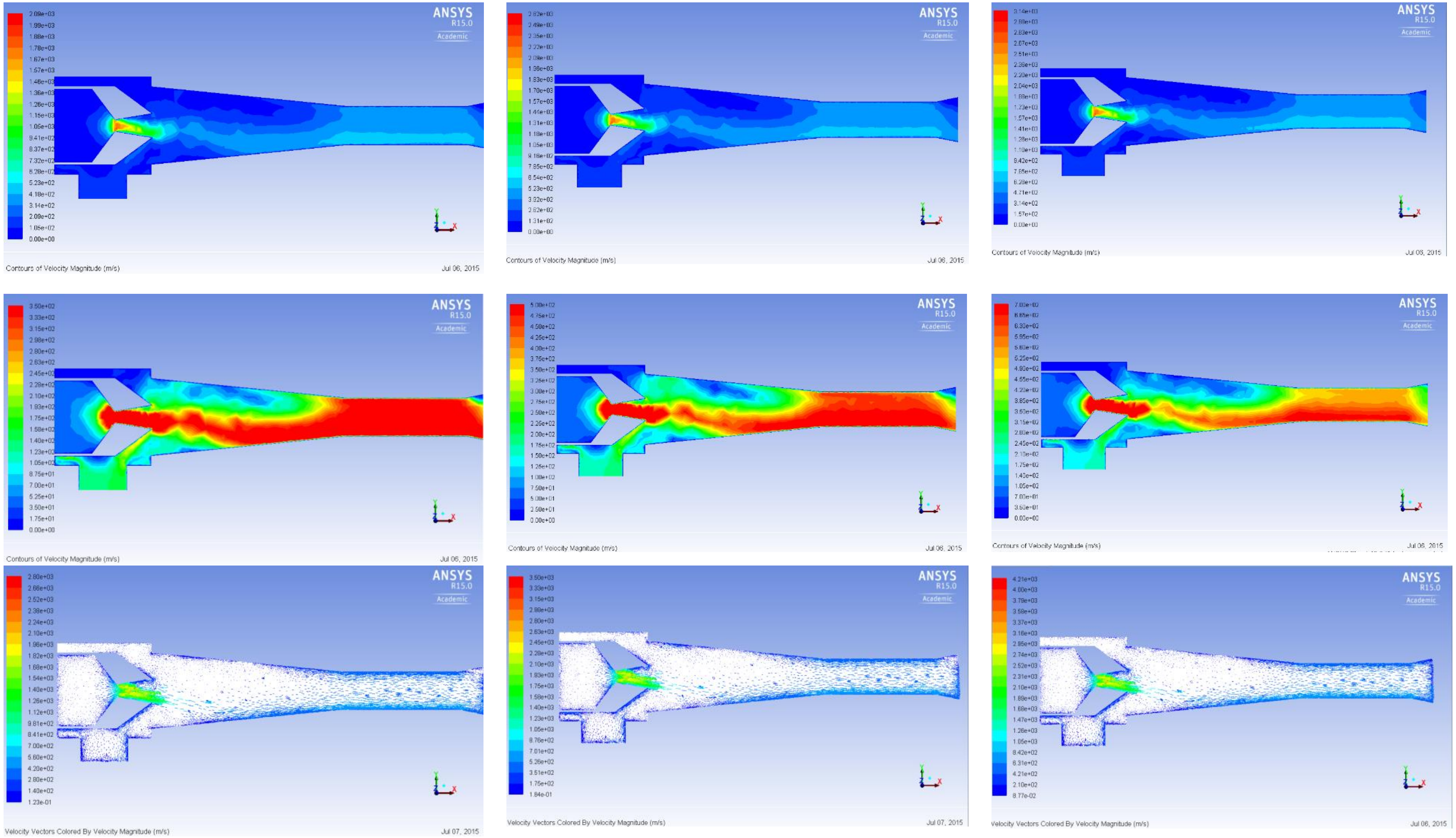

**Or-1st-30-5-10-80-60-0.01** **Or-1st-30-5-10-80-60-0.02** **Or-1st-30-5-10-80-60-0.03**

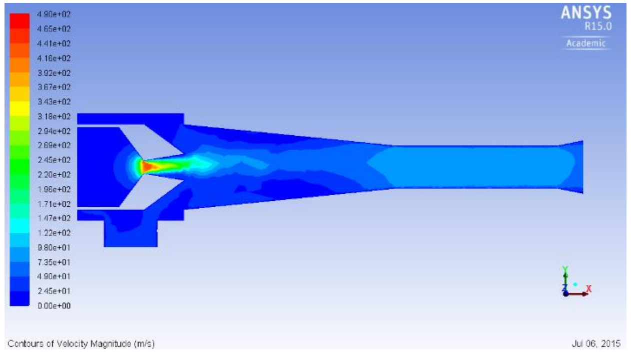


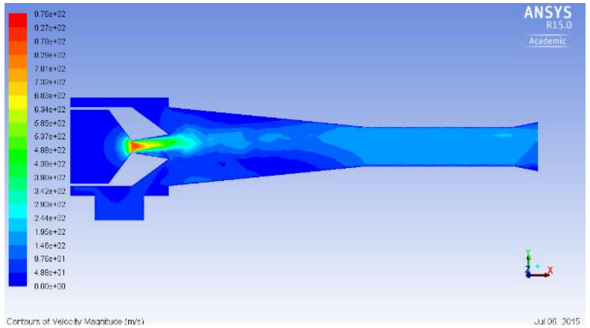


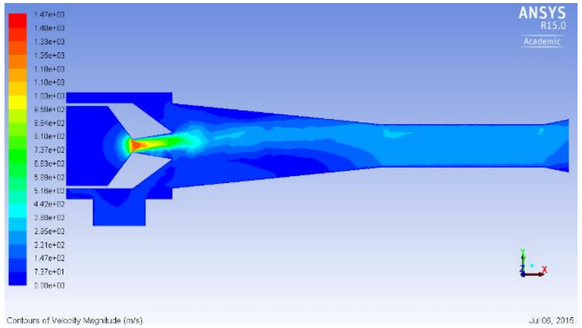


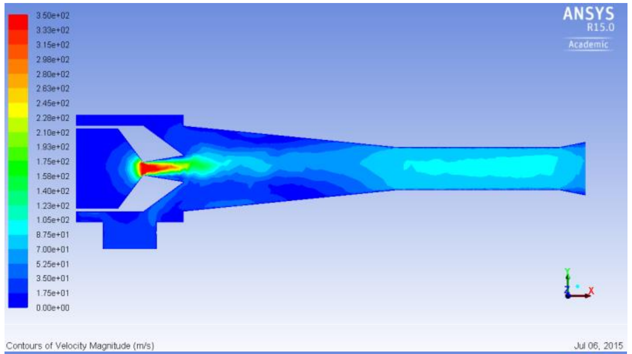


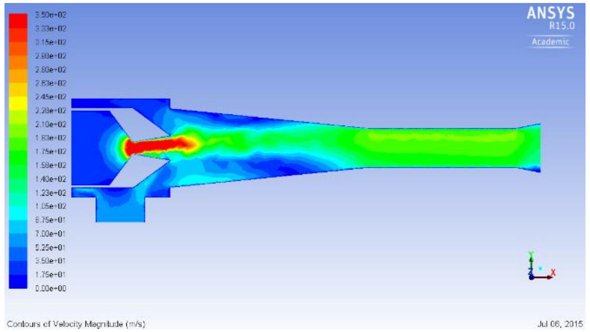


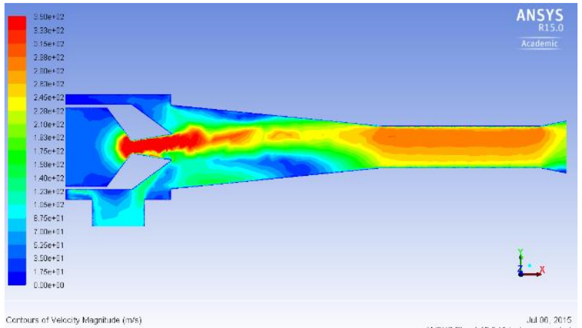


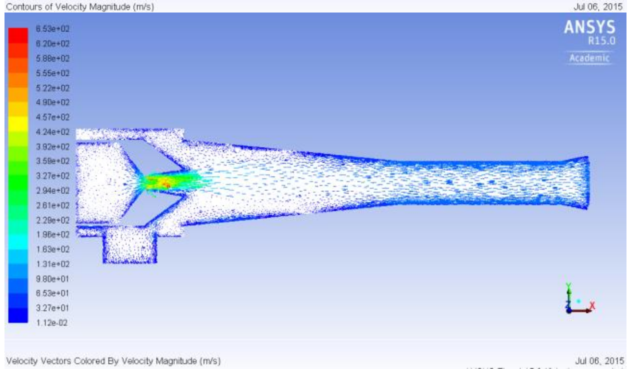


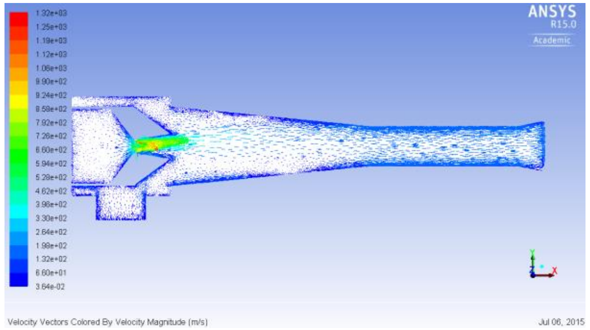


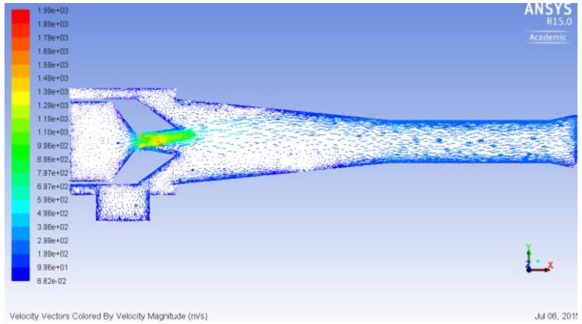

**Or-1st-30-5-10-80-60-0.04**

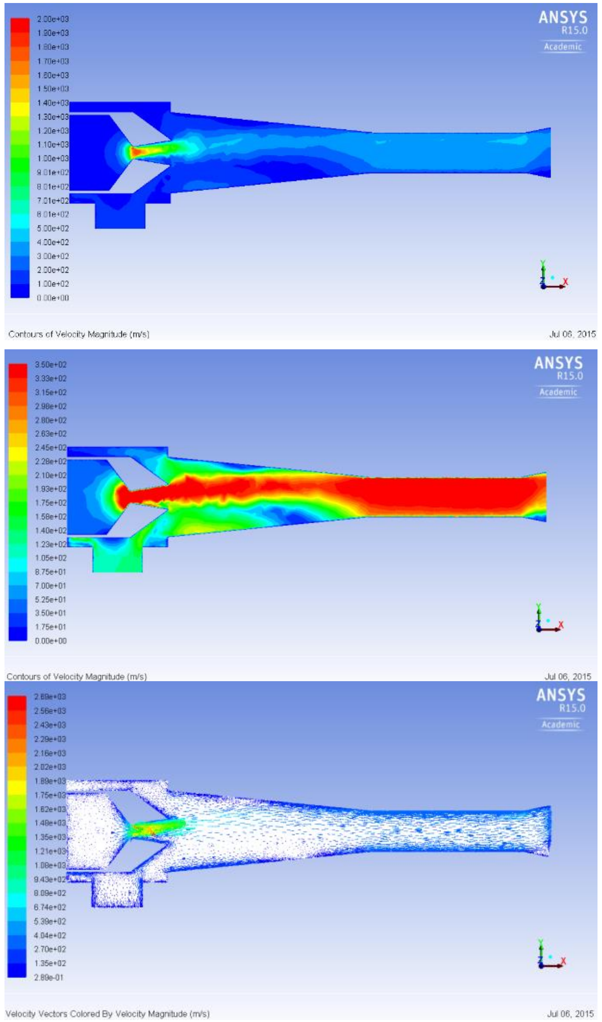


**Or-1st-30-5-10-80-60-0.05**

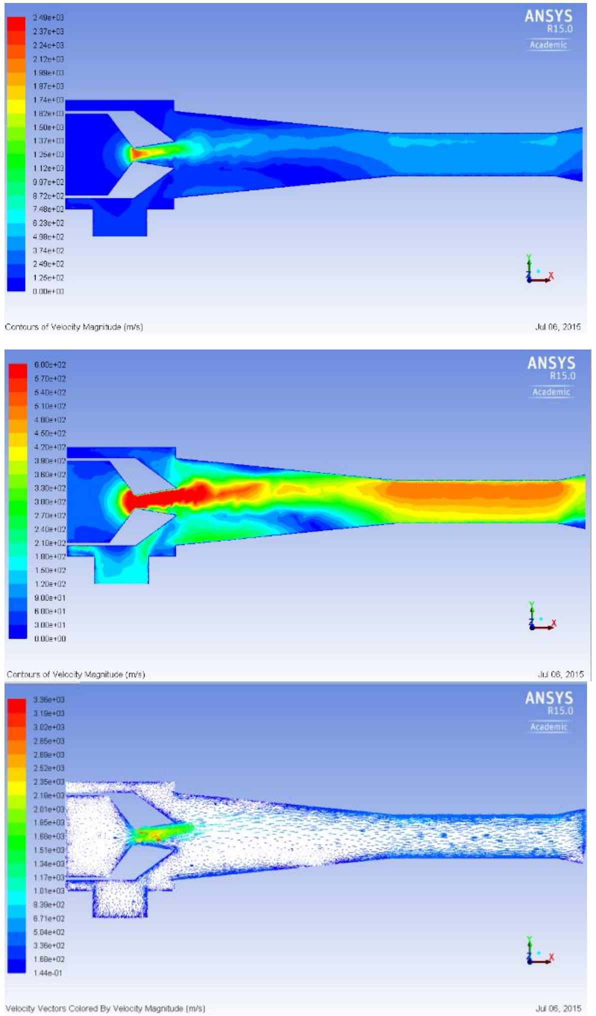


**Or-1st-30-5-10-80-60-0.06**

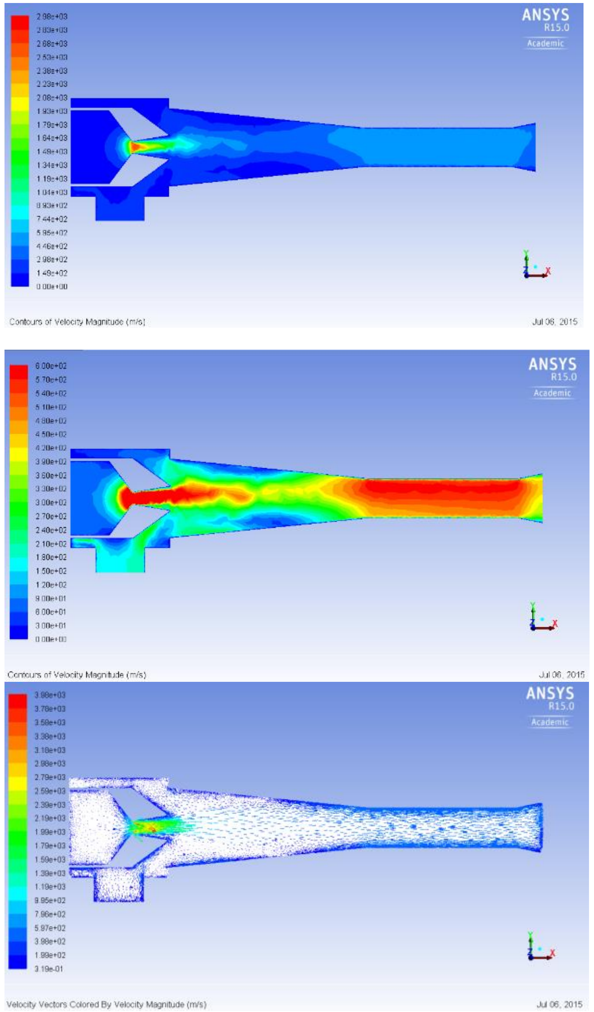

# Appendix C

## A sample of the power and voltage measurements worksheet

| | | |
|---|---|---|
| **Sample Count** | **3** | |
| | | |
| | | |
| **Sample No.1** | Ideal case | |
| **Date & Time** | 28/09/2016 19:47 | |
| | | |
| | | Ideal case |
| **V (V)** | I (A) | P (W) |
| **20.194** | 0.0163 | 0.329162 |
| **20.194** | 0.0326 | 0.658324 |
| **20.172** | 0.0489 | 0.986411 |
| **20.165** | 0.0652 | 1.314758 |
| **20.159** | 0.0815 | 1.642959 |
| **20.154** | 0.0978 | 1.971061 |
| **20.146** | 0.1141 | 2.298659 |
| **20.139** | 0.1304 | 2.626126 |
| **20.133** | 0.1467 | 2.953511 |
| **20.127** | 0.163 | 3.280701 |
| **20.118** | 0.1793 | 3.607158 |
| **20.113** | 0.1956 | 3.934103 |
| **20.106** | 0.2119 | 4.260462 |
| **20.099** | 0.2282 | 4.586592 |
| **20.092** | 0.2446 | 4.914503 |
| **20.085** | 0.2609 | 5.240176 |
| **20.078** | 0.2772 | 5.565622 |
| **20.07** | 0.2935 | 5.890545 |
| **20.064** | 0.3098 | 6.215827 |
| **20.058** | 0.3261 | 6.540914 |
| **20.052** | 0.3424 | 6.865805 |
| **20.044** | 0.3587 | 7.189782 |
| **20.034** | 0.375 | 7.51275 |
| **20.027** | 0.3913 | 7.836565 |
| **20.021** | 0.4076 | 8.16056 |
| **20.014** | 0.4239 | 8.483934 |
| **20.008** | 0.4402 | 8.807522 |
| **20.001** | 0.4565 | 9.130457 |
| **19.996** | 0.4728 | 9.454109 |
| **19.99** | 0.4892 | 9.779108 |
| **19.983** | 0.5055 | 10.10141 |
| **19.979** | 0.5218 | 10.42504 |
| **19.972** | 0.5381 | 10.74693 |

| | | |
|---|---|---|
| **19.966** | 0.5544 | 11.06915 |
| **19.958** | 0.5707 | 11.39003 |
| **V (V)** | I (A) | P (W) |
| **19.941** | 0.6033 | 12.03041 |
| **19.932** | 0.6196 | 12.34987 |
| **19.923** | 0.6359 | 12.66904 |
| **19.916** | 0.6522 | 12.98922 |
| **19.908** | 0.6685 | 13.3085 |
| **19.901** | 0.6848 | 13.6282 |
| **19.891** | 0.7011 | 13.94558 |
| **19.884** | 0.7174 | 14.26478 |
| **19.875** | 0.7338 | 14.58428 |
| **19.867** | 0.7501 | 14.90224 |
| **19.857** | 0.7664 | 15.2184 |
| **19.846** | 0.7827 | 15.53346 |
| **19.838** | 0.799 | 15.85056 |
| **19.83** | 0.8153 | 16.1674 |
| **19.817** | 0.8316 | 16.47982 |
| **19.812** | 0.8479 | 16.7986 |
| **19.803** | 0.8642 | 17.11375 |
| **19.794** | 0.8805 | 17.42862 |
| **19.782** | 0.8968 | 17.7405 |
| **19.776** | 0.9131 | 18.05747 |
| **19.764** | 0.9294 | 18.36866 |
| **19.755** | 0.9457 | 18.6823 |
| **19.745** | 0.962 | 18.99469 |
| **19.737** | 0.9784 | 19.31068 |
| **19.727** | 0.9947 | 19.62245 |
| **19.72** | 1.011 | 19.93692 |
| **19.709** | 1.0273 | 20.24706 |
| **19.7** | 1.0436 | 20.55892 |
| **19.691** | 1.0599 | 20.87049 |
| **19.68** | 1.0762 | 21.17962 |
| **19.672** | 1.0925 | 21.49166 |
| **19.663** | 1.1088 | 21.80233 |
| **19.652** | 1.1251 | 22.11047 |
| **19.642** | 1.1414 | 22.41938 |
| **19.63** | 1.1577 | 22.72565 |
| **19.621** | 1.174 | 23.03505 |
| **19.609** | 1.1903 | 23.34059 |
| **19.6** | 1.2066 | 23.64936 |
| **19.59** | 1.223 | 23.95857 |
| **19.58** | 1.2393 | 24.26549 |
| **19.571** | 1.2556 | 24.57335 |
| **19.558** | 1.2719 | 24.87582 |
| **19.548** | 1.2882 | 25.18173 |

| | | |
|---|---|---|
| **19.537** | 1.3045 | 25.48602 |
| **19.527** | 1.3208 | 25.79126 |
| **19.516** | 1.3371 | 26.09484 |
| **19.504** | 1.3534 | 26.39671 |
| **19.493** | 1.3697 | 26.69956 |
| **19.481** | 1.386 | 27.00067 |
| **19.469** | 1.4023 | 27.30138 |
| **19.458** | 1.4186 | 27.60312 |
| **19.448** | 1.4349 | 27.90594 |
| **19.434** | 1.4512 | 28.20262 |
| **19.422** | 1.4676 | 28.50373 |
| **19.409** | 1.4839 | 28.80101 |
| **19.398** | 1.5002 | 29.10088 |
| **19.384** | 1.5165 | 29.39584 |
| **19.37** | 1.5328 | 29.69034 |
| **19.358** | 1.5491 | 29.98748 |
| **19.346** | 1.5654 | 30.28423 |
| **19.333** | 1.5817 | 30.579 |
| **19.319** | 1.598 | 30.87176 |
| **19.305** | 1.6143 | 31.16406 |
| **19.293** | 1.6306 | 31.45916 |
| **19.278** | 1.6469 | 31.74894 |
| **19.266** | 1.6632 | 32.04321 |
| **19.252** | 1.6795 | 32.33373 |
| **19.237** | 1.6958 | 32.62211 |
| **19.222** | 1.7122 | 32.91191 |
| **19.209** | 1.7285 | 33.20276 |
| **19.193** | 1.7448 | 33.48795 |
| **19.175** | 1.7611 | 33.76909 |
| **19.162** | 1.7774 | 34.05854 |
| **19.145** | 1.7937 | 34.34039 |
| **19.128** | 1.81 | 34.62168 |
| **19.112** | 1.8263 | 34.90425 |
| **19.096** | 1.8426 | 35.18629 |
| **19.077** | 1.8589 | 35.46224 |
| **19.062** | 1.8752 | 35.74506 |
| **19.045** | 1.8915 | 36.02362 |
| **19.024** | 1.9078 | 36.29399 |
| **19.008** | 1.9241 | 36.57329 |
| **18.986** | 1.9404 | 36.84044 |
| **18.966** | 1.9568 | 37.11267 |
| **18.945** | 1.9731 | 37.38038 |
| **18.926** | 1.9894 | 37.65139 |
| **18.904** | 2.0057 | 37.91575 |
| **18.882** | 2.022 | 38.1794 |
| **18.858** | 2.0383 | 38.43826 |

| | | |
|---|---|---|
| **18.833** | 2.0546 | 38.69428 |
| **18.807** | 2.0709 | 38.94742 |
| **18.781** | 2.0872 | 39.1997 |
| **18.754** | 2.1035 | 39.44904 |
| **18.724** | 2.1198 | 39.69114 |
| **18.692** | 2.1361 | 39.92798 |
| **18.658** | 2.1524 | 40.15948 |
| **18.616** | 2.1687 | 40.37252 |
| **18.572** | 2.185 | 40.57982 |
| **18.517** | 2.2014 | 40.76332 |
| **18.451** | 2.2177 | 40.91878 |
| **18.34** | 2.234 | 40.97156 |
| **18.065** | 2.2503 | 40.65167 |
| **17.6** | 2.2666 | 39.89216 |
| **17.186** | 2.2829 | 39.23392 |
| **16.749** | 2.2992 | 38.5093 |
| **16.365** | 2.3155 | 37.89316 |
| **15.726** | 2.3318 | 36.66989 |
| **14.642** | 2.3481 | 34.38088 |
| **13.648** | 2.3644 | 32.26933 |
| **12.164** | 2.3807 | 28.95884 |
| **9.863** | 2.397 | 23.64161 |
| **7.76** | 2.4133 | 18.72721 |
| **5.73** | 2.4296 | 13.92161 |
| **3.344** | 2.446 | 8.179424 |

| Sample No. | 2 | |
|---|---|---|
| | Dust Effect | |
| | | |
| | | |
| **V (V)** | I (A) | P (W) |
| **17.65** | 0.0137 | 0.241805 |
| **17.649** | 0.0275 | 0.485348 |
| **17.624** | 0.0413 | 0.727871 |
| **17.618** | 0.0551 | 0.970752 |
| **17.612** | 0.0689 | 1.213467 |
| **17.606** | 0.0827 | 1.456016 |
| **17.6** | 0.0965 | 1.6984 |
| **17.593** | 0.1103 | 1.940508 |
| **17.588** | 0.1241 | 2.182671 |
| **17.581** | 0.1379 | 2.42442 |
| **17.576** | 0.1517 | 2.666279 |
| **17.568** | 0.1655 | 2.907504 |
| **17.561** | 0.1793 | 3.148687 |
| **17.554** | 0.1931 | 3.389677 |
| **17.548** | 0.2069 | 3.630681 |
| **17.542** | 0.2207 | 3.871519 |
| **17.535** | 0.2345 | 4.111958 |
| **17.529** | 0.2483 | 4.352451 |
| **17.523** | 0.2621 | 4.592778 |
| **17.515** | 0.2759 | 4.832389 |
| **17.508** | 0.2897 | 5.072068 |
| **17.503** | 0.3035 | 5.312161 |
| **17.496** | 0.3173 | 5.551481 |
| **17.489** | 0.3311 | 5.790608 |
| **17.482** | 0.3449 | 6.029542 |
| **17.475** | 0.3587 | 6.268283 |
| **17.468** | 0.3725 | 6.50683 |
| **17.46** | 0.3863 | 6.744798 |
| **17.454** | 0.4001 | 6.983345 |
| **17.447** | 0.4139 | 7.221313 |
| **17.441** | 0.4276 | 7.457772 |
| **17.434** | 0.4414 | 7.695368 |
| **17.426** | 0.4552 | 7.932315 |
| **17.42** | 0.469 | 8.16998 |
| **17.413** | 0.4828 | 8.406996 |
| **17.408** | 0.4966 | 8.644813 |
| **17.398** | 0.5104 | 8.879939 |
| **17.391** | 0.5242 | 9.116362 |
| **17.383** | 0.538 | 9.352054 |

| | | |
|---|---|---|
| **17.376** | 0.5518 | 9.588077 |
| **17.369** | 0.5656 | 9.823906 |
| **17.363** | 0.5794 | 10.06012 |
| **17.354** | 0.5932 | 10.29439 |
| **17.346** | 0.607 | 10.52902 |
| **17.34** | 0.6208 | 10.76467 |
| **17.333** | 0.6346 | 10.99952 |
| **17.324** | 0.6484 | 11.23288 |
| **17.317** | 0.6622 | 11.46732 |
| **17.309** | 0.676 | 11.70088 |
| **17.301** | 0.6898 | 11.93423 |
| **17.293** | 0.7036 | 12.16735 |
| **17.284** | 0.7174 | 12.39954 |
| **17.276** | 0.7312 | 12.63221 |
| **17.269** | 0.745 | 12.86541 |
| **17.261** | 0.7588 | 13.09765 |
| **17.253** | 0.7726 | 13.32967 |
| **17.245** | 0.7864 | 13.56147 |
| **17.236** | 0.8002 | 13.79225 |
| **17.228** | 0.814 | 14.02359 |
| **17.22** | 0.8278 | 14.25472 |
| **17.212** | 0.8415 | 14.4839 |
| **17.203** | 0.8553 | 14.71373 |
| **17.193** | 0.8691 | 14.94244 |
| **17.183** | 0.8829 | 15.17087 |
| **17.175** | 0.8967 | 15.40082 |
| **17.166** | 0.9105 | 15.62964 |
| **17.156** | 0.9243 | 15.85729 |
| **17.147** | 0.9381 | 16.0856 |
| **17.139** | 0.9519 | 16.31461 |
| **17.131** | 0.9657 | 16.54341 |
| **17.12** | 0.9795 | 16.76904 |
| **17.112** | 0.9933 | 16.99735 |
| **17.102** | 1.0071 | 17.22342 |
| **17.091** | 1.0209 | 17.4482 |
| **17.082** | 1.0347 | 17.67475 |
| **17.073** | 1.0485 | 17.90104 |
| **17.063** | 1.0623 | 18.12602 |
| **17.054** | 1.0761 | 18.35181 |
| **17.044** | 1.0899 | 18.57626 |
| **17.032** | 1.1037 | 18.79822 |
| **17.022** | 1.1175 | 19.02209 |
| **17.012** | 1.1313 | 19.24568 |
| **17** | 1.1451 | 19.4667 |

| | | |
|---|---|---|
| **16.991** | 1.1589 | 19.69087 |
| **16.978** | 1.1727 | 19.9101 |
| **16.967** | 1.1865 | 20.13135 |
| **16.955** | 1.2003 | 20.35109 |
| **16.944** | 1.2141 | 20.57171 |
| **16.934** | 1.2279 | 20.79326 |
| **16.921** | 1.2417 | 21.01081 |
| **16.91** | 1.2554 | 21.22881 |
| **16.898** | 1.2692 | 21.44694 |
| **16.885** | 1.283 | 21.66346 |
| **16.873** | 1.2968 | 21.88091 |
| **16.86** | 1.3106 | 22.09672 |
| **16.848** | 1.3244 | 22.31349 |
| **16.834** | 1.3382 | 22.52726 |
| **16.822** | 1.352 | 22.74334 |
| **16.809** | 1.3658 | 22.95773 |
| **16.796** | 1.3796 | 23.17176 |
| **16.782** | 1.3934 | 23.38404 |
| **16.767** | 1.4072 | 23.59452 |
| **16.753** | 1.421 | 23.80601 |
| **16.742** | 1.4348 | 24.02142 |
| **16.727** | 1.4486 | 24.23073 |
| **16.712** | 1.4624 | 24.43963 |
| **16.697** | 1.4762 | 24.64811 |
| **16.68** | 1.49 | 24.8532 |
| **16.666** | 1.5038 | 25.06233 |
| **16.651** | 1.5176 | 25.26956 |
| **16.634** | 1.5314 | 25.47331 |
| **16.617** | 1.5452 | 25.67659 |
| **16.6** | 1.559 | 25.8794 |
| **16.585** | 1.5728 | 26.08489 |
| **16.567** | 1.5866 | 26.2852 |
| **16.55** | 1.6004 | 26.48662 |
| **16.53** | 1.6142 | 26.68273 |
| **16.511** | 1.628 | 26.87991 |
| **16.493** | 1.6418 | 27.07821 |
| **16.474** | 1.6556 | 27.27435 |
| **16.454** | 1.6693 | 27.46666 |
| **16.432** | 1.6831 | 27.6567 |
| **16.409** | 1.6969 | 27.84443 |
| **16.382** | 1.7107 | 28.02469 |
| **16.361** | 1.7245 | 28.21454 |
| **16.335** | 1.7383 | 28.39513 |
| **16.306** | 1.7521 | 28.56974 |

| | | |
|---|---|---|
| **16.276** | 1.7659 | 28.74179 |
| **16.242** | 1.7797 | 28.90589 |
| **16.204** | 1.7935 | 29.06187 |
| **16.159** | 1.8073 | 29.20416 |
| **16.103** | 1.8211 | 29.32517 |
| **16.014** | 1.8349 | 29.38409 |
| **15.817** | 1.8487 | 29.24089 |
| **15.464** | 1.8625 | 28.8017 |
| **15.134** | 1.8763 | 28.39592 |
| **14.817** | 1.8901 | 28.00561 |
| **14.48** | 1.9039 | 27.56847 |
| **14.157** | 1.9177 | 27.14888 |
| **13.816** | 1.9315 | 26.6856 |
| **13.425** | 1.9453 | 26.11565 |
| **12.71** | 1.9591 | 24.90016 |
| **11.718** | 1.9729 | 23.11844 |
| **10.578** | 1.9867 | 21.01531 |
| **8.828** | 2.0005 | 17.66041 |
| **7.012** | 2.0143 | 14.12427 |
| **5.371** | 2.0281 | 10.89293 |
| **3.79** | 2.0419 | 7.738801 |
| **1.956** | 2.0557 | 4.020949 |
| **1.322** | 2.0695 | 2.735879 |
| | | |

| **Sample No.3** | **After cleaning** | |
|---|---|---|
| | | |
| | | |
| | | |
| **V (V)** | I (A) | P (W) |
| **19.503** | 0.0167 | 0.3257 |
| **19.503** | 0.0334 | 0.6514 |
| **19.477** | 0.0502 | 0.977745 |
| **19.468** | 0.0669 | 1.302409 |
| **19.46** | 0.0836 | 1.626856 |
| **19.453** | 0.1004 | 1.953081 |
| **19.447** | 0.1171 | 2.277244 |
| **19.438** | 0.1338 | 2.600804 |
| **19.429** | 0.1506 | 2.926007 |
| **19.422** | 0.1673 | 3.249301 |
| **19.414** | 0.184 | 3.572176 |
| **19.407** | 0.2008 | 3.896926 |
| **19.399** | 0.2175 | 4.219283 |
| **19.391** | 0.2342 | 4.541372 |
| **19.384** | 0.251 | 4.865384 |
| **19.374** | 0.2677 | 5.18642 |
| **19.366** | 0.2844 | 5.50769 |
| **19.359** | 0.3012 | 5.830931 |
| **19.352** | 0.3179 | 6.152001 |
| **19.343** | 0.3346 | 6.472168 |
| **19.335** | 0.3514 | 6.794319 |
| **19.328** | 0.3681 | 7.114637 |
| **19.321** | 0.3848 | 7.434721 |
| **19.313** | 0.4016 | 7.756101 |
| **19.303** | 0.4183 | 8.074445 |
| **19.296** | 0.435 | 8.39376 |
| **19.288** | 0.4518 | 8.714318 |
| **19.279** | 0.4685 | 9.032212 |
| **19.272** | 0.4852 | 9.350774 |
| **19.263** | 0.502 | 9.670026 |
| **19.255** | 0.5187 | 9.987569 |
| **19.247** | 0.5354 | 10.30484 |
| **19.238** | 0.5522 | 10.62322 |
| **19.232** | 0.5689 | 10.94108 |
| **19.222** | 0.5856 | 11.2564 |
| **19.213** | 0.6024 | 11.57391 |
| **19.206** | 0.6191 | 11.89043 |
| **19.198** | 0.6358 | 12.20609 |
| **19.19** | 0.6526 | 12.52339 |

| | | |
|---|---|---|
| **19.18** | 0.6693 | 12.83717 |
| **19.171** | 0.686 | 13.15131 |
| **19.161** | 0.7028 | 13.46635 |
| **19.153** | 0.7195 | 13.78058 |
| **19.143** | 0.7362 | 14.09308 |
| **19.135** | 0.753 | 14.40866 |
| **19.126** | 0.7697 | 14.72128 |
| **19.118** | 0.7864 | 15.0344 |
| **19.108** | 0.8032 | 15.34755 |
| **19.098** | 0.8199 | 15.65845 |
| **19.09** | 0.8366 | 15.97069 |
| **19.078** | 0.8534 | 16.28117 |
| **19.07** | 0.8701 | 16.59281 |
| **19.062** | 0.8868 | 16.90418 |
| **19.052** | 0.9036 | 17.21539 |
| **19.039** | 0.9203 | 17.52159 |
| **19.031** | 0.937 | 17.83205 |
| **19.019** | 0.9538 | 18.14032 |
| **19.01** | 0.9705 | 18.44921 |
| **19** | 0.9872 | 18.7568 |
| **18.989** | 1.004 | 19.06496 |
| **18.979** | 1.0207 | 19.37187 |
| **18.969** | 1.0374 | 19.67844 |
| **18.958** | 1.0542 | 19.98552 |
| **18.946** | 1.0709 | 20.28927 |
| **18.936** | 1.0876 | 20.59479 |
| **18.925** | 1.1044 | 20.90077 |
| **18.913** | 1.1211 | 21.20336 |
| **18.9** | 1.1378 | 21.50442 |
| **18.888** | 1.1546 | 21.80808 |
| **18.877** | 1.1713 | 22.11063 |
| **18.865** | 1.188 | 22.41162 |
| **18.854** | 1.2048 | 22.7153 |
| **18.841** | 1.2215 | 23.01428 |
| **18.831** | 1.2382 | 23.31654 |
| **18.819** | 1.255 | 23.61785 |
| **18.805** | 1.2717 | 23.91432 |
| **18.792** | 1.2884 | 24.21161 |
| **18.778** | 1.3052 | 24.50905 |
| **18.767** | 1.3219 | 24.8081 |
| **18.754** | 1.3386 | 25.1041 |
| **18.74** | 1.3554 | 25.4002 |
| **18.727** | 1.3721 | 25.69532 |
| **18.711** | 1.3888 | 25.98584 |

| | | |
|---|---|---|
| **18.697** | 1.4056 | 26.2805 |
| **18.684** | 1.4223 | 26.57425 |
| **18.671** | 1.439 | 26.86757 |
| **18.657** | 1.4558 | 27.16086 |
| **18.642** | 1.4725 | 27.45035 |
| **18.628** | 1.4892 | 27.74082 |
| **18.61** | 1.506 | 28.02666 |
| **18.595** | 1.5227 | 28.31461 |
| **18.578** | 1.5394 | 28.59897 |
| **18.564** | 1.5562 | 28.8893 |
| **18.549** | 1.5729 | 29.17572 |
| **18.531** | 1.5896 | 29.45688 |
| **18.514** | 1.6064 | 29.74089 |
| **18.496** | 1.6231 | 30.02086 |
| **18.48** | 1.6398 | 30.3035 |
| **18.462** | 1.6566 | 30.58415 |
| **18.447** | 1.6733 | 30.86737 |
| **18.426** | 1.69 | 31.13994 |
| **18.407** | 1.7068 | 31.41707 |
| **18.389** | 1.7235 | 31.69344 |
| **18.368** | 1.7402 | 31.96399 |
| **18.347** | 1.757 | 32.23568 |
| **18.327** | 1.7737 | 32.5066 |
| **18.306** | 1.7904 | 32.77506 |
| **18.282** | 1.8072 | 33.03923 |
| **18.259** | 1.8239 | 33.30259 |
| **18.236** | 1.8406 | 33.56518 |
| **18.208** | 1.8574 | 33.81954 |
| **18.185** | 1.8741 | 34.08051 |
| **18.158** | 1.8908 | 34.33315 |
| **18.131** | 1.9076 | 34.5867 |
| **18.099** | 1.9243 | 34.82791 |
| **18.067** | 1.941 | 35.06805 |
| **18.028** | 1.9578 | 35.29522 |
| **17.986** | 1.9745 | 35.51336 |
| **17.938** | 1.9912 | 35.71815 |
| **17.87** | 2.008 | 35.88296 |
| **17.696** | 2.0247 | 35.82909 |
| **17.352** | 2.0414 | 35.42237 |
| **16.943** | 2.0582 | 34.87208 |
| **16.562** | 2.0749 | 34.36449 |
| **16.197** | 2.0916 | 33.87765 |
| **15.862** | 2.1084 | 33.44344 |
| **15.478** | 2.1251 | 32.8923 |

| | | |
|---|---|---|
| **15.098** | 2.1418 | 32.3369 |
| **14.714** | 2.1586 | 31.76164 |
| **14.305** | 2.1753 | 31.11767 |
| **13.54** | 2.192 | 29.67968 |
| **12.489** | 2.2088 | 27.5857 |
| **11.553** | 2.2255 | 25.7112 |
| **10.666** | 2.2422 | 23.91531 |
| **9.853** | 2.259 | 22.25793 |
| **9.094** | 2.2757 | 20.69522 |
| **8.623** | 2.2924 | 19.76737 |
| **8.472** | 2.3092 | 19.56354 |
| **8.261** | 2.3259 | 19.21426 |
| **7.896** | 2.3426 | 18.49717 |
| **7.522** | 2.3594 | 17.74741 |
| **7.173** | 2.3761 | 17.04377 |
| **6.807** | 2.3928 | 16.28779 |
| **6.436** | 2.4096 | 15.50819 |
| **6.013** | 2.4263 | 14.58934 |
| **5.06** | 2.443 | 12.36158 |
| **3.595** | 2.4598 | 8.842981 |
| **2.342** | 2.4765 | 5.799963 |